Single-artificial-atom lasing of a dressed flux qubit

Dissertation

zur Erlangung des akademischen Grades

doctor rerum naturalium (Dr. rer. nat.)

vorgelegt dem Rat der Physikalisch-Astronomischen Fakultät
der Friedrich-Schiller-Universität Jena

von Dipl.-Phys. Gregor Oelsner
geboren am 22. August 1983 in Schleiz

Gutachter:

1. Prof. Dr. Paul Seidel
   Friedrich Schiller Universität, Jena
2. Prof. Dr. Frank Wilhelm-Mauch
   Universität des Saarlandes, Saarbrücken
3. Reader Dr. Alexandre Zagoskin
   Loughborough University, Loughborough, UK

Tag der Disputation: 3. November 2016

Contents

Introduction **1**

1 Basics - Superconductivity and Josephson effect **5**
1.1 Short introduction to superconductivity 5
1.2 Flux quantization 7
1.3 The Josephson effect 9
1.4 Quantum mechanics of a Josephson junction 11

2 Theoretical analysis of flux qubits and cavities **13**
2.1 The quantum two-level system 13
2.2 The superconducting flux qubit 14
2.3 The flux qubit as quantum two-level system 18
2.4 Coupling to the environment - Relaxation and Decoherence 20
2.5 The superconducting CPW resonator 22
2.6 Hamiltonian of a CPW resonator 24
2.7 Coupling the resonator to its environment 29
2.8 Relaxation of the resonator 32
2.9 Input field and transmission coefficient 33

3 Experimental requirements and setup **37**
3.1 Experimental setup 37
3.2 Measurement setup 38
3.3 Sample fabrication and preparation 40

4 Coupling a flux qubit to a resonator **43**
4.1 Magnetic coupling 43

4.2 Continuous monitoring of a flux qubit with a CPW resonator 46
4.3 Two-tone spectroscopy 49
4.4 Transmission of the qubit-resonator system 53

5 Dressed qubit-resonator system and lasing 61
5.1 Strong AC-Zeeman shift and three-tone spectroscopy 61
5.2 The dressed qubit 65
5.3 Coupling between the dressed qubit and the resonator 69
5.4 Dressed-state lasing of a single artificial two-level system 75
5.5 Emission from the dressed qubit and lasing 81
5.6 Strong driving - Beyond the two-level approximation 85

Summary 97

Acknowledgment 99

Appendix 101
A Notes to the qubit and the resonator 101
A.1 Kinetic part of the flux qubit Hamiltonian 101
A.2 Diagonalizing the Hamiltonian 102
A.3 Classical results of the resonator 104
B Time evolution of the density matrix by damping 106
B.1 Qubit dissipation 106
B.2 Resonator photon decay 107
C Basic transformations 110
C.1 Rotating frames 110
C.2 Dispersive regime 111
C.3 Dressed-state basis 112
C.4 Eigenbasis of the multiphoton driven qubit 118
C.5 Two-photon interaction with the fundamental mode 119

List of Symbols 121

References 129

Publications in Peer-reviewed Journals 141

Conference Contributions **143**

Ehrenwörtliche Erklärung **145**

Zusammenfassung **147**

Introduction

In general, a laser consists of a material for which an inverse level population can be created and that is brought into a cavity. The frequency of the level splitting should correspond to a supported mode of the cavity. For the creation of the inverse population at least a three level system is needed. By driving resonantly at the energy difference between the highest and lowest together with a fast decay from the highest to the middle level, the population is shifted to the middle level. In addition, the relaxation rate from the middle to the lowest level should be small. Then, by stimulated emission coherent photons are created inside the cavity giving several advantages over classical light sources [1].

Nevertheless, the first realization of a maser, a laser working in the microwave frequency domain, as reported in 1954 [2], used a slightly different approach. It separated the molecules that showed level inversion from the rest and brought them into a cavity. Importantly, it was found that if the microwave power drained from the molecules exceeds the losses of the cavity "self-sustained oscillations will result". The first lasing in the optical domain was observed in 1960 [3]. It exploited a three level scheme as described above on Ruby.

As already mentioned, the losses in the media and of the cavity need to be compensated by the stimulated emission. In addition, the atom field coupling in the optical domain is rather weak, because the dipole moment of classical atoms is small. Thus, in conventional lasers a large number of atoms with inverse population need to be brought into a cavity, and it was not before 2003 that lasing was found using only a single atom [4]. Many technical advancements were necessary to achieve the required strong atom-photon interaction, including the trapping of single atoms or ions [5–7], their laser cooling [8–10], and the development of the field of cavity quantum electrodynamic (CQED) [11]. On the other hand, CQED experiments are now repeated on other objects as well, including macroscopic solid-state systems such as superconducting quantum circuits.

Their key element is the Josephon junction [12] which acts as non-linear oscillator. For

small-scale junctions below sizes of 1 μm the system needs to be quantized and macroscopic quantum tunneling (MQT) has been discussed [13, 14] and observed [15–18] in various experiments. More control over the circuit parameters was gained with technical advances in the production of sub-micron sized Josephson junctions [19–21]. These methods enabled the first coherent experiments on artificial quantum structures [22]. Driven by the aim of quantum computing different building blocks such as the flux qubit [23, 24], the charge qubit [25–28], and latest the transmon [29, 30] were developed and investigated.

Two possible ways in the realization of quantum calculations can be identified. The first one follows the approach of adiabatic quantum computing [31–33]. There the calculation is done by adiabatically transferring a system from a starting, easy to prepare ground state to a configuration where the system encodes the solution of a problem in its ground state. The calculation speed is then limited by the effective level splitting between the lowest and any higher energetic state. For this purpose a low frequency tank circuit measurement technique was developed to identify the ground state of a superconducting quantum system [34–36]. For the implementation of different architectures scientific analyses were carried out on the entanglement of two coupled flux qubits [37, 38], the characterization of a three-qubit structure [39], and a four-qubit device [40]. In addition, schemes for controlling the coupling between two qubits were proposed and realized [41–44].

The second approach has a closer analogy to classical computers, thus exploring transitions between two states of a quantum object, whereat one encodes a logical zero and the other a one. In recent years, great achievements have been made in this field, including single qubit gate operations [45, 46], coupling and logical operations of two qubits [47–49], and the detection of quantum states [50–52]. They resulted in the realization of two-qubit algorithms [53] and the Toffoli gate [54] exploring solid-state quantum systems. The main difficulty in realizing large scale processors is the relatively fast decoherence of solid-state quantum systems [55]. It results from the strong coupling to external noise sources [56] that, on the other hand, ensures fast gate operations. Nevertheless, the systems were optimized for example by making the charge qubit insensitive to charge noise [30], developing a gradiometer type flux qubit reducing flux noise effects [57], and maybe most important including the qubits into a microwave cavity [58–61]. The longest coherence times have been achieved at transmon qubits placed in three dimensional cavities [62, 63]. Interestingly, the transmon qubits loose some of their controllability, since there level spacing is fixed by the fabrication process and the cavity shields the qubit from unwanted external signals. This smaller

coupling also brings difficulties in the entanglement with other external objects. Thus, the analogy to a real atom in a cavity becomes more pronounced.

These obvious similarities led to the repetition of original quantum optical experiments with solid-state objects in the microwave domain [64]. Important examples are the observation of the vacuum Rabi splitting [59], the resonance fluorescence of a single qubit placed to a transmission line [65], the observation of the Autler-Townes effect [66], and the electromagnetically induced transparency [67]. The main advantage of solid-state systems is their controllability. By a proper circuit design it is rather simple to achieve the strong coupling regime. Thus, it is not surprising that the single artificial-atom laser was realized [68]. Here, with full control over the excitation process the inverse population was achieved in a three level scheme.

In this work, a novel, different approach for lasing by a single flux qubit inside of a microwave cavity is developed. It makes use of only two qubit levels. By a strong off resonant driving signal the energy level splitting and the corresponding dissipative rates can be altered and controlled. Thus, a population inversion may be created by an effective excitation that is driven by the qubit's relaxation. This effect is experimentally investigated for the first time and supported by a corresponding quantum theory.

This thesis is organized in five chapters.

Chapter 1 gives a short overview of the basics of superconductivity and the Josephson effect that will be necessary for the description of superconducting qubits.

In **Chapter 2** a theoretical analysis is carried out, and a quantum theory for flux qubits as well as for coplanar waveguide (CPW) resonators is separately developed.

Chapter 3 deals briefly with experimental requirements and covers the measurement setup, methods for achieving the presented results as well as the sample fabrication.

Chapter 4 summarizes the basic characterization of the device. It explains the coupling between the sub-systems of Chapter 2. Also the system parameters are determined from experimental results and a mathematical analysis based on the density matrix formalism is derived.

Chapter 5 then introduces the scheme for creating the single-atom laser. The system is described in the dressed-state picture. Also, a detailed analysis of the modification of the level structure and of the dissipative rates is given. The achieved measurement results on an optimized device are presented and compared to theoretical predictions. Finally, a gen-

eral theory that summarizes experiments of the pump-probe kind is derived and applied to different achieved measurement results.

The essential findings of the thesis are summarized in a conclusion.

1 Basics - Superconductivity and Josephson effect

1.1 Short introduction to superconductivity

Electric resistivity of metals yields from the interaction of conduction electrons with lattice imperfections and phonons[1]. When lowering the temperature the number of thermal activated phonons is reduced. Therefore, one expects an increase of conductivity till it is limited only by impurities.

In 1911 Heike Kamerlingh Onnes discovered the "Disappearance of the resistance of mercury" at a temperature slightly above the boiling point of liquid Helium [69]. The effect he had found is superconductivity. It describes a phase transition at a critical temperature T_c that is found in several elements and materials. In table 1.1 the critical temperatures of metals used in this work are displayed.

Metal	T_c (K)	λ_L (nm)
Nb	9.2	32-44
Pb	7.2	32-39
Al	1.19	50

Table 1.1: Values of critical temperature T_c and London penetration depth $\lambda_L(T = 0)$ for selected materials (from [70]).

The vanishing of the resistance at low temperatures yields from the pairing of electrons with opposite spin to so called Cooper pairs. It arises from a weak attractive coupling mechanism,

[1] Phonons are quantized lattice vibration. They act as quasiparticles in solid-state physics, since a quasi-momentum (no mass transport) and energy can be assigned to them.

which for conventional superconductors is given by electron phonon interaction. The energy gap for single-particle excitations is found in the theory of Bardeen, Cooper and Schrieffer (BCS) [71] as $2G = 3.5k_{\mathrm{B}}T_{\mathrm{c}}$. Thus, low temperatures are needed to avoid breaking of the pairs by thermal excitation. Because the paired particles have an integral spin, they can be treated as Bosons. The total wave vector of a pair as sum of the electrons wave vectors $\vec{q} = \vec{k}_1 + \vec{k}_2$ is the same for all pairs. This quality enables the Cooper pairs to occupy the same quantum state. A description with only one wave function

$$\Psi(\vec{r}) = \Psi_0 \mathrm{e}^{-\mathrm{i}\chi(\vec{r})}, \tag{1.1}$$

where $\chi(\vec{r})$ is the coordinate dependent phase, becomes possible. This superconducting state is decoupled from the crystal lattice. Individual scattering of electrons cannot change the momentum $\vec{q}$, since it is common to all the Cooper pairs. With the momentum of the charge carriers being a conserved quantity ideal conductivity is achieved.

The BCS theory also gives explanations for various other phenomena connected with superconductivity. For example, the steep change in the specific heat and the Meissner effect are discussed. Latter was experimentally found in 1933 by Meissner and Ochsenfeld [72]. They observed that an external magnetic field is expelled completely from the bulk of a superconductor and, therefore, ideal diamagnetic properties are achieved.

An explanation was firstly given by London and London in 1935 [73]. They developed a phenomenological theory of the electromechanical properties from superconductors. By starting from the equation of motion of a single electron in the Drude model [74]

$$m\frac{\mathrm{d}\vec{v}}{\mathrm{d}t} + m\frac{\vec{v_{\mathrm{D}}}}{\tau} = -e\vec{E}, \tag{1.2}$$

where m is the mass and e the charge of a conduction electron, $\vec{E}$ the electric field, v the velocity , v_{D} the drift velocity, and τ the mean time to an interaction of an electron with the lattice, some general statements can be deduced. In the steady state $\mathrm{d}\vec{v}/\mathrm{d}t$ is equal to zero and one obtains Ohms law

$$\vec{j}_{\mathrm{N}} = -en_{\mathrm{N}}\vec{v_{\mathrm{D}}} = \frac{n_{\mathrm{N}}e^2\tau}{m}\vec{E}, \tag{1.3}$$

with $\vec{j}_{\mathrm{N}}$ being the current density and n_N the density of charge carriers in a normal conducting metal. A normal conductance $\sigma = ne^2\tau/m$ may be introduced. By assuming the time to an interaction with the lattice τ to be infinite for a superconductor[2] equation (1.2) becomes an

[2]This assumption expresses that no interaction with the lattice occurs.

"acceleration equation"

$$\dot{\vec{j}}_S = \frac{n_S q_S^2}{m}\vec{E}. \tag{1.4}$$

Here, the electron charge is replaced by the charge of a cooper pair q_S. A stationary current can be found in a superconducting material even if $\vec{E}$ =0 immediately by integration. After taking the curl, one can substitute the current density by the magnetic field $\vec{H}$ as $\vec{j_S} = \text{curl}\vec{H}$ and $\text{curl}\vec{E} = -\mu_0\dot{\vec{H}}$ as found from the Maxwell equations[3]. Integration with respect to the time together with the identity $\text{curl}\left(\text{curl}\vec{Y}\right) = \text{grad}(\text{div}\vec{Y}) - \Delta\vec{Y}$ and again one Maxwell equation, $\text{div}\vec{H} = 0$, yields the homogeneous screening relation for the magnetic field

$$\Delta\vec{H} = \frac{1}{\lambda_L^2}\vec{H}. \tag{1.5}$$

This equation includes the Meissner effect. The general solution gives an exponential decay of the magnetic field in a region of size $\lambda_L = \sqrt{m/n_S q_S^2 \mu_0}$, the London penetration depth, from the surface of the superconductor. The supercurrent follows the same exponential decay. A list of λ_L for different materials can be found in table 1.1.

The London theory has several limitations. For example, it gives no explanation for the dependence of the London penetration depth on temperature nor on the thickness of a superconducting film. The theory developed by Ginzburg and Landau in 1950 [75] to overcome these problems marked the first complete theoretical explanation of superconductivity and is still commonly used for describing inhomogeneous superconductors. Starting from the basic theory of phase transitions of the second kind[4], they introduced an ordering Parameter Ψ that is zero above the critical temperature. It can be identified with the common wave function for the superconducting charge carriers. The normalization is selected such that the ordering parameter will be connected to the density of superconducting charge carriers $|\Psi|^2 = n_S$. The phase $\chi(\vec{r})$ of this "effective" wave function (1.1) depends on the applied magnetic field due to the vector potential $\vec{A}$. The magnetic field is connected to the superconducting currents by the gradient of Ψ and, therefore, by the phase of the wave function.

1.2 Flux quantization

One important effect for the development and the understanding of superconducting electronics is the quantization of magnetic flux in a closed superconducting loop. As mentioned,

[3] The displacement current is neglected.

[4] Phase transitions without latent heat.

the Ginzburg-Landau theory connects the supercurrent $\vec{j_S}$ to the gradient of the phase $\phi(\vec{r})$ and the vector potential $\vec{A}$. This statement can be expressed by the equation [75]

$$\vec{j_S} = -\frac{iq_S\hbar}{2m}(\Psi^* \mathrm{grad}\Psi - \Psi \mathrm{grad}\Psi^*) - \frac{q_S^2}{m}|\Psi|^2\vec{A}, \tag{1.6}$$

where q_s denotes the charge and m the mass of the "superconducting electrons".

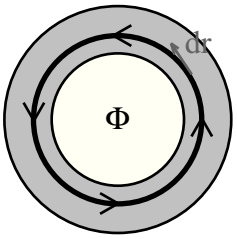

Figure 1-1: Sketch of a thin superconducting ring. A supercurrent represented by the current density j_S will create a magnetic flux in the loop. The line element for the integration in the text is always parallel to the vector of the current density.

Assuming the geometry shown in Fig. 1-1, integration of (1.6) along the closed superconducting ring together with (1.1) yields

$$\oint_{\partial D} \vec{j_S}\,\mathrm{d}\vec{r} = -\oint_{\partial D} \frac{q_S\hbar}{2m}|\Psi_0|^2 \mathrm{grad}\chi(r)\,\mathrm{d}\vec{r} - \frac{q_S^2}{m}|\Psi_0|^2 \oint_{\partial D} \vec{A}\,\mathrm{d}\vec{r}.$$

Here, D is the sphere enclosed by the circular integration path. The current density $\vec{j_S}$ can be set to zero, if the integration path is shifted away from the surface of the superconductor, because the supercurrents are located only in a small layer of thickness λ_L. A simplification to

$$\frac{q_S\hbar}{m}\oint \mathrm{grad}\chi\,\mathrm{d}\vec{r} = \frac{q_S^2}{m}\int_D \vec{B}\,\mathrm{d}\vec{F} \tag{1.7}$$

can be found by the use of Stoke's theorem and $|\Psi_0|^2 = n_S$. The integral on the right is equal to the magnetic flux in the loop Φ. The integral on the left side gives the phase difference between the wave function at the start and the end of the integration path. Because both points coincide and the wave function should be single valued, the integral necessarily has to be a multiple of 2π. Therefore, the total flux Φ enclosed by the loop has to be quantized. This quantization is expressed by

$$\Phi = n\frac{h}{q_s}. \tag{1.8}$$

The first experimental observations of quantized flux were reported independently from Doll and Näbauer [76] as well as from Deaver and Fairbank [77] in 1961. The value both groups found for the flux quantum is $\Phi_0 = h/2e$. A comparison with (1.8) shows that the charge of the supercurrent carriers is given by $2e$ and indicates the pairing of electrons.

1.3 The Josephson effect

The main building block of superconducting electronics, and therewith superconducting quantum bits, is the Josephson junction. It is named after B.D. Josephson. In 1962 he predicted "possible new effects" [12] on coupled superconductors by a general perturbation theory, today summarized as Josephson effect. It is found for superconductors separated by a region of weakened superconductivity or by thin layers of conducting or isolating materials. The latter type is sketched in Fig. 1-2 and called tunnel junction. Its non-superconducting layers have a typical thickness of several nanometers. All junctions considered in this work are tunnel junctions with an isolating barrier of aluminum oxide.

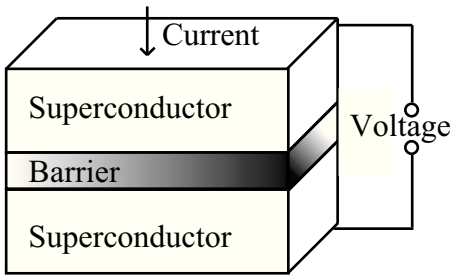

Figure 1-2: Schematic of a Josephson tunnel junction. Two superconductors are connected via an isolating barrier. The current through and the voltage across the junction are defined by its properties.

The electronic properties of a Josephson junction are found by simple considerations [78] assuming two superconductors with wave functions Ψ_1 and Ψ_2 and corresponding eigenenergies $E_{1,2}$. Their dynamic is given by the Schrödinger equation

$$\frac{\partial \Psi_k}{\partial t} = -\frac{\mathrm{i}}{\hbar}(E_k \Psi_k + K \Psi_l). \tag{1.9}$$

Here K is a weak coupling coefficient and the indices $k,l \in [1,2]; k \neq l$. A solution is given by (1.1) for each of the superconductors. Also the normalization of the Ginzburg-Landau theory $|\Psi_k| = \sqrt{n_k}$ can be used. Inserting $\Psi_k = \sqrt{n_k}\mathrm{e}^{\mathrm{i}\chi_k}$ into (1.9) yields

$$\frac{1}{2\sqrt{n_k}}\dot{n}_k + \mathrm{i}\dot{\chi}_k\sqrt{n_k} = -\frac{\mathrm{i}}{\hbar}\left(E_k\sqrt{n_k} + K\sqrt{n_l}\mathrm{e}^{\mathrm{i}[\chi_l - \chi_k]}\right). \tag{1.10}$$

Here the dot indicates a partial time derivative. Under the assumption that two superconductors of the same kind are used ($n_1 = n_2 = n_S$) the real part of the equation multiplied with charge $2e$ gives

$$j_S = 2e\dot{n} = \frac{4en_S K}{\hbar} \sin\varphi = j_c \sin\varphi, \tag{1.11}$$

where $\varphi = \chi_2 - \chi_1$ is the phase difference across the junction and j_c the critical current density. This equation describes the DC-Josephson effect and is known as the first Josephson equation. From it follows that a Josephson junction can carry a superconducting current that is created by the tunneling of Cooper pairs through the barrier. Its value depends on the phase difference across the junction and is limited to a maximum value of j_c. Another effect is found by considering the imaginary parts of (1.10) and subtracting them[5]

$$\dot{\varphi} = \frac{E_2 - E_1}{\hbar} = \frac{2eV}{\hbar}. \tag{1.12}$$

Here, V denotes the voltage across the junction. This equation explains the AC-Josephson effect, which states that a voltage drop at a Josephson junction is connected to a time varying phase difference. Furthermore, by integration of (1.12) and inserting into (1.11) the corresponding AC-current can be identified. Its frequency is given by $\nu = 2eV/h$.

Together with the voltage drop a discussion of further current channels, besides the supercurrent explained by (1.11), becomes necessary at the Josephson junction. It is summarized in the so-called RCSJ (Resistive and Capacitive Shunted Junction)-model, as illustrated in Fig. 1-3. There are two main additional channels to consider for a tunnel junction. On the

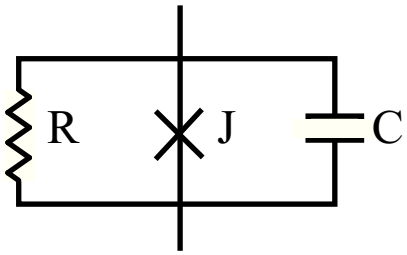

Figure 1-3: Circuit diagram of a Josephson junction in the RCSJ-model.

one hand, the superconducting electrodes together with the isolating barrier form a capacitor and therewith make a displacement current possible. The value of capacitance is given by the material and the size of the junction. A typical value for aluminum oxide barriers is

[5]To clarify, subtracting the equation for $\dot{\chi}_1$ from similar one for $\dot{\chi}_2$.

about 50 fF/μm^2. On the other hand, besides the tunneling of Cooper pairs also quasiparticles can give a contribution to the current flow. Because the propagation of these electrons is connected to losses, one can introduce a normal resistance R_N. This current channel can be neglected in most cases connected to superconducting quantum circuits because the junctions are usually kept in the superconducting state at temperatures well below T_c. Therefore, the quasi particle density can be neglected. In summary, by expressing the voltage with the derivative of the phase at the junction the sum of the currents is given by

$$I = I_\mathrm{c} \sin\varphi + \frac{\Phi_0}{2\pi R_\mathrm{N}}\dot{\varphi} + \frac{\Phi_0}{2\pi} C_\mathrm{J}\ddot{\varphi} \tag{1.13}$$

as firstly proposed in the works by Stewart [79] and McCumber [80].

1.4 Quantum mechanics of a Josephson junction

As described before, superconductivity as well as the Josephson effect are quantum phenomena. But in general also a quantum theory has to be considered for the observables (current and voltage or phase and charge) at the junction [81].

A first step is to find the Hamiltonian and, therefore, start with the energy conservation law on the Josephson junction. It can be found by multiplying (1.13) with the voltage (1.12). Neglecting the dissipative current channels yields

$$IV = \frac{\mathrm{d}}{\mathrm{d}t}\left(E_\mathrm{J}(1-\cos\varphi) + \frac{1}{2}\left(\frac{\Phi_0}{2\pi}\right)^2 C_\mathrm{J}\dot{\varphi}^2\right). \tag{1.14}$$

The Josephson coupling energy E_J is used, and its value is given by

$$E_\mathrm{J} = \Phi_0 I_\mathrm{c}/2\pi. \tag{1.15}$$

The potential ($U(\varphi)$) and kinetic ($E_\mathrm{k}(\dot{\varphi})$) energy form the Lagrangian $\mathscr{L}(\varphi,\dot{\varphi}) = E_\mathrm{k} - U$, from which the generalized momentum can be derived as

$$p = \frac{\partial\mathscr{L}}{\partial\dot{\varphi}} = \left(\frac{\Phi_0}{2\pi}\right)^2 C_\mathrm{J}\dot{\varphi}, \tag{1.16}$$

whereas the generalized coordinate is given by the phase φ. The Hamiltonian of the system is

$$\mathscr{H} = p\dot{\varphi} - \mathscr{L} = \frac{p^2}{2m} + E_\mathrm{J}(1-\cos\varphi),$$

where the mass is defined as $m = \hbar^2 C_\mathrm{J}/4e^2$. Furthermore, with the relation for the AC-Josephson effect (1.12), one can relate the charge Q to the momentum.

$$Q = C_\mathrm{J} V = C_\mathrm{J} \frac{\Phi_0}{2\pi} \dot{\varphi} = \frac{2e}{\hbar} p \tag{1.17}$$

The quantization is done by substitution the variables with operators. In the phase basis the momentum is $\hat{p} = -\mathrm{i}\hbar\partial/\partial\hat{\varphi}$ and the coordinate $\hat{\varphi}$. Hence, the Hamiltonian reads in the flux basis

$$H = -E_\mathrm{C} \frac{\partial^2}{\partial \hat{\varphi}^2} + E_\mathrm{J}(1 - \cos\hat{\varphi}). \tag{1.18}$$

Here, the symbol is changed to simply H to denote the quantum Hamiltonian and the charging energy E_C at the junction is used as

$$E_\mathrm{C} = \frac{2e^2}{C_\mathrm{J}} \tag{1.19}$$

With the expression for the momentum the commutation relation between the charge $\hat{Q}$ and phase $\hat{\varphi}$ at the junction can be easily found

$$\left[\hat{\varphi}, \hat{Q}\right] = \frac{2e}{\hbar} [\hat{\varphi}, \hat{p}] = 2\mathrm{i}e. \tag{1.20}$$

Here, the commutation relation[6] $[\hat{\varphi}, \hat{p}] = \mathrm{i}\hbar$ as well as (1.12) and the definition of the flux quantum by (1.8) are used. Because the phase and the charge do not commute, obviously, not both can be well defined at the junction at the same time. The critical parameter is the ratio between E_J and E_C. For example, if $E_\mathrm{J} \gg E_\mathrm{C}$ the phase and therewith the current through the junction are well defined. In this case, the charge degree of freedom can couple different stable phase states as described later.

These quantum effects at the Josephson junction are sometimes called "secondary quantum effects" because superconductivity or the Josephson effect themselves are quantum effects but form the basis for the considerations above.

[6] As found for the given observables by applying the commutator to the wave function (1.1), for example in the phase basis.

2 Theoretical analysis of flux qubits and cavities

2.1 The quantum two-level system

A quantum bit, or qubit, is a physical system containing two distinguishable states. The difference to a classical bit lays in the possibility for both states to exist in a superposition, what yields a statistical probability in the measurement result. This fact is expressed by the equation for the state vector of the qubit

$$|\Psi\rangle = p_{\mathrm{g}}|g\rangle + p_{\mathrm{e}}|e\rangle. \tag{2.1}$$

In this superposition p_n^2 denotes the probability to measure state $|n\rangle$. It can take values between zero and one. The basis state vectors $|g\rangle$ and $|e\rangle$ are normalized and orthogonal. The state Ψ itself should satisfy similar normalization condition, so that $p_{\mathrm{g}}^2 + p_{\mathrm{e}}^2 = 1$. Accordingly, the total probability to measure either state $|g\rangle$ or state $|e\rangle$ is one. For illustration of the superposition of the qubit and therewith operations on the qubit the so called Bloch sphere can be used. It is sketched in Fig. 2-1. The basic states $|g\rangle$ and $|e\rangle$ are located at the poles. Each point on this unit sphere corresponds to a superposition of the basic states. For example, at the equator a perfect superposition with $p_{\mathrm{g}}^2 = p_{\mathrm{e}}^2 = 1/2$ is found. Any operation changing the qubit's state corresponds to a rotation on the Bloch sphere. Furthermore, any of this operations can be composed by rotations around the axis x, y and z, and therefore simply by a linear combination of the Pauli matrices, listed below.

$$\sigma_x = \begin{pmatrix} 0 & 1 \\ 1 & 0 \end{pmatrix}, \sigma_y = \begin{pmatrix} 0 & -\mathrm{i} \\ \mathrm{i} & 0 \end{pmatrix}, \sigma_z = \begin{pmatrix} 1 & 0 \\ 0 & -1 \end{pmatrix} \tag{2.2}$$

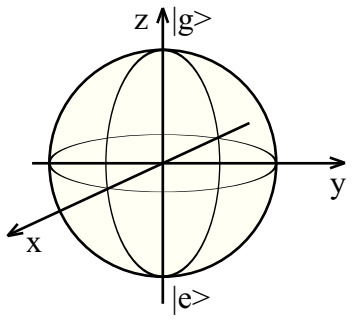

Figure 2-1: Sketch of the Bloch sphere. Each quantum state of the qubit corresponds to a single point on a unit sphere. The basis states $|g\rangle$ and $|e\rangle$ are located on the poles.

Two important examples of such linear combinations are the raising and lowering operators defined by

$$\sigma_{\pm} = \frac{1}{2}\left(\sigma_x \pm \mathrm{i}\sigma_y\right), \tag{2.3}$$

that only transform the ground to excited state and vice versa, respectively. Natural candidates for qubits are trapped ions, nuclear or electronic spins and quantum dots. In contrast, in this work the qubit is formed by a superconducting circuit.

The superconductivity ensures the coherence needed for a quantum system. Furthermore, as shown in chapter 1.4 Josephson junctions can be described using the laws of quantum mechanics. Following the statement in the mentioned chapter the solid-state qubits are distinguished depending on the well-defined quantum variable. For $E_\mathrm{J} \approx 20E_\mathrm{C}$ they are usually called flux qubits [23]. Other types include phase ($E_\mathrm{J} \approx 200E_\mathrm{C}$) and charge qubits [22] ($4E_\mathrm{J} \approx E_\mathrm{C}$) as well as transmons [29] ($E_\mathrm{J} \approx 100E_\mathrm{C}$)[1].

2.2 The superconducting flux qubit

The flux qubit consists of a superconducting loop interrupted by at least one Josephson junction. The Josephson junction needs to be considered when calculating the conditions of the flux quantization in the loop. Namely, the phase difference on the junctions is added to the

[1]Note that definition of the charging energy E_C differs in some works to the one given in this work. For example it can be defined concerning only a single electron instead of a cooper pair.

integration over the gradient of the superconducting phase (first term in (1.8))

$$\begin{aligned}\frac{\hbar}{2e}(\varphi+2\pi n) &= \Phi \\ \frac{\varphi}{2\pi} &= \frac{\Phi}{\Phi_0} - n.\end{aligned} \tag{2.4}$$

Therefore, the flux in the loop Φ is directly related to the phase difference φ at the junction. If, for a moment the inductance L_q of the qubit loop is considered, it is easy to find that

$$\Phi = \Phi_\mathrm{e} - L_\mathrm{q} I. \tag{2.5}$$

Here, Φ_e is the externally applied flux and I the current in the qubit loop. Equation (2.5) implies that the external flux is partly compensated by the flux created due to the circulating current I and it follows

$$\frac{\varphi}{2\pi} = \frac{\Phi_\mathrm{e}}{\Phi_0} - \frac{L_\mathrm{q} I}{\Phi_0} - n. \tag{2.6}$$

The effective flux in the loop may be defined as the difference between external flux and the one compensated by the current flowing through the loop inductance $\Phi = \Phi_\mathrm{e} - L_\mathrm{q} I$. Introducing more junctions with phase differences $\tilde{\varphi}_m$ to (2.4) gives

$$\frac{\varphi}{2\pi} = \frac{\Phi}{\Phi_0} - n - \sum_m \frac{\tilde{\varphi}_m}{2\pi}. \tag{2.7}$$

When comparing this equation to (2.6) it is obvious that the additional Josephson junctions have the same influence as the loop inductance [23]. Furthermore, smaller inductances are preferable, since they provide less coupling to the noisy environment (compare section 2.4). Therefore, usually three junctions are fabricated to a low inductance qubit loop. The typical shape of a flux qubit is sketched in Fig. 2-2.

To understand the quantum behavior of a flux qubit, it is necessary to find the corresponding Hamilton operator and therewith the energy level structure. As seen in Fig. 2-2 the standard flux qubit consists of a loop containing three Josephson junctions. Two junctions are designed to have identical size while the one of the third is scaled by a factor $\alpha < 1$. If the inductance of the loop is neglected the potential energy is given by the sum of the Josephson energies (1.14),

$$U(\varphi_1, \varphi_2) = E_\mathrm{J}\left(2 + \alpha - \cos\varphi_1 - \cos\varphi_2 - \alpha\cos\left[2\pi f + \varphi_1 - \varphi_2\right]\right). \tag{2.8}$$

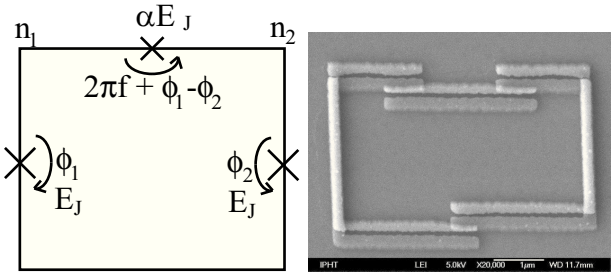

Figure 2-2: (left) Sketch of a flux qubit. It consists of a superconducting loop interrupted by three Josephson junctions. One of the junctions is designed to be smaller by a ratio α. The other two effectively increase the inductance of the loop. The qubit is controlled by an externally applied flux Φ_e which for a small loop inductances can be identified with the internal flux Φ (right) SEM-image of a fabricated flux qubit using standard two angle shadow evaporation technique.

Here, the flux quantization (2.7) is used to substitute the phase difference on the small junction[2]. The applied external flux, expressed by the friction $f = \Phi_e/\Phi_0$ and the design parameter α influence the shape of the potential. It is plotted for different parameters in Fig. 2-3.

When the external flux is tuned close to half a flux quantum the potential has two minima. They occur at positions $\varphi_1 = -\varphi_2 = \pm\varphi_p$. By using the first Josephson equation (1.11) it is easy to conclude that the both minima correspond to a circulating current in either clockwise or anticlockwise direction. The absolute value of this current is called the persistent[3] current I_p. The second part of the Hamiltonian, the kinetic part, is connected to the capacitance on the junction, and it is derived in Appendix A.1. Using the definition of the charging energy the complete Hamiltonian reads

$$\begin{aligned} H =& \frac{E_C}{\hbar^2}\frac{[1+\alpha]p_1^2 + 2\alpha p_1 p_2 + [1+\alpha]p_2^2}{1+2\alpha} \\ &+ E_J\left(2+\alpha-\cos\varphi_1-\cos\varphi_2-\alpha\cos\left[2\pi f+\varphi_1-\varphi_2\right]\right), \end{aligned} \tag{2.9}$$

where p_i are generalized momenta described in Appendix A.1. This Hamiltonian can be diagonalized analytically in a tight binding approximation [24] or numerically. The concrete procedure for the latter in the charge basis can be found in Appendix A.2. The resulting eigenenergies are plotted in Fig. 2-4 for realistic parameters. Far away from their degeneracy point ($\Phi_e = \Phi_0/2$) the energy of the lowest two states can be understood as the energy of a

[2]The direction of the phase difference is chosen opposite for φ_1 and φ_2 in order to achieve the same sign for the calculated charges on the islands N_1 and N_2

[3]Sometimes the flux qubit is also known as persistent current qubit.

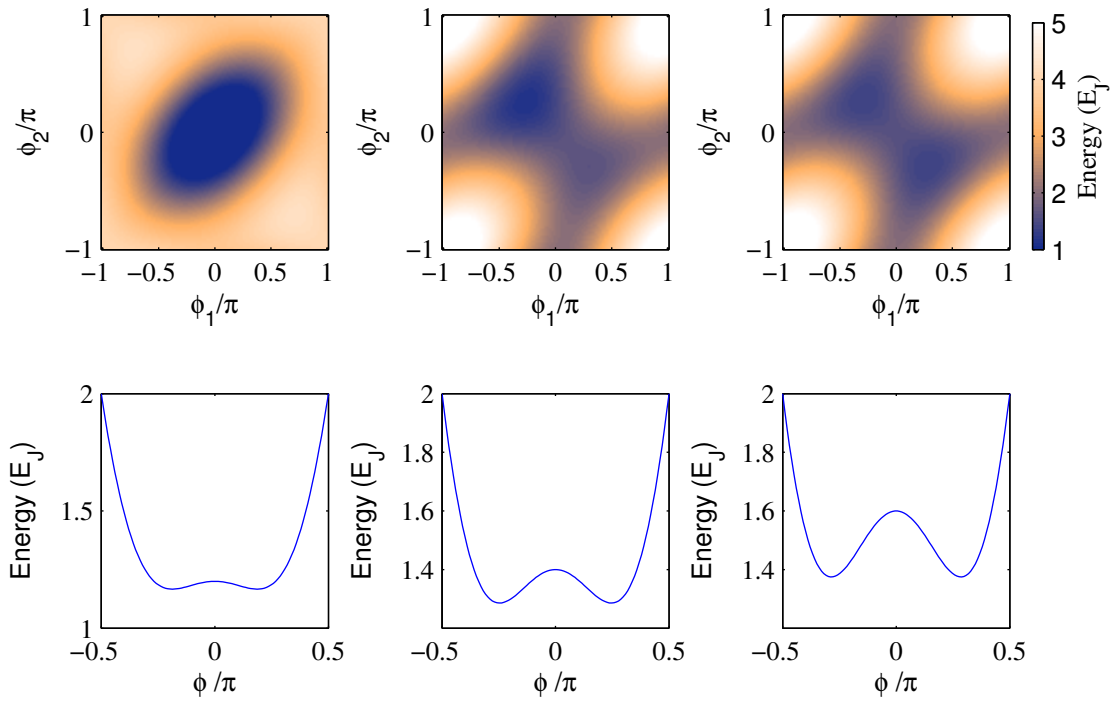

Figure 2-3: The upper 2D plots show the potential over the phase differences at the big junctions, which act as parameters. The value of α is fixed at 0.8. The three figures differ by the external flux, taking values (from left to right) of f = 0, 0.45, and 0.5. With approaching a friction of 0.5 two potential wells are formed. In the lower row cross section of the potential for a friction of $f = 0.5$ along $\varphi_1 = -\varphi_2$ for a changing value of α = 0.6, 0.7, and 0.8 are shown. The depth of the two potential wells increases, while the barrier between them increases with increasing α.

magnetic dipole, created by the circulating current parallel to the applied field for one and antiparallel for the other state. Therefore, their energies are linearly increasing (decreasing) with the external magnetic field and follow from

$$\varepsilon = \pm 2 I_\mathrm{p} (\Phi_\mathrm{e} + \frac{\Phi_0}{2}). \tag{2.10}$$

The value ε is the energy bias of the qubit. Close to the energetic degeneracy of these two flux states the kinetic part of the Hamitonian leads to quantum tunneling of the phase particle between the two wells. By that the degeneracy is lifted. The minimal splitting of the qubit's eigenenergies is given by this tunnel amplitude Δ (compare Fig. 2-4). Because the spacing of the first two levels is small compared to the distance to the next higher level, the flux qubit is considered as two-level system[4].

[4]Indeed the superconducting qubits, including the flux qubit can also be considered as anharmonic oscillator and for some experiments the third level can be of special importance [54]

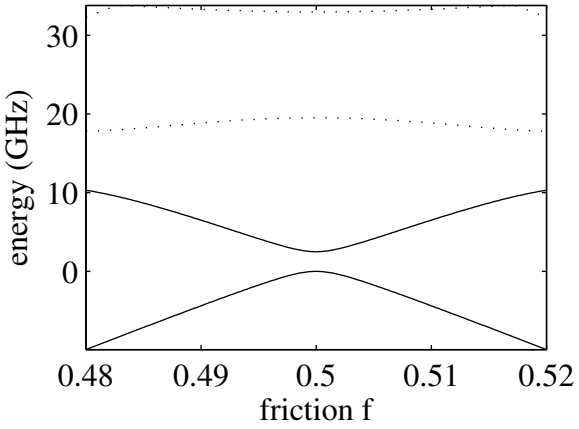

Figure 2-4: The first four eigenenergies of the flux qubit found by numerical diagonalization of its Hamiltonian (2.9) for parameters $\alpha = 0.7$, $j_c = 200$ A/cm^2, $c = 55$ fF/μm^2 and area of the big junctions 0.2×0.75 μm^2. The energy difference of the qubit levels (solid) can be tuned from its minimal value Δ, that here is 2.5 GHz. In comparison, the distance to higher levels (dotted) is large (> 20 GHz).

2.3 The flux qubit as quantum two-level system

If considered as two-level system the dynamics of the flux qubit can be fully described using the Pauli matrices, σ_x, σ_y, and σ_z. For example, σ_x describes transitions between the states of the qubit. In the basis of the flux states ($|L\rangle$ and $|R\rangle$ for left and right circulating current),

$$I_q = I_p \sigma_z \tag{2.11}$$

is the current operator and two terms contribute to the energy of the qubit [82]

$$H_q^{LR} = \frac{\varepsilon}{2}\sigma_z + \frac{\Delta}{2}\sigma_x. \tag{2.12}$$

It consists of the energy of the magnetic dipole created by the circulating current $\propto \varepsilon$ and the coupling term between the flux states via tunneling through the potential barrier with an amplitude Δ. This Hamiltonian can be easily diagonalized

$$H_q = \frac{\hbar\omega_q}{2}\sigma_z, \tag{2.13}$$

where the energy difference between the ground $|g\rangle$ and excited state $|e\rangle$ is given by

$$\hbar\omega_q = \sqrt{\varepsilon^2 + \Delta^2}. \tag{2.14}$$

The eigenstates are given by superpositions of the flux states

$$\begin{aligned} |e\rangle &= \sin\theta|L\rangle + \cos\theta|R\rangle \\ |g\rangle &= -\cos\theta|L\rangle + \sin\theta|R\rangle \end{aligned} \tag{2.15}$$

Here, $\theta = \frac{1}{2}\arctan\frac{-\Delta}{\varepsilon}$ is the so called mixing angle of the system[5]. Its value range from 0 to $\pi/2$ and it is a measure of the superposition of the two flux states to form the ground and excited state, respectively. Close to the degeneracy, where the energy bias is zero ($\varepsilon = 0$) its value is $\pi/4$. By considering (2.15) it can be concluded, that the energy states are formed by a perfect superposition of the flux states. The probability of measuring either current direction in the qubit is 0.5 for both ground and excited state. Therefore, the expectation value of the measured current is zero at the degeneracy point. The creation of the energy levels and the superposition is illustrated in Fig. 2-5. On the other hand, for big values of the energy bias ($|\varepsilon| > \Delta$) the qubit eigenstates can be identified with the flux states ($\theta \to 0$ for positive epsilon and $\theta \to \pi/2$ for negative).

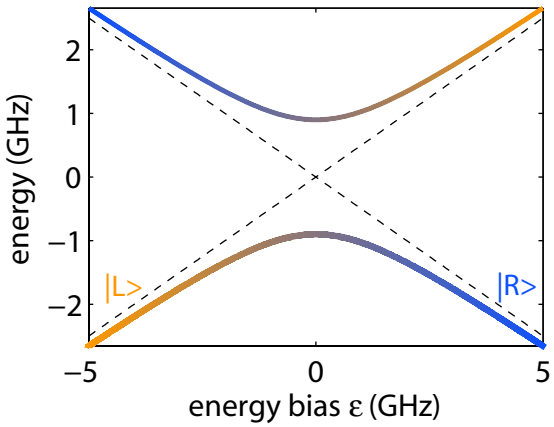

Figure 2-5: The qubit eigenenergies. The superposition of the flux states, illustrated as color gradient, gives the qubit's energy eigenstates. The corresponding eigenenergies have a hyperbolic dependence on the energy bias ε, which follows from the splitting at the degeneracy point. The coupling of the flux states is given by tunneling from one potential well to the other with amplitude Δ.

[5]For the given equation $H_q^{LR}|L\rangle = -\varepsilon/2|L\rangle + \Delta/2|R\rangle$ is assumed.

2.4 Coupling to the environment - Relaxation and Decoherence

The main advantage of the superconducting qubits over most other qubit types is good controllability, which is achieved by strong coupling to electromagnetic control fields via the macroscopic size of the devices. But also unwanted signals coming from external noise sources can couple strongly to the qubit [83]. Different origins can be identified [56]. For example, locally changing charge distributions can influence the charge on the islands of the qubit [84]. Furthermore, the discussed qubit type needs biasing with an external magnetic field, where fluctuations are hard to suppress completely [85]. Also two-level fluctuators located in interlayers or on the surface are discussed to contribute to the total noise [86].

These processes can be accounted for by mathematically coupling the qubit to an external bath, with a certain given noise spectrum $S(\omega)$. Also these noise sources can couple in different directions to the qubit. This assumption is in analogy to a loaded spin 1/2 particle, where an external magnetic field $\vec{H}_\mathrm{e}$ can be decomposed in its components along x, y, and z-direction to find the corresponding rotations on the Bloch sphere. As explained before, these rotations are expressed by the Pauli matrices. The Hamiltonian of the qubit in the natural flux basis may then be written as

$$\tilde{H}_\mathrm{q} = \frac{\Delta}{2}\sigma_x + \mu_0\mu_\mathrm{q}\vec{H}_\mathrm{e}\vec{S}, \tag{2.16}$$

where $\vec{S} = (\sigma_x, \sigma_y, \sigma_z)/2$ is the spin vector, $\mu_\mathrm{q} = 2I_\mathrm{p}A_\mathrm{q}$ the magneton of the qubit[6], and A_q the area of the qubit. The magnetic field can be expanded assuming that the noise is small and acts as perturbation [87]

$$\vec{H}_\mathrm{e} \approx \vec{H}_\mathrm{e}(\xi_0) + \left.\frac{\partial\vec{H}_\mathrm{e}}{\partial\xi}\right|_{\xi_0}\delta\xi + \frac{1}{2}\left.\frac{\partial^2\vec{H}_\mathrm{e}}{\partial\xi^2}\right|_{\xi_0}\delta\xi^2 + \dots\ . \tag{2.17}$$

Here, ξ is the expanding parameter and small. The term $\vec{H}_\mathrm{e}(\xi_0)$ has only a z-component and in the Hamiltonian it yields the diagonal term $\varepsilon\sigma_z/2 = \mu_0\mu_\mathrm{q}\vec{H}_{\mathrm{e,z}}(\xi_0)\vec{S}$ as in (2.12)[7]. By introducing the short notation $\vec{\delta H}_\mathrm{e}$ for the correction terms in (2.17) the total Hamiltonian reads

$$\tilde{H}_\mathrm{q} = \frac{\Delta}{2}\sigma_x + \frac{\varepsilon}{2}\sigma_z + \mu_\mathrm{q}\vec{\delta H}_\mathrm{e}\vec{S}, \tag{2.18}$$

[6]Note, due to its comparable large size a standard qubit has a magneton that is about six orders of magnitude larger than the Bohr magneton, and thus allows strong coupling to single photons.

[7]The product $A_\mathrm{q}H_{\mathrm{e,z}}(\xi_0)$ is the magnetic flux additionally applied to the ring to create an energy bias.

and it can be transformed to the eigenbasis of the undisturbed qubit

$$\tilde{H}_{\mathrm{q}} = \frac{\hbar\omega_{\mathrm{q}}}{2}\sigma_z + \frac{\hbar}{2}\left(X_\perp\sigma_\perp + X_z\sigma_z\right). \tag{2.19}$$

This equation is split in diagonal terms proportional and terms perpendicular to σ_z. The latter are denoted by the subscript $\perp$ and may include σ_x and σ_y. Note, (2.19) can also be found by assuming a bath observable coupled to the qubit [88]. To keep the equation in a compact form the abbreviations $X_z = \mu_{\mathrm{q}}/\hbar\omega_q\left[\Delta\vec{\delta H}_{\mathrm{e,x}} + \varepsilon\vec{\delta H}_{\mathrm{e,z}}\right]$ and $X_\perp\sigma_\perp = \mu_{\mathrm{q}}/\hbar\vec{\delta H}_{\mathrm{e,y}}\sigma_y + \mu_{\mathrm{q}}/\hbar\omega_q\left[-\varepsilon\vec{\delta H}_{\mathrm{e,x}} + \Delta\vec{\delta H}_{\mathrm{e,z}}\right]\sigma_x$ are used. Following the theories from Bloch [89] and Redfield [90] one can define the rates for relaxation Γ_{r}, excitation Γ_{e}, and pure dephasing γ_φ. With Fermi's golden rule they can be identified as

$$\Gamma_{\mathrm{r}} = \frac{1}{2}S_{X_\perp}(\omega_{\mathrm{q}}), \tag{2.20}$$

$$\Gamma_{\mathrm{e}} = \frac{1}{2}S_{X_\perp}(-\omega_{\mathrm{q}}), \tag{2.21}$$

$$\gamma_\varphi = S_{S_{X_z}}(\omega = 0). \tag{2.22}$$

Here, $S_X(\omega) = \int\langle\{X(t)X(0)\}\rangle\,\mathrm{e}^{-\mathrm{i}\omega t}dt$ is the quantum noise spectral density including the correlation of observable X and $S_{S_X}(\omega) = 0.5(S_X(\omega) + S_X(-\omega))$ the symmetrized spectral density. Also, it has to be assumed that the spectrum of the noise is regular. The relaxation and excitation rates are related to noise at the qubit frequency, whereas low frequency noise yields pure dephasing. If only flux noise is assumed, that is $\vec{\delta H}_{\mathrm{e,x}} = \vec{\delta H}_{\mathrm{e,y}} = 0$, the pure dephasing is scaled with $\varepsilon/\hbar\omega_q$ and, thus, vanishes at the degeneracy point. In addition, the relaxation and excitation rates have their maximum there and will decrease with $\Delta/\hbar\omega_q$.

To illustrate the origin of these rates, a general reservoir theory can be applied. In frame of such an approach the time evolution of the density matrix ρ_{S} of a quantum system S coupled to a reservoir R is given by [91]

$$\dot{\rho}_{\mathrm{S}} = -\frac{\mathrm{i}}{\hbar}\mathrm{Tr}_{\mathrm{R}}\left[\mathscr{V}(t), \rho_{\mathrm{S}}(t_i)\otimes\rho_{\mathrm{R}}(t_i)\right] - \frac{1}{\hbar^2}\mathrm{Tr}_{\mathrm{R}}\int_{t_i}^{t}\left[\mathscr{V}(t), \left[\mathscr{V}(t'), \rho_{\mathrm{S}}(t_i)\otimes\rho_{\mathrm{R}}(t_i)\right]\right]\mathrm{d}t'. \tag{2.23}$$

This equation follows in the Markov approximation, where the extended open reservoir is expressed by the density matrix ρ_{R}, the traces are taken over the reservoir coordinates, t_i is the initial time, and $\mathscr{V}(t)$ is the interaction energy of the system with the reservoir. Here, the latter is used in the interaction picture which follows from the above Hamiltonian (2.19) by the transformation

$$\mathscr{V}(t) = \hat{U}_1^\dagger\tilde{H}_{\mathrm{q}}\hat{U}_1 = \frac{\hbar}{2}\left(X_\perp\sigma_+\mathrm{e}^{\mathrm{i}\omega_{\mathrm{q}}t/2} + X_\perp\sigma_-\mathrm{e}^{-\mathrm{i}\omega_{\mathrm{q}}t/2} + X_z\sigma_z\right), \tag{2.24}$$

where $\hat{U}_1(t) = \mathrm{e}^{-\mathrm{i}H_\mathrm{q}t/\hbar} = \mathrm{e}^{-\mathrm{i}\omega_\mathrm{q}\sigma_z t/2}$ is the time evolution operator. An analysis of the incoherent time evolution of the density matrix of the qubit (2.23) is given in Appendix B.1. It can be summarized with the Lindblad term for the qubit

$$\dot{\rho}_\mathrm{q} = \hat{L}_\mathrm{q} = \frac{\Gamma_\mathrm{r}}{2}\left(2\sigma_-\rho_\mathrm{q}\sigma_+ - \sigma_+\sigma_-\rho_\mathrm{q} - \rho_\mathrm{q}\sigma_+\sigma_-\right) + \frac{\gamma_\varphi}{2}\left(\sigma_z\rho_\mathrm{q}\sigma_z - \rho_\mathrm{q}\right). \tag{2.25}$$

Here, the excitation is neglected because in thermal equilibrium the rates for excitation is related to the one for relaxation by the detailed balanced law

$$\Gamma_\mathrm{e} = \Gamma_\mathrm{r}\mathrm{e}^{\frac{-\hbar\omega_\mathrm{q}}{k_\mathrm{B}T}}. \tag{2.26}$$

To avoid thermal excitation of the superconducting qubit it is cooled down to very low temperatures in the order of a few tens of millikelvin.

The dissipative dynamics can also be summarized by the two times T_1 and T_2 because (2.25) yields for the elements of the density matrix

$$\dot{\rho}_\mathrm{ee} = -\Gamma_\mathrm{r}\rho_\mathrm{ee}, \qquad \dot{\rho}_\mathrm{gg} = \Gamma_\mathrm{r}\rho_\mathrm{ee},$$
$$\dot{\rho}_\mathrm{eg} = -\Gamma_\varphi\rho_\mathrm{eg}, \qquad \dot{\rho}_\mathrm{ge} = -\Gamma_\varphi\rho_\mathrm{ge},$$

where g and e stand for ground and excited state, $\rho_{xy} = \langle x|\rho|y\rangle$, $x, y \in (\mathrm{g}, \mathrm{e})$, and $\Gamma_\varphi = \gamma_\varphi + \frac{\Gamma_\mathrm{r}}{2}$ is the decoherence rate. The first line contains relaxation $T_1 = 1/\Gamma_\mathrm{r}$, and T_1 is the mean time of the decay of energy from the qubit. $T_2 = 1/\Gamma_\varphi$ is the coherence time of the qubit. In other words, the quantum state is lost after a time of this scale. It can be enhanced if the qubit is isolated from external noise sources, especially at low frequencies. Such isolation can, for example, be done if the qubit is placed inside of a cavity that only allows several eigenfrequencies.

2.5 The superconducting CPW resonator

A cavity for light fields in quantum optics has its counterpart in the superconducting coplanar waveguide (CPW) resonator. The coplanar line is created by a central conductor together with two ground plates on the same plane at each side[8]. The widths of the line and the distance to the plates are usually chosen to result in a 50 Ω wave impedance. The central line is interrupted at positions $x = -S/2$ and $x = S/2$ with a coupling capacity C_c to form a

[8]The name coplanar waveguide is used since all relevant layers are in the same plane.

resonator (see Fig. 2-6). The fundamental resonance is a $\lambda/2 = S$ standing wave, where λ is the corresponding wavelength, and it has a current antinode at the position $x = 0$ together with voltage antinodes at the coupling capacitances. The corresponding fundamental frequency $\omega_0/2\pi$ has a value of $\approx 2.5\ GHz$ for a resonator of length $S = 23$ mm fabricated out of Nb on an intrinsic silicon substrate. The geometric inductance can be estimated from the geometry to be $L \approx 10$ nH. Then from the relation $\omega_0 = \pi/\sqrt{LC}$ (see below) the total capacitance $C \approx 3.7$ pF can be estimated. From this value a reasonable capacitance per unit length of $c = 0.16$ nF/m [92, 93] results. For the resonators considered in this work the coupling capacitance are formed by a gap of 90 μm and take a value of the order of 1 fF.

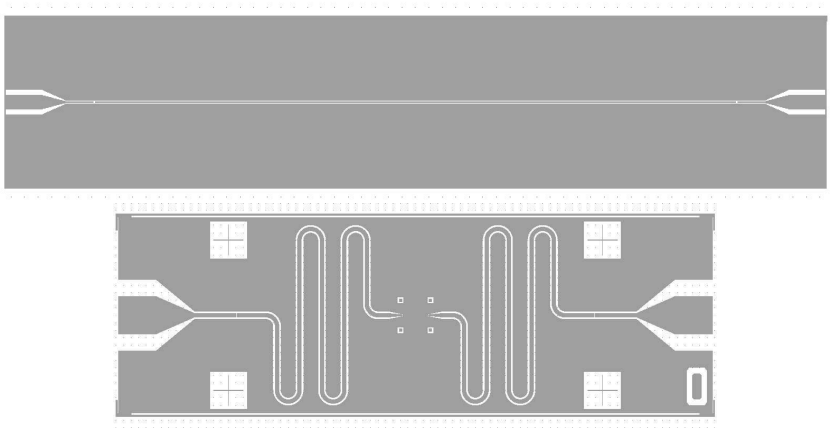

Figure 2-6: Possible designs of CPW resonators. The central conductor line has a length of 23 mm in both shown examples. In the lower picture the resonator is meandered to reduce the chip size from 32×6.4 mm in the upper to 8×3 mm in the lower example. In the lower picture also the markers for placing the qubit are visible.

At low temperatures of the order of tens of millikelvins the thermal occupation of the resonator is negligible. The Bose-Einstein statistics (see (B.21))

$$\langle N \rangle = \frac{1}{e^{\frac{\hbar\omega}{k_B T}} - 1} \tag{2.27}$$

gives for a temperature of 20 mK and a frequency of the considered mode of 2.5 GHz a mean photon number of 2.5e-3. Therefore, thermal excitation can be neglected for this order of frequencies, in contrast to experiments using tank circuits[9] for the readout of superconducting qubits [34, 39, 40, 43], where the resonator is always populated by at least tens of photons. Following the above estimations, a quantum theory is needed for the resonator.

[9]Formed usually by planar micro fabricated coils together with externally placed capacitances. See the given references in the text for details.

2.6 Hamiltonian of a CPW resonator

As a first step, it is necessary to find the Hamiltonian of the resonator. The Lagrangian formalism can be applied for this purpose [58, 94]. Following the geometry, a coplanar line can be understood as a series of connected inductances l, each shunted to the ground by a parallel connection of a capacitor c and a resistor r (see Fig. 2-7). Because all the parameters only depend on the coordinate along the symmetry axis of the resonator, the space dependence is only one-dimensional.

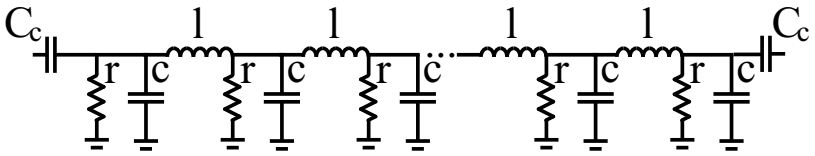

Figure 2-7: Circuit diagram of a CPW resonator. The resonator is coupled to the environment by the coupling capacitances C_c. The inductance per unit length is l, the capacitance c and the resistance r. The latter yields from dissipative connections of the central conduction line to the mass plates.

First it is worthwhile to discuss some properties of this system. The voltage V_n and currents I_n on each node are connected by the usual relations on circuits built up by resistances, inductances and capacitances. The Kirchhoff's circuit laws yield

$$V_n - V_{n-1} = -\dot{\Phi}_n = -l\Delta x \dot{I}_n, \quad I_{n+1} - I_n = -\dot{Q}_n = -c\Delta x \dot{V}_n - \frac{\Delta x}{r} V_n. \tag{2.28}$$

Here, $\Delta x = S/n$ is the size of the cell with n being the number of cells. In the continuum limit ($\Delta x \to 0$) the relations (2.28) give the known telegraph equations

$$\frac{\partial V}{\partial x} = -l\frac{\partial I}{\partial t}, \quad \frac{\partial I}{\partial x} = -c\frac{\partial V}{\partial t} - \frac{1}{r}V. \tag{2.29}$$

Derivation and inserting one equation into the other yields a wave equation for the voltage or the current:

$$\frac{1}{l}\frac{\partial^2 V}{\partial x^2} - c\frac{\partial^2 V}{\partial t^2} = \frac{1}{r}\frac{\partial V}{\partial t}, \quad \frac{\partial^2 I}{\partial x^2} - cl\frac{\partial^2 I}{\partial t^2} = \frac{l}{r}\frac{\partial I}{\partial t}. \tag{2.30}$$

With a wave ansatz for the voltage $V(x,t) = \tilde{V}e^{ikx-i\omega t}$ or the current $I(x,t) = \tilde{I}e^{ikx-i\omega t}$, respectively, these equations can be solved[10]. The phase velocity of the wave is $s = 1/cl$.

[10] At the moment only waves traveling in positive (right) direction are considered.

When inserting the ansatz directly to the telegraph equations the wave impedance Z as relation between voltage and current follows

$$\mathrm{i}k\tilde{V} = -\mathrm{i}l\omega\tilde{I}, \quad \mathrm{i}k\tilde{I} = -\mathrm{i}c\omega - \frac{1}{r}\tilde{V},$$
$$Z = \frac{l}{c - \frac{\mathrm{i}}{\omega r}}\frac{1}{Z} = \sqrt{\frac{l}{c - \frac{\mathrm{i}}{\omega r}}}.$$

For small losses, which means good isolation and therefore big values of the resistance r, the wave impedance is given by $Z = \sqrt{l/c}$. It is useful to introduce the flux field variable ϕ as the time integral of the voltage along a closed path. The variable ϕ can then be treated as generalized coordinate. Neglecting the dissipative losses in (2.30), the wave equation for the voltage gives the equation of motion of the flux field as

$$\frac{1}{l}\phi'' - c\ddot{\phi} = 0. \tag{2.31}$$

The appropriate Lagrangian density of a transmission line to reproduce this equation of motion by the Euler-Lagrange formula for fields $\partial\mathscr{L}_\mathrm{d}/\partial\phi - \mathrm{d}/\mathrm{d}t\,\partial\mathscr{L}_\mathrm{d}/\partial\dot{\phi} - \mathrm{d}/\mathrm{d}x\,\partial\mathscr{L}_\mathrm{d}/\partial\phi' = 0$ is [95]

$$\mathscr{L}_\mathrm{d} = \frac{1}{2}\left[c\left(\partial_t\phi\right)^2 - \frac{1}{l}\left(\partial_x\phi\right)^2\right]. \tag{2.32}$$

A CPW resonator consists of a transmission line interrupted by two coupling capacities C_c. Thus, the Lagrangian of the CPW resonator is given by integration of (2.32) over the length of the resonator

$$\mathscr{L}_\mathrm{r} = \int_{-S/2}^{S/2}\mathscr{L}_\mathrm{d}\,\mathrm{d}x = \frac{1}{2}\int_{-S/2}^{S/2}\left[c\left(\partial_t\phi\right)^2 - \frac{1}{l}\left(\partial_x\phi\right)^2\right]\mathrm{d}x. \tag{2.33}$$

The coupling capacities at the end of the resonator produce standing electromagnetic waves. They can be expressed by traveling waves for the flux in right (positive) and left (negative) direction

$$\begin{aligned}\phi(x,t) &= \phi^{(\mathrm{r})} + \phi^{(\mathrm{l})} \\ &= \sum_n \frac{1}{\sqrt{2}A_n}\left(\alpha_n^{(\mathrm{r})}\,\mathrm{e}^{\mathrm{i}k_nx - \mathrm{i}\omega_nt} + \alpha_n^{(\mathrm{l})}\,\mathrm{e}^{-\mathrm{i}k_nx - \mathrm{i}\omega_nt}\right) + \mathrm{c.c.} \\ &= \sum_n \frac{1}{\sqrt{2}A_n}\left(\left[\alpha_n^{(\mathrm{r})} + \alpha_n^{(\mathrm{l})}\right]\cos k_nx + \mathrm{i}\left[\alpha_n^{(\mathrm{r})} - \alpha_n^{(\mathrm{l})}\right]\sin k_nx\right)\,\mathrm{e}^{-\mathrm{i}\omega_nt} + \mathrm{c.c.}\end{aligned}$$

Here, c.c. stands for complex conjugate, and α_n, ω_n, and $k_n = n\pi/S$ are the complex amplitudes, eigenfrequencies, and wave numbers of the n-th. mode, respectively. The constants

A_n are chosen such that the α_n are unitless and can be found below. The complex conjugate terms correspond to waves with negative frequencies. Those are important in the quantum domain because they result in absorption processes, while in the positive frequency components only emission is included. At positions $\pm S/2$ current nodes and voltage antinodes are expected. This requirement is incorporated by open boundary conditions for the flux variable, expressed by $\partial_x \phi(\pm S/2) = \int \partial_x V dt \propto I = 0$. Solutions are given by choosing $\alpha_n = \frac{1}{2\mathrm{i}}\alpha_n^{(\mathrm{l})} = -\frac{1}{2\mathrm{i}}\alpha_n^{(\mathrm{r})}$ for odd n and $\phi_n = \frac{1}{2}\alpha_n^{(\mathrm{l})} = \frac{1}{2}\alpha_n^{(\mathrm{r})}$ for even n[11] and yield

$$\phi(x,t) = \sum_n \frac{1}{\sqrt{2}A_n}\left(\alpha_{2n+1}(t)\sin k_{2n+1}x\,\mathrm{e}^{-\mathrm{i}\omega_{2n+1}t} + \alpha_{2n}(t)\cos k_{2n}x\,\mathrm{e}^{-\mathrm{i}\omega_{2n+1}t}\right) + \text{c.c.}\,. \quad (2.34)$$

To shorten this equation, the translated coordinate $\tilde{x} = x + S/2$ can be introduced and it follows

$$\phi(x,t) = \sum_n \phi_n(t)\cos k_n\tilde{x}, \quad (2.35)$$

where the amplitudes include the harmonic time dependence

$$\phi_n(t) = \frac{1}{\sqrt{2}A_n}\left(\alpha_n\,\mathrm{e}^{-\mathrm{i}\omega_n t} + \alpha_n^*\,\mathrm{e}^{\mathrm{i}\omega_n t}\right). \quad (2.36)$$

With this definition the phase amplitudes $\phi_n(t)$ are self-adjoint. The mode expansion of the flux variable (2.35) can be substituted into the Lagrangian, where only elements of $\sin^2$ and $\cos^2$ will contribute from the product of the sums because all others are removed by integration. [12]

$$\begin{aligned}\mathscr{L}_\mathrm{r} =& \frac{1}{2}\sum_n \int_0^S \left[c\dot{\phi}_n^2(\cos k_n\tilde{x})^2 - \frac{1}{l}\phi_n^2(k_n\sin k_n\tilde{x})^2\right]\mathrm{d}\tilde{x},\\ =& \frac{1}{2}\sum_n \left[c\dot{\phi}_n^2\left(\frac{\tilde{x}}{2} + \frac{\sin 2k_n\tilde{x}}{4k_n}\right) - \frac{\phi_n^2 k_n^2}{l}\left(\frac{\tilde{x}}{2} - \frac{\sin 2k_n\tilde{x}}{4k_n}\right)\right]\Bigg|_0^S.\end{aligned}$$

After introducing the total capacitance $C = cS/2$ and the mode number dependent inductance $L_n = 2lS/n^2\pi^2$ of an equivalent lumped element resonator (compare [92]) and inserting the integration bounds the Lagrangian of the resonator reads

$$\mathscr{L}_\mathrm{r} = \frac{1}{2}\sum_n \left(C\dot{\phi}_n^2 - \frac{\phi_n^2}{L_n}\right). \quad (2.37)$$

[11] And similar for the complex conjugate.

[12] This conclusion follows directly from the fact, that sine and cosine functions span an orthonormal basis for functions in the given interval $[0, S]$.

In this Lagrangian the flux amplitudes correspond to generalized coordinates and the generalized momenta read

$$p_n = \frac{\partial \mathscr{L}_\mathrm{r}}{\partial \dot{\phi}_n} = C\dot{\phi}_n, \tag{2.38}$$

and they correspond to the charge amplitudes in the resonator. The Hamilton function

$$\begin{aligned}\mathscr{H}_\mathrm{r} &= \sum_n \dot{\phi}_n p_n - \mathscr{L}_\mathrm{r} \\ &= \frac{1}{2}\sum_n \left(\frac{p_n^2}{C} + \frac{\phi_n^2}{L_n}\right).\end{aligned} \tag{2.39}$$

can be derived. The Hamiltonian (2.39) corresponds to the sum of harmonic oscillator Hamiltonians. A quantization yields the canonical operators $\hat{\phi}_n$ and $\hat{q}_n$, for which the commutation relation

$$\left[\hat{\phi}_n, \hat{p}_m\right] = \mathrm{i}\hbar\delta_{nm}, \tag{2.40}$$

where δ_{nm} is the Kronecker delta, is valid.[13] This relation raises the possibility to introduce creation and annihilation operators, $a_n^\dagger$ and a_n, for the photons of the n-th. mode as

$$a_n\,\mathrm{e}^{-\mathrm{i}\omega_n t} = \frac{1}{\sqrt{2}}\left(A_n\hat{\phi}_n + \mathrm{i}B_n\hat{p}_n\right), \quad a_n^\dagger\,\mathrm{e}^{\mathrm{i}\omega_n t} = \frac{1}{\sqrt{2}}\left(A_n\hat{\phi}_n - \mathrm{i}B_n\hat{p}_n\right), \tag{2.41}$$

Note, that these equations can also be found using (2.36) and identifying the complex amplitudes α and α^* with the time independent operators $a(0)$ and $a^\dagger(0)$, respectively. The Hamiltonian is expressed by

$$H_\mathrm{r} = \sum_n \hbar\omega_n\left(a_n^\dagger a_n + \frac{1}{2}\right), \tag{2.42}$$

where the symbol for the Hamiltonian in the quantum regime is changed from $\mathscr{H}$ to simply H. From a short calculation and comparing with (2.39)

$$H_\mathrm{r} = \sum_n \hbar\omega_n\left(A_n^2\hat{\phi}_n^2 + B_n^2\hat{p}_n^2 + \mathrm{i}A_nB_n\left[\hat{\phi}_n, \hat{p}_n\right] + 1\right),$$

the constants can be defined as

$$\begin{aligned}A_n &= \sqrt{\frac{1}{2\hbar\omega_n L_n}},\ B_n = \sqrt{\frac{1}{2\hbar\omega_n C}} \\ \omega_n &= \frac{1}{\sqrt{L_n C}} = \frac{n}{\sqrt{LC}} = n\omega_0.\end{aligned} \tag{2.43}$$

[13] Please note, while here the commutator is written for flux and charge in contrast in (1.20) phase and charge are discussed.

Here, $L = lS/\pi^2$ is used as the inductance of the coplanar waveguide resonator. The eigenfrequencies ω_n of the modes follow the usual relation on an electric oscillator for the lumped element representation. They have a linear dependence on the mode number n. For convenience, in the rest of the text the subscript 1 is omitted for the creation and annihilation operators and changed to 0 for the circular frequency of the fundamental resonator mode.

By combining the quantum expressions for the amplitudes of the flux and the charge (2.41) with the mode expansion for the flux (2.35) the quantum expressions for the voltage and current of the resonators are found to be

$$V_\mathrm{r} = \frac{\partial\phi(x,t)}{\partial t} = -\sum_n \mathrm{i}\sqrt{\frac{\hbar\omega_n}{C}}\left(a_n(0)\,\mathrm{e}^{-\mathrm{i}\omega_n t} - a_n^\dagger(0)\,\mathrm{e}^{\mathrm{i}\omega_n t}\right)\cos k_n\tilde{x}, \tag{2.44}$$

$$I_\mathrm{r} = \int \frac{1}{l}\frac{\partial V}{\partial x}\mathrm{d}t = \frac{1}{l}\frac{\partial\phi(x,t)}{\partial x} = \sum_n \sqrt{\frac{\hbar\omega_n}{L_n}}\left(a_n(0)\,\mathrm{e}^{-\mathrm{i}\omega_n t} + a_n^\dagger(0)\,\mathrm{e}^{\mathrm{i}\omega_n t}\right)\sin k_n\tilde{x}. \tag{2.45}$$

In the equation of the current one of the telegraph equations (2.29) is used. Note, that the voltage can be expressed as $V = \sum_n \hat{q}_n/C\,\cos k_n\tilde{x}$. It may be useful to introduce the zero point voltage $V_0 = \sqrt{\hbar\omega/C}$ and the zero point current $I_0 = \sqrt{\hbar\omega/L_1}$. A multiplication with the square root of the mode number n for the voltage and $\sqrt{n^3}$ for the current yields the respective voltages and currents of the higher modes.

Finally, the equations above can be represented in the interaction picture. Note, that the Hamiltonian (2.42) expresses the conserved energy of the resonator and is time independent. Following the Heisenberg equation for the time evolution of an operator yields for the annihilation operator [96] of mode n

$$\begin{aligned}\frac{\mathrm{d}a_n}{\mathrm{d}t} &= \frac{\mathrm{i}}{\hbar}\left[H_\mathrm{r}, a_n(0)\right] = \mathrm{i}\sum_m\left[\omega_m a_m^\dagger a_m, a_n(0)\right] = -\mathrm{i}\omega_n a_n \\ a_n &= a_n(t) = \mathrm{e}^{-\mathrm{i}\omega_n t}a_n(0)\end{aligned} \tag{2.46}$$

and similar for the creation operator

$$a_n^\dagger = a_n^\dagger(t) = \mathrm{e}^{\mathrm{i}\omega_n t}a_n^\dagger(0). \tag{2.47}$$

These expressions can be inserted into (2.44) and (2.45) giving the expressions for the voltage and the current in the interaction and Heisenberg picture.

2.7 Coupling the resonator to its environment

As considered above, the resonator is isolated from the outside world. Still, for manipulation of the system and to get information of its properties, it is necessary to couple the oscillator to the outside leads. When coupled to the outside, modifications of the system are required that need to be identified. That enables the description of the driving Hamiltonian, the including of photon decay, and an equation for the transmission coefficient of the resonator.

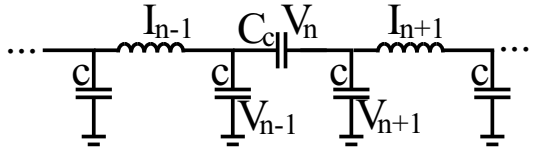

Figure 2-8: The coupling capacitance is included between the cells with indices $n-1$ and $n+1$. The change of the charge on each plate of C_c is given by the total currents in the adjoined cells, and their sum gives the current through the coupling capacitance. In addition, the voltage at cell n is identified by definition with the one at C_c.

A possible way for introducing the coupling capacitance is to consider an infinite transmission line interrupted at positions $\pm S/2$ [97]. Assuming a constant capacitance c and inductance l per unit length for the whole transmission line the wave equations (2.30) are valid at any coordinate. Still, the discontinuities by the coupling capacitances need to be added. The current through the coupling capacitance at position $-S/2$ assuming cell with index n, as sketched in Fig. 2-8 can be found by

$$I_{C_c} = I_{n+1} + c\Delta x \partial_t V_{n+1} - I_{n-1} - c\Delta x \partial_t V_{n-1}, \tag{2.48}$$

It may be replaced by the time derivative of the charge and, thus, by the one of the voltage $I_{C_c} = -C_c \partial_t V_n$, where the voltage at the capacitance is identified with the one in the n-th. cell. The latter is given by $V_n = V_{n+1} - V_{n-1}$. Sorting, taking the continues limit, and considering both coupling slids yields

$$\partial_x I = -c\partial_t V - C_c \partial_t V \left(\delta(x - S/2) + \delta(x + S/2)\right). \tag{2.49}$$

Here, $\delta(x)$ denotes the delta function and enters from the limit $\Delta x \to 0$ from the terms $V_{C_c}/\Delta x$. Derivation and inserting the second unchanged telegraph equation gives the modified wave

equations for voltage or the flux field variable[14]

$$0 = \left[\frac{1}{l}\partial_x^2 - c\partial_t^2 - C_\mathrm{c}\partial_t^2\left(\delta(x-S/2)+\delta(x+S/2)\right)\right]\times[V,\phi]. \tag{2.50}$$

Now it is easy to identify the Lagrangian as

$$\begin{aligned}\mathscr{L}_r &= \frac{1}{2}\int_{-\infty}^{\infty}\left[c\left(\partial_t\phi\right)^2 - \frac{1}{l}\left(\partial_x\phi\right)^2 + C_\mathrm{c}\left(\partial_t\phi\right)^2\left(\delta(x-S/2)+\delta(x+S/2)\right)\right]\mathrm{d}x \\ &= \frac{1}{2}\int_{-\infty}^{\infty}\left[c\left(\partial_t\phi\right)^2 - \frac{1}{l}\left(\partial_x\phi\right)^2\right]\mathrm{d}x + \frac{C_\mathrm{c}}{2}\left(\left(\partial_t\phi\right)^2(-S/2) + \left(\partial_t\phi\right)^2(S/2)\right).\end{aligned} \tag{2.51}$$

This equation corresponds to the same Lagrangian as used before, with added energy of the coupling capacitances and, therefore, changed boundary conditions at the positions $-S/2$ and $S/2$. They may be defined as $\partial_x\phi(\pm S/2) = lI(\pm S/2)$. The corresponding current can be found as the change of the charge on each capacitor plate and, thus, as follows from the voltage difference between the sides of the capacitor

$$I(\pm S/2) = \partial_t Q(\pm S/2_+) - \partial_t Q(\pm S/2_-) = C_\mathrm{c}\left(\partial_t V(\pm S/2_+) - \partial_t V(\pm S/2_-)\right). \tag{2.52}$$

Here, $\dot{V}(S/2_\pm)$ denotes, respectively, the voltage on the right and left side of C_c at position $S/2$. The voltages may be replaced by the currents with the second telegraph equation, giving

$$I(\pm S/2) = \frac{C_\mathrm{c}}{c}\left(\partial_x I(\pm S/2_+) - \partial_x I(\pm S/2_-)\right), \tag{2.53}$$

which may be used to identify the boundary condition for the flux field

$$\partial_x\phi(\pm S/2) = \frac{C_\mathrm{c}}{c}\left(\partial_x^2\phi(\pm S/2_+) - \partial_x^2\phi(\pm S/2_-)\right). \tag{2.54}$$

The voltage at these capacitances can be replaced by the ones at the left and right values of the transmission lines also from this condition, namely by time integration of (2.52)

$$\begin{aligned}V(\pm S/2) &= \frac{1}{C_\mathrm{c}}\int I(\pm S/2)dt = \left(\partial_t\phi(\pm S/2_+) - \partial_t\phi(\pm S/2_-)\right) \\ \partial_t\phi(\pm S/2) &= \left(\partial_t\phi(\pm S/2_+) - \partial_t\phi(\pm S/2_-)\right).\end{aligned} \tag{2.55}$$

The total Lagrangian then reads

$$\begin{aligned}\mathscr{L}_\mathrm{r} =& \frac{1}{2}\int_{-\infty}^{\infty}\left[c\left(\partial_t\phi\right)^2 - \frac{1}{l}\left(\partial_x\phi\right)^2\right]dx \\ &- \frac{C_\mathrm{c}}{2}\left(\left(\partial_t\phi\left(-\frac{S}{2_+}\right) - \partial_t\phi\left(-\frac{S}{2_-}\right)\right)^2 + \left(\partial_t\phi\left(+\frac{S}{2_+}\right) - \partial_t\phi\left(+\frac{S}{2_-}\right)\right)^2\right).\end{aligned} \tag{2.56}$$

[14] Starting with the Kirchhoff equation of the voltage yields the wave equation for current and charge that only differs by constants.

The square terms in the lower line of the above equation consist of three different terms each. Two include only the field variable on one of the sides of the capacitances and result in a shift of the resonance frequency. The mixing terms between the field variables on the two sides of the capacitances describe the coupling between the field inside and outside of the resonator.

For simplicity and because the calculation is analog, first only the center part of the transmission line is considered and the other parts are assumed grounded. Also the calculations will be restricted to the fundamental mode. The square terms on the side modify the wave numbers k_1 as found by inserting $\phi(x) = \phi_1 \sin k_1 x$ into the boundary condition (2.54)[15]

$$\cot\left(\frac{S}{2}k_1\right) = \frac{C_c k_1}{c}. \tag{2.57}$$

For small coupling capacitances C_c the wave vector will only slightly vary from the uncoupled value π/S as $k_1 = \pi/S(1-\varepsilon)$ with $\varepsilon \ll 1$. On the right hand side of (2.57) the small ε term will be neglected and on the left the tangent[16] can be approximated by its argument $\pi\varepsilon/2$ thus the condition for ε is

$$\varepsilon = \frac{2C_c}{cS} \ll 1. \tag{2.58}$$

This requirement is realized in the experiment because the coupling capacitance is small compared to the total one of the resonator. The mode expansion enters into the Lagrangian (2.56). When analyzing the terms in its lower line it is found

$$\partial_t \phi\left(-\frac{S}{2_+}\right) = \partial_t \phi_1 \sin\left[-k_1\frac{S}{2}\right] = -\partial_t \phi_1 \cos\left[\frac{\pi\varepsilon}{2}\right]. \tag{2.59}$$

Because the argument of the cosine is small it can be approximated with unity. The rest of the integration is analog to the one in 2.6. Thus, the total Lagrangian of the central part, where the mode expansion is inserted and the integration is carried out, reads

$$\mathscr{L}_r = \frac{1}{2}\left(\left[C_1 + 2C_c\right]\dot{\phi}_1^2 - \frac{\phi_1^2}{L_1}\right). \tag{2.60}$$

From here the quantization of the central part is analog to the one in 2.6. With the change of the effective capacitance of the resonator the oscillation frequency is shifted to lower values $\tilde{\omega}_0 = \omega_0/\sqrt{1+\varepsilon}$, which for small ε gives the same result as $k_1/\sqrt{lc} = \omega_0(1-\varepsilon)$. The shift originates from a longer wavelength and can be understood from the wave inside the

[15] In contrast to (2.35), the unshifted coordinate x is used.

[16] The cotangent is shifted by $\pi/2$.

resonator leaking out to the external transmission lines. The so achieved coupling between the central resonator and the external lines is mediated by the coupling energy $C_c V_0 V_{out}$, where V_0 is the zero point voltage amplitude inside and V_{out} the corresponding outside of the resonator. Those are given by $V_0 = \sqrt{\hbar\omega_0/C}$ and $V_{out}(\omega_0) = \sqrt{\hbar\omega_0/cS_{out}}$, where S_{out} is the length of the outside transmission line.

2.8 Relaxation of the resonator

There may be two contributions to the process of photon decay. Those are losses inside of the cavity as well as through the coupling capacitances. A straightforward way of incorporating the damping into a quantum description seems to be by including them in the Lagrangian formalism (2.6) because they are already part in the wave equations (2.30), which is the equation of motion of the resonator. A proper Lagrangian to reproduce it by the Euler Lagrange formula was found by Bateman [98]. Nevertheless, an additional degree of freedom is introduced, and a quantum theory has several difficulties [99]. To avoid these, here the losses through the coupling capacitances are considered and dissipative currents are neglected $r = \infty$. As seen in A.3 the total relaxation may then be found by rescaling the coupling capacitance as well as the resistance of the leads.

The influence of the coupling capacitances on a system involving the center resonator and two infinite long transmission lines at each side is discussed above. Again the discussion is restricted to the fundamental mode. When quantizing all parts the total Hamiltonian reads

$$\begin{aligned}\tilde{H}_r =& \hbar\omega_0 a^\dagger a + \sum_k \hbar\omega_k b^\dagger_{k,\mathrm{L}} b_{k,\mathrm{L}} + \sum_k \hbar\omega_k b^\dagger_{k,\mathrm{R}} b_{k,\mathrm{R}} \\ & - \hbar\sum_k g_k \left(a - a^\dagger\right)\left(b_{k,\mathrm{L}} - b^\dagger_{k,\mathrm{L}}\right) + \hbar\sum_k g_k \left(a - a^\dagger\right)\left(b_{k,\mathrm{R}} - b^\dagger_{k,\mathrm{R}}\right)\end{aligned} \tag{2.61}$$

The quantization of the outside fields is analog to the resonator field with S_{out} instead of S as length of the transmission lines. Also, the coupling constants are given by $g_k = C_c V_0 V_{out}/\hbar$. The Hamiltonian above corresponds to the start point of a standard description of damping [91], as similarly discussed in 2.4 for the qubit. The lower line corresponds to the interaction Hamiltonian, and it reads in a rotating wave approximation, neglecting fast oscillating terms with frequencies $\omega_0 + \omega_k$ such as $ab_{k,\mathrm{L}}$,

$$\mathcal{V}_r(t) = \hbar\sum_k g_k \left(a^\dagger b_{k,\mathrm{L}} e^{-i(\omega_0-\omega_k)t} + a b^\dagger_{k,\mathrm{L}} e^{i(\omega_0-\omega_k)t}\right) - \hbar\sum_k g_k \left(a^\dagger b_{k,\mathrm{R}} e^{-i(\omega_0-\omega_k)t} + a b^\dagger_{k,\mathrm{R}} e^{i(\omega_0-\omega_k)t}\right)$$

(2.62)

By assuming the fields in the transmission lines to be in thermal equilibrium, the result of the time evolution of the resonator's density matrix is found from (2.23) with the above interaction Hamiltonian. It is given by [91]

$$\dot{\rho}_\mathrm{r} = \hat{L}_r(\rho_\mathrm{r}) = -\frac{\kappa}{2}\left(\bar{n}_\mathrm{th}+1\right)\left(a^\dagger a\rho_\mathrm{r} - 2a\rho_\mathrm{r}a^\dagger + \rho_\mathrm{r}a^\dagger a\right) \tag{2.63}$$

where

$$\kappa = 2\omega_0^2 C_\mathrm{c}^2 Z/C \tag{2.64}$$

is the photon decay constant (compare (A.14)), Z the load resistance in the external lines, and $\bar{n}_\mathrm{th}$ the mean thermal photon number at frequency ω_0. The latter may be set to zero for the parameters of the experiment. Details of the calculations for the one dimensional CPW resonator are shown in B.2.

2.9 Input field and transmission coefficient

The input field coupling is already described in 2.7, and its quantum representation is explicitly given in 2.8. Assuming a classical probing field $V_\mathrm{in} = V_\mathrm{p}\sin\omega_\mathrm{p}t$, with amplitude V_p and circular frequency ω_p applied through the transmission line to the resonator, the coupling Hamiltonian is given by[17]

$$H_\mathrm{p} = -\mathrm{i}C_\mathrm{c}V_0V_\mathrm{p}\sin\omega_\mathrm{p}t\left(a^\dagger - a\right). \tag{2.65}$$

With only keeping the slow rotating terms, see (2.46) and (2.47), and introducing the probing amplitude

$$\Omega_\mathrm{p} = \frac{C_\mathrm{c}V_0V_\mathrm{p}}{2\hbar}, \tag{2.66}$$

the Hamiltonian can be expressed as

$$H_\mathrm{p} = \hbar\Omega_\mathrm{p}\left(a^\dagger \mathrm{e}^{-\mathrm{i}\omega_\mathrm{p}t} + a\mathrm{e}^{\mathrm{i}\omega_\mathrm{p}t}\right). \tag{2.67}$$

This calculation is restricted to the fundamental mode because ω_p is assumed close to its frequency. In principle, the sum of all modes may be entered and all fast oscillating terms in

[17] The minus sign is due to the negative voltage amplitude at $-S/2$ of the resonator.

2.67 may then be omitted. The driving in other resonator modes can be identified completely analog.

To characterize the resonator the transmission t_r defined as $V_\mathrm{out}/V_\mathrm{in}$ can be measured at a probing frequency $\omega_\mathrm{p}/2\pi$. The output voltage is defined from the series circuit of the output coupling capacitance C_c and the load resistance[18],

$$V_{out} = \frac{Z}{Z_\mathrm{c}+Z}\langle V_\mathrm{r}\rangle \approx \mathrm{i}\omega_\mathrm{p} C_\mathrm{c} Z \langle V_\mathrm{r}\rangle. \tag{2.68}$$

Here, $\langle V_\mathrm{r}\rangle$ is the expectation value of the voltage at the output coupling capacitance and corresponds to the voltage amplitude in the resonator ($\tilde{x} = S$ in (2.44)). In addition, $Z_\mathrm{c} = 1/\mathrm{i}\omega_\mathrm{p} C_\mathrm{c}$ is the coupling capacitance impedance, where $\omega_\mathrm{p}/2\pi$ is the frequency of the voltage field excited in the resonator. For high quality resonators the coupling impedance is significantly larger than the wave impedance which justifies the assumption in (2.68). By considering an excited first mode of the resonator, the expectation value can also be expressed by

$$\begin{aligned}\langle V\rangle &= -\mathrm{i}V_0\langle a\,\mathrm{e}^{-\mathrm{i}\omega_\mathrm{p}t} - a^\dagger \mathrm{e}^{\mathrm{i}\omega_\mathrm{p}t}\rangle \\ &= -\mathrm{i}V_0\left(\langle a\rangle\,\mathrm{e}^{-\mathrm{i}\omega_\mathrm{p}t} - \langle a^\dagger\rangle \mathrm{e}^{\mathrm{i}\omega_\mathrm{p}t}\right) \\ &= 2V_0\left(Re(\langle a\rangle)\sin\omega_\mathrm{p}t - Im(\langle a\rangle)\cos\omega_\mathrm{p}t\right),\end{aligned}$$

where $Re(\langle a\rangle)$ and $Im(\langle a\rangle)$ are the real and imaginary part of the expectation value of the field operator a, respectively. A network analyzer mixes the output signal with the input signal and an $\pi/2$ shifted copy of the input. After a normalization to the input amplitude V_p this mixing results in the quadratures Q and I as "in phase" and "out of phase" signal. They are taken as real and imaginary part of the complex output signal and transmission amplitude $t_\mathrm{r} = \sqrt{Q^2+I^2}$ and phase $\phi_{t_\mathrm{r}} = \arctan(I/Q)$ may be calculated. Thus, the transmission coefficient as measured by a network analyzer is

$$t_\mathrm{r} = \mathrm{i}\frac{2\omega_\mathrm{p} C_\mathrm{c} Z V_0}{V_\mathrm{p}}\langle a\rangle. \tag{2.69}$$

With the definitions of the zero point voltage V_0 (see 2.6), the loss rate(2.64), the driving amplitude (2.66), and under the assumption that the resonator is probed close to the fundamental mode $\omega_\mathrm{p} \approx \omega_0$ it reads

$$t_\mathrm{r} = \mathrm{i}\frac{\kappa}{2\Omega_\mathrm{p}}\langle a\rangle. \tag{2.70}$$

[18] Or the wave impedance Z outside of the resonator, which has the same value as the load of the measurement device or the amplifier.

Information of the system can also be gained without the need of a probing signal by the use of a spectrum analyzer. Then amplitudes of signals emitted from the resonator at different frequencies are collected, e.g. giving information about excited resonator modes.

3 Experimental requirements and setup

3.1 Experimental setup

The characteristic frequencies of the discussed superconducting qubits lay in the microwave regime between 1 GHz and 20 GHz. To perform quantum type experiments, it is necessary that the system can relax into the ground state and to avoid thermal population in the corresponding resonators. Although classical resonators can be used to probe the quantum nature of the two-level systems [34] and to test several effects, such as different coupling types [40] or the so called Sisyphus effect [100], a real quantum coupling implies a resonator in its ground state as well. Furthermore, the quantum space can be limited to a small amount of states, and a quantum theory can lead to analytic results [93].

To ensure that no thermal excitations occur, the energy of the surrounding bath needs to be well below the energy of a single photon. Assuming an energy splitting of the states of about 2.5 GHz this requirement demands a temperature

$$T < \frac{h\nu}{k_\mathrm{B}} = 130\,\mathrm{mK} \tag{3.1}$$

This relation illustrates that experiments need to be performed in a dilution refrigerator (see Schematic in Fig. 3-1), where a mixture of He^3 and He^4 is used to achieve temperatures around 10 mK. This mixture is condensed after cooling with a pumped He^4 pot and expanding on an imped-ance in the so-called condensing tube. Below a temperature of 1.2 K a phase separation into a phase rich on He^3 and one which has almost no He^3 is occurring. The latter is mainly collected in the so-called still. By pumping He^3 from it an evaporation of He^3 into this quasi vacuum from the second phase located in the mixing chamber is achieved. For this process heat is required, and a cooling effect working down to several mK results. With the use of heat exchangers to cool the mixture that is condensing with the He^3 that is pumped, a closed cycle can be realized. In addition, any impurities in the closed cycle of the mixture

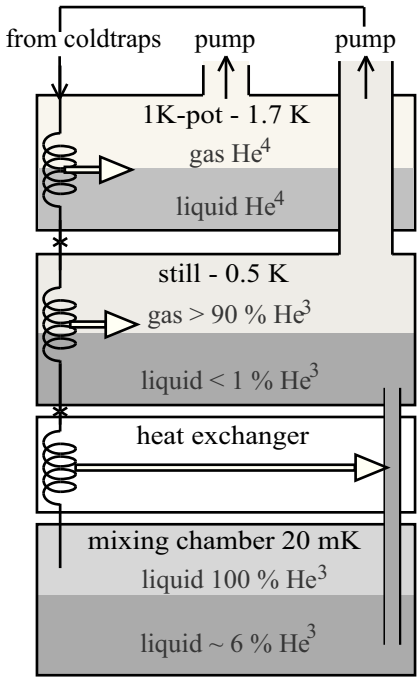

Figure 3-1: Schematic of a dilution refrigerator. The different components as well as the process of cooling are discussed in the text.

need to be avoided. The purity of the gas can be ensured by the use of different cold traps working with liquid nitrogen and helium.

To increase the amount of He^3 that is circulating, usually the still is heated with a power in the mW range[1]. Still, the cooling effect is reduced with decreasing temperatures; therefore, any heat load on the cold stages needs to be avoided. Thus, in a measurement setup all the cables used need to be thermally anchored at each temperature state.

3.2 Measurement setup

Cabling to the sample not only is needed to apply probing or manipulating signals and reading its response, but it also connects the 300 K environment of the measurement devices to it. Since the corresponding noise would also lead to excitation from the ground state, damping and filtering is applied for the different lines. A principle sketch of the used measurement setup is shown in Fig. 3-2. In the MW-part 20 dB attenuators are used at the 1-K and mixing chamber stages to thermalize the signal. There the 300 K noise from the room temperature

[1]For more details see for example [101]

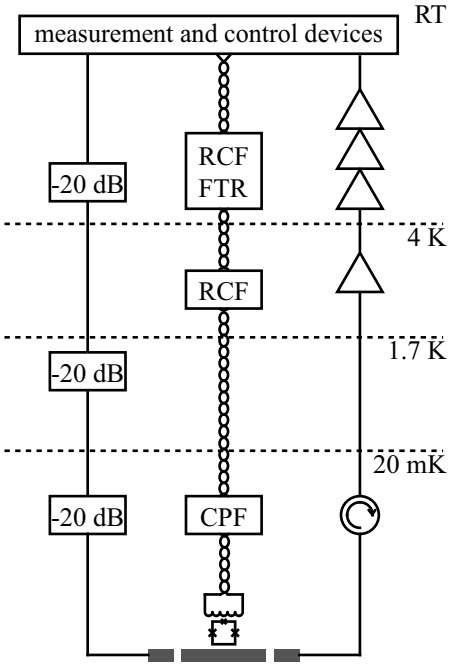

Figure 3-2: Schematic of the cabling of the samples. The resonators input and output are connected by microwave lines. A cold amplifier together with a series of room temperature amplifiers provide a total gain of about 75 dB. An external coil is used for applying the energy bias to the qubit. The sample is isolated from the noise of the measurement devices by attenuators in the MW-input lines and filters (RCF - rc-filter, FTR - feedthrough-filter, and CPF - copper-powder-filter) in the DC lines. The noise reaching the sample from the amplifier is suppressed by an isolator.

devices is reduced together with the signal by a factor of 1000. This suppression results in an effective noise less than 30 mK at the sample. Because the output signal is small, a series of commercial amplifiers are used. The noise background in the measurement is mainly given by the noise temperature of the first cold amplifier which is about 10 K. The sample is protected from the amplifier noise by the use of an isolator placed at the 20 mK stage.

The MW-lines are realized by semi-rigid coaxial cables with an impedance of 50 Ohm. For the connection from 300 K to the 1 K stage 2.2 mm thick cables with copper beryllium inner and stainless steel outer conductor are used. The input lines from 1 K to the sample are 0.8 mm thick and made from stainless steel, while for the output from the sample NbTi wires are used with a thickness of 2.2 mm. The DC- lines are realized as shielded twisted pairs and made from brass from 300 K to the 4 K filter and from NbTi below.

To achieve stable measurement conditions, the influence of external fields to the sample should be avoided. Therefore, it is enclosed by mu-metal and superconducting shields. The

first mentioned suppresses external magnetic fields, while the latter freezes the remaining magnetic field when cooled below the superconducting transition.

To characterize the sample, transmission type measurements can be performed or its output spectrum can be recorded. For this purpose a vector network analyzer or a spectrum analyzer is used, respectively. Additional microwave signals can be applied to the input by the use of combiners and microwave generators.

3.3 Sample fabrication and preparation

The fabrication of a sample consists of two steps. At first a 200 nm thick Nb film is deposited on an intrinsic silicon substrate. The resonator is then structured by e-beam lithography and CF_4-reactive ion etching. The minimal structure size is of the order of 1 μm, and limited by the aspect ratio of the etching.

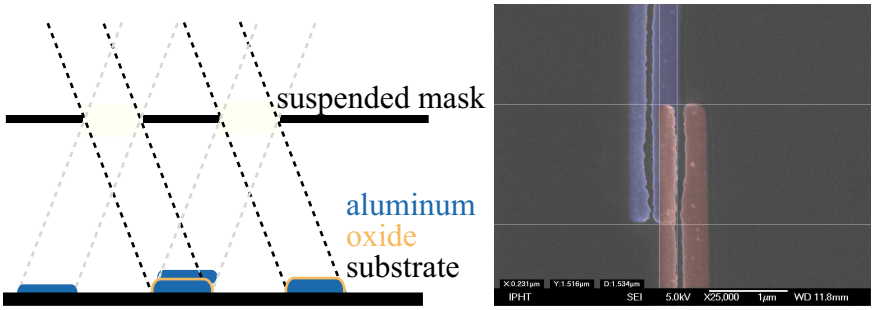

Figure 3-3: (left) Principle sketch of the shadow evaporation technique explained in the main text. (right) SEM image of a single Josephson junction fabricated in such way. For a better visibility the lower layer is coloured in blue, the upper in red.

In a second step the qubit structures are formed by the shadow evaporation technique [19], see Fig. 3-3. Evaporation of two layers of Al with thicknesses of 50 nm and 80 nm, respectively, at two different angles through a suspended mask formed by e-beam lithography can create an overlap between the two layers. A Josephson tunnel junction is formed in this overlap region, when an oxidation between the two evaporation steps is introduced. The parameters of the junction mainly depend on the oxidation time and pressure. The openings in the mask for a flux qubit usually have a linewidth of 150 nm and the overlap region for the junctions a dimension of about 500 nm. A final lift-off finishes the qubit fabrication.

The experimentally investigated samples considered below are all designed as three junction flux qubits. The sizes range from 120×550 nm^2 to 180×800 nm^2 for the two large junctions in one loop. The third junction is about 20 % to 35 % smaller.

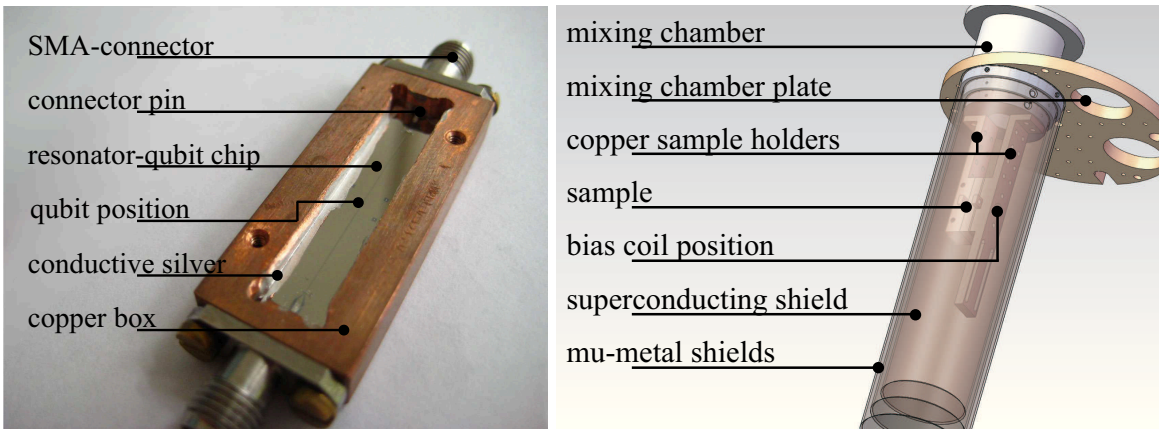

Figure 3-4: (left) Picture of opened complete sample. The resonator-qubit chip is placed inside a copper box and wired to SMA-connectors, thus forming the total sample. (right) It is mounted at the bottom of the mk-plate of a dilution refrigerator. In addition bias coils and different shields are used.

The sample is placed inside of a copper box, see left image in Fig. 3-4. The box is designed such, that directly below and above the chip no copper is placed along the central resonator line. This design reduces losses of the resonator.

SMA-connectors are mounted on each side of the copper box, their pins lying directly on the chip's microwave bond pads. The connection between the both as well as between the mass plates of the sample and the copper box is achieved with connective silver for good microwave contact. The in that way finished sample is pressed between two fingers mounted at the base of a dilution refrigerator as shown in the right of Fig. 3-4. Those are made from copper for good thermal contact and also carry two coils, centered above and below the qubit's position for dc flux bias. Finally, SMA-cables[2] for in- and output are connected before one superconducting and two mu-metal shields close the experimental setup.

[2]The cables, SMA-connectors, and the final 20 dB attenuator are not shown in the figure.

4 Coupling a flux qubit to a resonator

In this chapter the basic coupling mechanism of the qubit-resonator system will be discussed. For doing that a weak probing signal is applied close to the fundamental mode frequency. The coupling then enables to experimentally determine the properties of the complete system from the transmitted signal, which will be discussed comparatively for two samples with different parameters. Finally, the direct qubit-resonator resonance will be closer investigated and a theoretical description developed.

4.1 Magnetic coupling

The dimensions of a single flux qubit are small compared to the wavelength of its corresponding eigenfrequencies. Thus, it can be physically placed at any position inside the resonator. As discussed in chapter 2.2, the flux qubit is tunable with magnetic fields. To achieve coupling between the two systems, the qubit should therefore be placed at a position where the magnetic field of the resonator has a maximum - at a current antinode. For a $\lambda/2$ resonator and its fundamental mode[1] it lays in the middle of the resonator (see (2.45)). The coupling energy between the two systems in the qubit's flux basis is then given by

$$H_{\mathrm{c}} = MI_{\mathrm{q}}I_{\mathrm{r}} = \hbar g\left(a + a^{\dagger}\right)\sigma_z. \tag{4.1}$$

Here, the coupling constant to the fundamental mode is given by $g = MI_0I_{\mathrm{p}}$, where M is the mutual inductance between the resonator and the qubit, I_0 the zero point current in the resonator, and I_{p} the persistent current of the qubit. The coupling for all odd harmonics is similar found. The origin of the above equation can be understood, by considering MI_{r} as changing flux that is added to (2.5). That gives an extra term in (2.12), which corresponds to (4.1). Also, the current in the resonator is given by (2.45), and on a scale of the qubit around

[1] And for all the odd harmonics.

the center of the resonator the sinusoidal term for the space dependence can safely be put to one for all odd modes. The back action on the resonator can be understood by interpreting the qubit as additional magnetic moment given by the mean current in the loop. In the same way as an iron core in a coil, the qubit can change the effective inductance of the resonator and, therewith, its resonance frequency.

The mutual inductance is only given by the geometry of the fabricated sample. One can estimate the value by assuming a current I inside the infinite one dimensional center conductor and using the Biot-Savart law. The magnetic field at the qubit's position is perpendicular to the qubit area and has a value of

$$B = \frac{\mu_0 I}{2\pi y}, \tag{4.2}$$

where y is the distance from the center of the conductor. Integration of this field over the area of the qubit gives the flux and the mutual inductance follows as

$$M = \frac{\Phi}{I} = \frac{\mu_0 l_\mathrm{q}}{2\pi} \ln\left(\frac{h_\mathrm{q} + d_\mathrm{q}}{d_\mathrm{q}}\right). \tag{4.3}$$

Here, l_q is the length, h_q the height, and d_q the distance from the center conductor of the qubit. Assuming reasonable values, as a qubit size of $5x5$ μm^2 and a distance from the center of 2 μm^2, the value of the mutual inductance is about 0.3 pH. It may be enlarged by increasing the magnetic flux created by the resonator inside of the qubit loop. Thus, either the size of the qubit should be increased or the magnetic field in the qubit loop enhanced. Latter may be achieved by tapering the resonator, or in other words decreasing the slid between the center conductor and the ground planes of the resonator.

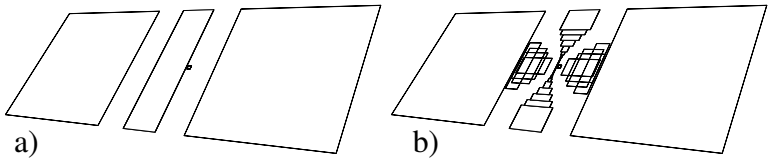

Figure 4-1: Central part of the qubit-resonator-structures calculated with FASTHENRY. a) Straight geometry. The central conductor has a width of 50 μm width a gap of 30 μm to the ground planes. b) Tapered geometry. The central line of the resonator is tapered to a width of 1 μm while the size of the gap to the ground plane is decreased to 9 μ. In both shown geometries a qubit loop of size 5×5 μm^2 is placed in the remaining slid.

The assumption above can be tested by the use of simulation programs such as FASTHENRY [102]. To do so the geometries shown in Fig. 4-1 have been simulated and the resulting

inductance values are listed in table 4.1. In this example the tapering of the resonator yields

geometry	qubit size (μm^2)	L (nH)	M (pH)
straight	5×2.5	10.5	0.2
straight	5×5	10.5	0.3
tapered	5×2.5	13.7	0.8
tapered	5×5	13.7	1.3

Table 4.1: Results for the inductance of the resonator L and the mutual inductance M of the FASTHENRY simulations for the geometries shown in Fig. 4-1 and different qubit sizes.

an increase of the mutual inductance by a factor of four. Interestingly the value for the not tapered resonator and a qubit size of 5×5 μm^2 corresponds well to the analytic estimate. This fact indicates that the field created by the current in the ground plane can be neglected if its distance to the center conductor and the qubit is large compared to the qubit size. By analyzing (4.1) a direct exchange of energy between the subsystems can occur. This interaction can be identified even more obvious by a transformation of (4.1) into the qubit's energy eigenstates

$$H_c = g\left(a + a^\dagger\right)\left(\frac{\varepsilon}{\omega_\mathrm{q}}\sigma_z + \frac{\Delta}{\omega_\mathrm{q}}\sigma_x\right). \tag{4.4}$$

Here, terms of direct energy exchange $a^\dagger\sigma_-$ and $a\sigma_+$ are included[2], in the sense that a photon in the resonator is destroyed while the qubit state is changed from ground to the excited state and vice versa. Interestingly, there are two coupling terms. The one proportional to σ_x is similar to the dipole coupling between an atom and a light field [91]. On the other hand, the diagonal coupling term proportional to σ_z does only occur for tunable systems. In other words, at the degeneracy point the potential is symmetric and thus the states have a well-defined parity. In that case, the selection rules are the same as for the dipole moment of an atom [103]. Away from the degeneracy point the symmetry of the potential is broken. This fact can lead to the coexistence of single and multi-photon transitions [104] and, as shown later, to transitions that in first order are not observable in quantum optics with atoms.

[2]Note that $\sigma_x = \sigma_+ + \sigma_-$.

4.2 Continuous monitoring of a flux qubit with a CPW resonator

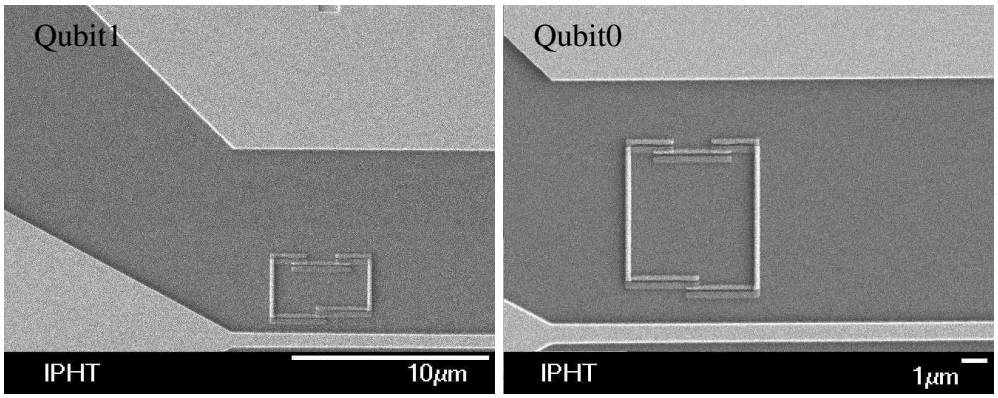

Figure 4-2: SEM-image of the two samples with different qubit sizes. Each qubit is placed close to the center of the resonator inside of the gap between the tapered center line of the resonator (bottom) and its ground plane (top).

In a first experiment two samples are considered. They are named as Qubit0 and Qubit1; and each has a single qubit placed inside of a resonator, tapered as described above. In Fig.4-2 SEM images displaying the center part of the resonator with the qubits are shown. They have nominal sizes of 5×2.5 μm^2 for Qubit1 and 5×5 μm^2 for the Qubit0. By applying a weak probe signal and measuring the transmission through the resonator, the samples can be characterized.

First, the resonator properties are found by sweeping the probing signal frequency ω_p and measuring the transmission coefficient $|t_r|$, while the qubits are detuned far away from there degeneracy point $|\varepsilon_{0,1}| \gg 0$. From fitting the Lorentzian line shapes, as shown in Fig. 4-3, the resonant frequencies $\omega_0/2\pi$ and quality factors Q are accurately found to be 2.585 GHz and 2.2×10^4 for Qubit1 and 2.590 GHz and 12×10^4 for Qubit0, respectively. Both resonators have a similar design. They are under coupled, meaning that the quality factor is mainly determined by internal losses. This property may explain the quite different numbers because in that case several aspects, like sample mounting, contacting, and so on, can contribute to additional losses.

Next, the probing frequency is fixed at the resonator center frequency $\omega_p = \omega_0$. Then, by sweeping the magnetic field applied by the external coil the phase of the transmitted signal

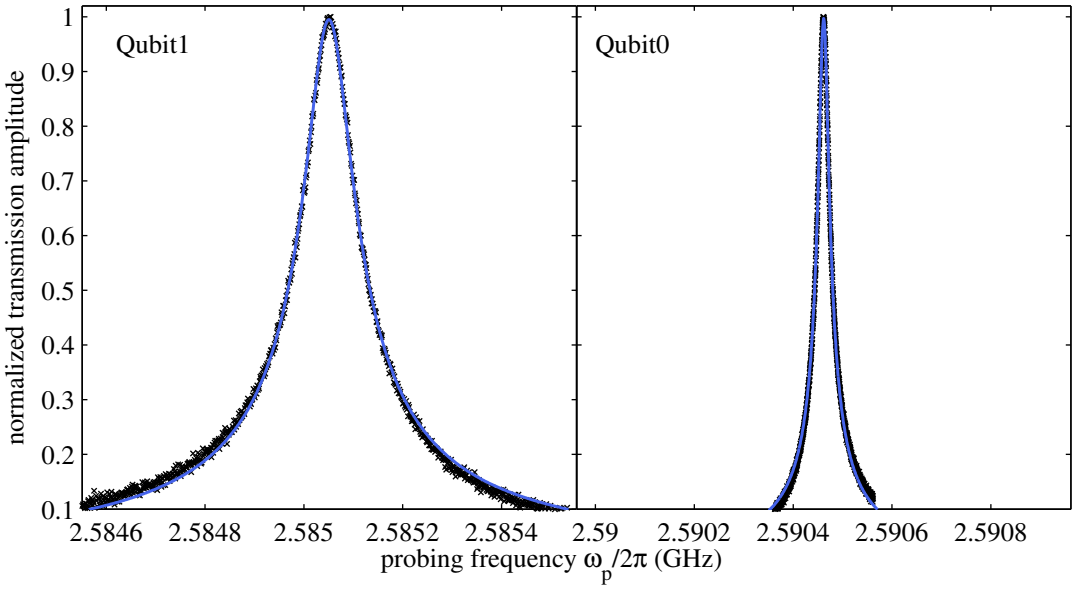

Figure 4-3: Measured normalized transmission of a weak probing signal through the resonators (black crosses). The probing frequency is varied around the resonant frequency of the two resonators and fitted with (A.11) for each of the samples (blue solid lines). For better comparison the x-axes of the two plots is scaled similar.

is changed in dependence of the qubits' properties. The phase change corresponds in both cases to a dispersive shift of the resonant frequency of the resonator, when the detuning between the resonator and qubit energy splitting becomes smaller. As displayed in Fig. 4-4, the qubit on sample Qubit1 shifts the resonant frequency only to smaller frequencies, while the other one has two symmetric phase jumps. The quite different shapes occur because of the different minimal energy splitting.

To explain these different responses the total systems Hamiltonian

$$H = \hbar\frac{\omega_\mathrm{q}}{2}\sigma_z + \hbar\omega_0 a^\dagger a + g\left(a+a^\dagger\right)\left(\frac{\varepsilon}{\omega_\mathrm{q}}\sigma_z + \frac{\Delta}{\omega_\mathrm{q}}\sigma_x\right) + \hbar\Omega_\mathrm{p}\left(a^\dagger \mathrm{e}^{-\mathrm{i}\omega_\mathrm{p}t} + a\mathrm{e}^{\mathrm{i}\omega_\mathrm{p}t}\right) \quad (4.5)$$

has to be considered. Here, the terms account for the energy of the qubit (2.13), the resonator (2.42), the coupling between both (4.4), and the probing signal (2.67). After an unitary transformation to a frame rotating with the probing frequency using $\hat{U}_2 = \mathrm{e}^{\mathrm{i}\omega_\mathrm{p}\left(\frac{\sigma_z}{2}+a^\dagger a\right)}$ (for details see appendix C.1), Hamiltonian (4.5) reads

$$H = \hbar\frac{\delta_\mathrm{qp}}{2}\sigma_z + \hbar\delta_\mathrm{rp}a^\dagger a + \hbar g_\Delta\left(a\sigma_+ + a^\dagger\sigma_-\right) + \hbar\Omega_\mathrm{p}\left(a^\dagger + a\right). \quad (4.6)$$

Above the qubit lowering and raising operators $\sigma_\pm$ are used. Terms rotating with frequencies ω_p and $2\omega_\mathrm{p}$ have been neglected because they would average out fast. This assumption

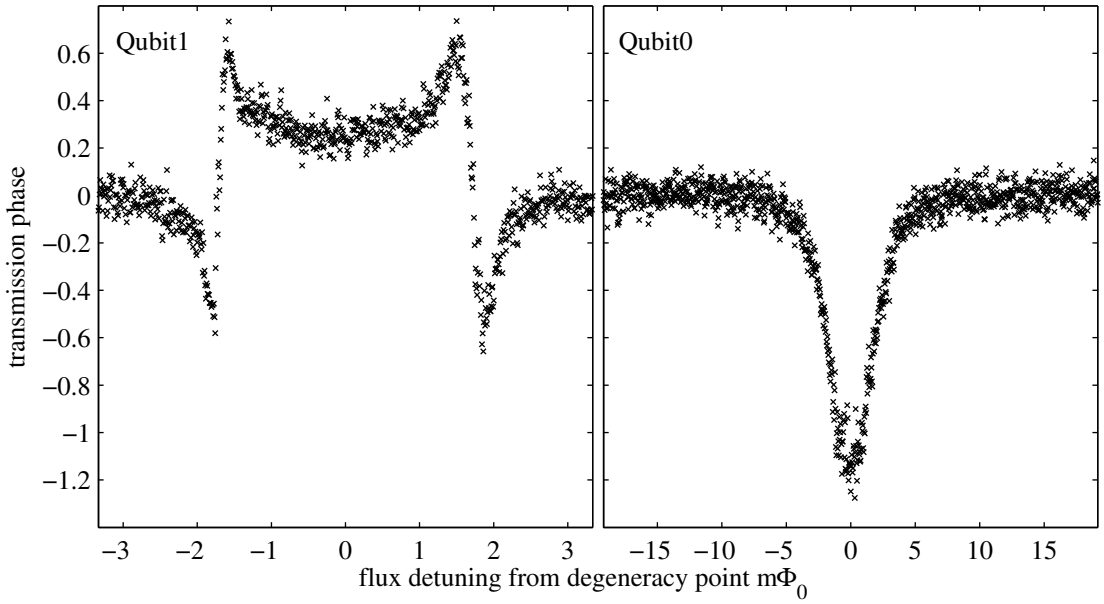

Figure 4-4: When sweeping the magnetic field with the external coil while the signal frequency is fixed at the resonant frequency, a characteristic phase shift of the transmitted signal reveals the coupling to the qubits. The different shape of the curves is due to the different minimal energy splitting, as explained in the text.

is called the rotating wave approximation (RWA). The variables $\delta_{\mathrm{qp}} = \omega_{\mathrm{q}} - \omega_{\mathrm{p}}$ and $\delta_{\mathrm{rp}} = \omega_0 - \omega_p$ denote the detuning between the probing frequency and the qubit as well as between probing signal and resonator, respectively. Also, the coupling constant is rescaled with the ratio between the qubit gap and its total energy $g_\Delta = g\frac{\Delta}{\hbar\omega_{\mathrm{q}}}$ and has its maximum at the degeneracy point. Note, the first three terms of (4.6) correspond to the Jaynes-Cummings Hamiltonian and describe the basic energy exchange between a photon field and an atom.

A second transformation $\hat{U}_3 = \mathrm{e}^{\frac{g_\Delta}{\delta_{\mathrm{qr}}}\left(a\sigma_+ - a^\dagger\sigma_-\right)}$ [58], which is expanded to the second order in g_Δ (see App. C.2) brings the Hamiltonian into the form

$$H \approx \hbar\left(\omega_0 + \frac{{g_\Delta}^2}{\delta_{\mathrm{qr}}}\sigma_z\right)a^\dagger a + \frac{\hbar}{2}\left(\omega_{\mathrm{q}} + \frac{{g_\Delta}^2}{\delta_{\mathrm{qr}}}\right)\sigma_z. \tag{4.7}$$

It illustrates the origin of the measurement results in the dispersive regime, when the detuning between resonator and qubit $\delta_{\mathrm{qr}} = \omega_{\mathrm{q}} - \omega_0$ is large. The first term gives the resonance frequency depending on the qubit state. If the qubit stays in the ground state ($\langle\sigma_z\rangle = -1$), the dispersive shift of the resonator frequency depends on detuning and rescaling of the coupling. Since only a shift to negative frequencies is observed for Qubit0, the qubit gap frequency has to be above the one of the resonator $\Delta > \omega_0$. In other words, the qubit level splitting lays for

all values of the energy bias ε above the one of the resonator. The strongest shift corresponds to minimal detuning, which is achieved at the degeneracy point where $\hbar\omega_\mathrm{q} = \Delta$. On the other side, the phase jumps in the response from Qubit1 correspond to direct resonances between the resonator and the qubit $\omega_\mathrm{q} = \omega_0$ at bias values for which the detuning changes it sign. Since $\delta_\mathrm{qr} = 0$ at this points the estimation for Hamiltonian (4.7) breaks down. Nevertheless, a measurement procedure for reconstructing the qubit parameters can be found in it.

4.3 Two-tone spectroscopy

As explained above, the resonance frequency of the resonator in the dispersive regime depends on the qubit state. A continuous signal applied at the qubit frequency produces a superposition between ground and excited state. This result can be concluded from the Hamiltonian of a qubit driven by a classical field. In the flux basis and assuming the qubit coupled to the magnetic component of the ac-drive, it reads[3]

$$H_\mathrm{d} = \frac{\Delta}{2}\sigma_x + \frac{\varepsilon}{2}\sigma_z + \hbar\Omega_\mathrm{cl}\cos\omega_\mathrm{d}t\,\sigma_z. \tag{4.8}$$

Here, the amplitude of the classical drive $\Omega_\mathrm{cl} = 2g\sqrt{N}$ includes the coupling of the signal to the qubit and the mean number of photons in the resonator. Note, the Hamiltonian above is also used as start point for the analysis of Landau-Zener-Stückelberg interferometry [105]. If the driving signal is applied directly to the resonator the amplitude reaching the qubit is small because the resonator acts as bandpass filter. Thus, high driving amplitudes are needed.

The above Hamiltonian reads in the eigenbasis of the qubit and in a frame rotating with frequency ω_d around σ_z

$$H_\mathrm{d} = \hbar\frac{\delta_\mathrm{qd}}{2}\sigma_z + \hbar\frac{\Omega'_\mathrm{cl}}{2}\sigma_x, \tag{4.9}$$

where $\Omega'_\mathrm{cl} = \Omega_\mathrm{cl}\frac{\Delta}{\hbar\omega_\mathrm{q}}$, and again terms rotating with frequencies larger or equal ω_d have been neglected. Also, $\delta_\mathrm{qd} = \omega_q - \omega_d$ describes the detuning between driving and qubit frequency. A physical interpretation of Ω_cl may easily be found in the resonance case $\delta_\mathrm{qd} = 0$. Then

[3]The Hamiltonian can be found from (4.5) in the flux basis $H = \varepsilon\sigma_z/2 + \Delta\sigma_x/2 + \hbar g\sigma_z(a^\dagger + a) + \hbar\Omega_\mathrm{d}\left(a^\dagger \mathrm{e}^{-\mathrm{i}\omega_\mathrm{d}t} + a\mathrm{e}^{\mathrm{i}\omega_\mathrm{d}t}\right)$, where the eigenenergy of the resonator is neglected. By transforming to a rotating frame with $\hat{U}_4 = \mathrm{e}^{\mathrm{i}\omega_\mathrm{d}t a^\dagger a}$ the time dependency is shifted to the coupling term. A coherent field can be assumed in the resonator $\alpha = \langle a\rangle = \sqrt{N}$ with N the mean number of photons in the resonator. Finally, the constant energy term $\propto \Omega_\mathrm{d}$ can be neglected.

by solving the Schrödinger equation, an oscillation of the population between ground and excited state with frequency $\Omega_{\mathrm{cl}}/2\pi$ is found. Such oscillations are called Rabi oscillations and the corresponding frequency at the interaction point is named the on-resonance Rabi frequency $\Omega_{\mathrm{R0}} = \Omega'_{\mathrm{cl}}$.

The expectation value for the population of the qubit's state is

$$\langle \sigma_z \rangle = \rho_{\mathrm{ee}} - \rho_{\mathrm{gg}}.$$

Its value can be calculated by solving the stationary master equation

$$\dot{\rho}_{\mathrm{q}} = \frac{\mathrm{i}}{\hbar}\left[H_{\mathrm{d}}, \rho_{\mathrm{q}}\right] + \hat{L}_{\mathrm{q}}(\rho_{\mathrm{q}}) \tag{4.10}$$

for the given Hamiltonian and $\hat{L}_{\mathrm{q}}$ as in (2.25). The master equation gives four equations for the components of the density matrix, which can be written as

$$\begin{pmatrix} \dot{\rho}_{\mathrm{ee}} \\ \dot{\rho}_{\mathrm{gg}} \\ \dot{\rho}_{\mathrm{eg}} \\ \dot{\rho}_{\mathrm{ge}} \end{pmatrix} = \begin{pmatrix} -\Gamma_{\mathrm{r}} & 0 & \mathrm{i}\Omega'_{\mathrm{cl}}/2 & -\mathrm{i}\Omega'_{\mathrm{cl}}/2 \\ \Gamma_{\mathrm{r}} & 0 & -\mathrm{i}\Omega'_{\mathrm{cl}}/2 & \mathrm{i}\Omega'_{\mathrm{cl}}/2 \\ \mathrm{i}\Omega'_{\mathrm{cl}}/2 & -\mathrm{i}\Omega'_{\mathrm{cl}}/2 & -\Gamma_{\varphi} - \mathrm{i}\delta_{\mathrm{qd}} & 0 \\ -\mathrm{i}\Omega'_{\mathrm{cl}}/2 & \mathrm{i}\Omega'_{\mathrm{cl}}/2 & 0 & -\Gamma_{\varphi} + \mathrm{i}\delta_{\mathrm{qd}} \end{pmatrix} \begin{pmatrix} \rho_{\mathrm{ee}} \\ \rho_{\mathrm{gg}} \\ \rho_{\mathrm{eg}} \\ \rho_{\mathrm{ge}} \end{pmatrix} \tag{4.11}$$

In addition, the trace of the density matrix is one, $\rho_{\mathrm{ee}} + \rho_{\mathrm{gg}} = 1$. By introducing the new variables $\rho_0 = \rho_{\mathrm{ee}} - \rho_{\mathrm{gg}}$, $\rho_+ = \rho_{\mathrm{eg}} + \rho_{\mathrm{ge}}$, and $\rho_- = \rho_{\mathrm{eg}} - \rho_{\mathrm{ge}}$ [106] only three equations remain. Note the above introduced values are the elements of Bloch-vector and correspond to the expectation values of the Pauli-operators σ_z, σ_x, and σ_y, respectively. Their time evolution is given by the Bloch-equations [107]

$$\begin{aligned} \dot{\rho}_0 &= -\Gamma_{\mathrm{r}}(1+\rho_0) + \mathrm{i}\Omega'_{\mathrm{cl}}\rho_- \\ \dot{\rho}_+ &= -\Gamma_{\varphi}\rho_+ - \mathrm{i}\delta_{\mathrm{qd}}\rho_- \\ \dot{\rho}_- &= \mathrm{i}\Omega'_{\mathrm{cl}}\rho_0 - \mathrm{i}\delta_{\mathrm{qd}}\rho_+ - \Gamma_{\varphi}\rho_- \end{aligned} \tag{4.12}$$

and the steady state solution ($\dot{\rho} = 0$) gives

$$\begin{aligned} \rho_0 = \langle \sigma_z \rangle &= -\frac{\Gamma_{\mathrm{r}}}{\frac{{\Omega'_{\mathrm{cl}}}^2}{\Gamma'_{\varphi}} + \Gamma_{\mathrm{r}}} \\ \rho_+ &= -\frac{\mathrm{i}\Omega'_{\mathrm{cl}}\Gamma_{\mathrm{r}}}{\Gamma_{\mathrm{r}}\Gamma'_{\varphi} + {\Omega'_{\mathrm{cl}}}^2} \\ \rho_- &= -\frac{\delta_{\mathrm{qd}}}{\Gamma_{\varphi}} \frac{\Omega'_{\mathrm{cl}}\Gamma_{\mathrm{r}}}{\Gamma_{\mathrm{r}}\Gamma'_{\varphi} + {\Omega'_{\mathrm{cl}}}^2}, \end{aligned} \tag{4.13}$$

where $\Gamma'_\varphi = \frac{\delta_{qd}^2+\Gamma_\varphi^2}{\Gamma_\varphi}$. Due to relaxation and dephasing the Rabi oscillation and the oscillation of coherences get damped, so that a steady state results. By interpreting (4.13), the dispersive shift can be reduced by driving the qubit in resonance $\delta_{qd} = 0$. A corresponding measurement result is shown for both discussed samples in Fig. 4-5.

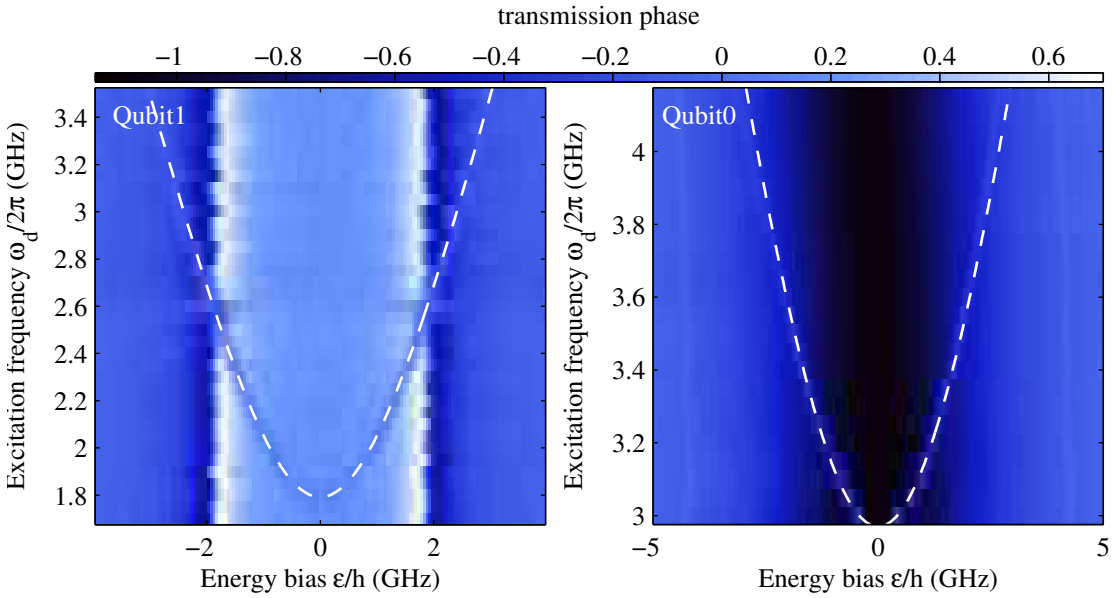

Figure 4-5: Qubit spectroscopy. Phase of the transmitted signal in dependence of the qubit bias and the driving frequency. The color scale gives the dispersive shift, which is always negative for the Qubit0 sample and produces a phase jump in the measurement of qubit1 at a bias value, where the detuning between probing and qubit frequency changes its sign. When the driving signal fits the qubit level splitting, the dispersive shift is reduced, and gives the parabolic shaped curves in both pictures. The dashed lines correspond to fits with the equation for the qubit energy (2.14).

There, the transmission phase is recorded at different driving frequencies and qubit biases. The points at which the dispersive shift is reduced correspond to resonances between the qubit and driving signal. A fit of their dependence on the energy bias with (2.14) gives the energy gap frequencies $\Delta_1/h = 1.79$ GHz and $\Delta_0/h = 2.97$ GHz as well as the persistent currents $I_{p1} = 180$ nA and $I_{p0} = 160$ nA, respectively.

In addition, the expectation value for the population of the driven qubit depends on the relaxation rates. Following (4.13) the ratio between driving strength and relaxation rate Γ_r defines the height of the spectroscopy line, while the ratio between the driving and the decoherence rate Γ_φ gives its width. In addition, the bias dependence of the effective driving Ω'_{cl} gives the possibility to identify all the parameters, when the spectroscopy signal for

different frequencies is fitted. This parameter reconstruction is demonstrated in Fig. 4-6.

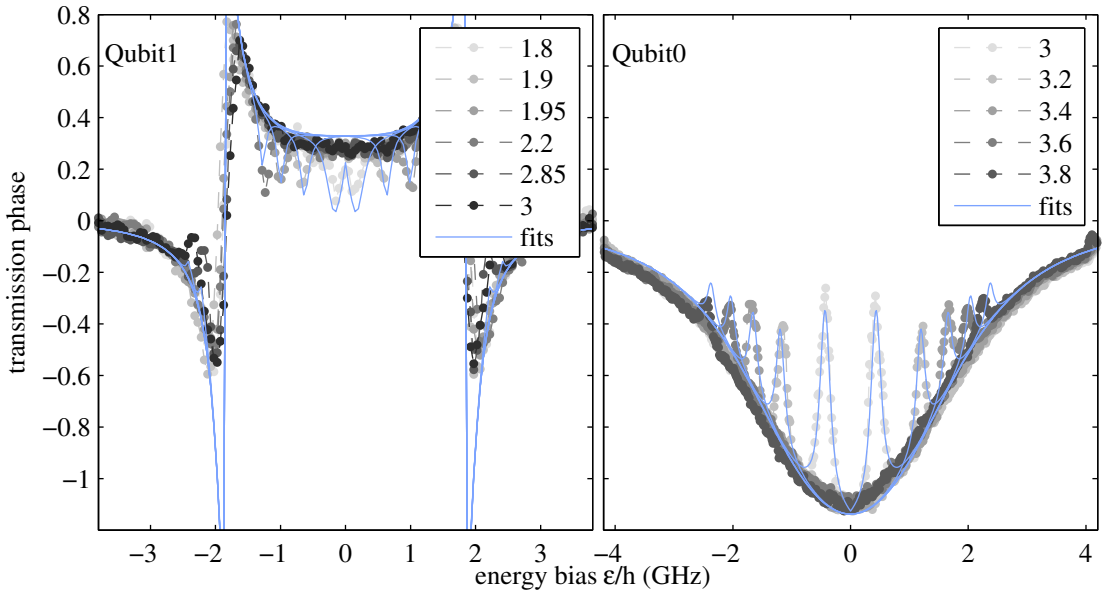

Figure 4-6: Horizontal cuts of Fig.4-5 for different driving frequencies. The phase response reveals the dispersive shift. Close to the resonance conditions where $\delta_{qd} \approx 0$ the dispersive shift is cancelled giving the spectroscopy lines in Fig.4-5. The blue lines are calculated by the frequency shift explained in (4.7) and with an expectation value of σ_z given by the first equation in (4.13). The corresponding relaxation rates are given in the main text.

There, the dispersive responses of qubit0 and qubit1 are shown as transmitted phase signals. Each of the traces is measured at different driving frequencies. The solid lines correspond to calculation results of the dispersive shift considering (4.7) and (4.13). In addition, it is necessary to add a bias dependence for the pure dephasing. For a good correspondence, a proportionality of the effective pure dephasing to the first derivative of the energy $\gamma_\varphi \propto \varepsilon/\omega_q$ is introduced (see 2.4). This requirement indicates flux noise as main source of decoherence [85].

Note, (4.7) is valid only away from the resonance point, that is $\delta_{qr} \gg g_\varepsilon$, which explains the discrepancy between measurement result and calculation where the phase changes its sign at the Qubit1 sample. Also, the dispersive shift without additional driving of the qubit gives the coupling constant g. Therefore, all of the parameters of the two qubits are reconstructed by measuring the two-tone spectroscopy.

In summary, all of them are listed in table 4.2. The reconstructed mutual inductance agrees well with the values found by numerical analysis of the geometry, compare to table 4.1. In

	Qubit1	Qubit0
gap frequency Δ/h (GHz)	1.79	2.97
persistent current I_p (nA)	180	160
coupling constant $g/2\pi$ (MHz)	3	4
mutual inductance M (pH)	0.8	1.2
relaxation rate $\Gamma_\mathrm{r}/2\pi$ (MHz)	0.75	0.75
pure dephasing $\gamma_\varphi/2\pi$ (MHz)	20	30

Table 4.2: List of qubit paramters for samples qubit1 and qubit0

addition, the driving amplitudes $\Omega_\mathrm{cl}/2\pi$ used for the measurements reconstruct to 4 MHz for Qubit1 and 3 MHz for Qubit0, respectively.

4.4 Transmission of the qubit-resonator system

The system parameters as found above suggest that the system is in an intermediate coupling regime. That means, the coupling constant is well above the resonator decay rate $g \gg \kappa$ but almost of the same order as the relaxation and decoherence rates of the qubit $g \approx \Gamma_\mathrm{r}, \Gamma_\varphi$. The latter is in contrast to the well analyzed strong coupling regime, where $g \gg \kappa, \Gamma$ [59, 60]. With the intermediate coupling the resonator still is a good detector for the qubit states; but on the other hand, when the states of the resonator are mixed with the qubit levels, the decoherence of the qubit will influence the resonator's linewidth. This impact is observable by measuring at the resonance point between the two. Because for Qubit0 the gap of the qubit is above the fundamental resonator mode, in the following the Qubit1 sample is considered.

In Fig. 4-7 (a) the measurement result of the resonator's transmission amplitude is plotted around its resonance frequency for different qubit energy bias values. The white, dashed vertical lines mark the resonance point where the detuning δ_qr vanishes. In addition, the solid white lines are the first two calculated eigenfrequencies of Hamiltonian (4.5) with neglected probing signal ($\Omega_\mathrm{p} = 0$) and diagonal coupling (see below). The latter is neglected because the diagonal coupling proportional to σ_z is small compared to the distance of the levels that it couples. Therefore, its influence to the level structure is negligible for small photon numbers. Then, the energy conserving qubit-resonator dynamic only involves a subspace of

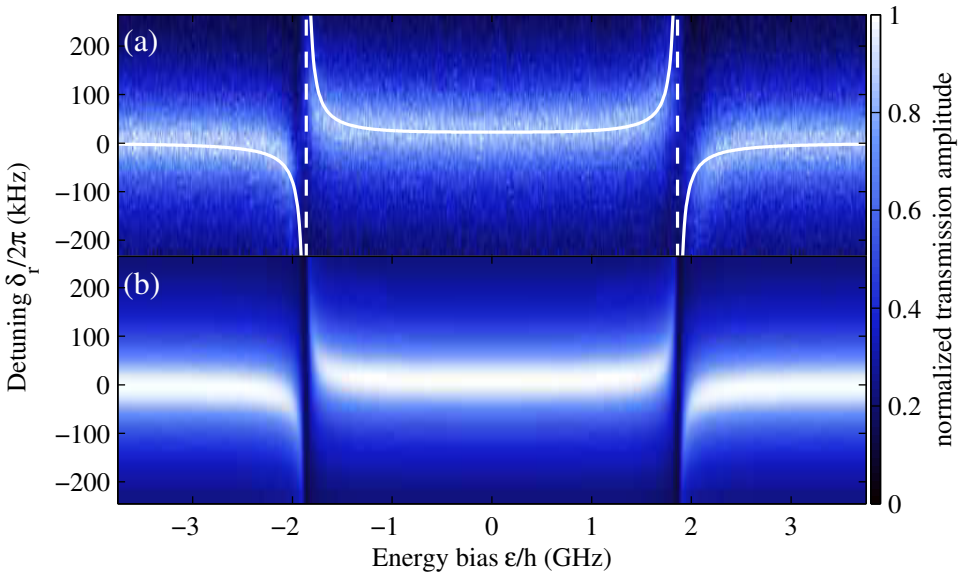

Figure 4-7: Transmission through the qubit-resonator system at different probing frequencies by sweeping the energy bias. (a) Experimental results. The picture is measured with low probing powers Ω_p, ensuring a mean photon number in the resonator less than one. Each vertical traces gives the Lorentzian line shape of the resonator. The solid white lines correspond to the first eigenfrequencies (4.14), while the dashed lines show the points of resonance between qubit and resonator. (b) Calculated transmission amplitude using (4.29)

levels $|g,N\rangle$ and $|e,N-1\rangle$. The eigenenergies of this subsystem can be presented as

$$\frac{E_{\pm,N}}{\hbar} = N\omega_0 + \frac{\delta_{qr}}{2} \pm \frac{1}{2}\sqrt{\delta_{qr}^2 + 4\left(\frac{g\Delta}{\hbar\omega_q}\right)^2 N}. \tag{4.14}$$

These energy levels are often called dressed qubit states. They give a ladder of stairs, where the levels on one step - the two levels for plus and minus in the above equation - have a constant total amount of excitations N. We can identify the square root in the above equation as generalized Rabi frequency, which involves both, the detuning between resonator and qubit as well as the excitation dependent splitting

$$\Omega_R = \sqrt{\delta_{qr}^2 + \left(\frac{2g\Delta}{\hbar\omega_q}\sqrt{N}\right)^2}. \tag{4.15}$$

The term in the brackets proportional[4] to $\sqrt{N}$ is again the on-resonance Rabi frequency. For the measurement in Fig. 4-7 (a) the resonance frequency follows the lines for a total excitation $N = 1$. Therefore, when applying a signal at an energy bias close to the resonance

[4]This proportionality means that the splitting is proportional to the signal amplitude in the resonator.

the dressed states get probed, which explains the measured frequency shift. A quantitative analysis of Fig. 4-7 (a) can again be carried out by solving the stationary Master equation. When restricting to a sub-space involving only the zero and one photon cavity states as well as the qubit states, already 16 equations for the time dependence of the density matrix elements need to be solved. Thus, it is worthwhile to rewrite the Master equation to the expectation values of the corresponding operators. In general, the time dependency of the expectation value of an operator A in a system with Hamiltonian H and dissipative Lindblad term L is

$$\begin{aligned}\frac{\mathrm{d}\langle A\rangle}{\mathrm{d}t} &= \frac{\mathrm{d}}{\mathrm{d}t}Tr\left(A\rho\right) = Tr\left(A\frac{\partial\rho}{\partial t}\right)\\ &= Tr\left(-A\frac{\mathrm{i}}{\hbar}\left[H,\rho\right]+A\hat{L}(\rho)\right)\\ &= -\frac{\mathrm{i}}{\hbar}Tr\left(AH\rho - A\rho H\right)+Tr\left(A\hat{L}(\rho)\right)\\ &= -\frac{\mathrm{i}}{\hbar}\langle[A,H]\rangle+Tr\left(A\hat{L}(\rho)\right).\end{aligned} \tag{4.16}$$

For the last line the invariance of the trace under cyclic permutations is used. To describe the experimental data of Fig. 4-7 the Hamiltonian of the system in RWA (4.6) and the Lindblad terms for the resonator (2.63) and qubit (2.25) need to be considered. Then the so called Maxwell-Bloch-equations [108, 109] for the expectation values of the operators a, σ_z, σ_-, and $N = a^\dagger a$ are found[5]

$$\frac{\mathrm{d}\langle a\rangle}{\mathrm{d}t} = -\mathrm{i}\delta_{\mathrm{rp}}\langle a\rangle - \mathrm{i}g_\Delta\langle\sigma_-\rangle - \mathrm{i}\Omega_{\mathrm{p}} - \frac{\kappa}{2}\langle a\rangle \tag{4.17}$$

$$\frac{\mathrm{d}\langle\sigma_-\rangle}{\mathrm{d}t} = -\mathrm{i}\delta_{\mathrm{qp}}\langle\sigma_-\rangle + \mathrm{i}g_\Delta\langle a\sigma_z\rangle - \Gamma_\varphi\langle\sigma_-\rangle \tag{4.18}$$

$$\frac{\mathrm{d}\langle\sigma_z\rangle}{\mathrm{d}t} = -2\mathrm{i}g_\Delta\left(\langle a\sigma_+\rangle - \langle a^\dagger\sigma_-\rangle\right) - \Gamma_{\mathrm{r}}\left(\langle\sigma_z\rangle + 1\right) \tag{4.19}$$

$$\frac{\mathrm{d}\langle a^\dagger a\rangle}{\mathrm{d}t} = -\mathrm{i}g_\Delta\left(\langle a^\dagger\sigma_-\rangle - \langle a\sigma_+\rangle\right) - \mathrm{i}\Omega_{\mathrm{p}}\left(\langle a^\dagger\rangle - \langle a\rangle\right) - \kappa\langle a^\dagger a\rangle \tag{4.20}$$

$$\begin{aligned}\frac{\mathrm{d}\langle a\sigma_z\rangle}{\mathrm{d}t} &= -\mathrm{i}\delta_{\mathrm{rp}}\langle a\sigma_z\rangle - \mathrm{i}g_\Delta\left(2\langle aa\sigma_+\rangle - \langle\sigma_-\rangle - 2\langle a^\dagger a\sigma_-\rangle\right) - \mathrm{i}\Omega_{\mathrm{p}}\langle\sigma_z\rangle\\ &\quad - \frac{\kappa}{2}\langle a\sigma_z\rangle - \Gamma_{\mathrm{r}}\left(\langle a\sigma_z\rangle + \langle a\rangle\right).\end{aligned} \tag{4.21}$$

Here, again cyclic permutations of the operators under the trace as well as commutation relations like $\left[a,a^\dagger a\right] = a$ are used. Only the first four of infinite coupled equations are

[5] Compared to the Bloch equations (4.12), here the expectation values of the field and correlations to the two-level system are included.

shown above. Higher order correlations between the operators enter when trying to describe the full dynamics. They can be avoided by certain assumptions as shown below.

At first, the properties of the bare resonator may be obtained, when the coupling between qubit and resonator is neglected. Than from the steady state solution[6] of (4.18), (4.17), and (4.20) follows $\langle\sigma_-\rangle = 0$,

$$\langle a\rangle_0 = -\frac{2\Omega_\mathrm{p}}{2\delta_\mathrm{rp} - \mathrm{i}\kappa}, \tag{4.22}$$

and the mean photon number in the resonator

$$\langle n\rangle_0 = -\frac{\Omega_\mathrm{p}}{\kappa} 2\mathrm{Im}\left(\langle a\rangle_0\right) = \frac{4\Omega_\mathrm{p}^2}{4\delta_\mathrm{rp}^2 + \kappa^2}. \tag{4.23}$$

A generalization of the above equations allows relating the driving or probing amplitudes at any harmonic with the corresponding mean number of photons. In resonance $\delta_\mathrm{rp} = 0$, it is given by the simple relation of probing (or driving) amplitude and loss from the cavity $\langle n\rangle = 4\Omega_\mathrm{p}^2/\kappa^2$. This relation can be interpreted as the power exciting the cavity divided by the loss from it [60]. Nevertheless, it is important to note that the effective driving or probing not only depends on the input voltage but also on the coupling capacitance.(see (2.66)).

When the systems are coupled and in the case of weak probing amplitudes Ω_p, the correlations containing three operators can be neglected in (4.21). This assumption is valid if the mean photon number $\langle a^\dagger a\rangle$ is small and corresponds in the language of density matrix elements to a restriction to the lowest energy states, when the resonator is populated mostly in the ground state $\langle 0|\rho|0\rangle \gg \langle N|\rho|N\rangle$ for all $N > 0$. Then the steady state expressions of (4.17), (4.18), and (4.21) can be used to find an expression for the expectation value of the field operator

$$\langle a\rangle = \frac{-\Omega_\mathrm{p}}{\widetilde{\delta}_\mathrm{rp}\widetilde{\delta}_\mathrm{qp} - g_\Delta^2}\left(\widetilde{\delta}_\mathrm{qp} - \frac{\mathrm{i}g_\Delta^2\left[\langle\sigma_z\rangle + 1\right]}{\mathrm{i}\widetilde{\delta}_\mathrm{rp} + \Gamma_\mathrm{r}}\right). \tag{4.24}$$

Here, the redefined detunings include the decoherence rates $\widetilde{\delta}_\mathrm{rp} = \delta_\mathrm{rp} - \mathrm{i}\kappa/2$ and $\widetilde{\delta}_\mathrm{qp} = \delta_\mathrm{qp} - \mathrm{i}\Gamma_\varphi$. The above equation can be rearranged as

$$\langle a\rangle = \frac{-\Omega_\mathrm{p}}{\widetilde{\delta}_\mathrm{rp} + \frac{g_\Delta^2}{\widetilde{\delta}_\mathrm{qp}} S_q}, \tag{4.25}$$

[6] That means zero left hand sides.

where

$$S_q = \frac{\widetilde{\delta}_{\mathrm{qp}}\left(\mathrm{i}\widetilde{\delta}_{\mathrm{rp}}\langle\sigma_z\rangle - \Gamma_{\mathrm{r}}\right)}{\widetilde{\delta}_{\mathrm{qp}}\left(\mathrm{i}\widetilde{\delta}_{\mathrm{r}} + \Gamma_{\mathrm{r}}\right) - \mathrm{i}g_\Delta^2\left[1 + \langle\sigma_z\rangle\right]} \tag{4.26}$$

depends on the population of the qubit $\langle\sigma_z\rangle$. Again, if the probing power is weak $\langle\sigma_z\rangle$ will be changed only slightly. Indeed, it only acquires changes of the second order in the probing amplitude $\sigma_z \approx \langle\sigma_z\rangle_0 + O(\Omega_p^2)$. Here, $\langle\sigma_z\rangle_0 = -1$ is the population of the undisturbed qubit, that can be recovered from the steady state solution of (4.19), when the coupling between resonator and qubit is neglected $g = 0$. Therefore, in the first order of the probing amplitude (4.26) yields $S = -1$.

Interestingly, similar results can be found for high probing amplitudes, when assuming the expectation values of products of qubit and resonator operators to factorize $\langle a\sigma_z\rangle = \langle a\rangle\langle\sigma_z\rangle$. Then, the stationary solution of (4.17) to (4.19) can be found. With excluding σ_- the remaining equations read

$$\langle a\rangle = \frac{-\Omega_{\mathrm{p}}}{\widetilde{\delta}_{\mathrm{rp}} + \frac{g_\Delta^2}{\widetilde{\delta}_{\mathrm{qp}}}\langle\sigma_z\rangle}, \tag{4.27}$$

$$\langle\sigma_z\rangle = -\frac{\Gamma_{\mathrm{r}}}{\frac{4g_\Delta^2}{\Gamma'_\varphi}\langle a\rangle\langle a^\dagger\rangle + \Gamma_{\mathrm{r}}}. \tag{4.28}$$

Here, Γ'_φ is defined in the same way as in 4.3.
The second of the above equations coincides with the result for the population of a driven qubit (4.13), when the driving amplitude Ω'_{cl} is replaced with $2g_\Delta\sqrt{\langle a\rangle\langle a^\dagger\rangle}$. Although, the limit of small probing amplitudes is beyond the semi-classical approach, if the field expectation value is assumed small the qubit will stay in the ground state and the approximation $\langle\sigma_z\rangle = -1$ can be found. Note that by driving the maximum achievable value for this expectation value is zero.

From the first equation (4.27) together with (2.70) the transmission of the qubit resonator system follows as

$$t_{\mathrm{r}} = \frac{\mathrm{i}}{2}\frac{\kappa}{\widetilde{\delta}_{\mathrm{rp}} + \frac{g_\Delta^2}{\widetilde{\delta}_{\mathrm{qp}}}\langle\sigma_z\rangle}. \tag{4.29}$$

Interestingly, the denominator can be interpreted as the total detuning of the probing signal from the effective resonator frequency. Its first term gives the probe-resonator detuning

added to the photon decay rate of the cavity ($\kappa/2$), while, in comparison to (4.7), the second term is a generalized dispersive shift, that includes the decoherence of the qubit. If the coupling between qubit and resonator vanishes, the Lorentzian shaped transmission amplitude of the resonator is recovered. That can be validated by taking the absolute value of (4.29) and comparing it to the normalized classical result (A.11). The same also applies for a large detuning between qubit and probing signal.

Finally, the equation for the transmission can be used to explain the experimental data. As seen in Fig. 4-7 the correspondence between the experimental (a) and the theoretical (b) plot is good. This agreement justifies the assumptions above of factorization of the expectation values and the small probing power keeping the qubit in the ground state. In addition, with the theory in hand, the influence of the relation of the coupling constant to the decoherence rate can be analyzed in the resonance point where $\omega_q = \omega_0$.

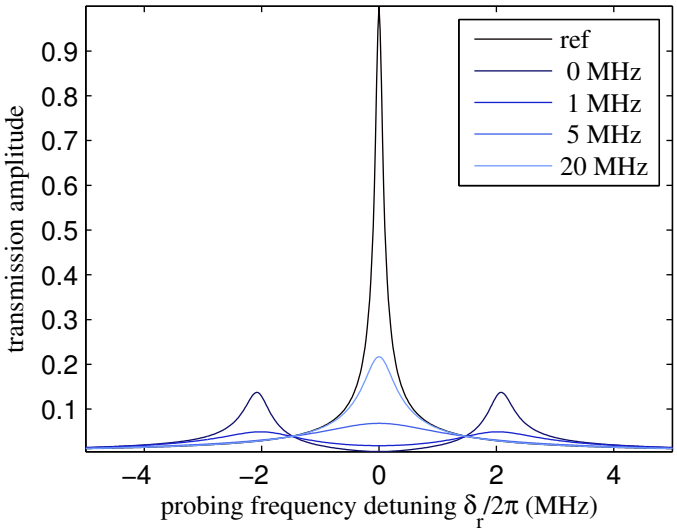

Figure 4-8: Calculated transmission amplitude using (4.29) at resonance $\omega_q = \omega_0$ for different probing frequencies. The different curves are calculated using the parameters of qubit1 except the pure dephasing rate γ_φ which is increased according to the legend. The reference curve displays the undisturbed resonator transmission $g = 0$. When the total decoherence rate is smaller than the coupling, two peaks are visible.

As seen in Fig. 4-8, in resonance two peaks are visible for small decoherence rates. For the experimental observation of these so called vacuum Rabi split peaks a coupling constant above the decoherence rate of the qubit (and of the cavity) is necessary. With increasing decoherence the Rabi peaks vanish and a single Lorentzain peak with reduced quality appears

at the undisturbed resonator frequency. Although the dispersive shift of the resonator frequency gives a clear indication of the avoided crossing between resonator and qubit energy levels, a high decoherence of the qubit destroys the coherent coupling of the dressed states in this intermediate coupling regime. Another insight arises if the decoherence is interpreted as the width of the energy levels. In that view, a separation of the energy levels is only possible if their distance, given by the coupling constant g_Δ, is larger than the width.

5 Dressed qubit-resonator system and lasing

In extension to the already discussed experiments, in this chapter two signals are applied to the qubit-resonator system. Again close to the fundamental mode frequency a small probing signal is applied and its transmission is recorded. In addition, a second strong driving signal is used at a harmonic frequency of the resonator. As discussed further it will have an effect on both, the level structure and the dissipative rates of the combined qubit-resonator system.

5.1 Strong AC-Zeeman shift and three-tone spectroscopy

As a first step, the level structure of the qubit coupled to a strong field in the third harmonic should be analyzed. Therefore, the probing signal and the fundamental mode are neglected. Then the dynamic between the harmonic and the qubit is described by a Hamiltonian of the form (4.5). Note, although in the experiment the third harmonic is used, the theory applies to a strong driving at any harmonic that couples to the qubit. Thus, below a_h and $a_\mathrm{h}^\dagger$ are used for the annihilation and creation operators of the driven resonator harmonic. In the same way as in 4.2, when the detuning between the harmonic frequency ω_h and the qubit $\delta_\mathrm{qh} = \omega_\mathrm{q} - \omega_\mathrm{h}$ is large , the Hamiltonian can be transformed into the same form as (4.7).

The discussion in 4.2 concentrated on the qubit's influence on the resonator frequency. To estimate the influence of the resonator mode on the qubit one can present it for the harmonic as

$$H_\mathrm{h,q} \approx \hbar\omega_\mathrm{h} a_\mathrm{h}^\dagger a_\mathrm{h} + \frac{\hbar}{2}\left(\frac{\omega_\mathrm{q}}{2} + \frac{g_\mathrm{h,\Delta}^2}{\delta_\mathrm{qh}}\left[\frac{1}{2} + a_\mathrm{h}^\dagger a_\mathrm{h}\right]\right)\sigma_z. \tag{5.1}$$

The term in the brackets can be interpreted as an effective qubit level splitting valid away

from the resonance. The term dependent on the mean photon number $N = \langle a_h^\dagger a_h \rangle$ is called the AC Zeeman shift[1]. Since high photon numbers can be achieved in the cavity, the splitting between the qubit states may be strongly changed compared to the undisturbed qubit. Furthermore, the direction of the shift of the levels depends on the sign of the detuning. In that way it should be possible to reduce the minimal qubit level splitting below the gap frequency.

An experimental test of this prediction is carried out on qubit0 sample. To prove the assumption above, a small probing signal is again applied at the resonator's fundamental mode. Then its dispersive shift is recorded for different energy bias and applied driving powers in the third harmonic. The results are shown in Fig. 5-1.

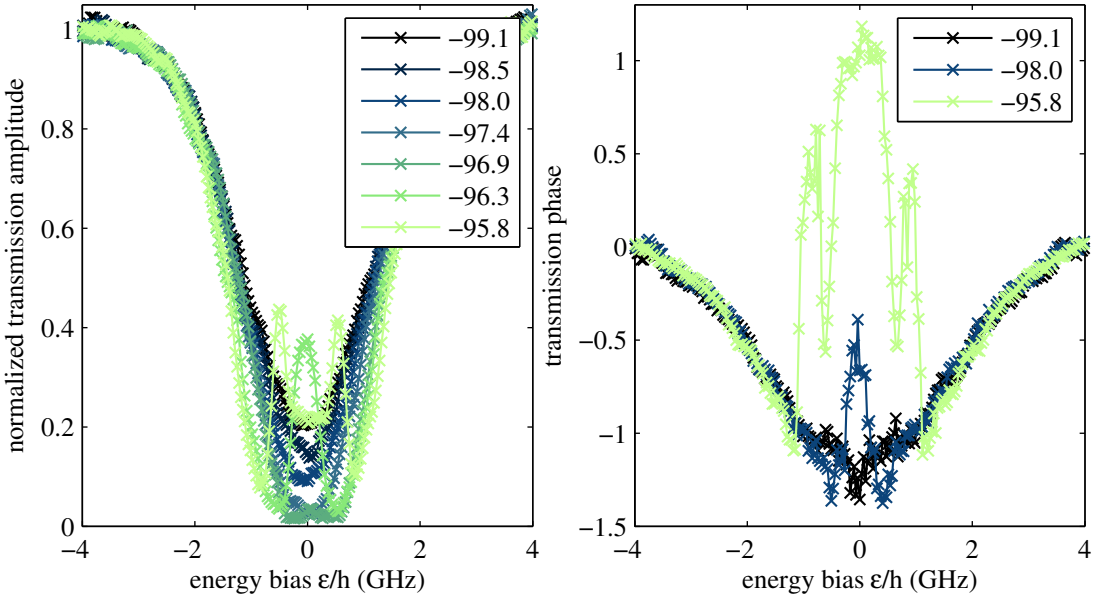

Figure 5-1: Amplitude (left) and phase (right) of the transmitted probing signal by sweeping the energy bias for different driving powers. As visible from the plots, the qubit dip is first increased with the driving. From a certain power two dips appear, and by a further increase they show phase jumps that indicate avoided level crossings between the effective qubit and fundamental mode levels.

Indeed, when the driving power is increased the qubit dip is increased and eventually splits into two, showing characteristic phase jumps. Both indicate that the effective qubit splitting is decreased. That is due to the increase of the dispersive shift of the fundamental mode because the detuning between qubit and probed resonator is decreased (compare discussion of the dispersive shift in 4.2). When the effective minimal splitting of the qubit becomes

[1]The same shift is observable for charge qubits by MW-driving, but since the coupling there is mediated by the electric field in this case it would be named AC-Stark shift.

smaller than the one of the resonator an avoided level crossing produces two symmetric phase jumps. In that sense, the phase response is changed from the one of qubit0 to the one of qubit1.

As discussed in 4.3, with a spectroscopy the qubit level splitting can be directly determined. For investigation of the Zeeman-shifted qubit levels, three signals have to be applied to the resonator. The first strong driving signal is applied at the third harmonic, introducing the change in the qubit spectrum. This spectrum is then probed by a second strong driving signal with changeable frequency, so that the dispersive shift of the fundamental mode will be canceled if the frequencies match. Finally, the total dispersive shift of the fundamental mode is recorded by measuring the transmission of a weak probe signal at its frequency. In that way the measurement data in Fig 5-2 is recorded.

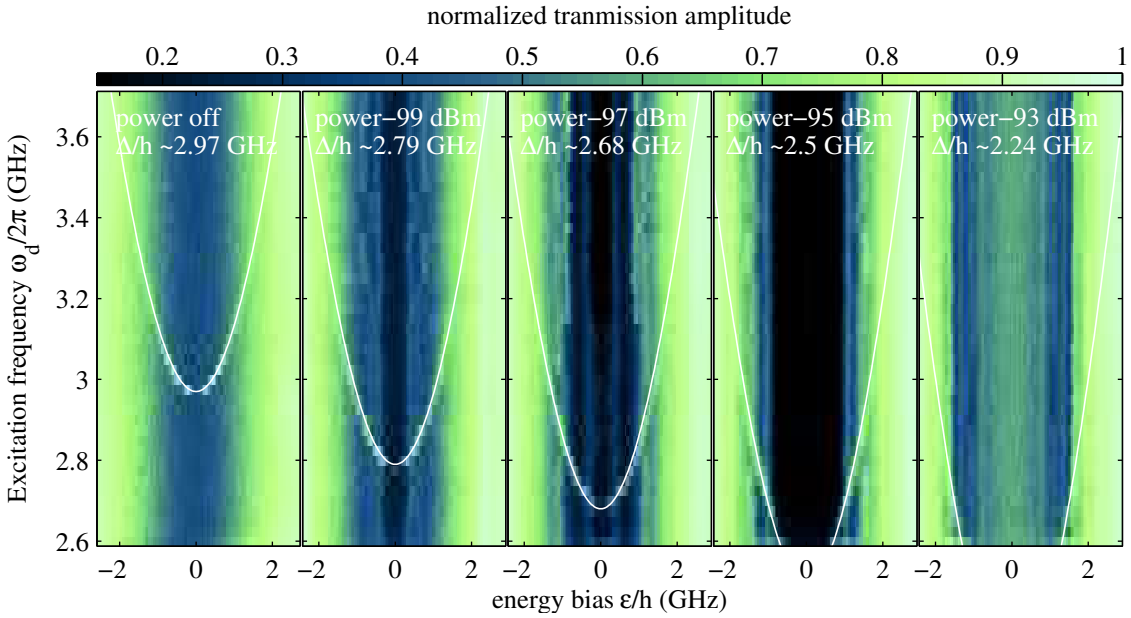

Figure 5-2: Spectroscopy in the transmission amplitude measured for the AC-Zeeman-shifted qubit levels for different driving powers. The spectra are measured in the same way as in 4.3. The picture on the left shows a reference plot without driving in the third harmonic. Then from left to right the driving power in the third harmonic is increased in two dBm steps. This results in a reduction of the qubit gap even below the fundamental mode frequency. The power values are given for the input of the sample.

In the analyzed driving power range the effective level splitting follows almost perfectly to the prediction by the dispersive shift. In the experiment it is possible to reduce the gap frequency Δ from about 3 GHz below the fundamental mode at about 2.5 GHz. As seen

before, the driving will also influence the population of the qubit states (compare (4.13)). Still, the visibility of the spectroscopic line indicates that the expectation value σ_z of the qubit is not yet saturated in the analyzed bias range. In other words, the population difference between ground and excited level remains, allowing a bias dependent dispersive shift for the detection of the qubit's spectrum.

An interesting question is how far the minimal qubit frequency can be shifted. One can even imagine putting the higher energetic level below the ground states position. For an experimental test the transmission amplitude and phase of the probe signal is plotted versus qubit bias and driving amplitude in Fig. 5-3.

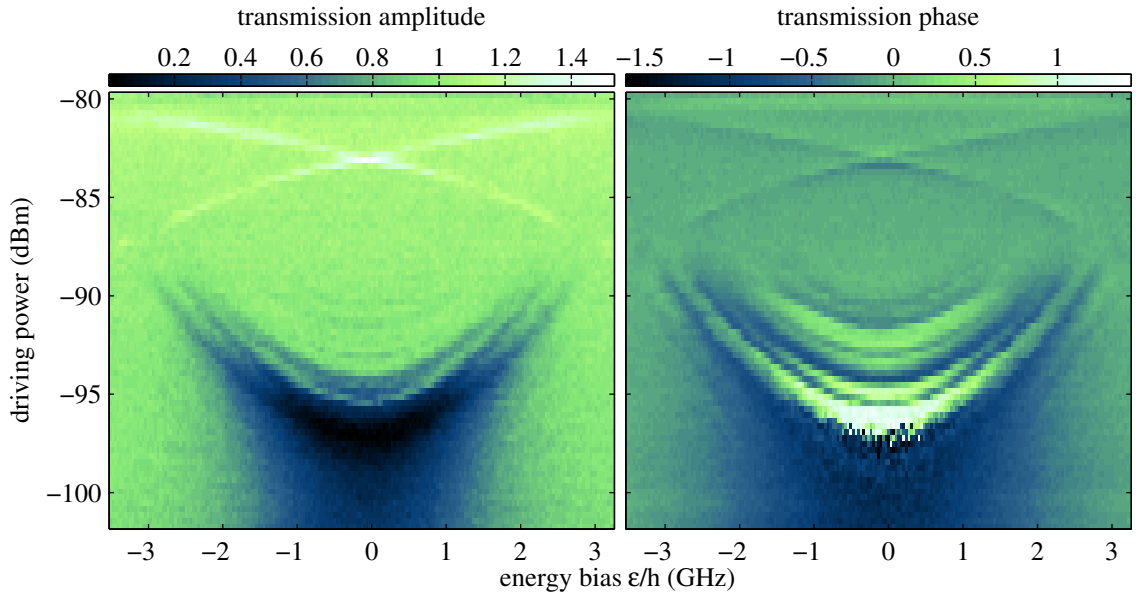

Figure 5-3: Transmission amplitude (left) and phase (right) measured at the fundamental mode in dependence of the qubit energy bias and the driving power at the third harmonic frequency. For the latter the values at the input of the sample are given.

For low power the dispersive qubit shift of the resonator produces a single dip around the degeneracy point. With increasing power the dip becomes larger, since the detuning between qubit and fundamental mode is reduced. When the gap of the qubit becomes smaller than the fundamental mode frequency the dip is split into two. These correspond to the resonant interaction regions. These move for further increased power to higher bias values. After a region where the transmission amplitude is constant, for very strong driving again lines appear. Surprisingly, they show transmission amplitudes bigger than one. This amplification process has to be connected to the σ_x coupling term in (4.4), since the diagonal coupling

vanishes. Also it indicates an effective shift of the minimal qubit splitting to negative values. In this inversed qubit a relaxation ends in the upper state and by the interaction with the resonator energy may be added to the transmitted signal.

5.2 The dressed qubit

In the chapter above the discussion is restricted to the dispersive regime, where a description of the measured effects is rather simple. When considering the qubit spectrum close to the resonance point between qubit and third harmonic mode, it is worthwhile to transform the Hamiltonian of the third harmonic coupled to the qubit

$$H_{\mathrm{h,q}} = \hbar\omega_{\mathrm{h}}\left[a_{\mathrm{h}}^{\dagger}a_{\mathrm{h}} + \frac{1}{2}\right] + \frac{\hbar\omega_{\mathrm{q}}}{2}\sigma_z + g_{\mathrm{h}}\left(\frac{\Delta}{\omega_{\mathrm{q}}}\sigma_x + \frac{\varepsilon}{\omega_{\mathrm{q}}}\sigma_z\right)\left[a_{\mathrm{h}}^{\dagger} + a_{\mathrm{h}}\right] \tag{5.2}$$

to the dressed-state basis. This transformation is done by introducing the basis vectors [110, 111] similar as for the qubit energy eigenstates (2.15)

$$\begin{aligned} |1N\rangle &= \cos\theta|eN-1\rangle + \sin\theta|gN\rangle \\ |2N\rangle &= \sin\theta|eN-1\rangle - \cos\theta|gN\rangle. \end{aligned} \tag{5.3}$$

Here, $|gN\rangle$ and $|eN\rangle$ are the basis vectors for the state with N photons in the harmonic and the qubit in the ground or excited state, respectively. The numbers 1 and 2 denote the higher and lower energetic level, respectively. The mixing angle $\tan 2\theta = \Omega_{\mathrm{R0}}/\delta_{\mathrm{qh}}$ depends on the detuning between harmonic and qubit frequency δ_{qh} and the resonance splitting $\hbar\Omega_{\mathrm{R0}}$. The latter is given by the on-resonance Rabi frequency, which is proportional to the amplitude in the cavity[2]

$$\Omega_{\mathrm{R0}} = 2\frac{g_{\mathrm{h}}\Delta}{\hbar\omega_{\mathrm{q}}}\sqrt{N}. \tag{5.4}$$

The definition of θ leads to the following expressions[3]

$$\sin 2\theta = \frac{\Omega_{\mathrm{R0}}}{\Omega_{\mathrm{R}}},\ \cos 2\theta \ = \frac{\delta_{\mathrm{qh}}}{\Omega_{\mathrm{R}}},\ \sin\theta = \frac{1}{\sqrt{2}}\sqrt{1-\frac{\delta_{\mathrm{qh}}}{\Omega_{\mathrm{R}}}},\ \cos\theta \ = \frac{1}{\sqrt{2}}\sqrt{1+\frac{\delta_{\mathrm{qh}}}{\Omega_{\mathrm{R}}}} \tag{5.5}$$

[2]Note, the amplitude is given by the expectation value of the annihilation operator a_{h} and, therefore, the square root of N.

[3]Note, the Rabi frequency Ω_{R} is defined as in (4.15) for the harmonic values g_{h}, δ_{qh}, and the photon number in the harmonic N.

With the definition above the dressed states 1 and 2 have the same total number of excitation N. It also ensures the normalization and orthogonality of the basis vectors. Neglecting the diagonal coupling term, proportional to σ_z, and the non-resonant terms ($a_\mathrm{h}\sigma_-$ and $a_\mathrm{h}\dagger\,\sigma_+$), the Hamiltonian in the dressed basis reads [112]

$$H_\mathrm{R} = \hbar\omega_\mathrm{h}\hat{n} + \hbar\frac{\hat{\Omega}_\mathrm{R}}{2}, \tag{5.6}$$

where the excitation number operator $\hat{n} = \sum_N N\left(|1N\rangle\langle 1N| + |2N\rangle\langle 2N|\right)$ replaces the number operator $a_\mathrm{h}^\dagger a_\mathrm{h}$ and the Rabi operator $\hat{\Omega}_\mathrm{R} = \sum_N \Omega_\mathrm{R}(N)\left(|1N\rangle\langle 1N| - |2N\rangle|2N\rangle\right)$ gives the splitting of the states on one step of the dressed ladder. The Hamiltonian (5.6) is of diagonal form in the dressed-state basis. The generalized Rabi frequency is defined as in (4.15)

$$\Omega_R(N) = \sqrt{\delta_\mathrm{qh}^2 + \Omega_\mathrm{R0}^2}. \tag{5.7}$$

The formation of the dressed levels is sketched for two different photon numbers and for the parameters of Qubit0 sample in Fig. 5-4.

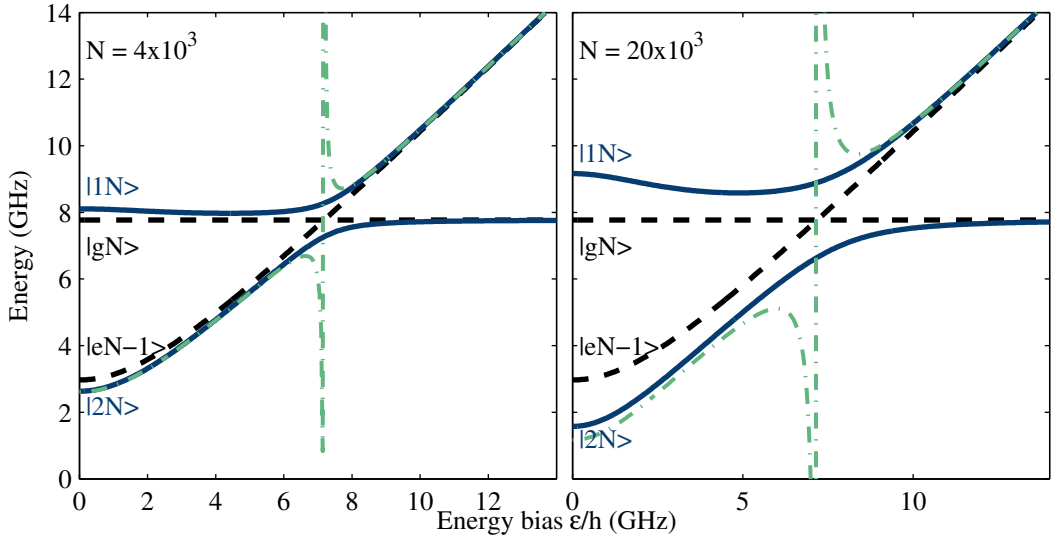

Figure 5-4: Step of the dressed ladder at photon numbers of 4×10^3 and 20×10^3 in the third harmonic for the parameters of Qubit0 sample. The black dashed lines show the original qubit-resonator states, while the blue solid lines are the dressed states. The dash-dotted green curve demonstrates the dispersive shift of the qubit level splitting by (5.1). The degeneracy of the states $|gN\rangle$ and $|eN-1\rangle$ is lifted due to the coupling term $a_\mathrm{h}\sigma_+ + a_\mathrm{h}^\dagger\sigma_-$ in Hamiltonian (5.2). Away from the resonance the calculated dispersive shift corresponds well to the dressed states as long as $g_{\mathrm{h},\Delta}\sqrt{N}$ is small compared to the eigenenergies.

When assuming the third harmonic to be driven with a high amplitude signal, a coherent state is created in the resonator. Then the mean number of photons $\langle N \rangle$ is large and the generalized Rabi frequency can be set to the constant value $\Omega_{\mathrm{R}}(\langle N \rangle)$. After tracing out the photon degree of freedom and neglecting the constant energy from the first term in (5.7), the Hamiltonian of an effective two-level system is found

$$\tilde{H}_{\mathrm{R}} = \hbar \frac{\Omega_{\mathrm{R}}}{2} \sigma_z. \tag{5.8}$$

This procedure is summarized in Fig. 5-5

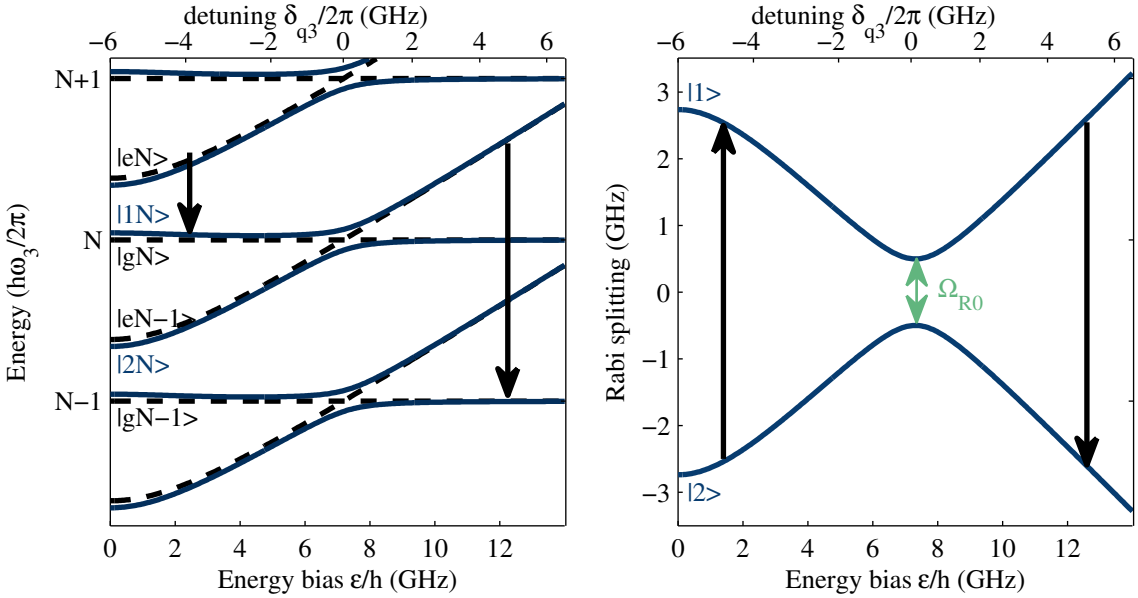

Figure 5-5: Formation of the dressed states effective two-level system. The dressed ladder is shown around the mean photon number N (left). The relaxation of the qubit is indicated by the black arrows. It shifts the population from an excited to a ground state qubit without changing the photon number N. Therefore, the population is concentrated for the uncoupled system in the horizontal levels. When coupled, the population depends on the weight of the ground state in a dressed level. After tracing out the driving photon degree of freedom an effective two-level system (right) is recovered. Its splitting is given by the generalized Rabi frequency (5.7). Depending on the sign of the detuning $\delta_{q\mathrm{h}}$, the qubit's relaxation can lead to relaxation or excitation. Close to the resonance, where $\delta_{q\mathrm{h}} \approx 0$, an almost equal population is predicted by (4.13).

According to (4.13) or (4.28) for strong driving signals the population of the driven level may be changed. Especially in resonance, an almost equal population is expected for the qubit and, therewith, also for the traced dressed levels. Another interpretation can be given

by looking at the creation of the dressed states, as they are formed by a superposition of the ground and the excited state of the qubit. Depending on the weight of the ground state in each of the dressed levels an higher or lower population may be expected. In that sense, it is necessary to transform the incoherent dynamics, in other words the dissipative Lindblad terms, into the dressed-state basis. The terms which remain under a RWA in frames rotating around the σ_z-axis are (see Appendix C.3 for a detailed calculation)

$$\begin{aligned}\hat{L}_{11} &= -\frac{\Gamma_\mathrm{r}}{2}\frac{\delta_\mathrm{qh}}{\Omega_\mathrm{R}}\left(\rho_{11}+\rho_{22}\right)+\left[\frac{\Gamma_\mathrm{r}}{2}\frac{\delta_\mathrm{qh}^2}{\Omega_\mathrm{R}^2}-\frac{\Gamma_\varphi}{2}\frac{\Omega_\mathrm{R0}^2}{\Omega_\mathrm{R}^2}\right]\left(\rho_{11}-\rho_{22}\right),\\ \hat{L}_{22} &= -\hat{L}_{11},\end{aligned} \tag{5.9}$$

$$\begin{aligned}\hat{L}_{12} &= \left[-\Gamma_\varphi+\frac{\Omega_\mathrm{R0}^2}{2\Omega_\mathrm{R}^2}\left(\Gamma_\varphi-\Gamma_\mathrm{r}\right)\right]\rho_{12}, \text{and}\\ \hat{L}_{21} &= \left[-\Gamma_\varphi+\frac{\Omega_\mathrm{R0}^2}{2\Omega_\mathrm{R}^2}\left(\Gamma_\varphi-\Gamma_\mathrm{r}\right)\right]\rho_{21}.\end{aligned} \tag{5.10}$$

Here, $\hat{L}_{ij}=\sum_N\langle iN|\hat{L}|jN\rangle$ and $\rho_{ij}=\sum_N\langle iN|\rho|jN\rangle$ are reduced elements of the Linblad and density operator, respectively. As seen from the first of the equations above, depending on the sign of the detuning δ_qh, either relaxation or excitation is dominant at the effective dressed two level system. For large detuning $\left|\delta_\mathrm{qh}\right|\approx\Omega_\mathrm{R}$, pure excitation with the qubit relaxation rate Γ_r is found for negative detuning. Within the same limit, (5.10) demonstrates a similar decoherence of the dressed levels compared to the one of the qubit.

On the other hand, close to the resonance where $\Omega_\mathrm{R}\approx\Omega_\mathrm{R0}$, (5.9) is dominated by the term proportional to the decoherence rate Γ_φ. Since it is multiplied to the population difference between higher and lower level, the decoherence rate of the qubit yields a fast equalization of the state's population. Interestingly, (5.10) suggests that the decoherence of the dressed levels may be reduced to almost half, if the qubit relaxation is small. The effective rates defined in (5.9) and (5.10) reflect the change of the matrix elements. Nevertheless, as calculated in C.3 one can define relaxation, excitation, and pure dephasing of the dressed qubit as defined by (C.53) by the rates

$$\begin{aligned}\Gamma_\mathrm{r}^{(\mathrm{dr})} &= \frac{\Gamma_\mathrm{r}}{2}\left(1+\frac{\delta_\mathrm{qh}}{\Omega_\mathrm{R}}\right)+\left(\Gamma_\varphi-\Gamma_\mathrm{r}\right)\frac{\Omega_\mathrm{R0}^2}{2\Omega_\mathrm{R}^2},\\ \Gamma_\mathrm{e}^{(\mathrm{dr})} &= \frac{\Gamma_\mathrm{r}}{2}\left(1-\frac{\delta_\mathrm{qh}}{\Omega_R}\right)+\left(\Gamma_\varphi-\Gamma_\mathrm{r}\right)\frac{\Omega_\mathrm{R0}^2}{2\Omega_\mathrm{R}^2}, \text{and}\\ \gamma_\varphi^{(\mathrm{dr})} &= \Gamma_\varphi-\frac{\Gamma_\mathrm{r}}{2}-\left(\Gamma_\varphi-\Gamma_\mathrm{r}\right)\frac{\Omega_\mathrm{R0}^2}{\Omega_\mathrm{R}^2}.\end{aligned} \tag{5.11}$$

In summary, an effective two-level system can be created by driving the qubit strongly in one of the harmonics of the resonator. Its splitting can be tuned by both, the detuning of the driving signal to the qubit and the driving amplitude. Also the population of the levels is dependent on the detuning and a level inversion can be achieved. Since the coupling constant can be reasonable large for superconducting qubits and the photon number in the harmonic can achieve high values, a splitting of the order of the resonator's fundamental mode may be achieved. Still, it should be cleared, whether a coupling constant is found between the both. Note that the dipole moment in quantum optics does not allow these transitions.

5.3 Coupling between the dressed qubit and the resonator

The question raised above, whether the fundamental mode of the resonator couples to the Rabi-split states, may be answered by transforming the total systems Hamiltonian into the dressed-state basis. In the eigenbasis of the qubit it takes the form

$$H_\mathrm{t} = H_\mathrm{h,q} + \hbar\omega_0 a^\dagger a + g\left[\frac{\Delta}{\omega_\mathrm{q}}\sigma_x + \frac{\varepsilon}{\omega_\mathrm{q}}\sigma_z\right]\left[a + a^\dagger\right] + \hbar\Omega_\mathrm{p}\left[a\mathrm{e}^{\mathrm{i}\omega_\mathrm{p}t} + a^\dagger\mathrm{e}^{-\mathrm{i}\omega_\mathrm{p}t}\right] \tag{5.12}$$

Here, $H_\mathrm{h,q}$ is given by (5.2) and includes the harmonic of the resonator, the qubit, and the coupling between both. In addition, the fundamental mode is considered to be coupled to the qubit and probed by a small amplitude signal with frequency ω_p and amplitude Ω_p. As described before, the first term can be transformed to the effective two-level-system Hamiltonian (5.8). The pure fundamental mode terms will also not be effected by the transformation to the dressed states. Therefore, the two coupling terms proportional to σ_x and σ_z need to be considered. As demonstrated in Appendix C.3, only the σ_z term gives transitions between the Rabi-split states of one manifold, keeping the total excitation number N constant. Close to the resonance between the Rabi levels and the fundamental mode $\Omega_\mathrm{R} \approx \omega_0$ the non-resonant terms given by σ_x can be neglected and the Hamiltonian of the complete system

$$\tilde{H}_\mathrm{dr} = \hbar\frac{\Omega_\mathrm{R}}{2}\sigma_z + \hbar\omega_0 a^\dagger a + \hbar g_\varepsilon\left[\frac{\Omega_\mathrm{R0}}{\Omega_\mathrm{R}}\sigma_x + \frac{\delta_\mathrm{qh}}{\Omega_\mathrm{R}}\sigma_z\right]\left[a + a^\dagger\right] + \hbar\Omega_\mathrm{p}\left[a\mathrm{e}^{\mathrm{i}\omega_\mathrm{p}t} + a^\dagger\mathrm{e}^{-\mathrm{i}\omega_\mathrm{p}t}\right] \tag{5.13}$$

takes the exact form of (4.5), where the qubit is solely coupled to the fundamental mode. The coupling constant $g_\varepsilon = g\varepsilon/\hbar\omega_\mathrm{q}$ is rescaled with the energy bias and becomes zero at the degeneracy point.

From the Hamiltonian above a resonant interaction is expected when the Rabi frequency (5.7) equals the one of the resonator's fundamental mode. Therefore, an experiment is carried out on sample Qubit0, where a strong driving signal in the third harmonic of the resonator creates a coherent state, with large photon number N. Then, while the qubit bias is varied, the transmission amplitude and phase of a probe signal at the fundamental mode are recorded. The results are shown in Fig. 5-6 for two different probing powers.

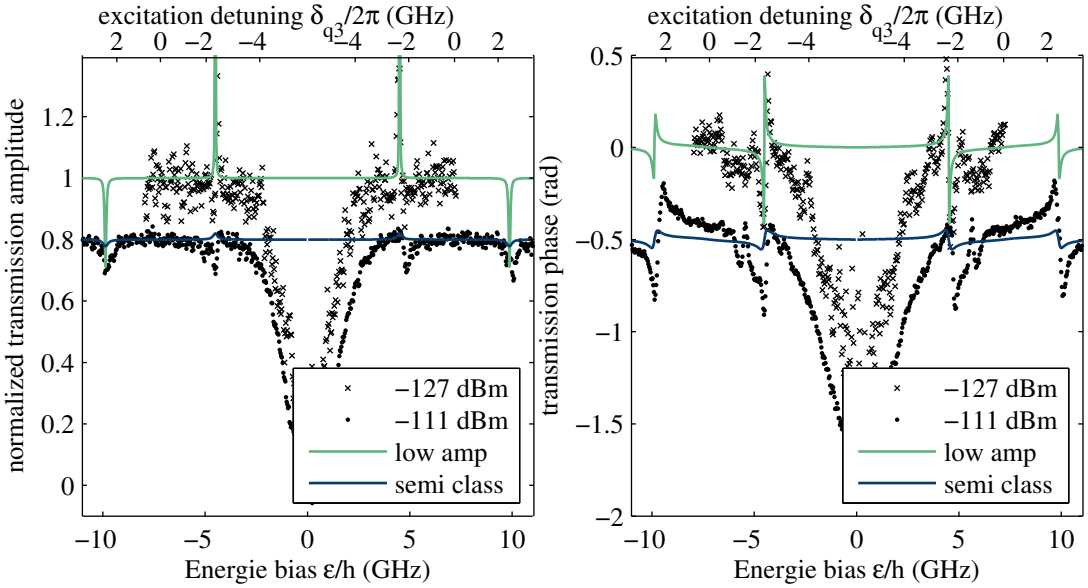

Figure 5-6: Transmission amplitude and phase for a dressed qubit coupled to the fundamental mode. Each plot contains two curves for different probing powers and calculation results from the low amplitude and semi-classical equations. The curves with higher probing amplitudes are shifted down by 0.2 for the amplitude and 0.5 rad for the phase for better visibility. For convenience, also the detuning between qubit and third harmonic frequency is given as x-axis label.

In addition to the dispersive ground state response[4], four resonance points are visible, indicated by the typical phase jumps. For the resonances closer to the degeneracy point, amplification of almost 30% is observed. This amplification vanishes for higher probing amplitudes, while the characteristic of the resonant interaction, the peak dip structure in the phase, remains. The reason lays in the limited amount of energy that can be produced per cycle in the resonator's fundamental mode by the dressed qubit. The theoretical calculations below, which are plotted as blue solid lines, show a good correspondence for weak probing ampli-

[4]The dispersive response is not reproduced by the theoretical lines in Fig. 5-6 because the off-diagonal coupling term in Hamiltonian (5.12) is lost during the transformation to the dressed-state basis.

tudes, both qualitative and quantitative. On the other hand, the semi-classical model does predict a vanishing of the amplification, but cannot accurately reproduce the measured signal. The photon number in the third harmonic is set to 3.6 thousand and a probing amplitude of 300 kHz in the semi-classical limit is used.

To calculate the transmission of a probe field a similar procedure as in 4.4 can be used, while the modified level splitting and population of the dressed system should be considered.
In a first step, (5.13) is transformed to a frame rotating with ω_p. In RWA only the coupling terms $a\sigma_+$ and $a^\dagger\sigma_-$ remain and the Hamiltonian reads

$$\tilde{H}_\mathrm{dr} = \hbar\frac{\delta_\mathrm{Rp}}{2}\sigma_z + \hbar\delta_\mathrm{rp}a^\dagger a + \hbar g_\varepsilon\frac{\Omega_\mathrm{R0}}{\Omega_\mathrm{R}}\left(a\sigma_+ + a^\dagger\sigma_-\right) + \Omega_\mathrm{p}\left(a + a^\dagger\right), \tag{5.14}$$

where $\delta_\mathrm{Rp} = \Omega_\mathrm{R} - \omega_\mathrm{p}$ is the detuning between probe and Rabi frequency, and the resonator detuning δ_rp is defined as before. The Maxwell-Bloch equations for the system expectation values are then given by (4.16) considering the Hamiltonian (5.14) and the Lindblad term (C.49). They read similar to (4.17) - (4.21)

$$\frac{\mathrm{d}\langle a\rangle}{\mathrm{d}t} = -\mathrm{i}\delta_\mathrm{rp}\langle a\rangle - \mathrm{i}g_\mathrm{dr}\langle\sigma_-\rangle - \mathrm{i}\Omega_\mathrm{p} - \frac{\kappa}{2}\langle a\rangle \tag{5.15}$$

$$\frac{\mathrm{d}\langle\sigma_-\rangle}{\mathrm{d}t} = -\mathrm{i}\delta_\mathrm{Rp}\langle\sigma_-\rangle + \mathrm{i}g_\mathrm{dr}\langle a\sigma_z\rangle - \Gamma_{\mathrm{dr}\varphi}\langle\sigma_-\rangle \tag{5.16}$$

$$\frac{\mathrm{d}\langle\sigma_z\rangle}{\mathrm{d}t} = -2\mathrm{i}g_\mathrm{dr}\left(\langle a\sigma_+\rangle - \langle a^\dagger\sigma_-\rangle\right) - \Gamma_\mathrm{dr1} - \Gamma_\mathrm{dr2}\langle\sigma_z\rangle \tag{5.17}$$

$$\frac{\mathrm{d}\langle a^\dagger a\rangle}{\mathrm{d}t} = \mathrm{i}g_\mathrm{dr}\left(\langle a\sigma_+\rangle - \langle a^\dagger\sigma_-\rangle\right) - \mathrm{i}\Omega_\mathrm{p}\left(\langle a^\dagger\rangle - \langle a\rangle\right) - \kappa\langle a^\dagger a\rangle \tag{5.18}$$

$$\begin{aligned}\frac{\mathrm{d}\langle a\sigma_z\rangle}{\mathrm{d}t} =& -\mathrm{i}\delta_\mathrm{rp}\langle a\sigma_z\rangle - \mathrm{i}g_\mathrm{dr}\left(2\langle aa\sigma_+\rangle - \langle\sigma_-\rangle - 2\langle a^\dagger a\sigma_-\rangle\right) - \mathrm{i}\Omega_\mathrm{p}\langle\sigma_z\rangle \\ & - \frac{\kappa}{2}\langle a\sigma_z\rangle - \Gamma_\mathrm{dr1}\langle a\rangle - \Gamma_\mathrm{dr2}\langle a\sigma_z\rangle\end{aligned} \tag{5.19}$$

Here, the abbreviations

$$g_\mathrm{dr} = g\frac{\varepsilon\Omega_\mathrm{R0}}{\hbar\omega_\mathrm{q}\Omega_\mathrm{R}}, \qquad \Gamma_{\mathrm{dr}\varphi} = \Gamma_\varphi - \left[\Gamma_\varphi - \Gamma_\mathrm{r}\right]\frac{\Omega_\mathrm{R0}^2}{2\Omega_\mathrm{R}^2},$$

$$\Gamma_\mathrm{dr1} = \Gamma_\mathrm{r}\frac{\delta_\mathrm{qh}}{\Omega_\mathrm{R}}, \text{ and} \qquad \Gamma_\mathrm{dr2} = \Gamma_\mathrm{r}\frac{\delta_\mathrm{qh}^2}{\Omega_\mathrm{R}^2} + \Gamma_\varphi\frac{\Omega_\mathrm{R0}^2}{\Omega_\mathrm{R}^2}.$$

are introduced. As discussed in the last chapter, the above defined rates reflect the change of the matrix elements of the density matrix. For example, $\Gamma_{\mathrm{dr}\varphi}$ is the total decoherence of the dressed qubit, as it reflects the decay rate of the off-diagonal density matrix elements. It would also be possible to start with the relaxation, excitation, and dephasing rates as defined

by (C.53) and given in (5.11). Nevertheless, the calculation would finally result in the same terms as used in (5.15) to (5.19).

Similar as in 4.4, for low probing powers the correlations involving three operators are neglected in (5.19). Then, the quasi steady state solution of (5.15), (5.16), and (5.19) is given by

$$\langle a \rangle = -\frac{\Omega_\mathrm{p}}{\widetilde{\delta}_\mathrm{rp} + \frac{g_\mathrm{dr}^2}{\widetilde{\delta}_\mathrm{R}} S_q^{(\mathrm{dr})}}, \tag{5.20}$$

where the generalized detuning of the Rabi levels is $\widetilde{\delta}_\mathrm{Rp} = \delta_\mathrm{R} - \mathrm{i}\Gamma_{\mathrm{dr}\varphi}$, $\widetilde{\delta}_\mathrm{rp}$ defined as in 4.4, and

$$S_q^{(\mathrm{dr})} = \frac{\widetilde{\delta}_\mathrm{Rp}\left(\mathrm{i}\widetilde{\delta}_\mathrm{rp}\langle\sigma_z\rangle - \Gamma_\mathrm{dr1}\right)}{\left(\mathrm{i}\widetilde{\delta}_\mathrm{rp} + \Gamma_\mathrm{dr2}\right)\widetilde{\delta}_\mathrm{Rp} - \mathrm{i}g_\mathrm{dr}^2\left(1 + \langle\sigma_z\rangle\right)}. \tag{5.21}$$

The analogy of the Hamiltonians and Lindblad operators of the coupled dressed qubit resonator system to the one of a simple qubit coupled to the fundamental mode is again reflected in a similar form of (5.20) and (5.21), as compared to their counterparts in 4.4. As already mentioned in the last chapter, the relaxation and excitation rates of the dressed system depend on the variables driving amplitude and energy bias. From (5.17) the population of the dressed levels for vanishing coupling to the fundamental mode[5] can be recovered. This undisturbed population of the dressed levels is

$$\langle\sigma_z\rangle_0 = -\frac{\Gamma_\mathrm{dr1}}{\Gamma_\mathrm{dr2}}. \tag{5.22}$$

Its dependency on the driving photon number N is shown in Fig. 5-7.

Without a signal in the harmonic $N = 0$ no coupling is achieved and the qubit stays in the ground state. From the definition of the dressed levels their population changes its sign at the resonance point $\omega_\mathrm{q} = \omega_\mathrm{h}$. This steep change is washed out with increasing photon numbers, as follows from the mixing of the ground and excited qubit state. In the same way, as the states get mixed also a coupling to the fundamental mode is achieved. For small driving it is concentrated close to the resonance point. In the limit of strong driving, e.g. where $N = 10^6$, the higher and lower energetic dressed levels become mostly equal occupied and the coupling reaches almost the value of the effective qubit coupling.

[5] Or zero field in the fundamental mode.

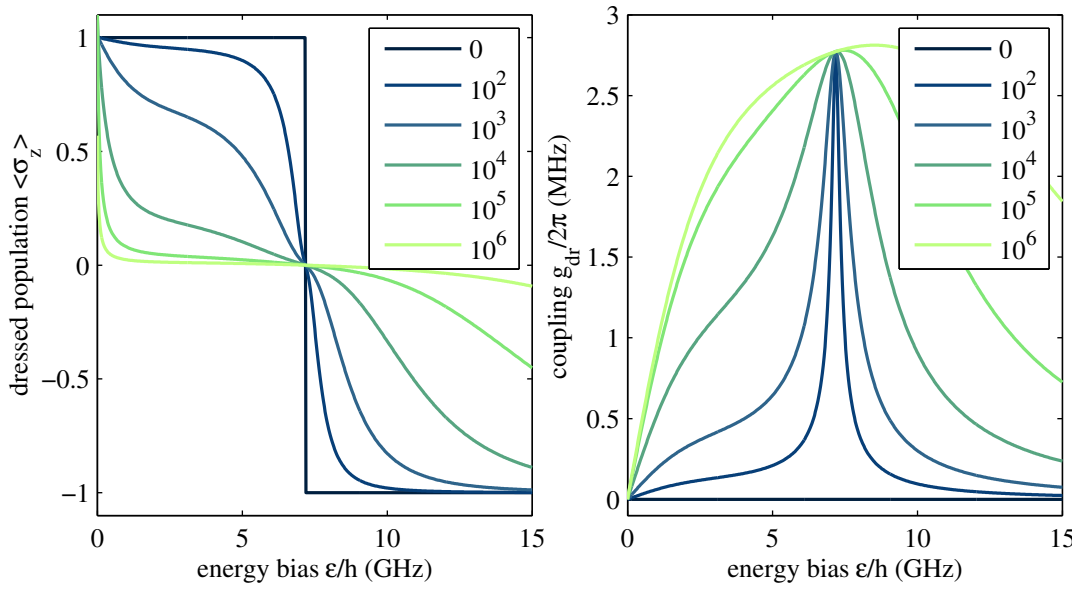

Figure 5-7: Population (left) and effective coupling (right) to the fundamental mode of the dressed-two-level system for different photon numbers. The plots assume the parameters from qubit0 sample.

Finally, the transmission in the weak probing limit is defined by (2.70) together with (5.20) as

$$t_\mathrm{r} = \mathrm{i}\frac{\kappa\widetilde{\delta}_\mathrm{Rp}}{\widetilde{\delta}_\mathrm{rp}\widetilde{\delta}_\mathrm{Rp} - g_\mathrm{dr}^2 S_q^{(\mathrm{dr})}}. \tag{5.23}$$

The transmission coefficient above does not depend on the probing amplitude Ω_p. This result is well justified, if the signal is small and therefore, it has no influence on the dressed levels population. On the other side, in the experiment the probing amplitude may not always be small.

In the semi-classical limit, a solution can be found for arbitrary probing amplitudes. By assuming the expectation values of the qubit and resonator operators to factorize, the calculation of the quasi steady state solution of (5.15) to (5.17) is the same as in 4.4. The so found expressions for the resonator field and dressed-state population expectation values

$$\langle a\rangle = \frac{-\Omega_\mathrm{p}}{\widetilde{\delta}_\mathrm{rp} + \frac{g_\mathrm{dr}^2}{\widetilde{\delta}_\mathrm{Rp}}\langle\sigma_z\rangle} \tag{5.24}$$

$$\langle\sigma_z\rangle = -\frac{\Gamma_\mathrm{dr1}}{\frac{4g_\mathrm{dr}^2}{\Gamma'_\mathrm{dr\varphi}}\langle a\rangle\langle a^\dagger\rangle + \Gamma_\mathrm{dr2}} \tag{5.25}$$

have a similar form as (4.27) and (4.28). Here, the additional introduced variable is $\Gamma'_\mathrm{dr\varphi} =$

$\frac{\Gamma_{dr\varphi}^2+\delta_{Rp}^2}{\Gamma_{dr\varphi}}$. The population of the dressed qubit then acquires changes given by

$$\langle\sigma_z\rangle = \langle\sigma_z\rangle_0 - \frac{2i\Omega_p}{\Gamma_{dr2}}\left(\langle a^\dagger\rangle - \langle a\rangle\right) - \frac{2\kappa}{\Gamma_{dr2}}\langle a\rangle\langle a^\dagger\rangle. \tag{5.26}$$

This equation can be found by removing $\langle\sigma_-\rangle$ in (5.17) with (5.15). Inserting (5.24), it becomes obvious that the corrections are proportional to Ω_p^2. The population is then given by a cubic equation which may be solved analytically. Since the expression is long and not easy to interpret, only the results for $\langle\sigma_z\rangle$ are plotted for different probing amplitudes in Fig. 5-8.

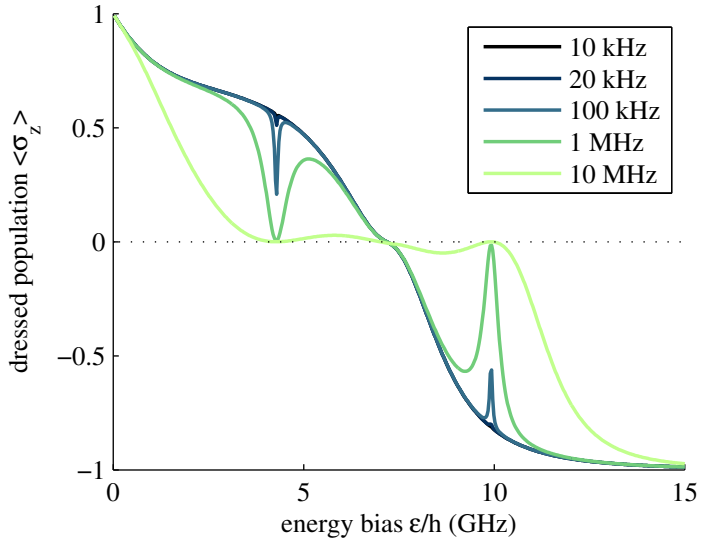

Figure 5-8: Population of the probed dressed-two-level system for different probing amplitudes. The plots assume the parameters from qubit0 sample and a photon number of $N = 500$ in the third harmonic. The black dotted line is inserted for a better visibility of the equal population value.

For low probing powers the curves follow the result for the undisturbed dressed levels. When the power is increased the interaction with the fundamental mode mixes the higher and lower energetic dressed levels with the resonator states. Close to the resonances the population of the dressed-two-level system is then reduced to a value of equal population, and for strong probing signals it is equalized over a wide range around the resonances. Therefore, the visibility of amplification and damping effects is best for probing signals with small amplitudes.

For high amplitudes the found values for $\langle\sigma_z\rangle$ have to be used in the equation for the transmission in the semi-classical limit

$$t_r = \frac{i}{2}\frac{\kappa\widetilde{\delta}_{Rp}}{\widetilde{\delta}_{rp}\widetilde{\delta}_{Rp} + g_{dr}^2\langle\sigma_z\rangle}. \tag{5.27}$$

In 4.4 the results for weak amplitudes and for factorization of the operators coincided when the expectation value of the qubit population is set to its undisturbed value $\langle\sigma_z\rangle = \langle\sigma_z\rangle_0 = -1$. This relation can be also reformulated as $S_q(\langle\sigma_z\rangle_0) = \langle\sigma_z\rangle_0$. Similar, the parameter $S_q^{(\mathrm{dr})}(\langle\sigma_z\rangle_0)$ coincides with the undisturbed value $\langle\sigma_z\rangle_0$, if the coupling can be neglected, and it gives in first order the same result as the probe power dependence (5.26) plotted in Fig. 5-8.

5.4 Dressed-state lasing of a single artificial two-level system

Lasers are based on the population inversion between two levels of an atom in a cavity. The energy splitting of these levels needs to be equal to the eigenfrequency of the cavity. By stimulated emission the light field in the cavity can then be coherently increased. This process sets certain requirements on the coupled systems time constants. The fastest process needs to be the excitation to the higher energetic state by a pump, since the atomic system should not be excited by the light in the cavity. Otherwise damping would be achieved. The coupling between the atom and the light should also be faster than the relaxation of photons from the cavity. This condition is needed for one photon to coherently create a secondary one before it leaves the resonator.

In a simple scheme atomic laser systems usually require at least three levels to create an inversion population. It is then achieved by a strong pump between the first and third level and a fast relaxation from the third to the second. Considering a two-level system a pumping in resonance would in maximum equalize the population, as can be seen from the discussion above (especially 4.13). With full control, one could also expect a coherent excitation by sending only a series of so called π-pulses[6], but to achieve lasing a high timing accuracy would be necessary and, in addition, the pump would directly couple into the cavity. But on the other hand, the use of a detuned drive leads to the dressed system as explained in 5.2, where an excitation to the higher level is achieved by the qubit's relaxation rate.

In order to fulfill the requirements mentioned above on the time constants of a possible lasing system using a single superconducting flux qubit, a new sample has been specially designed

[6] A resonant signal drives the qubit between ground and excited state. If the driving is stopped when the excited state is achieved the pulse length corresponds to one quarter of a full Rabi oscillation. Therefore, a resonant pulse of this length is called π-pulse.

(see also [112]). The resonator's gap capacitance is slightly increased by reducing the gap in the center line to 15 μm to enhance the output coupling of the cavity. The qubit itself is enlarged to a size of 10×3.5 μm^2 to increase its coupling to the resonator field. Also the effective excitation of the qubit is proportional to the relaxation rate of the qubit. In order to achieve faster relaxation, a gold resistor is placed next to the qubit loop. A SEM image of the sample's center part, including the center conductor of the resonator, the qubit, and the gold plate resistor is shown in Fig. 5-9.

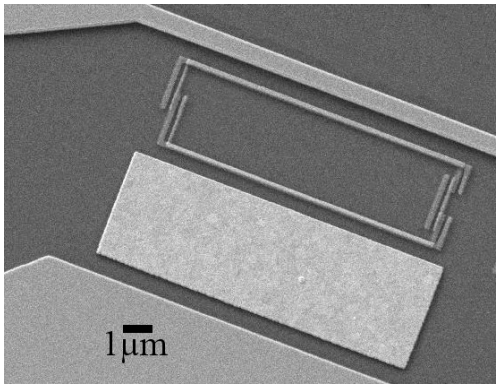

Figure 5-9: SEM image of the sample for demonstrating dressed-state lasing. The picture shows the center part of the resonator. The light straight line is the center conductor of the resonator with a width of 1 μm. In the gap to the ground plane the qubit with a size of 10×3.5 μm is placed together with a 10×4 μm gold plate resistor. The latter should enhance the relaxation of the qubit.

The resonator has similar parameters as the ones considered above with a center frequency of 2.59 GHz and a quality factor of about 50000. The mutual inductance of the qubit is found by numerical calculations with fasthenry to be 3.5 pH. The qubit parameters are reconstructed by fitting the dispersive ground state response and found to be $\Delta_{\mathrm{L}}/h = 3.7$ GHz, $I_{\mathrm{pL}} = 12$ nA and $g_{\mathrm{L}} = 1.6$ MHz, where the subscript L emphasizes that this parameters are connected to the lasing sample. For verification, the resonance points of the qubit with higher harmonics of the resonator are recorded by measuring their transmission and varying the qubit bias.[7] Because the persistent current is unexpectedly small compared to the other samples, also the coupling constant is reduced. This reduction certainly is a result of the deposition of the gold film next to the qubit loop. With the smaller relation between Josephson and charging energy at the junctions the qubit becomes more sensitive to electric fields. Nevertheless, during the experiment no charge noise effects, as shifting of the qubit gap are observed. In addition,

[7]The data is not shown, because no additional information is recovered.

a direct spectroscopy is observable which also made an estimation of the dissipative rates of the qubit as in 4.3 impossible. They are, therefore, used as fitting parameters of the later shown amplification data. Considering (4.13), indeed the dissipative rates may be enhanced by the design modification and therefore the driving amplitude Ω_d did not reach comparable high values to observe the spectroscopic signal.

In a first experiment the transmission of a weak probe beam close to the fundamental mode frequency is measured while the system is driven with a strong amplitude at the third harmonic and the qubit bias is changed. The powers applied are -122 dBm at the fundamental and -104 dBm at the third mode. The result is plotted in Fig. 5-10 a).

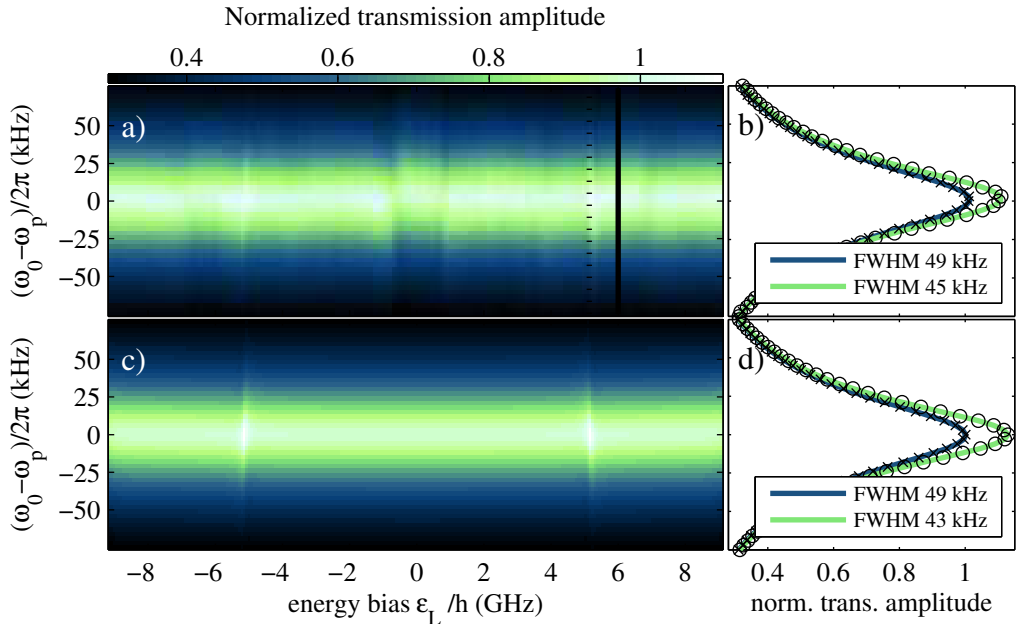

Figure 5-10: Amplification of the probe signal by the dressed qubit. a) The measured normalized transmission amplitude is plotted for changing frequency of the probe beam and different energy bias. An additional applied strong driving signal at the third harmonic dresses the qubit states. At an energy bias $\varepsilon_L/h \approx \pm 5$ GHz the resonator's fundamental mode is in resonance with the dressed levels. Thus, amplification is found. b) The Lorentzian shaped transmission is plotted in the amplification point (circles) and away from it (crosses). They correspond to the solid and dashed lines in a). For convenience the same y-axis is used in a) and b). The results of the calculation using (5.23) are presented in the same way in c) and d).

Symmetric around the degeneracy point an amplification of the probe signal is observed for an energy bias of $\varepsilon_L/h \approx \pm 5$ GHz. Here, the fundamental mode of the resonator is resonant to the Rabi splitting. The latter is induced by a high photon number in the third

harmonic. Experimentally the transmission is enhanced by about 10% and also the width of the Lorentzian curve is reduced by the same percentage compared to the curves away from resonance. These results are illustrated in Fig. 5-10 b) where the transmission curves are plotted in dependency of the probing frequency detuning in and away from this resonance point. The increased quality demonstrates an energy transfer from the dressed qubit to the fundamental mode. To clarify, after starting with a constant N, the number of photons in the third harmonic would be reduced due to the relaxation of the qubit as well as by the energy transfer used for the amplification. Nevertheless, in the calculations the quasi steady state for the dressed qubit resonator system is faster achieved than a significant change of this photon number. That is justifying the assumption of a constant Rabi splitting. In addition, the driving signal balances the additional losses to the fundamental mode in the experiment.

The experimental data on the Rabi resonance can accurately be reproduced by the equation for the transmission in the weak probing limit (5.23) as demonstrated in Fig. 5-10 c) and 5-10 d). For the fitting, the parameters $\Gamma_{\mathrm{rL}}/2\pi = 15\mathrm{MHz}$, $\gamma_{\varphi\mathrm{L}}/2\pi = 90\mathrm{MHz}$, and a mean photon number $\langle N\rangle = 48\times 10^3$ are used. The values differ from the ones given in our paper [112], since the theoretical model is improved and the pure dephasing considered. The value for the relaxation rate reconstructed in that way is significantly increased compared to the one of qubit0 and qubit1 sample, as intended by the gold film resistor. Note, the theoretical approach does not include the direct interaction of the Zeeman shifted qubit with the resonator's fundamental mode (see 5.1). Nevertheless, these resonances are experimentally observed close to the degeneracy point at a qubit bias of about 1 GHz. The amplification in the theoretical curve is slightly higher than in the experimental one, which indicates that the probing power may not have been sufficiently low. To investigate the dependency of the amplification on the amplitudes of the applied fields two more experiments were carried out.

At first, the energy bias is limited to a close range around the amplification feature while the probe is fixed at the fundamental mode frequency and the probing power is varied. In Fig. 5-11 (a) this measured probe power dependency is plotted together with calculation results in (b), using (5.27) and a numerical defined population from (5.26) and (5.24).

Both show amplification at a detuning of $\delta_{\mathrm{qh}} \approx -1.58$ GHz. In the experimental picture around -110 dBm the amplification signal is lost, which may be explained by flux noise shifting the system away from the resonance point. The transmission is increased in maximum by about 15%. With increasing probing power the amplification is reduced, which can be understood in two ways. As visible in Fig. 5-8 the population inversion is reduced with

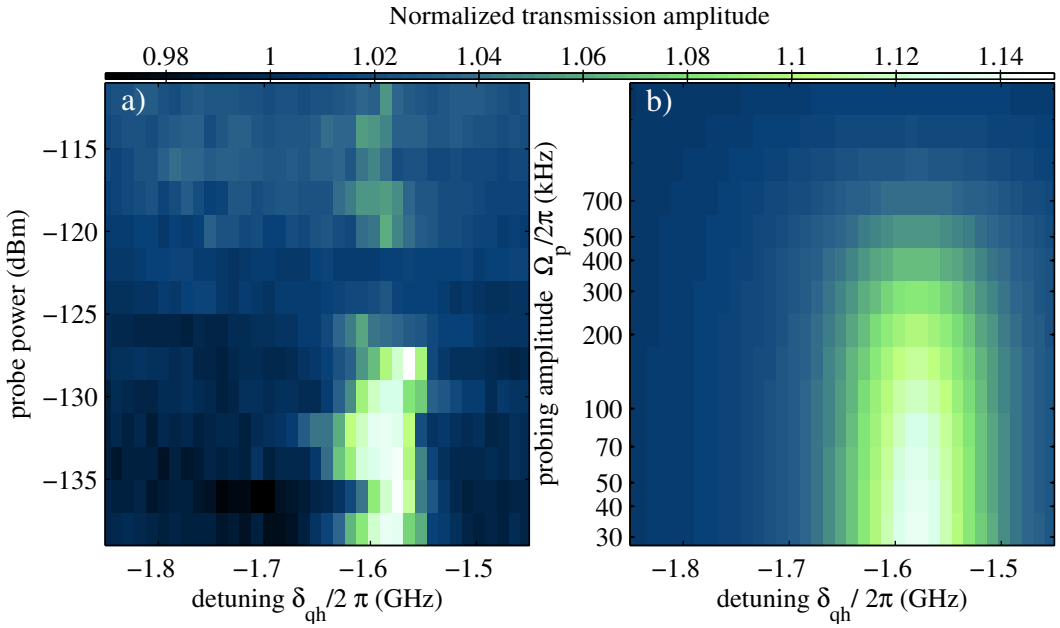

Figure 5-11: Probe power dependence of the dressed-state amplification. Measured (a) and calculated (b) transmission amplitude for an energy bias (given as the qubit detuning from the third harmonic frequency) around the resonance of the fundamental mode with the dressed qubit and different probing powers. The y-axis of the right plot is calculated from the one of the left using (2.66). The photon number in the third harmonic is found to be $N \approx 44 \times 10^3$.

increasing field amplitude at the fundamental mode. This result means it is less likely to find the dressed qubit in its higher energetic state and stimulated emission is reduced while absorption of photons in the cavity may be enhanced. On the other hand, only a certain amount of energy can be transferred from the dressed qubit to the cavity per resonator cycle. Its value depends on the system coupling and excitation rates. The total field in the cavity is then given by a sum of the one induced by and proportional to the probe beam and this constant energy transfer. For the transmission coefficient the signal leaving the cavity is divided by the value of the probing amplitude. When increasing the latter the component from the dressed qubit is, therefore, reduced.

For the theoretical plot in Fig. 5-11, the probing amplitude is calculated directly from the applied probing power using (2.66) and the values for the capacitances given in 2.5. Although the coupling capacitance is only estimated and the probing power at the input of the resonator depends on the contacting of the sample and cable losses, the correspondence between the measured result and the theory is good. The amplification signal starts to vanish around the same value, about -128 dBm or 150 kHz. For weak amplitudes the amplification is

saturated. The minimal photon number created by the probing signal is below one photon. Note, the semi-classical approach used for calculation is not valid for low probing powers in general, but for the explanation of the experimental data a dependency of the transmission on the power is essential.

These data illustrate the small discrepancy between experimental and calculation results in Fig. 5-10 since for the probing power used there (-118 dBm) the maximum of amplification is not expected. Another interesting analysis is the dependency on the driving amplitude and, thus, on the mean photon number in the third harmonic.

In a second experiment the probing power is fixed at -135 dBm, which corresponds to about one photon at the resonator's fundamental mode. Then the qubit bias as well as the driving amplitude are varied around the already found resonance point, while the frequencies of drive and probe are fixed at the resonator's first and third harmonic. The results are plotted again together with calculation data in Fig. 5-12.

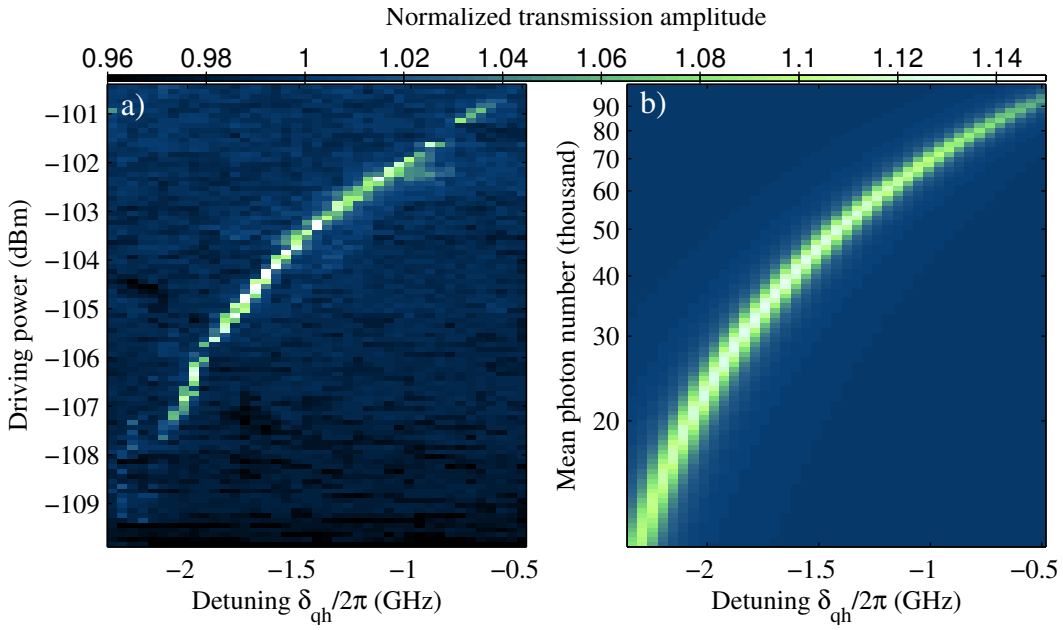

Figure 5-12: Driving power dependence of the dressed-state amplification. Measured (a) and calculated (b) transmission amplitude for an energy bias (given as the qubit detuning from the third harmonic frequency) around the resonance of the fundamental mode with the dressed qubit and different driving powers. Here, the y-axis of the left plot is mapped to the one of the right with the resonance condition $\Omega_R = \omega_0$ and the corresponding definition of the Rabi frequency (5.7). The probing power is fixed at -135 dBm.

The amplification point moves for higher driving powers to smaller absolute detunings $\left|\delta_{qh}\right|$

and thus closer to the resonance between qubit and driving signal. In that way, the Rabi frequency (5.7) in the amplification region is always close to the frequency of the fundamental mode, thus fulfilling the resonance condition $\Omega_R(\langle N\rangle) = \omega_0$. This quality enables a direct mapping of the mean photon number $\langle N\rangle$ to the driving power, since all other parameters in this relation are known. One could expect the width of the resonance line to be increased by the distribution of the coherent state at the third harmonic over many photon number states. Indeed, when estimating this value at its maximum[8] as $\Omega_R\left(\sqrt{\langle N\rangle}\right)/2\pi = 2g_h\Delta N^{0.25}/h\omega_q \approx 100$ MHz, it is of the same order of magnitude as the qubit decoherence rate and, therewith, of the natural width of the dressed qubit levels.

The driving power dependency of the amplification demonstrated in Fig. 5-12 shows a maximum in a region around $\delta_{qh}/2\pi \approx -1.5$ GHz. That can be explained by the dependency of the coupling to the fundamental mode and the dressed population (see Fig. 5-8). For small photon numbers and negative detunings the excitation rate of the qubit is given by the relaxation rate of the qubit. On the other hand, the coupling of the dressed qubit to the fundamental mode close to their resonance would be weak. Note, in this case this resonance point is close to a detuning of $\delta_{qh}/2\pi \approx -2.5$ GHz. Therefore, only a small amplification is expected. In contrast, for high photon numbers in the harmonic the contribution of Ω_{R0} to the Rabi splitting is dominant and the resonance is observed for a smaller absolute detuning $\left|\delta_{qh}\right|$. Thus, the coupling is monotonically increased with reducing the detuning but the population of the dressed qubit is lowered. In that way, the occurrence of an optimum in a region with reasonable excitation rate and coupling constant g_{dr} can be explained. This optimum is observable in both, the experimental and the calculated plot in Fig. 5-12.

To this point only amplification, meaning an increase in transmission compared to the one of the undisturbed resonator is discussed. As seen by the power dependency above, an optimum for this amplification can be found. On the other hand, the value of amplification depends on the probing amplitude, making it difficult to quantify the process effectiveness. Therefore, it is worthwhile to study the emission of the dressed qubit system at the fundamental mode.

5.5 Emission from the dressed qubit and lasing

To quantify the emission spectrum of the dressed system close to the fundamental mode, in another experiment the network analyzer is replaced by a spectrum analyzer. In the experi-

[8] There the photon number is maximal and, thus, the detuning δ_{qh} becomes zero.

ment the probe beam is removed. Because the emission from the resonator is weak compared to the thermal noise of the cold amplifier, long averaging times are needed. To exclude the influence of low frequency noise between a measurement and its reference part and to exclude heating effects by the driving signal, the experiment is carried out in the following way: The driving signal is continuously switched OFF and ON. In each case the emission spectrum is recorded in a span of 300 kHz around the fundamental mode frequency $\omega_0/2\pi$. The spectrum is taken at 101 equidistant points with a resolution bandwidth of 5.1 kHz and a video bandwidth of 510 Hz. These parameters ensure a fast sweep time of 90 ms per curve. The data is then recorded and averaged over a total of 120 000 iterations. With the processing of the data a total measurement time of one spectrum is then eleven hours for the used setup. During the measurement the bias point of the qubit as well as the power for the driving signal is kept constant. The collected data as shown in Fig. 5-13 is recorded for the optimal parameters found in the amplification measurements (see last chapter). That is an energy bias giving as detuning $\delta_{\mathrm{qh}}/2\pi = -1.4$ GHz and a driving signal amplitude that supplies a photon number of about 48000 in the third harmonic.

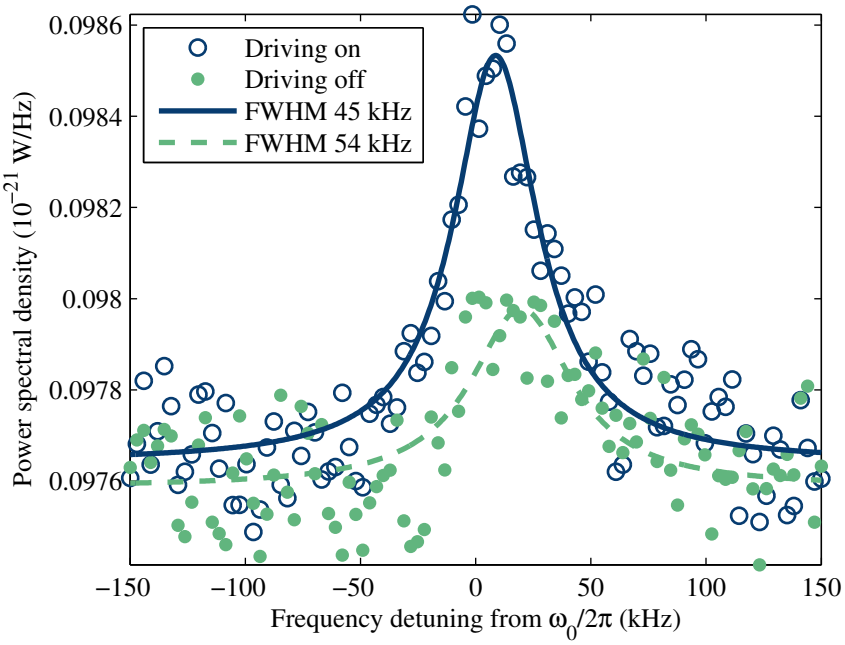

Figure 5-13: Emission from the qubit-resonator system with (circles) and without (dots) the dressing signal is recorded as power spectral density for frequencies around the fundamental mode. The curves are fitted with Lorentzian functions (square of (A.11)) and the line widths are given in the legend.

A clear difference between the spectra with and without the driving signal at the third har-

monic is observable. The curve without driving corresponds to the emission of a thermal resonator at an effective temperature of 30 mK above the noise floor of the cold amplifier. The latter gives the background of 97.6×10^{-24} W/Hz what corresponds to a noise temperature of 7 K, which is in good agreement with the amplifiers specification. The Lorentzian fit of the thermal curve gives an R square value of 0.69 and with 95 % confidence bounds the curve width is found to be $\kappa/2\pi = (54 \pm 14)$ kHz. On the other hand, the emission from the dressed system into the resonator's fundamental mode yields a signal clear distinguishable from the noise floor. Its maximum is found about 1×10^{-24} W/Hz above the noise floor. Thus, the amplitude is more than doubled compared to the thermal response. The corresponding Lorentzian fit gives a R square of 0.86 and a linewidth of $\kappa/2\pi = (45 \pm 7)$ kHz. The latter is reduced by approximately 20 % compared to the thermal response and about 10 % to the transmission measurements. The smaller linewidth and increased emission is an indication of lasing of the dressed-qubit-resonator system.

A better analysis of the line shapes is possible if the data is smoothed with a moving average as in Fig. 5-14.

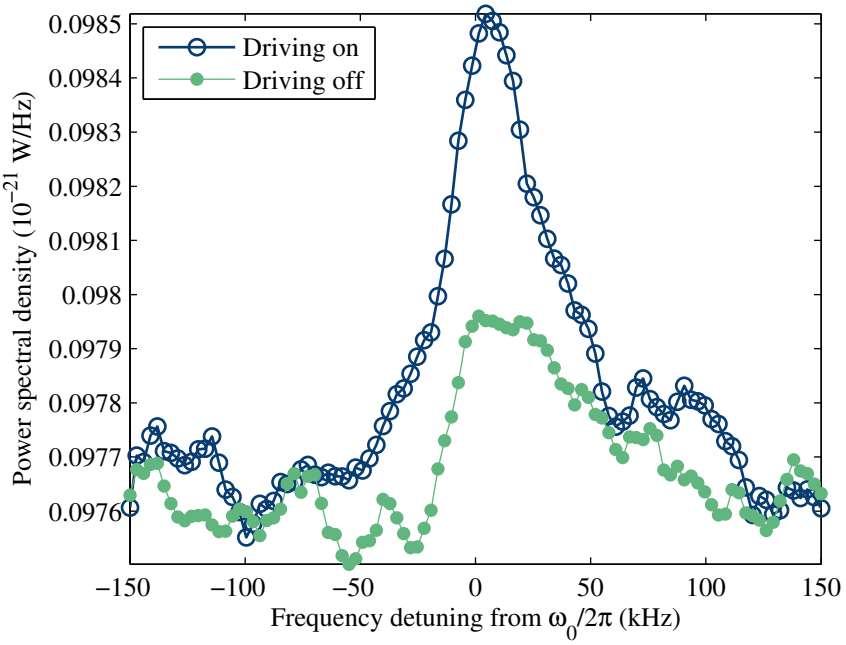

Figure 5-14: The emission from the qubit-resonator system with (circles) and without (dots) the dressing signal as power spectral density for frequencies around the fundamental mode. For better visibility of the line shapes a moving average with size five is used.

Here, the thermal response is seen to be nonlinear. Indeed, the shape reminds a Fano reso-

nance [113], which may be explained by the competition of the excitation to the quantized resonator states and to the continuum of states of the transmission line. Also, when the dressing signal is on, two small side peaks are observable at about -120 kHz and 100 kHz. Such a spectrum with several peaks can be explained in different ways. First, one could expect the observation of a Mollow triplet, as the incoherent scattered part of the cavity photons with the dressed-two-level system [114]. Nevertheless, the distance from the central peak to the ones on the side should then be of the order of the effective coupling constant g_{dr}. However for the given parameters it is ≈ 1 MHz. In addition, the dressed-two-level system actually is a multilevel system. Therefore, a second explanation may be the direct observation of the different Rabi frequencies. The differences in the frequency splitting of the states of manifold N compared to $N-1$ is for the above chosen bias point and mean photon number $\langle N\rangle = N$ of the order of several tens of kHz. Although that gives the right magnitude of the distance to the side peaks, their width then raises questions. Since the dressed levels are composed by qubit and (third harmonic) resonator states, one would expect their width to be of the order of the qubit's decoherence rate. This requirement is not supported by to the observed data because the width of all the peaks is close to the resonator's photon decay rate. Still, the collected data has a small signal to noise ratio, so that the side peaks may be a measurement artefact. A continuation of the spectral investigation with improved coupling, resonator output, and noise properties of the output circuitry is therefore necessary for further investigations.

Finally, to exclude other effects, like heating or parametric down conversion as reasons for an increased power spectral density when the driving signal is on, the experiment is repeated at different bias points while all other parameters are kept unchanged. For better comparison the area under the difference curve between the spectra with and without driving is recorded instead of plotting the whole spectra in the different cases. After subtracting the minimal value found for a positive bias value, a curve as plotted in Fig. 5-15 is received.

A maximum of power emitted from the cavity is found close the expected resonance between fundamental mode and Rabi frequency at a detuning of $\delta_{\mathrm{qh}} \approx -1.4$ GHz. For a bias shifted away from resonance the power emission value is almost constant. The point taken for a positive bias value is close to the Rabi resonance where the effective relaxation brings the dressed-state system into its lower energetic state. Thus, some signal is taken from the resonator's fundamental mode for excitation of the qubit and the smallest emitted power is measured. This reduction corresponds to cooling the resonator.

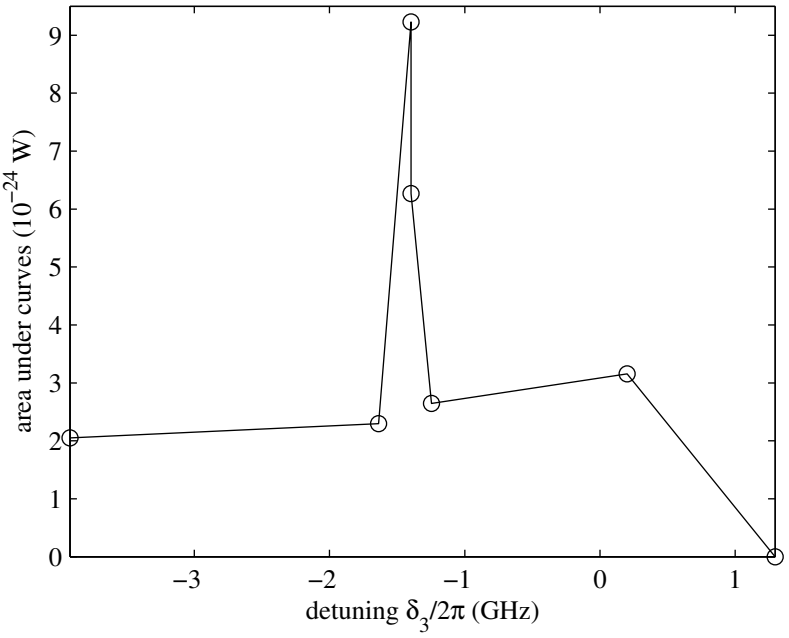

Figure 5-15: Area under the difference between the spectra with and without the driving signal for varying detuning. The values are plotted in relation to the the minimal area measured for $\delta_{\mathrm{qh}} \approx$ 1.3 GHz.

5.6 Strong driving - Beyond the two-level approximation

In this final chapter the situation of even higher driving signals in a harmonic will be considered. From the above model one could expect a constant increase of the on-resonance Rabi frequency with the driving amplitude. But, this increase would apply for all the steps of the dressed ladder. Thus, the levels of different manifolds would come closer together giving raise to new observable interactions and changes in the level structure. Also, with higher driving amplitudes, the probability of multiphoton excitations becomes larger. To test such predictions, a simple experiment can be carried out: The transmission of the resonator's fundamental mode is measured for different energy bias and with increasing driving amplitude in the third harmonic. The results of such a measurement on sample Qubit0 is shown in Fig. 5-16.

Several features found in this plot are already explained above. For example, close to the degeneracy point the strong AC-Zeeman shift, induced by the driving, pushes the effective minimal level spacing below the resonator's fundamental mode frequency. Thus, the dispersive shift of the resonator frequency is first increased until resonant interactions occur at

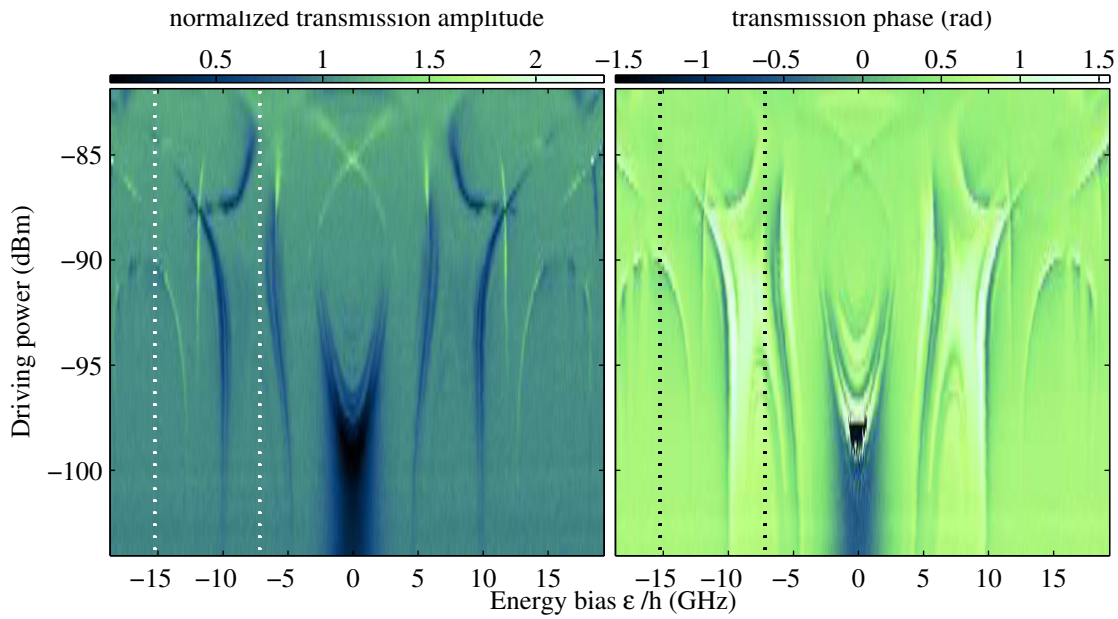

Figure 5-16: Normalized transmission amplitude and transmission phase of a probe signal applied at the fundamental mode frequency, while the qubit energy bias and the driving amplitude are changed. The latter is applied in the third harmonic of the resonator. The dotted (white and black) lines mark the positions on the negative bias axes where $\omega_q = n\omega_h$ with $n \in \{1,2\}$. The probing power takes a value of -127 dBm.

around -98 dBm (compare to Fig.5-3). Then the two resonances move away from the degeneracy point and eventually vanish. Two resonances appear close to the degeneracy point for further increase of the power. There amplification is found that may be explained by pushing the excited state of the qubit below its ground state.

Second, in a distance of about 2.5 GHz from the dotted lines resonant interactions appear. The corresponding driving powers are about -100 dBm for the closer and about -96 dBm for the further line from the degeneracy point, respectively. They are characterized by a change of amplitude and characteristic phase jumps. These resonances correspond to the Rabi resonance discussed in the last few sub-chapters for one photon and two-photon driving. Thus, they are found around the lines for zero detunings $\delta_{qh} = \omega_q - \omega_h$ and $\delta_{qh}^{(2)} = \omega_q - 2\omega_h$. Interestingly, the power dependence of these resonances is different. While the positive and negative detuned resonances for the two-photon drive move for higher powers to one point, they are always separated for the one photon drive. This property suggests a non-monotonic dependence of the on resonance Rabi frequency. Note, the probing power used in this experiment is to high to find amplification for the negative detuned Rabi resonance in

the one photon case[9]. In addition, further resonance lines appear for strong driving, which are not explained with the considerations above.

A mathematical description aimed for better correspondence between theory and experiment should again start at the basic system Hamiltonian. That means considering a qubit with two driving signals applied in the harmonics of a resonator. In the eigenbasis of the qubit it reads

$$\begin{aligned} H_\mathrm{t} =& \hbar\frac{\omega_\mathrm{q}}{2}\sigma_z + \hbar\omega_\mathrm{h} a_\mathrm{h}^\dagger a_\mathrm{h} + \frac{g_\mathrm{h}}{\omega_\mathrm{h}}\left(\varepsilon\sigma_z + \Delta\sigma_x\right)\left[a_\mathrm{h}^\dagger + a_\mathrm{h}\right] + \hbar\Omega_\mathrm{d}\left[a_\mathrm{h}^\dagger \mathrm{e}^{-\mathrm{i}\omega_\mathrm{d}t} + a_\mathrm{h}\mathrm{e}^{\mathrm{i}\omega_\mathrm{d}t}\right] \\ &+ \frac{g}{\omega_\mathrm{q}}\left(\varepsilon\sigma_z + \Delta\sigma_x\right)\left[a^\dagger + a\right] + H_\mathrm{a}. \end{aligned} \tag{5.28}$$

Here, $H_\mathrm{a} = \hbar\omega_0 a^\dagger a + \hbar\Omega_\mathrm{p}\left[a^\dagger \mathrm{e}^{-\mathrm{i}\omega_\mathrm{p}t} + a\mathrm{e}^{\mathrm{i}\omega_\mathrm{p}t}\right]$ contains solely field operators of the fundamental mode[10].

As shown in our papers, two ways to deal with this Hamiltonian [109, 115] are possible. Here, only the first method using RWA will be sketched. First, to proceed the system can be transformed into a frame rotating with the driving frequency ω_d around $a_\mathrm{h}^\dagger a_\mathrm{h}$ by the transformation $\hat{U}_5 = \mathrm{e}^{\mathrm{i}\omega_d t a_\mathrm{h}^\dagger a_\mathrm{h}}$, giving

$$\begin{aligned} H_\mathrm{t} =& \hbar\frac{\omega_\mathrm{q}}{2}\sigma_z + \hbar\delta_\mathrm{hd} a_\mathrm{h}^\dagger a_\mathrm{h} + \frac{g_\mathrm{h}}{\omega_\mathrm{q}}\left(\varepsilon\sigma_z + \Delta\sigma_x\right)\left[a_\mathrm{h}^\dagger \mathrm{e}^{\mathrm{i}\omega_\mathrm{d}t} + a_\mathrm{h}\mathrm{e}^{-\mathrm{i}\omega_\mathrm{d}t}\right] + \hbar\Omega_\mathrm{d}\left[a_\mathrm{h}^\dagger + a_\mathrm{h}\right] \\ &+ \frac{g}{\omega_\mathrm{q}}\left(\varepsilon\sigma_z + \Delta\sigma_x\right)\left[a^\dagger + a\right] + H_\mathrm{a}. \end{aligned} \tag{5.29}$$

Here, $\delta_\mathrm{hd} = \omega_\mathrm{h} - \omega_\mathrm{d}$ is the detuning of the drive from the third harmonic. The driving and also the probing signal will produce a coherent state in the corresponding harmonic. Since the driving in the third harmonic is strong, it is worthwhile to average (5.29) over this coherent state $|\alpha_\mathrm{h}\rangle$, that is an eigenstate of the annihilation operator $a_\mathrm{h}|\alpha_\mathrm{h}\rangle = \alpha_\mathrm{h}|\alpha_\mathrm{h}\rangle$ with $\alpha_\mathrm{h} = \sqrt{\langle N\rangle}$

$$\begin{aligned} \tilde{H}_\mathrm{t} =& \frac{\hbar\omega_\mathrm{q}}{2}\sigma_z + \frac{\varepsilon}{2\omega_\mathrm{q}}\Omega_\mathrm{h}\cos\omega_\mathrm{d}t\,\sigma_z + \frac{\Delta}{2\omega_\mathrm{q}}\Omega_\mathrm{h}\cos\omega_\mathrm{d}t\,\sigma_x \\ &+ \frac{g}{\omega_\mathrm{q}}\left(\varepsilon\sigma_z + \Delta\sigma_x\right)\left[a^\dagger + a\right] + H_\mathrm{a}, \end{aligned} \tag{5.30}$$

where $\Omega_\mathrm{h} = 4g_\mathrm{h}\sqrt{\langle N\rangle}$ and the constant energy terms $\hbar\delta_\mathrm{hd}\alpha_\mathrm{h}^2$ and $\hbar\Omega_\mathrm{d}\alpha_\mathrm{h}$ are omitted. To remove the second term from the right-hand side of (5.30), a unitary transformation $\hat{U}_6 =$

[9] Nevertheless, as tested by experiments with lower probing power they are observable also for this sample.

[10] Before a high photon number in the harmonic is assumed without asking the question how to create it. Now a driving signal is explicitly added to the Hamiltonian, that creates a coherent state in the harmonic.

$e^{i\eta\sigma_z/2}$ with $\eta = \frac{\varepsilon}{\hbar\omega_q\omega_d}\Omega_h \sin\omega_d t$ is applied.

$$\begin{aligned} H_t = &\frac{\hbar\omega_q}{2}\sigma_z + \frac{\Delta}{2\omega_q}\Omega_h \cos\omega_d t \left[e^{i\eta}\sigma_+ + e^{-i\eta}\sigma_-\right] \\ &+ \frac{g}{\omega_q}\left(\varepsilon\sigma_z + \Delta\left[e^{i\eta}\sigma_+ + e^{-i\eta}\sigma_-\right]\right)\left[a^\dagger + a\right] + H_a. \end{aligned} \tag{5.31}$$

Using the Jacobi-Anger expansion $e^{iz\sin x} = \sum_{l=-\infty}^{\infty} J_l(z)e^{ilx}$, where J_l denote the Bessel function of the first kind, the Hamiltonian can be rewritten as

$$\begin{aligned} H_t = &\frac{\hbar\omega_q}{2}\sigma_z + \frac{\Delta}{4\omega_q}\Omega_h\left(e^{i\omega_d t} + e^{-i\omega_d t}\right)\sum_{l=-\infty}^{\infty} J_l\left(\frac{\varepsilon\Omega_h}{\hbar\omega_q\omega_d}\right)\left[e^{il\omega_d t}\sigma_+ + e^{-il\omega_d t}\sigma_-\right] \\ &+ \frac{g}{\omega_q}\left(\varepsilon\sigma_z + \Delta\sum_{l=-\infty}^{\infty} J_l\left(\frac{\varepsilon\Omega_h}{\hbar\omega_q\omega_d}\right)\left[e^{il\omega_d t}\sigma_+ + e^{-il\omega_d t}\sigma_-\right]\right)\left[a^\dagger + a\right] + H_a. \end{aligned} \tag{5.32}$$

A final unitary transformation $\hat{U}_7 = e^{ik\omega_d t\sigma_z/2}$ and omitting terms oscillating with multiples of frequencies ω_d yields

$$H_t = \hbar\frac{\delta_{qk}}{2}\sigma_z + \hbar\frac{\Omega_{k0}}{2}\sigma_x + \frac{g}{\omega_q}\left(\varepsilon\sigma_z + \Delta'_k\sigma_x\right)\left[a^\dagger + a\right] + H_{fa}. \tag{5.33}$$

Here, $\delta_{qk} = \omega_q - k\omega_d$ is the detuning of the qubit frequency from its k-th. resonance with the driving signal, $\Omega'_h = -\frac{\varepsilon\Omega_h}{\hbar\omega_q\omega_d}$ the argument of the Bessel function[11], and $\Omega_{k0} = -\frac{k\omega_d\Delta}{\varepsilon}J_k\left(\Omega'_h\right)$ the additional splitting between qubit and driving states induced by the k-th. resonance[12]. In addition the σ_x coupling term to the fundamental mode is rescaled with $\Delta'_k = \Delta J_k\left(\Omega'_h\right)$. The system Hamiltonian reads in the eigenbasis of the uncoupled states

$$H_t = \frac{\hbar\Omega_k}{2}\sigma_z + \frac{g}{\omega_q}\left[a^\dagger + a\right]\left(\frac{\varepsilon\Omega_{k0} + \Delta'_k\delta_{qk}}{\Omega_k}\sigma_x + \frac{\varepsilon\delta_{qk} - \Delta'_k\Omega_{k0}}{\Omega_k}\sigma_z\right) + H_a \tag{5.34}$$

In the following the abbreviations $g_{zk} = g\frac{\varepsilon\delta_{qk} - \Delta'_k\Omega_{k0}}{\hbar\omega_q\Omega_k}$ and $g_{xk} = g\frac{\varepsilon\Omega_{k0} + \Delta'_k\delta_{qk}}{\hbar\omega_q\Omega_k}$ will be used. The above Hamiltonian describes a tunable two-level system with frequency splitting $\Omega_k = \sqrt{\delta_{qk}^2 + \Omega_{k0}^2}$ coupled to the fundamental mode and is equivalent to (4.5) and (5.13). The effect of the different resonances becomes clear when the corresponding splittings and coupling constants are plotted.

In Fig. 5-17 such plots are shown for the first three resonances $k \in \{0,1,2\}$. For $k = 0$ the level splitting between the effective states is not changing when increasing the photon

[11] The minus appears because of the condition for non-fast rotating terms, $l = -k \pm 1$ in the first Bessel function term and $l = -k$ in the second of (5.32), together with the property $J_{-k}(x) = J_k(-x)$ of the Bessel function.

[12] Here, $J_{k+1}(x) + J_{k-1}(x) = 2kJ_k(x)/x$ is used.

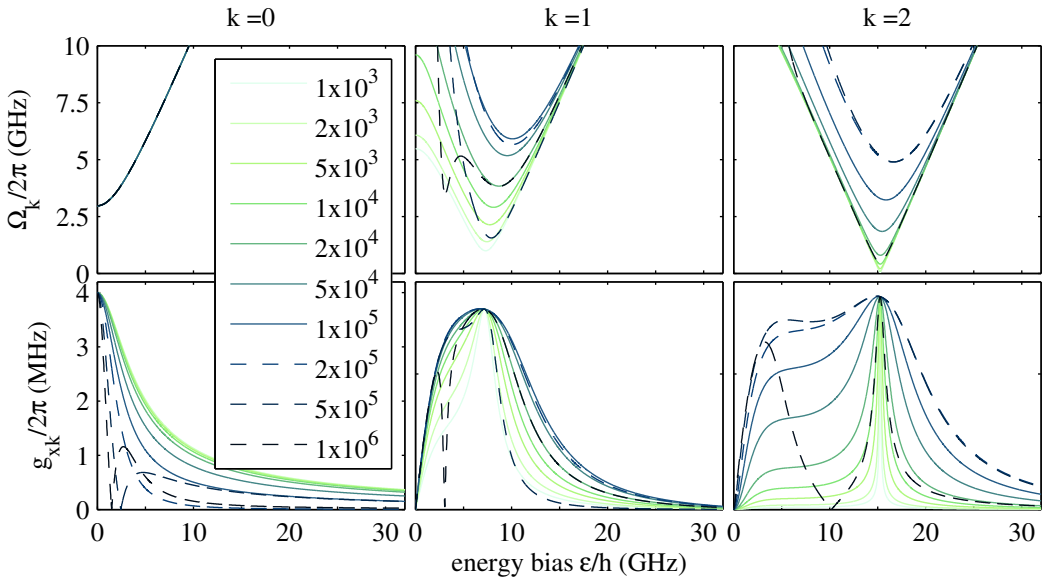

Figure 5-17: Splitting between the effective two levels (upper row) and corresponding off diagonal coupling constant (lower row) in dependence of the energy bias of the qubit for different mean photon numbers $\langle N \rangle$ in the third harmonic and the first three resonances $k \in \{0,1,2\}$. For the plots the parameters of qubit0 sample are used.

number and is identical to the undisturbed qubit levels. This observation is not surprising because $\Omega_{k0} = 0$ follows from the properties of the Bessel function $J_{-n}(z) = (-1)^n J_n(z)$. Although the levels are unchanged, the off diagonal coupling constant indeed depends on the driving signal. For higher values of k, Rabi splittings are observed around an energy bias where $\delta_{qk} = 0$. With higher photon numbers, or in other words stronger driving, these splittings are first increased. The Bessel function behavior then leads to an oscillation of the total splitting, while also the shape around the resonance is modified. The corresponding coupling constants are increased around the k-th resonance.

The incoherent dynamics of the qubit will not be changed by the transformations $\hat{U}_5$ to $\hat{U}_7$, since they either involve only operators of the third harmonic field or σ_z[13]. The rotation of (5.33) into the eigenbasis of the uncoupled systems can also be written down by a unitary transformation with $\hat{U}_8 = e^{i\theta\sigma_y}$ and $\tan 2\theta = \Omega_{k0}/\delta_{qk}$. This procedure is analog to the rotation of the basis as shown in 5.2 and can be understood from writing $e^{i\theta\sigma_y} = \cos\theta + i\sigma_y \sin\theta$, where $\sigma_y^{2n} = 1$ and $\sigma_y^{2n+1} = \sigma_y$ are used for integer n. The calculation of the dissipative rates

[13]The latter yields a multiplication with oscillating terms that have positive frequency for σ_+ and negative for σ_- (see C.1). Since these operators contribute equally to the relaxation and decoherence, the additional terms are canceled.

for the new basis in a matrix calculation approach is demonstrated in App. C.4 and gives in the form the exact same result as found by the evaluation of the change of the elements of the dressed density matrix as shown in App. C.3. The found relaxation, excitation, dephasing, and decoherence rates read

$$\begin{aligned}
\Gamma_{\mathrm{r}k} &= \frac{\Gamma_\mathrm{r}}{2}\left(1+\frac{\delta_{\mathrm{q}k}}{\Omega_k}\right)+\left(\Gamma_\varphi-\Gamma_\mathrm{r}\right)\frac{\Omega_{k0}^2}{2\Omega_k^2},\\
\Gamma_{\mathrm{e}k} &= \frac{\Gamma_\mathrm{r}}{2}\left(1-\frac{\delta_{\mathrm{q}k}}{\Omega_k}\right)+\left(\Gamma_\varphi-\Gamma_r\right)\frac{\Omega_{k0}^2}{2\Omega_k^2},\\
\gamma_{\varphi k} &= \Gamma_\varphi-\frac{\Gamma_\mathrm{r}}{2}-\left(\Gamma_\varphi-\Gamma_\mathrm{r}\right)\frac{\Omega_{k0}^2}{\Omega_k^2},\\
\Gamma_{\varphi k} &= \Gamma_\varphi-\left(\Gamma_\varphi-\Gamma_\mathrm{r}\right)\frac{\Omega_{k0}^2}{2\Omega_k^2},
\end{aligned} \tag{5.35}$$

respectively. The effective excitation and decoherence rates are plotted in Fig. 5-18 for $k\in\{0,1,2\}$. For $k=0$ no excitation is found and the relaxation and decoherence rates coincide with the ones of the undisturbed qubit. In contrast, for $k>0$ a maximum of relaxation and excitation is found around the resonances $\omega_\mathrm{q}=k\omega_\mathrm{d}$. There, these rates are mainly dominated by the term proportional to $\Omega_{k0}^2/2\Omega_k^2$. Furthermore, $\delta_{\mathrm{q}k}$ is small, thus both excitation and relaxation take the same values creating an equal population of higher and lower energetic state. Away from the resonance and especially for small photon numbers in the third harmonic, the relaxation and excitation depend on the sign of $\delta_{\mathrm{q}k}$, and they are of the order of the undisturbed resonator relaxation. This result is best visible in the plot for $k=2$. The decoherence around the resonance is reduced to approximately half of its undisturbed value. That corresponds to an increase in the coherence time when considering Rabi levels, compared to the undisturbed qubit levels. With higher photon numbers this effect can be extended to a wider range in the energy bias and is eventually canceled by the Bessel function behavior.

It is useful to consider the σ_z coupling term as well. Therefore, a small rotation described by the unitary transformation $\hat{U}_9=\mathrm{e}^{g_{zk}/\omega_0\left(a^\dagger-a\right)\sigma_z}$ is considered, where $g_{zk}\sqrt{N_0}/\omega_0$ is assumed small and N_0 corresponds to the mean photon number in the fundamental resonator mode. When expanding only to the first order it transforms the diagonal coupling into a two-photon off-diagonal coupling. The calculation is demonstrated in App. C.5 and yields

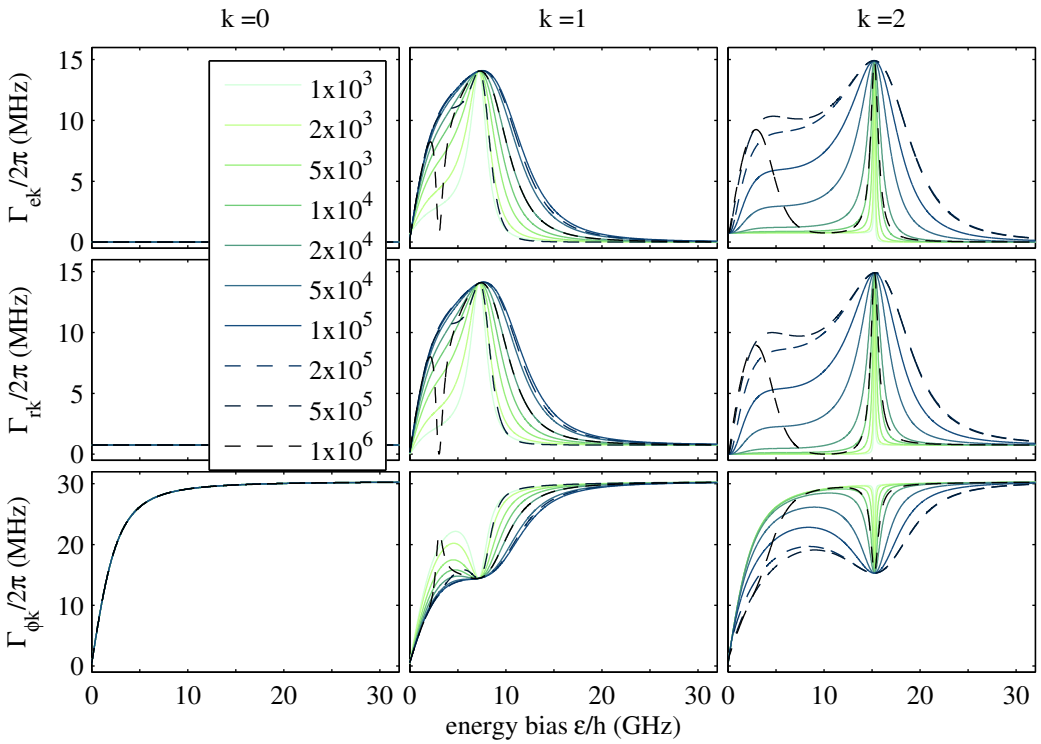

Figure 5-18: Excitation (upper row), relaxation (middle row), and decoherence (lower row) rate between the effective two levels in dependence of the energy bias of the qubit for different mean photon numbers $\langle N \rangle$ in the third harmonic and the first three resonances $k \in \{0,1,2\}$. For the plots the parameters of qubit0 sample are used.

an approximate Hamiltonian

$$\begin{aligned}\widetilde{H}_{\mathrm{t}} =& \frac{\hbar\Omega_k}{2}\sigma_z + \hbar\omega_0 a^\dagger a + \Omega_{\mathrm{p}}\left(a^\dagger \mathrm{e}^{-\mathrm{i}\omega_{\mathrm{p}}t} + a\mathrm{e}^{\mathrm{i}\omega_{\mathrm{p}}t}\right) \\ &+ \hbar g_{\mathrm{x}k}\left[a^\dagger + a\right]\sigma_x + 2i\hbar\frac{g_{\mathrm{x}k}g_{\mathrm{z}k}}{\omega_0}\sigma_{\mathrm{y}}\left(a^\dagger a^\dagger - aa\right),\end{aligned} \tag{5.36}$$

where small terms of the order of $g_i g_j/\omega_0, [i,j] \in [x,z]$, that are not multiplied by photon field operators and higher orders in g_i are neglected. Note, the above rotation will not influence the relaxation rates of the effective two-level system, see (5.35).

The calculation of the transmission of the system is again done in a rotating frame with the probe frequency ω_{p} around $a^\dagger a$ and $m \times \sigma_z$, with m an integer number.(5.34)[14] The Hamiltonian than reads for $m = 1$ in RWA

$$\tilde{H}_{\mathrm{t}} = \hbar\delta_{\mathrm{rp}} a^\dagger a + \frac{\hbar\delta_{\mathrm{kp1}}}{2}\sigma_z + g_{\mathrm{x}k}\left[a\sigma_+ + a^\dagger\sigma_-\right] + \hbar\Omega_{\mathrm{p}}\left[a^\dagger + a\right], \tag{5.37}$$

[14]The Lindblad term is invariant under this rotation.

where $\delta_{k\mathrm{p}1} = \Omega_k - \omega_\mathrm{p}$. The Hamiltonian (5.37) together with the dissipative rates (5.35) have the same form as the corresponding equations in 5.3. Thus, the calculation of the transmission coefficient is completely analog and the results from 5.3 in the small-photon limit as well as in the semi-classical limit can be applied with replacing the corresponding dressed transition frequency, coupling, and dissipative rates by the one for the multi-photon resonance of interest[15].

The two-photon processes can be analyzed in a frame rotating with double frequency $m = 2$ around σ_z compared to (5.37). The corresponding Hamiltonian then reads

$$\tilde{H}_\mathrm{t} = \hbar\delta_\mathrm{rp} a^\dagger a + \frac{\hbar\delta_{k\mathrm{p}2}}{2}\sigma_z - \frac{2g_{\mathrm{x}k}g_{\mathrm{z}k}}{\omega_0}\left[aa\sigma_+ + a^\dagger a^\dagger \sigma_-\right] + \hbar\Omega_\mathrm{p}\left[a^\dagger + a\right], \tag{5.38}$$

where $\delta_{k\mathrm{p}2} = \Omega_k - 2\omega_\mathrm{p}$. While the Lindblad term is again unchanged, the Maxwell-Bloch equations need to be slightly modified

$$\frac{\mathrm{d}\langle a\rangle}{\mathrm{d}t} = -\mathrm{i}\delta_\mathrm{rp}\langle a\rangle + \mathrm{i}\frac{4g_{\mathrm{x}k}g_{\mathrm{z}k}}{\omega_0}\langle a^\dagger\sigma_-\rangle - \mathrm{i}\Omega_\mathrm{p} - \frac{\kappa}{2}\langle a\rangle \tag{5.39}$$

$$\frac{\mathrm{d}\langle\sigma_-\rangle}{\mathrm{d}t} = -\mathrm{i}\delta_{k\mathrm{p}2}\langle\sigma_-\rangle - \mathrm{i}\frac{2g_{\mathrm{x}k}g_{\mathrm{z}k}}{\omega_0}\langle aa\sigma_z\rangle - \Gamma_{\varphi k}\langle\sigma_-\rangle \tag{5.40}$$

$$\frac{\mathrm{d}\langle\sigma_z\rangle}{\mathrm{d}t} = \mathrm{i}\frac{4g_{\mathrm{x}k}g_{\mathrm{z}k}}{\omega_0}\left(\langle aa\sigma_+\rangle - \langle a^\dagger a^\dagger\sigma_-\rangle\right) - \Gamma_{k1} - \Gamma_{k2}\langle\sigma_z\rangle \tag{5.41}$$

$$\frac{\mathrm{d}\langle a^\dagger a\rangle}{\mathrm{d}t} = -\mathrm{i}\frac{4g_{\mathrm{x}k}g_{\mathrm{z}k}}{\omega_0}\left(\langle aa\sigma_+\rangle - \langle a^\dagger a^\dagger\sigma_-\rangle\right) - \mathrm{i}\Omega_\mathrm{p}\left(\langle a^\dagger\rangle - \langle a\rangle\right) - \kappa\langle a^\dagger a\rangle. \tag{5.42}$$

Here, $\Gamma_{k1} = \Gamma_{\mathrm{r}k} - \Gamma_{\mathrm{e}k}$ and $\Gamma_{k2} = \Gamma_{\mathrm{r}k} + \Gamma_{\mathrm{e}k}$. As seen below, the two-photon process becomes more likely for high photon numbers in the fundamental mode. Thus, only the semi-classical limit will be discussed, and it can be assumed that all expectation values factorize. The steady state solution of (5.39) - (5.42) can be brought into a similar form as in 5.3, e.g. by removing $\langle\sigma_-\rangle$ in (5.39) with (5.40)

$$\langle a\rangle = \frac{-\Omega_\mathrm{p}}{\widetilde{\delta}_\mathrm{rp} + \frac{8g_{\mathrm{x}k}^2 g_{\mathrm{z}k}^2}{\omega_0^2\widetilde{\delta}_{k\mathrm{p}2}}\langle a^\dagger\rangle\langle a\rangle\langle\sigma_z\rangle} \tag{5.43}$$

and removing the coupling terms in (5.41) with (5.42)

$$\langle\sigma_z\rangle = -\frac{\Gamma_{k1}}{\Gamma_{k2}} - \frac{\mathrm{i}\Omega_p}{\Gamma_{k2}}\left(\langle a^\dagger\rangle - \langle a\rangle\right) - \frac{\kappa}{\Gamma_{k2}}\langle a^\dagger a\rangle. \tag{5.44}$$

Note, the latter equations are valid without assuming high photon numbers. The parameters $\tilde{\delta}_\mathrm{rp}$ and $\widetilde{\delta}_{k\mathrm{p}2} = \delta_{k\mathrm{p}2} - i\Gamma_{\varphi k}$ are introduced similar as in 5.3. Comparing (5.24) to (5.43), the

[15] In other words it is necessary to choose an index k to describe the measurement results in a given parameter range.

effective coupling constant for the two-photon process to the fundamental mode is scaled with the corresponding photon number as $g_{2\mathrm{ph}} = 2\sqrt{2}g_{\mathrm{x}k}g_{\mathrm{z}k}\sqrt{N}/\omega_0$. If the probing amplitude is large this photon number may be set to the value as found for the uncoupled system $g_{\mathrm{x}k} = g_{\mathrm{z}k} = 0$ from (5.39) and (5.42)

$$\langle a^\dagger a\rangle_0 = \frac{4\Omega_{\mathrm{p}}^2}{4\delta_{\mathrm{rp}}^2 + \kappa^2}. \tag{5.45}$$

This estimation is valid if the mean photon number is not influenced much by the interaction with the dressed qubit as compared to the influence of the probing amplitude. When considering such a rescaled coupling, the calculation of the transmission coefficient is analog to the case of the one photon resonance. The results of such calculations are summarized in Fig. 5-19.

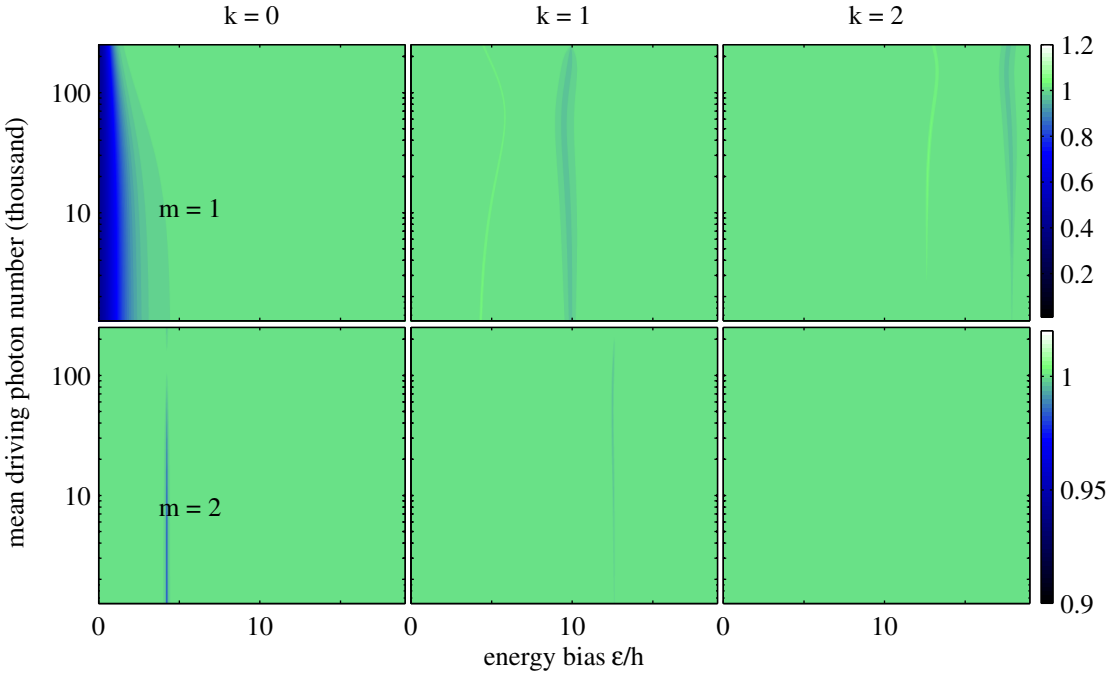

Figure 5-19: Calculated normalized transmission through the driven qubit-resonator system. The one and two-photon interactions with the fundamental mode are plotted in the upper and lower row, respectively. The columns correspond to a multiphoton drive with zero to two photons. The plots are shown for different energy bias and driving amplitude. The latter is given in mean photon number in the resonator and corresponds approximately to the same values as in Fig. 5-16.

There for indexes $k \in [0,1,2]$ and $m \in [1,2]$ the normalized transmission amplitude is plotted for the sample parameters of qubit0 and varying bias and driving power. The probing power

is set to 220 kHz, a value where both the one and two-photon processes are visible. By further increase the equalization of the qubit population is reducing both, the one and two-photon response. On the other hand, the effective coupling constant of the two-photon process is increased. For $k = 0$ the dispersive qubit dip is observed. Its shape is slightly altered by the power dependency of the coupling constant. Because in this case the qubit energy is not changed, also the two-photon resonance gives only a single vertical line at a bias where $2\omega_0 = \omega_q$. In the case of one and two-photon driving, $k = 1,2$ we find characteristic peak-dip structures around the resonances $k\omega_d = \omega_q$ in the one photon interaction $m = 1$. For $k = 1$ this structure is similar to the above discussed interaction with the dressed states. Nevertheless, the Bessel-function behavior keeps the splitting of the effective two levels close to resonance in an interval between 0 and ω_d, since the diagonal coupling term creates avoided-level crossings between the states of different manifolds. This additional interaction leads to a non-monotonic behavior of the on-resonance Rabi frequency. Furthermore, this effect is so strong for the given parameters, that the lines for amplification and damping are not connected together, as predicted in 5.2.

The coupling constants of the fundamental mode to the effective two-level systems takes a maximum close to the resonances $\omega_q = k\omega_d$ and decreases fast with detuning δ_{kp} for $k > 0$. Thus, in the two-photon interaction $m = 2$ only a single sharp damping line is visible in the $k = 1$ picture. At higher orders of dressing the two-photon interaction with the fundamental mode is negligible.

Note, for small driving amplitudes the two-photon damping for $k = 0$ is found approximately at the same bias point as the one photon amplification for $k = 1$. This fact explains the change from amplification to damping when the probing amplitude is increased[16]. Still, the positions of the different interactions only follow from considering a single interaction with index k. To improve the correspondence between measurement and experiment the shifts induced by all resonances with indexes $k = 1,2$ are summed in a hand waving approach to the total effective level splitting for each single index k. The rest of the calculation stays the same.

As demonstrated in Fig. 5-20, this procedure allows the reconstruction of main features of the experiment. Most pronounced the vanishing of the qubit dip is nicely reproduced in the upper left subplot. It occurs from shifting the minimal qubit level splitting below the resonator's fundamental mode frequency. The sharp lines that are then bent for higher probing amplitudes correspond to resonant interactions, where $\omega_k = \omega_0$. The corresponding

[16]Compare Fig. 5-6 and corresponding discussion

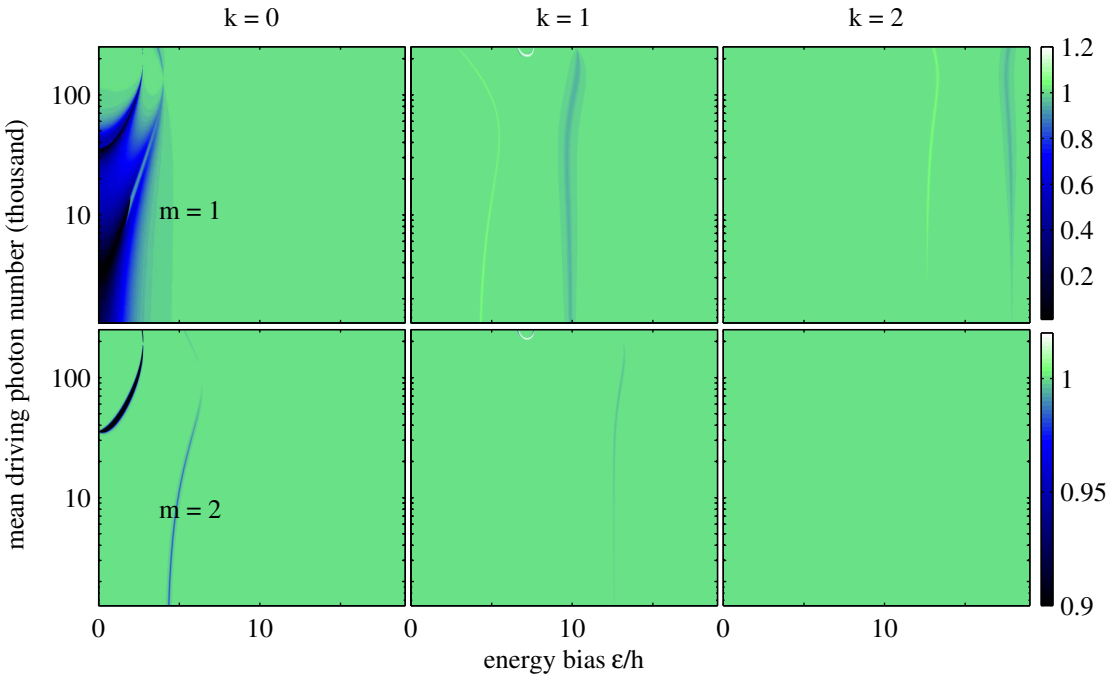

Figure 5-20: Same plot as in Fig. 5-19 but taking in each picture the level shift of all indices k from -2 to 2 into account.

two-photon process follows the same curve as the one photon amplification for $k = 2$ to amplitudes $\langle N \rangle \approx 20\,000$. Thus, in the experiment damping is observed, which for higher driving may be changed to amplification, when the effective coupling constant for $k = 0$ and $m = 2$ becomes smaller. Both is explained well by the theoretical calculated plots.

Nevertheless, when comparing to Fig.5-16 several differences remain. They include the amplification close to the degeneracy point, the closed curves around the first and second resonance $k = 1, 2$[17], the strength of the two-photon response, and in general, the positions of the curves for high photon numbers in the third harmonic. Reason may be manifold. For example, it may be necessary to include higher orders of driving $k > 2$ as well as negative ones[18] or the third qubit level may become important due to the high excitation number in the harmonic of the resonator.

[17] The one close to the first resonance is mainly visible in the phase.

[18] From negative frequency components that give shifts of the effective qubit energy in different direction and include as example the Bloch-Siegert shift(see e.g. [110]).

Summary

A single artificial atom (qubit) is used to achieve lasing characterized by linewidth narrowing and increase in the output power of a superconducting cavity. Compared to classical lasing schemes, for the first time only a single two-level system is needed. For a convenient analysis of this lasing effect, the interaction of a superconducting flux qubit coupled to a coplanar waveguide resonator has been studied experimentally and theoretically in an intermediate coupling regime. Both systems are introduced separately, and a corresponding quantum theory is derived from first principles. The basic mechanism of coupling, via the magnetic field, was used to design appropriate samples and is included into the theoretical approach. These samples have been measured at temperatures close to absolute zero in order to avoid thermal excitation. In addition, the measurement environment has been designed and optimized for these samples, involving sample mounting, thermal anchoring, shielding, signal filtering, and thermalization.

In a first experimental part basic properties of the coupled system are studied. A theoretical analysis and analytical reproduction of the measurement results allowed a full reconstruction of the parameters of the total system. In addition, the dissipative rates of the two subsystems are estimated from the results of weak continues measurements, thus from the measurement of steady state values.

One important result of this thesis is that a microwave signal applied to the qubit may be used for further controllability. This additional knob involves both, the shift of the qubit levels as well as control over their population. The main part of the work focuses on the manipulation of the qubit to achieve an inversion population. It is realized by a strong off-resonant driving of the qubit that enables a controllability of the population of the evolving dressed states by external parameters. The reason is the rescaling of the relaxation rates of the qubit. In other words, the relaxation of the qubit can lead to an excitation in the dressed-state basis. In addition, the calculations show a first order coupling of these Rabi-split states

to the resonator, which is contrary to similar systems made from atoms because their dipole moment does not allow such transitions.

Experimentally amplification and damping both are observed. A theoretical description for the steady state of the transmission coefficient reproduces the measurements qualitatively and quantitatively. In addition, the measurement of the power spectral density emitted from the cavity for the first time demonstrates self-oscillations in the resonator created by the interaction with a dressed qubit. Also, effects from the probing signal or heating are excluded, and the spectral measurements allow a real quantification of this lasing effect. A linewidth narrowing of about 20 % and an increase in the emitted power to a more than doubled value are found. In follow up works, this lasing effect is optimized together with the Bratislava group to a factor of 10 in narrowing and a factor of 9 increase of the emitted power in a two photon process [116].

In a final experiment the driving power is further increased to identify the limits of the dressed-state approach for describing the experimental situation. As a result an extension to a multiphoton-dressed-state approach can improve the understanding of the observed resonances. Nevertheless, some interesting features, as the amplification at the degeneracy point, are not fully reproduced. Note, the general theory can be applied to explain many effects in frame of the pump-probe technique, such as the spectroscopy data or multiphoton interaction for high probing powers.

In follow up studies possible ways to increase the amplification, either by exploring the two-photon process [116] or by identifying optimal parameter combinations [117], are discussed. An additional spectral analysis, especially to observe the fluorescence spectrum of the qubit may give further insights.

The lasing effect discussed in this work has several possible applications. They range from the amplification of test signals to the signal generation on a chip. Furthermore, the use of a strong radiation field to control the population of a two-level system and additionally their splitting gives a valuable tool in studying the basic light-matter interaction.

Acknowledgment

First I like to thank my supervisor Prof. Paul Seidel for his guidance and professional advice, especially in the preparation of this work.

I am deeply grateful to my supervisor at the IPHT, Evgeni Il'ichev, for his persistent great support, for discussing the experimental data or physical problems, and for introducing me to so many great scientists. I always enjoyed the cordial atmosphere in our small group.

I thank the whole department quantum detection at the IPHT-Jena for creating a great working atmosphere. Particularly, I like to mention our group leader Torsten May and department director Hans-Georg Meyer for their support. I express my sincere gratitude to my colleagues from the clean room that prepared the samples and mainly Uwe Hübner and Solveig Anders, who have been my first contacts when a new sample design needed to be fabricated. I like to thank our technical staff and mainly Marion Sondermann and Heike Schneider, who not only helped in the sample mounting. I want to include my colleagues from the workshop, especially Michael Wiedemann. It always was impressive for me to get the parts to my hands that I had drawn on paper. Also I acknowledge the support of Jürgen Kunert in sample design and for planning the supply with liquid helium. The latter has been a great relief during the measurement time and gave me more focus on the experiments. The experiments would not have been possible without the work of Detlef Born and Thomas Wagner to keep the cryostats alive, Thomas also teaching me how to run cryostats of different types.

Special thanks go to my former colleagues and fellow PhD. students Boris Ivanov, Pascal Macha, and Simon van der Ploeg. Your work in and outside the lab pushed and motivated me to achieve good results. I enjoyed our joined work in the lab even during nights, weekends, or holidays.

I thank all of our guests at the IPHT during the time of my PhD because everyone gave me an additional perspective not only to the experimental data, but also to life. I thank Oleg

Astafiev for sharing his scientific knowledge and teaching me the theory to understand and reconstruct experimental results. I acknowledge the support in the theoretical description of the experiments by Sergey Shevchenko and Yakov Greenberg. Special thanks go to Yakov for his great hospitality during my visit in Novosibirsk, for professional scientific discussions, and for proofreading parts of the thesis. I thank Miroslav Grajcar, Pavol Neilinger, and Matus Rehak for many interesting discussions and the great joined work. Miro, I thank you for teaching me to look at things from different perspectives.

Finally, I want to acknowledge the support of my family and friends. I especially like to mention Frank Ohme, Sven Döring, Martin Kielhorn, and Matthias Schmidt for keeping life beside work alive. I am deeply thankful to my mother and my late father for their great support through all my life and to my sisters Jenny and Aniane who are always willing to listen to my problems.

Most grateful I am to my wife Karoline, who probably suffered the most from the long working hours during the many measurement runs, but who always is insightful and patient. Last but for sure not least, I am so happy with and thankful to my son Johann, who, in the short time we have now been together, already ensured me that there are many important things in life beside work.

Appendix

A Notes to the qubit and the resonator

A.1 Kinetic part of the flux qubit Hamiltonian

The second Josephson equation (1.12) connects the voltages at the Josephson junctions to the time derivative of the phase difference $\dot{\varphi}$. Thus, the kinetic energy of the qubit is related to the voltages at the junctions, and its total value is found by the sum of the kinetic energies of each junction

$$E_\mathrm{k} = \frac{1}{2} C_{\mathrm{J}1} V_{\mathrm{J}1}^2 + C_{\mathrm{J}2} V_{\mathrm{J}2}^2 + C_{\mathrm{J}3} V_{\mathrm{J}3}^2.$$

Here, the voltages $V_{\mathrm{J}i}$ and capacitances $C_{\mathrm{J}i}$ at the different junctions in the qubit loop are used. The junctions 1 and 2 have the same capacitance, whereas at the small junction it will be reduced by the factor α. With the second Josephson equation (1.12) the voltages can be substituted with the phase differences as

$$E_\mathrm{k} = \frac{\Phi_0^2}{8\pi^2} C_\mathrm{J} \left({\dot{\varphi}_1}^2 + {\dot{\varphi}_2}^2 + \alpha {\dot{\varphi}_3}^2 \right).$$

Removing the phase difference at the small junction using the flux quantization yields

$$E_\mathrm{k} = \frac{\Phi_0^2}{8\pi^2} C_\mathrm{J} \left({\dot{\varphi}_1}^2 + {\dot{\varphi}_2}^2 + \alpha \left[\dot{\varphi}_1 - \dot{\varphi}_2 \right]^2 \right) = \frac{\Phi_0^2}{8\pi^2} C_\mathrm{J} \dot{\vec{\varphi}}^\mathrm{T} \begin{pmatrix} 1+\alpha & -\alpha \\ -\alpha & 1+\alpha \end{pmatrix} \dot{\vec{\varphi}}. \tag{A.1}$$

Possible time dependent magnetic fields are neglected ($\dot{f} = 0$) and a vector notation ($\dot{\vec{\varphi}}^\mathrm{T} = (\dot{\varphi}_1 \dot{\varphi}_2)$) is used to give compact equations. The latter allows a straightforward extension to a loop with even more junctions. The superscript T denotes the transpose of a vector. In a next step, a differentiation of the Lagrangian will give the generalized momenta. Please note,

the potential (2.8) does not explicitly depend on the time derivatives of the phase difference. Thus, the momenta are

$$p_i = \frac{\partial E_\mathrm{k}}{\partial \dot{\varphi}_i}$$
$$\vec{p} = \frac{\Phi_0^2}{4\pi^2} C_\mathrm{J} \begin{pmatrix} 1+\alpha & -\alpha \\ -\alpha & 1+\alpha \end{pmatrix} \dot{\vec{\varphi}}. \tag{A.2}$$

When rewriting these equations, the time differentiated phase differences are expressed with the generalized momenta

$$\dot{\vec{\varphi}} = \frac{4\pi^2}{C_\mathrm{J}\Phi_0^2} \Xi \vec{p},$$

where

$$\Xi = \frac{1}{1+2\alpha} \begin{pmatrix} 1+\alpha & \alpha \\ \alpha & 1+\alpha \end{pmatrix}$$

is the inverse of the transformation matrix in (A.2). The Hamilton function is defined as

$$\begin{aligned} H &= \vec{p}^\mathrm{T}\dot{\vec{\varphi}} - L(\varphi_1, \varphi_2, \dot{\varphi}_1, \dot{\varphi}_2) = \frac{4\pi^2}{C_\mathrm{J}\Phi_0^2}\vec{p}^\mathrm{T}\Xi\vec{p} - \frac{1}{2}\dot{\vec{\varphi}}^\mathrm{T}\vec{p} + U(\varphi_1, \varphi_2) \\ &= \frac{4\pi^2}{C_\mathrm{J}\Phi_0^2}\vec{p}^\mathrm{T}\Xi\vec{p} - \frac{1}{2}\frac{4\pi^2}{C_\mathrm{J}\Phi_0^2}\vec{p}^T\Xi\vec{p} + U(\varphi_1, \varphi_2) \\ &= \frac{2\pi^2}{C\Phi_0^2}\vec{p}^T\Xi\vec{p} + U(\varphi_1, \varphi_2) \end{aligned} \tag{A.3}$$

Finally, by expanding the first term the final Hamiltonian reads

$$H = \frac{E_\mathrm{C}}{\hbar^2}\frac{1}{2\alpha+1}\left([1+\alpha][p_1^2+p_2^2] + 2\alpha p_1 p_2\right) + U(\varphi_1, \varphi_2) \tag{A.4}$$

A.2 Diagonalizing the Hamiltonian

To find the eigenenergies numerically, it is necessary to understand, how the operators in the Hamiltonian act on the states. Below the charge basis will be used. Their basic states correspond to the charge on the islands between the junctions in units of cooper pairs, as will be seen later. At the moment, the description is possible in the general coordinate x and momentum p notation. Here the momentum states are chosen. The momentum and the

coordinate are connected by the Fourier transform, so writing an arbitrary momentum state as Fourier series is possible

$$\langle p|f\rangle = f(p) = \frac{1}{\sqrt{2\pi\hbar}} \int f(x) \mathrm{e}^{\frac{-\mathrm{i}px}{\hbar}} \mathrm{d}x.$$

Here, the $\hbar$ yields from using momentum instead of wave vector $\vec{k}$. On the other hand, inserting the closure relation $\int |x\rangle\langle x| \mathrm{d}x$ on the left hand side gives

$$\langle p|f\rangle = \int \langle p|x\rangle\langle x|f\rangle \mathrm{d}x = \int \langle p|x\rangle f(x) \mathrm{d}x.$$

As conclusion

$$\langle p|x\rangle = \frac{1}{\sqrt{2\pi\hbar}} \mathrm{e}^{\frac{-\mathrm{i}px}{\hbar}}$$

and it is possible to represent the momentum in the coordinate basis

$$|p\rangle = \int |x\rangle\langle x|p\rangle dx = \frac{1}{\sqrt{2\pi\hbar}} \int \mathrm{e}^{\frac{\mathrm{i}px}{\hbar}} |x\rangle dx. \tag{A.5}$$

In the Hamiltonian only terms which are directly the momentum operator together with cosine functions of the phase difference occur. Their influence on the momentum states is

$$\begin{aligned} \hat{p}|p\rangle &= p|p\rangle \\ \cos\hat{x}|p\rangle &= \int \frac{1}{2} \left(\mathrm{e}^{\mathrm{i}x} + \mathrm{e}^{-\mathrm{i}x}\right) \mathrm{e}^{\frac{\mathrm{i}px}{\hbar}} dx \\ &= \frac{1}{2} \left(|p+\hbar\rangle + |p-\hbar\rangle\right). \end{aligned} \tag{A.6}$$

This behavior is illustrative in the discrete charge basis. The momentum states give the number of cooper pairs on an island N_i. On the other hand, the cosine operators of the phase can change the number of Cooper pairs by one. The latter can be identified with tunneling of cooper pairs through and, thus, the current over the junction. The complete, discrete Hamiltonian for integration to a numerical calculation reads

$$\begin{aligned} H = &\left[E_\mathrm{C} \frac{(1+\alpha)N_1^2 + 2\alpha N_1 N_2 + (1+\alpha)N_2^2}{1+2\alpha} + E_\mathrm{J}(2+\alpha)\right] |N_1,N_2\rangle\langle N_1,N_2| \\ &- \frac{E_\mathrm{J}}{2} \Big[|N_1+1,N_2\rangle\langle N_1,N_2| + |N_1-1,N_2\rangle\langle N_1,N_2| + |N_1,N_2+1\rangle\langle N_1,N_2| \cdot \\ &+ |N_1,N_2-1\rangle\langle N_1,N_2| + \alpha \mathrm{e}^{\mathrm{i}2\pi f} |N_1+1,N_2-1\rangle\langle N_1,N_2| \\ &+ \alpha \mathrm{e}^{-\mathrm{i}2\pi f} |N_1-1,N_2+1\rangle\langle N_1,N_2| \Big], \end{aligned} \tag{A.7}$$

where (1.17) is used and $|N_1,N_2\rangle$ are the possible charge states. By the numerical definition of a set of basis states, the Hamiltonian above can be expressed in matrix form. Then a numerical diagonalization yields the eigenenergies.

A.3 Classical results of the resonator

It is useful to compare the results of the quantum calculation on a CPW-resonator with the classical calculations on a lumped element representation, since several results, as for example the frequency dependence of the transmission, should be equivalent.

As explained in the main text, the lumped element resonator has an inductance L and capacitance C. Here, the dependency of the inductance on the mode number n is neglected, and the calculations are restricted to the fundamental mode. The internal losses are introduced by a resistance R and the coupling to the environment can be treated via two coupling capacitances C_c together with the loads R_L (compare Fig. -1 a) The dynamic of the voltage $V(t)$

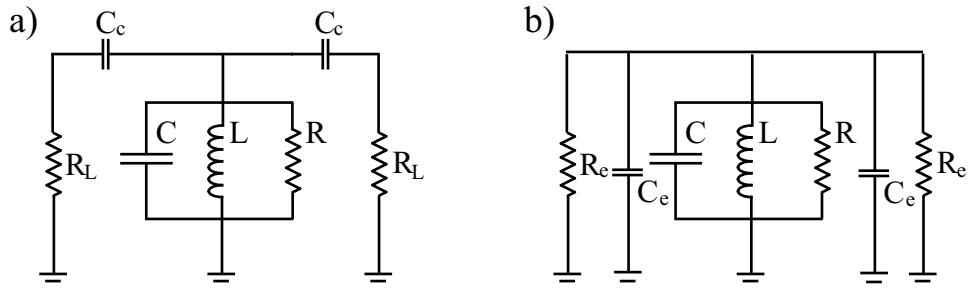

Figure -1: a) Lumped element representation of a CPW resonator including the internal losses given by R and the coupling to the loads R_L by the coupling capacitances C_c. b) The series circuit of C_c and R_L can be transformed to a parallel one with values C_e and R_e.

at the resonator is described by the differential equation

$$V + \frac{cl}{k_0^2}\frac{\partial^2 V}{\partial t^2} + \frac{l}{k_0^2 r}\frac{\partial V}{\partial t} = LC\frac{\partial^2 V}{\partial t^2} + \frac{L}{R}\frac{\partial V}{\partial t} + V = 0, \tag{A.8}$$

where the definitions of k_0, C, and L are used and $R = 2r/S$. It is found from the wave equation (2.30) when inserting the mode expansion for the voltage, which in turn follows from the one for the flux (2.35). The dependence on the coordinate is thereby removed.

A driving force at a probing frequency ω_p can be added, which is applied by an oscillating voltage at the coupling capacitor C_c (at positions $x = -S/2$ or $\tilde{x} = 0$).

$$\frac{\partial^2 V}{\partial t^2} + \kappa\frac{\partial V}{\partial t} + \omega_0^2 V = \omega_0^2 V_\mathrm{in}\cos\omega_\mathrm{p} t. \tag{A.9}$$

Here, $\omega_0 = 1/\sqrt{LC}$ is the loss free resonance frequency and $\kappa = 1/CR$ describes the damping rate. Note, the driving voltage is, in principle, applied at the external lead R_L. Then

it is necessary to find the voltage V_{in} in the resonator from the relation of the different impedances. For details see 2.9 and especially (2.68). The oscillations in the resonator follow the frequency of the external drive. Therefore, one solution of the above equation is $V = \tilde{V}\cos(\omega t + \phi)$. Inserting together with a short calculation yield the amplitude $\tilde{V}$ and the phase shift ϕ of this driven oscillations

$$\tilde{V} = V_{\mathrm{in}} \frac{\omega_0^2}{\sqrt{\left(\omega_0^2 - \omega_{\mathrm{p}}^2\right)^2 + \left(\kappa\omega_{\mathrm{p}}\right)^2}},\ \phi = \arctan\left(\frac{\kappa\omega_0}{\omega_{\mathrm{p}}^2 - \omega_0^2}\right). \tag{A.10}$$

These may be rewritten close to the resonance by applying $\omega_0^2 - \omega_{\mathrm{p}}^2 = \left(\omega_0 + \omega_{\mathrm{p}}\right)\left(\omega_0 - \omega_{\mathrm{p}}\right) \approx 2\omega_0\left(\omega_0 - \omega_{\mathrm{p}}\right)$ to find

$$\tilde{V} = V_{\mathrm{in}} \frac{\omega_0}{\sqrt{4\left(\omega_0 - \omega_{\mathrm{p}}\right)^2 + \kappa^2}},\ \phi = \arctan\left(\frac{\kappa}{2\left(\omega_{\mathrm{p}} - \omega_0\right)}\right). \tag{A.11}$$

The normalized result above is in correspondence with the absolute value of the quantum solution (4.29) if the coupling to the qubit is neglected. When these functions are plotted versus the frequency, they show a resonance peak for the voltage $\tilde{V}$ and a phase shift from $-\pi/2$ to $\pi/2$ around the resonance frequency. The width of the curve where the amplitude is reduced to $1/\sqrt{2}$ of its maximum value is κ. Note that the power, as $\propto V^2$, gives a Lorentzian line shape with kappa being the FWHM (full width at half maximum).

After a transformation of the series circuit of C_{c} and R_{L} to a parallel circuit with values R_{e} and C_{e} one can directly identify their influence to the resonance frequency and the quality (compare Fig. -1 b)).

$$\frac{1}{\mathrm{i}\omega C_{\mathrm{c}}} + R_{\mathrm{L}} = \left(\mathrm{i}\omega C_{\mathrm{e}} + \frac{1}{R_{\mathrm{e}}}\right)^{-1} = \frac{R_{\mathrm{e}}}{\mathrm{i}\omega C_{\mathrm{e}} R_{\mathrm{e}} + 1}. \tag{A.12}$$

Real and imaginary part give two equations for defining the unknown parameters R_{e} and C_{e}. A short calculation yields

$$R_e = \frac{\omega^2 {C_{\mathrm{c}}}^2 {R_{\mathrm{L}}}^2 + 1}{\omega^2 {C_{\mathrm{c}}}^2 R_{\mathrm{L}}},\quad C_e = \frac{C_{\mathrm{c}}}{\omega^2 {C_{\mathrm{c}}}^2 {R_{\mathrm{L}}}^2 + 1}. \tag{A.13}$$

The total relaxation rate of the cavity is finally found as

$$\kappa = \frac{2}{\left(2C_{\mathrm{e}} + C\right)\left(2R_{\mathrm{e}}^{-1} + R^{-1}\right)} \approx \frac{2\omega^2 C_{\mathrm{c}}^2 R_{\mathrm{L}}}{C}. \tag{A.14}$$

Here, the factors of two are introduced to account for coupling to the leads on both sides of the resonator. Also C_{c} is neglected compared C as well as R^{-1} versus R_{e}^{-1}, and $\omega^2 {C_{\mathrm{c}}}^2 {R_{\mathrm{L}}}^2 \ll$

1 is used. Note, the value for κ calculated for the parameters of the resonators are about one order of magnitude smaller than the measured ones. Thus, the internal losses are dominating in the experiment. Nevertheless, calculation results using this experimental value give results that correspond to normalized measurement data.

B Time evolution of the density matrix by damping

B.1 Qubit dissipation

Time evolution of the qubits density matrix is given by (2.23), where the coupling to the environment is given by the interaction energy $\mathscr{V}(t)$. If written down explicitly the latter reads

$$\mathscr{V}(t) = \frac{\hbar}{2}\left(X_+\sigma_+ \mathrm{e}^{\mathrm{i}\omega_q t} + X_-\sigma_- e^{-\mathrm{i}\omega_\mathrm{q} t} + X_z\sigma_z\right). \tag{B.15}$$

The noise variables are defined in the same way as the raising and lowering operators (2.3) $X_+ = X_x + \mathrm{i}X_y$ and $X_- = X_x - \mathrm{i}X_y$, where $X_\perp\sigma_\perp = X_x\sigma_x + \mathrm{i}X_y\sigma_y$ is assumed. The time evolution reads

$$\begin{aligned}
\dot{\rho}_\mathrm{S} = &-\frac{\mathrm{i}}{2}\langle X_+(t)\rangle \mathrm{e}^{\mathrm{i}\omega_\mathrm{q} t}\left(\sigma_+\rho_\mathrm{S} - \rho_\mathrm{S}\sigma_+\right) - \frac{\mathrm{i}}{2}\langle X_z(t)\rangle\sigma_z\rho_\mathrm{S} \\
&-\frac{1}{4}\int_{t_i}^{t}\left[\langle X_+(t)X_+(t')\rangle \mathrm{e}^{\mathrm{i}\omega_\mathrm{q}(t+t')}\sigma_+\rho_\mathrm{S}\sigma_+ + \langle X_-(t)X_-(t')\rangle \mathrm{e}^{-\mathrm{i}\omega_\mathrm{q}(t+t')}\sigma_-\rho_\mathrm{S}\sigma_-\right]\mathrm{d}t' \\
&-\frac{1}{4}\int_{t_i}^{t}\langle X_z(t)X_z(t')\rangle \mathrm{d}t'\left(\sigma_z\rho_\mathrm{S}\sigma_z - \rho_\mathrm{S}\right) \\
&-\frac{1}{4}\int_{t_i}^{t}\langle X_+(t)X_-(t')\rangle \mathrm{e}^{\mathrm{i}\omega_\mathrm{q}(t-t')}\left(\sigma_+\sigma_-\rho_\mathrm{S} - \sigma_+\rho_\mathrm{S}\sigma_-\right)\mathrm{d}t' \\
&-\frac{1}{4}\int_{t_i}^{t}\langle X_-(t)X_+(t')\rangle \mathrm{e}^{-i\omega_\mathrm{q}(t-t')}\left(\sigma_-\sigma_+\rho_\mathrm{S} - \sigma_-\rho_\mathrm{S}\sigma_+\right)\mathrm{d}t' + \mathrm{h.c.}
\end{aligned} \tag{B.16}$$

Here, h.c. stands for hermitian conjugate and $\sigma_\pm^2 = 0$, $\sigma_z^2 = 1$ are used. Also each field noise component is assumed uncorrelated with the other two[19], so that $\langle X_z(t)X_\pm(t')\rangle = \langle X_\pm(t)X_z(t')\rangle = 0$ is used. The first three terms in the equation above can be set to zero

[19] As X_x and X_z are constructed from the same field noise components one may expect correlations. Still, a careful analysis shows, that they will sum to zero, since $\langle X_z(t)X_x(t')\rangle \propto \Delta\varepsilon\left(\langle\delta\vec{H}_{\mathrm{e,z}}\delta\vec{H}_{\mathrm{e,z}}\rangle - \langle\delta\vec{H}_{\mathrm{e,x}}\delta\vec{H}_{\mathrm{e,x}}\rangle\right)$ and the correlations of the noise are assumed identical in different directions.

because the expectation value of the noise field and also of any of its components is assumed zero. The noise correlation terms in the second line of (B.16) can be rewritten by using the definitions of $X_\pm$ as

$$\int \langle X_\pm(t)X_\pm(t')\rangle \mathrm{e}^{\pm \mathrm{i}\omega_\mathrm{q}(t+t')}\mathrm{d}t' \\ = \int \langle X_x(t)X_x(t')\rangle \mathrm{e}^{\pm \mathrm{i}\omega_q(t+t')}\mathrm{d}t' - \int \langle X_y(t)X_y(t')\rangle \mathrm{e}^{\pm \mathrm{i}\omega_\mathrm{q}(t+t')}\mathrm{d}t' = 0,$$

where again the different components are assumed uncorrelated[20]. In addition, the correlation of the noise spectrum for different components is supposed identical. This assumption means that the noise has no preferential direction. A coordinate transformation $\tilde{t} = t' - t$ in the integrals of the remaining terms in (B.16) yields

$$\begin{aligned}\dot{\rho}_\mathrm{S} = &-\frac{1}{4}\int_{t_i-t}^{0} \langle X_z(t)X_z(t+\tilde{t})\rangle \,\mathrm{d}\tilde{t}\,(\sigma_z\rho_S\sigma_z - \rho_S) \\ &-\frac{1}{4}\int_{t_i-t}^{0} \langle X_+(t)X_-(t+\tilde{t})\rangle \mathrm{e}^{-\mathrm{i}\omega_\mathrm{q}\tilde{t}}\,\mathrm{d}\tilde{t}\,(\sigma_+\sigma_-\rho_\mathrm{S} - \sigma_+\rho_\mathrm{S}\sigma_-) \\ &-\frac{1}{4}\int_{t_i-t}^{0} \langle X_-(t)X_+(t+\tilde{t})\mathrm{e}^{\mathrm{i}\omega_\mathrm{q}\tilde{t}}\,\mathrm{d}\tilde{t}\,(\sigma_-\sigma_+\rho_\mathrm{S} - \sigma_-\rho_\mathrm{S}\sigma_+) + \mathrm{h.c.}.\end{aligned} \tag{B.17}$$

Note that the correlation of the noise enters from the time the correlation starts t_i to the time of interest t. For the qubit one can safely put $t_i \to -\infty$. Then, using $\langle X_\pm(t)X_\mp(t')\rangle = \langle X_x(t)X_x(t')\rangle + \langle X_y(t)X_y(t')\rangle$, where the mixing terms again are neglected because of uncorrelated noise components, and the definitions of the damping rates (2.22) yields

$$\dot{\rho_\mathrm{S}} = \frac{\Gamma_\mathrm{R}}{2}(\sigma_+\rho_\mathrm{S}\sigma_- - \sigma_+\sigma_-\rho_\mathrm{S}) + \frac{\Gamma_\mathrm{E}}{2}(\sigma_-\rho_\mathrm{S}\sigma_+ - \sigma_-\sigma_+\rho_\mathrm{S}) - \frac{\gamma_\varphi}{4}(\sigma_z\rho_\mathrm{S}\sigma_z - \rho_\mathrm{S}) + \mathrm{h.c.} \tag{B.18}$$

Note, the decoherence is caused by noise at low frequencies $\omega \approx 0$. Thus, one can imagine an included factor of $\mathrm{e}^{-\mathrm{i}\omega\tau} \approx 1$ in the corresponding time integrals in (B.17).

B.2 Resonator photon decay

Compared to the corresponding Hamiltonian of the qubit 2.24, Hamiltonian 2.62, describing the coupling of the resonator field a to the environment, has a rather clear interpretation: The photons can enter or leave the cavity via the coupling capacitances. Whenever a photon is annihilated in the cavity a corresponding one is created in the external lines. To analyze the effect of this damping on the cavity, it is necessary to trace over the external degrees of

[20] In other words mixing terms as $\langle X_\pm(t)X_\mp(t')\rangle$ are zero.

freedom. To simplify the calculation below, only the field in the transmission line on the left is considered (in (2.62)), since the same calculation is necessary for the right side, except a minus sign. The time evolution of the resonators density matrix ρ_r is then given by

$$\begin{aligned}\dot{\rho}_\mathrm{r} =& -\mathrm{i}\sum_k g_k\langle b_k\rangle e^{-i(\omega-\omega_k)t}\left(a^\dagger\rho_\mathrm{r}(t)-\rho_\mathrm{r}(t)a^\dagger\right)-i\sum_k g_k\langle b_k^\dagger\rangle \mathrm{e}^{-\mathrm{i}(\omega-\omega_k)t}(a\rho_\mathrm{r}(t)-\rho_\mathrm{r}(t)a)\\
&-\sum_{k,l} g_k g_l\int_{t_1}^{t}\Big[\langle b_k b_l\rangle \mathrm{e}^{-\mathrm{i}(\omega t+\omega t'-\omega_k t-\omega_l t')}\left(a^\dagger a^\dagger\rho_\mathrm{r}(t')-2a^\dagger\rho_\mathrm{r}(t')a^\dagger+\rho_\mathrm{r}(t')a^\dagger a^\dagger\right)\\
&-\langle b_k^\dagger b_l^\dagger\rangle \mathrm{e}^{\mathrm{i}(\omega t+\omega t'-\omega_k t-\omega_l t')}\left(aa\rho_\mathrm{r}(t')-2a\rho_\mathrm{r}(t')a+\rho_\mathrm{r}(t')aa\right)+\mathrm{e}^{-\mathrm{i}(\omega t+\omega t'-\omega_k t-\omega_l t')}\\
&\times\left(a^\dagger a\rho_\mathrm{r}(t')\langle b_k b_l^\dagger\rangle-a^\dagger\rho_\mathrm{r}(t')a\langle b_l^\dagger b_k\rangle-a\rho_\mathrm{r}(t')a^\dagger\langle b_k b_l^\dagger\rangle+\rho_\mathrm{r}(t')aa^\dagger\langle b_l^\dagger b_k\rangle\right)\\
&+\left(aa^\dagger\rho_\mathrm{r}(t')\langle b_k^\dagger b_l\rangle-a\rho_\mathrm{r}(t')a^\dagger\langle b_l b_k^\dagger\rangle-a^\dagger\rho_\mathrm{r}(t')a\langle b_k^\dagger b_l\rangle+\rho_\mathrm{r}(t')a^\dagger a\langle b_l b_k^\dagger\rangle\right)\\
&\times\mathrm{e}^{\mathrm{i}(\omega t+\omega t'-\omega_k t-\omega_l t')}\Big]\,\mathrm{d}t'.\end{aligned} \tag{B.19}$$

The writing is shorted by substituting $b_{k,\mathrm{L}}$ and $b_{k,\mathrm{L}}^\dagger$ with b_k and $b_k^\dagger$, respectively. The transmission lines on both sides of the resonator are assumed in thermal equilibrium. Thus, the distribution function is given by a canonical ensemble [118] and the density matrix of the resonator's environment ρ_R follows as

$$\rho_\mathrm{R}=\frac{\mathrm{e}^{-\beta H}}{\mathrm{Tr}(\mathrm{e}^{-\beta H})}=\prod_k\frac{1}{\mathrm{Tr}(\mathrm{e}^{-\beta\hbar\omega_k b_k^\dagger b_k})}\mathrm{e}^{-\beta\hbar\omega_k b_k^\dagger b_k}, \tag{B.20}$$

where $\beta=1/k_\mathrm{B}T$ and the Hamilton operator H in the outside transmission line is inserted. Considering only a single mode, the trace in the equation above is found by the expansion of the operator in the number state basis

$$\begin{aligned}\mathrm{Tr}(\mathrm{e}^{-\beta\hbar\omega_k b_k^\dagger b_k})&=\mathrm{Tr}\left(\mathrm{e}^{-\beta\hbar\omega_k N_k}|N_k\rangle\langle N_k|\right)=\sum_{N_k=0}^{\infty}\mathrm{e}^{-\beta\hbar\omega_k N_k}\\
&=\frac{\mathrm{e}^{\beta\hbar\omega_k}}{\mathrm{e}^{\beta\hbar\omega_k}-1}=\frac{1}{1-\mathrm{e}^{-\beta\hbar\omega_k}}.\end{aligned}$$

In the same way, the photon number expectation is calculated by first taking the following trace

$$\mathrm{Tr}(b_k^\dagger b_k\mathrm{e}^{-\beta\hbar\omega_k b_k^\dagger b_k})=\sum_{N_k=0}^{\infty}N_k\mathrm{e}^{-\beta\hbar\omega_k N_k}=\frac{\mathrm{e}^{\beta\hbar\omega_k}}{\left(\mathrm{e}^{\beta\hbar\omega_k}-1\right)^2},$$

and then dividing the last two equations. This step yields the Bose-Einstein statistics for the thermal population of the k-th. mode

$$\langle N_k\rangle=\mathrm{Tr}\left(b_k^\dagger b_k\rho_\mathrm{R}\right)=\frac{1}{\mathrm{e}^{\beta\hbar\omega_k}-1}. \tag{B.21}$$

To proceed, the total density matrix of the thermal state is given as

$$\rho_{\mathrm{R}} = \prod_k \left(1 - \mathrm{e}^{-\beta\hbar\omega_k}\right) \mathrm{e}^{-\beta\hbar\omega_k b_k^\dagger b_k}. \tag{B.22}$$

With the above considerations the density matrix only has elements on the main diagonal. Thus, the different expectation values in (B.19) are non-zero only if they include the same number of creation and annihilation operators

$$\begin{aligned} &\langle b_k \rangle = \langle b_k^\dagger \rangle = \langle b_l b_k \rangle = \langle b_l^\dagger b_k^\dagger \rangle = 0 \\ &\langle b_l^\dagger b_k \rangle = \delta_{lk} N_k \\ &\langle b_l b_k^\dagger \rangle = \delta_{lk}(N_k + 1) \end{aligned} \tag{B.23}$$

With these relations (B.19) simplifies to

$$\begin{aligned} \dot{\rho}_{\mathrm{r}} = -\int_{t_1}^{t} \sum_k g_k^2 \Big[\Big(\Big[a^\dagger a \rho_{\mathrm{r}}(t') - a \rho_{\mathrm{r}}(t') a^\dagger \Big] (N_k + 1) + \Big[\rho_{\mathrm{r}}(t') a a^\dagger - a^\dagger \rho_{\mathrm{r}}(t') a \Big] N_k \Big) \mathrm{e}^{-\mathrm{i}(\omega - \omega_k)(t - t')} \\ + \Big(\Big[a a^\dagger \rho_{\mathrm{r}}(t') - a^\dagger \rho_{\mathrm{r}}(t') a \Big] N_k + \Big[\rho_{\mathrm{r}}(t') a^\dagger a - a \rho_{\mathrm{r}}(t') a^\dagger \Big] (N_k + 1) \Big) \mathrm{e}^{\mathrm{i}(\omega - \omega_k)(t - t')} \Big] \mathrm{d}t'. \end{aligned} \tag{B.24}$$

The sum in the equation above may be replaced with an integral by $\sum_k \to S_{\mathrm{out}}/2\pi \int \mathrm{d}k$, where S_{out}, as before, is the length of the external transmission line, and k is changed from an index to the wave number. With the relation of the phase velocity the integration can be carried out for frequencies $\int_0^\infty \mathrm{d}k = \frac{1}{s} \int_0^\infty \mathrm{d}\omega_k$. Note, the time integral in (B.24) is non-negligible where ω_k is close to ω, which describes that frequencies close to the resonators eigenfrequency can be coupled into and out from the resonator. Thus, the lower integration bound for the frequency integration can be set to $-\infty$, $\bar{n}_{\mathrm{th}}$ will be used for the thermal photon number at ω in the transmission lines, and ω_k may be replaced with ω in $g_k = C_{\mathrm{c}} \sqrt{\frac{\omega_k \omega}{C c S_{\mathrm{out}}}}$ With $\int_{-\infty}^{\infty} \mathrm{e}^{\pm\mathrm{i}(\omega - \omega_k)(t - t')} \mathrm{d}\omega_k = 2\pi\delta(t - t')$, where δ denotes the Dirac delta function, the time integral in (B.24) can be solved and the evolution of the density matrix of the resonator reads

$$\dot{\rho}_{\mathrm{r}} = -\frac{C_{\mathrm{c}}^2 \omega^2}{C} \frac{1}{sc} \left[\bar{n}_{\mathrm{th}} \left(a a^\dagger \rho_{\mathrm{r}} - 2 a^\dagger \rho_{\mathrm{r}} a + \rho_{\mathrm{r}} a a^\dagger \right) + (\bar{n}_{\mathrm{th}} + 1) \left(a^\dagger a \rho_{\mathrm{r}} - 2 a \rho_{\mathrm{r}} a^\dagger + \rho_{\mathrm{r}} a^\dagger a \right) \right] \tag{B.25}$$

As all expectation values with mixing terms between operators of the two sides are zero, the calculation for the right side is analogue. Furthermore, all remaining terms yield from the integral in (2.23), where the sign of $\mathscr{V}$ is squared. Thus, the same terms are recovered for the right side transmission line, and a factor of two can be inserted into (B.25) to account for the

left and right side transmission lines. The relaxation constant is found in consistency with the classical calculation $\kappa = \frac{2\omega^2 C_c^2 Z}{C_r}$ (compare (A.14)), where $s = 1/\sqrt{lc}$ and $Z = \sqrt{l/c}$ are used. Furthermore, for low temperatures the mean number of photons in the transmission lines can be set zero $\bar{n}_{th} = 0$ and only the photon decay remains

$$\dot{\rho}_\mathrm{r} = -\frac{\kappa}{2}\left(a^\dagger a\rho_\mathrm{r} - 2a\rho_\mathrm{r}a^\dagger + \rho_\mathrm{r}a^\dagger a\right) \tag{B.26}$$

C Basic transformations

C.1 Rotating frames

In this section the transformation of basic operators into rotating frames are shown. In general a transformation of a basis η to a new basis ζ is given by $\zeta = \hat{U}\eta$, where $\hat{U}$ is a unitary operator. The Schrödinger equation remains valid in the new basis, so that

$$\begin{aligned}
\mathrm{i}\hbar\partial_t\zeta &= \tilde{H}\zeta \\
\mathrm{i}\hbar\partial_t\left(\hat{U}\eta\right) &= \tilde{H}\hat{U}\eta \\
\mathrm{i}\hbar\left(\dot{\hat{U}}\eta + \hat{U}\dot{\eta}\right) &= \tilde{H}\hat{U}\eta \\
\mathrm{i}\hbar\partial_t\eta &= \left(\hat{U}^\dagger\tilde{H}\hat{U} - \mathrm{i}\hbar\hat{U}^\dagger\dot{\hat{U}}\right)\eta.
\end{aligned} \tag{C.27}$$

Since the last line is the Schrödinger equation in the old basis, the term in brackets corresponds to the original Hamiltonian H, so that

$$\tilde{H} = \hat{U}H\hat{U}^\dagger + i\hbar\dot{U}U^\dagger. \tag{C.28}$$

As a first step the lowering and raising operators $\sigma_\pm$ will be transformed into a frame rotating around the σ_z axis with an angular frequency ω. Therefore the transformation operator reads $\hat{U}_1 = \mathrm{e}^{\frac{\mathrm{i}\omega t\sigma_z}{2}}$.

$$\begin{aligned}
\hat{U}_1\sigma_\pm\hat{U}_1^\dagger &= \hat{U}_1\sigma_\pm\mathrm{e}^{-\frac{\mathrm{i}\omega t\sigma_z}{2}} \\
&= \hat{U}_1\left[\sigma_\pm\cos\left(\frac{\omega t}{2}\sigma_z\right) - \mathrm{i}\sigma_\pm\sin\left(\frac{\omega t}{2}\sigma_z\right)\right].
\end{aligned}$$

Note, the cosine function only includes even powers of its argument and the sine only odd. The fact $\sigma_i^{2n} = 1$ and $\sigma_i^{2n+1} = \sigma_i$ for the Pauli matrices ($i \in \{x,y,z\}$) together with $\sigma_\pm\sigma_z =$

$\mp\sigma_\pm$ and $\sigma_z\sigma_\pm = \pm\sigma_\pm$ yields

$$\begin{aligned}\hat{U}_1\sigma_\pm\hat{U}_1^\dagger &= \hat{U}_1\left[\cos\left(\frac{\omega t}{2}\right) \pm \mathrm{i}\sin\left(\frac{\omega t}{2}\right)\right]\sigma_\pm \\ &= \mathrm{e}^{\pm\frac{\mathrm{i}\omega t}{2}}\mathrm{e}^{\frac{\mathrm{i}\omega t}{2}\sigma_z}\sigma_\pm \\ &= e^{\pm\frac{\mathrm{i}\omega t}{2}}\mathrm{e}^{\pm\frac{\mathrm{i}\omega t}{2}}\sigma_\pm \\ &= \mathrm{e}^{\pm\mathrm{i}\omega t}\sigma_\pm \end{aligned} \tag{C.29}$$

Second, the transformation of the photon field operators a and $a^\dagger$ into a frame rotating with frequency ω around $a^\dagger a$ can be easily concluded from its time evolution (2.46) [96]. The transformation follows from

$$a(t) = \mathrm{e}^{\mathrm{i}\omega t a^\dagger a}a(0)\mathrm{e}^{-\mathrm{i}\omega t a^\dagger a} = a(0)\mathrm{e}^{-\mathrm{i}\omega t},$$

as

$$e^{i\omega t a^\dagger a}(a+a^\dagger)e^{-i\omega t a^\dagger a} = ae^{-i\omega t} + a^\dagger e^{i\omega t} \tag{C.30}$$

C.2 Dispersive regime

Hamiltonian (4.6) may be transformed by the unitary transformation $\hat{U}_3 = \mathrm{e}^G$ with generator $G = \frac{g_\Delta}{\delta_{\mathrm{qr}}}\left(a\sigma_+ - a^\dagger\sigma_-\right)$ for identifying the dispersive shift. Nevertheless, it is worthwhile to start by transforming Hamiltonian (4.5). When neglecting the probing terms as well as the diagonal coupling and off resonant interactions the Jaynes-Cummings Hamiltonian remains

$$H = \frac{\hbar\omega_{\mathrm{q}}}{2}\sigma_z + \hbar\omega_0 a^\dagger a + \hbar g_\Delta\left(a\sigma_+ + a^\dagger\sigma_-\right). \tag{C.31}$$

In the regime where the detuning δ_{qr} is much smaller than the coupling constant g_Δ an expansion of $\hat{U}_3$ to the second order of its argument is sufficient

$$\hat{U}_3 H\hat{U}_3^\dagger \approx H + [G,H] - 2GHG + \frac{1}{2}GGH + \frac{1}{2}HGG. \tag{C.32}$$

The transformation of each operator in the considered Hamiltonian is then

$$\left[G, \frac{\hbar\omega_{\mathrm{q}}}{2}\sigma_z\right] = -\hbar\omega_{\mathrm{q}}\frac{g_\Delta}{\delta_{\mathrm{qr}}}\left(a\sigma_+ + a^\dagger\sigma_-\right) \tag{C.33}$$

$$\left[G, \hbar\omega_0 a^\dagger a\right] = \hbar\omega_0\frac{g_\Delta}{\delta_{\mathrm{qr}}}\left(a\sigma_+ + a^\dagger\sigma_-\right) \tag{C.34}$$

$$\left[G, \hbar g_\Delta \left(a\sigma_+ + a^\dagger \sigma_-\right)\right] = \hbar \frac{g_\Delta^2}{\delta_{\mathrm{qr}}} \left(2a^\dagger a \sigma_z + \sigma_z + 1\right) \tag{C.35}$$

In the following only terms to second order in g_Δ are kept. They read

$$\begin{aligned} \frac{\hbar\omega_\mathrm{q}}{2}\left(-G\sigma_z G + \frac{1}{2}G^2\sigma_z + \frac{1}{2}\sigma_z G^2\right) &= \frac{\hbar\omega_\mathrm{q}}{2}\frac{g_\Delta^2}{\delta \mathrm{qr}^2}\left(2a^\dagger a\sigma_-\sigma_+ - 2aa^\dagger\sigma_+\sigma_-\right) \\ &= -\frac{\hbar\omega_\mathrm{q}}{2}\frac{g_\Delta^2}{\delta_{\mathrm{qr}}^2}\left(2a^\dagger a\sigma_z + \sigma_z + 1\right) \end{aligned} \tag{C.36}$$

and

$$\begin{aligned} \hbar\omega_0\left(-Ga^\dagger aG + \frac{1}{2}G^2 a^\dagger a + \frac{1}{2}a^\dagger a G^2\right) = \frac{\hbar\omega_0}{2}\frac{g_\Delta^2}{\delta_{\mathrm{qr}}^2}\Big(&2aa^\dagger aa^\dagger\sigma_+\sigma_- + 2a^\dagger a^\dagger aa\sigma_-\sigma_+ \\ &-aa^\dagger a^\dagger a\sigma_+\sigma_- - 2a^\dagger aa^\dagger a\sigma_-\sigma_+ - a^\dagger aaa^\dagger\sigma_+\sigma_-\Big) \\ =\frac{\hbar\omega_0}{2}\frac{g_\Delta^2}{\delta_{\mathrm{qr}}^2}&\left(2\left[a^\dagger a + 1\right]\sigma_+\sigma_- - 2a^\dagger a\sigma_-\sigma_+\right) \\ =\frac{\hbar\omega_0}{2}\frac{g_\Delta^2}{\delta_{\mathrm{qr}}^2}&\left(2a^\dagger a\sigma_z + \sigma_z + 1\right). \end{aligned} \tag{C.37}$$

For calculating the commutation relation of the field operators $\left[a, a^\dagger\right] = 1$ as well as properties of the lowering and rasing operators $\sigma_z\sigma_\pm = -\sigma_\pm\sigma_z = \pm\sigma_\pm$, $\sigma_\pm^2 = 0$, and $2\sigma_\pm\sigma_\mp = 1 \pm \sigma_z$ are used. The sum of (C.33) and (C.34) cancels the coupling term in the Hamiltonian. The additional terms given by the sum of (C.35) to (C.37) include the dispersive shift. The total transformed Hamiltonian reads

$$H \approx \hbar\left(\omega_0 + \frac{g_\Delta^2}{\delta_{\mathrm{qr}}}\sigma_z\right)a^\dagger a + \frac{\hbar}{2}\left(\omega_\mathrm{q} + \frac{g_\Delta^2}{\delta_{\mathrm{qr}}}\right)\sigma_z, \tag{C.38}$$

where the constant energy $\frac{g_\Delta^2}{2\delta_{\mathrm{qr}}}$ is neglected.

C.3 Dressed-state basis

Following the definition of the dressed levels (5.3) and the back transformation

$$\begin{aligned} |gN\rangle &= \sin\theta|1N\rangle - \cos\theta|2N\rangle \\ |eN-1\rangle &= \cos\theta|1N\rangle + \sin\theta|2N\rangle, \end{aligned} \tag{C.39}$$

the Hamiltonian as well as the Lindblad term of the driven qubit can be transformed to the dressed-state basis. The elements of the Lindblad operator transform as

$$\begin{aligned}
\langle 1N|L_\mathrm{q}|1N\rangle =& \sin^2\theta\langle gN|L_\mathrm{q}|gN\rangle + \cos^2\theta\langle eN-1|L_\mathrm{q}|eN-1\rangle \\
&+ \sin\theta\cos\theta\left[\langle gN|L_\mathrm{q}|eN-1\rangle + \langle eN-1|L_\mathrm{q}|gN\rangle\right] \\
=&\Gamma_\mathrm{r}\left[\sin^2\theta\langle eN|\rho|eN\rangle - \cos^2\theta\langle eN-1|\rho|eN-1\rangle\right] \\
&- \Gamma_\varphi\sin\theta\cos\theta\left[\langle gN|\rho|eN-1\rangle + \langle eN-1|\rho|gN\rangle\right] \\
=&\Gamma_\mathrm{r}\sin^2\theta\cos^2\theta\langle 1N+1|\rho|1N+1\rangle + \Gamma_\mathrm{r}\sin^4\theta\langle 2N+1|\rho|2N+1\rangle \\
&+ \Gamma_\mathrm{r}\sin^3\theta\cos\theta\left[\langle 1N+1|\rho|2N+1\rangle + \langle 2N+1|\rho|1N+1\rangle\right] \\
&- \Gamma_\mathrm{r}\cos^4\theta\langle 1N|\rho|1N\rangle - \Gamma_\mathrm{r}\sin^2\theta\cos^2\theta\langle 2N|\rho|2N\rangle \\
&- \Gamma_\mathrm{r}\sin\theta\cos^3\theta\langle 1N|\rho|2N\rangle - \Gamma_\mathrm{r}\sin\theta\cos^3\theta\langle 2N|\rho|1N\rangle \\
&- 2\Gamma_\varphi\sin^2\theta\cos^2\theta\left[\langle 1N|\rho|1N\rangle - \langle 2N|\rho|2N\rangle\right] \\
&+ \Gamma_\varphi\sin\theta\cos\theta\cos 2\theta\left[\langle 1N|\rho|2N\rangle + \langle 2N|\rho|1N\rangle\right]
\end{aligned} \tag{C.40}$$

Note, the decoherence only produces terms with same photon number N. But due to the relaxation, populations and coherences of the step $(N+1)$ above the considered one of the dressed ladder contribute to the Lindblad operator in the dressed basis. The reason is that the decoherence cannot change the total number of excitations N. On the other hand, the relaxation can remove one excitation from the system. The same is true for the remaining terms. They read

$$\begin{aligned}
\langle 2N|L_\mathrm{q}|2N\rangle =& \cos^2\theta\langle gN|L_\mathrm{q}|gN\rangle + \sin^2\theta\langle eN-1|L_\mathrm{q}|eN-1\rangle \\
&- \sin\theta\cos\theta\left[\langle gN|L_\mathrm{q}|eN-1\rangle + \langle eN-1|L_\mathrm{q}|gN\rangle\right] \\
=&\Gamma_\mathrm{r}\left[\cos^2\theta\langle eN|\rho|eN\rangle - \sin^2\theta\langle eN-1|\rho|eN-1\rangle\right] \\
&+ \Gamma_\varphi\sin\theta\cos\theta\left[\langle gN|\rho|eN-1\rangle + \langle eN-1|\rho|gN\rangle\right] \\
=&\Gamma_\mathrm{r}\cos^4\theta\langle 1N+1|\rho|1N+1\rangle + \Gamma_\mathrm{r}\sin^2\theta\cos^2\theta\langle 2N+1|\rho|2N+1\rangle \\
&+ \Gamma_\mathrm{r}\sin\theta\cos^3\theta\left[\langle 1N+1|\rho|2N+1\rangle + \langle 2N+1|\rho|1N+1\rangle\right] \\
&- \Gamma_\mathrm{r}\sin^2\cos^2\theta\langle 1N|\rho|1N\rangle - \Gamma_\mathrm{r}\sin^4\theta\langle 2N|\rho|2N\rangle \\
&- \Gamma_\mathrm{r}\sin^3\theta\cos\theta\langle 1N|\rho|2N\rangle - \Gamma_\mathrm{r}\sin^3\theta\cos\theta\langle 2N|\rho|1N\rangle \\
&+ 2\Gamma_\varphi\sin^2\theta\cos^2\theta\left[\langle 1N|\rho|1N\rangle - \langle 2N|\rho|2N\rangle\right] \\
&- \Gamma_\varphi\sin\theta\cos\theta\cos 2\theta\left[\langle 1N|\rho|2N\rangle + \langle 2N|\rho|1N\rangle\right],
\end{aligned} \tag{C.41}$$

$$
\begin{aligned}
\langle 1N|L_{\mathrm{q}}|2N\rangle =& -\sin\theta\cos\theta\langle gN|L_{\mathrm{q}}|gN\rangle + \sin\theta\cos\theta\langle eN-1|L_{\mathrm{q}}|eN-1\rangle \\
&+\sin^2\theta\langle gN|L_{\mathrm{q}}|eN-1\rangle - \cos^2\theta\langle eN-1|L_{\mathrm{q}}|gN\rangle \\
=&\Gamma_{\mathrm{r}}\left[-\sin\theta\cos\theta\langle eN|\rho|eN\rangle - \sin\theta\cos\theta\langle eN-1|\rho|eN-1\rangle\right] \\
&-\Gamma_{\varphi}\sin^2\theta\langle gN|\rho|eN-1\rangle + \Gamma_{\varphi}\cos^2\theta\langle eN-1|\rho|gN\rangle \\
=&-\Gamma_{\mathrm{r}}\sin\theta\cos^3\theta\langle 1N+1|\rho|1N+1\rangle - \Gamma_{\mathrm{r}}\sin^3\theta\cos\theta\langle 2N+1|\rho|2N+1\rangle \\
&-\Gamma_{\mathrm{r}}\sin^2\theta\cos^2\theta\left[\langle 1N+1|\rho|2N+1\rangle + \langle 2N+1|\rho|1N+1\rangle\right] \\
&-\Gamma_{\mathrm{r}}\sin\theta\cos^3\theta\langle 1N|\rho|1N\rangle - \Gamma_{\mathrm{r}}\sin^3\theta\cos\theta\langle 2N|\rho|2N\rangle \\
&-\Gamma_{\mathrm{r}}\sin^2\theta\cos^2\theta\left[\langle 1N|\rho|2N\rangle + \langle 2N|\rho|1N\rangle\right] \\
&+\Gamma_{\varphi}\sin\theta\cos\theta\left[\cos^2\theta-\sin^2\theta\right]\left[\langle 1N|\rho|1N\rangle - \langle 2N|\rho|2N\rangle\right] \\
&-\Gamma_{\varphi}\left[\sin^4\theta+\cos^4\theta\right]\langle 1N|\rho|2N\rangle + 2\Gamma_{\varphi}\sin^2\theta\cos^2\theta\langle 2N|\rho|1N\rangle,
\end{aligned}
\tag{C.42}
$$

$$
\begin{aligned}
\langle 2N|L_{\mathrm{q}}|1N\rangle =& -\sin\theta\cos\theta\langle gN|L_{\mathrm{q}}|gN\rangle + \sin\theta\cos\theta\langle eN-1|L_{\mathrm{q}}|eN-1\rangle \\
&-\cos^2\theta\langle gN|L_{\mathrm{q}}|eN-1\rangle + \sin^2\theta\langle eN-1|L_{\mathrm{q}}|gN\rangle \\
=&\Gamma_{\mathrm{r}}\left[-\sin\theta\cos\theta\langle eN|\rho|eN\rangle - \sin\theta\cos\theta\langle eN-1|\rho|eN-1\rangle\right] \\
&+\Gamma_{\varphi}\cos^2\theta\langle gN|\rho|eN-1\rangle - \Gamma_{\varphi}\sin^2\theta\langle eN-1|\rho|gN\rangle \\
=&-\Gamma_{\mathrm{r}}\sin\theta\cos^3\theta\langle 1N+1|\rho|1N+1\rangle - \Gamma_{\mathrm{r}}\sin^3\theta\cos\theta\langle 2N+1|\rho|2N+1\rangle \\
&-\Gamma_{\mathrm{r}}\sin^2\theta\cos^2\theta\left[\langle 1N+1|\rho|2N+1\rangle + \langle 2N+1|\rho|1N+1\rangle\right] \\
&-\Gamma_{\mathrm{r}}\sin\theta\cos^3\theta\langle 1N|\rho|1N\rangle - \Gamma_{\mathrm{r}}\sin^3\theta\cos\theta\langle 2N|\rho|2N\rangle \\
&-\Gamma_{\mathrm{r}}\sin^2\theta\cos^2\theta\left[\langle 1N|\rho|2N\rangle + \langle 2N|\rho|1N\rangle\right] \\
&+\Gamma_{\varphi}\sin\theta\cos\theta\left[\cos^2\theta-\sin^2\theta\right]\left[\langle 1N|\rho|1N\rangle - \langle 2N|\rho|2N\rangle\right] \\
&+2\Gamma_{\varphi}\sin^2\theta\cos^2\theta\langle 1N|\rho|2N\rangle - \Gamma_{\varphi}\left[\sin^4\theta+\cos^4\theta\right]\langle 2N|\rho|1N\rangle.
\end{aligned}
\tag{C.43}
$$

After tracing the equations over the photon number N of the driving field, the reduced elements of the Linblad operator $L_{ij} = \langle i|L_{q,dr}|j\rangle = \mathrm{Tr}_N\langle iN|L_{q,dr}|jN\rangle$ with $[i,j]] \in \{1,2\}$ in dependence of the reduced density matrix elements $\rho_{ij} = \mathrm{Tr}_N\langle iN|\rho|jN\rangle$ read

$$
\begin{aligned}
L_{11} =& -\left[\Gamma_{\mathrm{r}}\cos^2\theta\cos 2\theta + \frac{\Gamma_{\varphi}}{2}\sin^2 2\theta\right]\rho_{11} - \left[\Gamma_{\mathrm{r}}\sin^2\theta\cos 2\theta - \frac{\Gamma_{\varphi}}{2}\sin^2 2\theta\right]\rho_{22} \\
&+\frac{\Gamma_{\varphi}-\Gamma_{\mathrm{r}}}{2}\sin 2\theta\cos 2\theta\left(\rho_{12}+\rho_{21}\right),
\end{aligned}
\tag{C.44}
$$

$$
\begin{aligned}
L_{22} = &\left[\Gamma_{\mathrm{r}}\cos^2\theta\cos2\theta+\frac{\Gamma_\varphi}{2}\sin^2 2\theta\right]\rho_{11}+\left[\Gamma_{\mathrm{r}}\sin^2\theta\cos2\theta-\frac{\Gamma_\varphi}{2}\sin^2 2\theta\right]\rho_{22}\\
&-\frac{\Gamma_\varphi-\Gamma_{\mathrm{r}}}{2}\sin 2\theta\cos 2\theta\,(\rho_{12}+\rho_{21}),\\
=&-L_{11}
\end{aligned}
\tag{C.45}
$$

$$
\begin{aligned}
L_{12} = &\left[-\Gamma_{\mathrm{r}}\cos^2\theta\sin2\theta+\frac{\Gamma_\varphi}{2}\sin2\theta\cos2\theta\right]\rho_{11}+\left[-\Gamma_{\mathrm{r}}\sin^2\theta\sin2\theta-\frac{\Gamma_\varphi}{2}\sin2\theta\cos2\theta\right]\rho_{22}\\
&+\left[\Gamma_\varphi-\Gamma_{\mathrm{r}}\right]\frac{\sin^2 2\theta}{2}\,(\rho_{12}+\rho_{21})-\Gamma_\varphi\rho_{12},
\end{aligned}
\tag{C.46}
$$

$$
\begin{aligned}
L_{21} = &\left[-\Gamma_{r}\cos^2\theta\sin2\theta+\frac{\Gamma_\varphi}{2}\sin2\theta\cos2\theta\right]\rho_{11}+\left[-\Gamma_{r}\sin^2\theta\sin2\theta-\frac{\Gamma_\varphi}{2}\sin2\theta\cos2\theta\right]\rho_{22}\\
&+\left[\Gamma_\varphi-\Gamma_{r}\right]\frac{\sin^2 2\theta}{2}\,(\rho_{12}+\rho_{21})-\Gamma_\varphi\rho_{21}.
\end{aligned}
\tag{C.47}
$$

The total Lindblad operator of the qubit in the dressed-state basis can be summarized in matrix form as

$$
\begin{aligned}
L_{\mathrm{q,dr}} = &-\frac{\Gamma_{\mathrm{r}}}{2}\frac{\delta_{\mathrm{qh}}}{\Omega_{\mathrm{R}}}\left[\sigma_+\sigma_-\rho\sigma_+\sigma_- +\sigma_+\rho\sigma_- -\sigma_-\rho\sigma_+ -\sigma_-\sigma_+\rho\sigma_-\sigma_+\right]\\
&-\left(\frac{\Gamma_{\mathrm{r}}}{2}\frac{\delta_{\mathrm{qh}}^2}{\Omega_{\mathrm{R}}^2}+\frac{\Gamma_\varphi}{2}\frac{\Omega_{\mathrm{R0}}^2}{\Omega_{\mathrm{R}}^2}\right)\left[\sigma_+\sigma_-\rho\sigma_+\sigma_- -\sigma_+\rho\sigma_- -\sigma_-\rho\sigma_+ +\sigma_-\sigma_+\rho\sigma_-\sigma_+\right]\\
&-\left(\Gamma_\varphi-\Gamma_{\mathrm{r}}\right)\frac{\delta_{\mathrm{qh}}\Omega_{\mathrm{R0}}}{\Omega_{\mathrm{R}}^2}\left[\sigma_+\sigma_-\rho\sigma_- +\sigma_+\rho\sigma_+\sigma_- -\sigma_-\rho\sigma_-\sigma_+ -\sigma_-\sigma_+\rho\sigma_+\right]\\
&-\frac{\Gamma_{\mathrm{r}}}{2}\frac{\Omega_{\mathrm{R0}}}{\Omega_{\mathrm{R}}}\left[\sigma_+\sigma_-\rho\sigma_+ +\sigma_+\rho\sigma_-\sigma_+ +\sigma_-\rho\sigma_+\sigma_- +\sigma_-\sigma_+\rho\sigma_-\right]\\
&+\left(\Gamma_\varphi-\Gamma_{\mathrm{r}}\right)\frac{\Omega_{\mathrm{R0}}\delta_{\mathrm{qh}}}{2\Omega_{\mathrm{R}}^2}\left[\sigma_+\sigma_-\rho\sigma_+ -\sigma_+\rho\sigma_-\sigma_+ +\sigma_-\rho\sigma_+\sigma_- -\sigma_-\sigma_+\rho\sigma_-\right]\\
&+\left(-\Gamma_\varphi+\left(\Gamma_\varphi-\Gamma_{\mathrm{r}}\right)\frac{\Omega_{\mathrm{R0}}^2}{2\Omega_{\mathrm{R}}^2}\right)\left[\sigma_+\sigma_-\rho\sigma_-\sigma_+ +\sigma_-\sigma_+\rho\sigma_+\sigma_-\right]\\
&+\left(\Gamma_\varphi-\Gamma_{\mathrm{r}}\right)\frac{\Omega_{\mathrm{R0}}^2}{2\Omega_{\mathrm{R}}}\left[\sigma_+\rho\sigma_+ +\sigma_-\rho\sigma_-\right].
\end{aligned}
\tag{C.48}
$$

Note, in the sixth line the terms $\sigma_+\sigma_-\rho\sigma_-\sigma_+ +\sigma_-\sigma_+\rho\sigma_+\sigma_-$ can be replaced by the identical term $(-\sigma_z\rho\sigma_z+\rho)/2$. It is worthwhile to reduce the above equation to the terms that

remain after a RWA in a frame rotating around the σ_z axis. Therefore, terms with unequal contribution regarding σ_+ and σ_- will be neglected[21], since they would oscillate fast and, thus, average out. The invariant part of the Lindblad operator then is

$$\begin{aligned} L_{\mathrm{q,dr}} =& -\frac{\Gamma_\mathrm{r}}{2}\frac{\delta_\mathrm{qh}}{\Omega_\mathrm{R}}\left[\sigma_+\sigma_-\rho\sigma_+\sigma_- + \sigma_+\rho\sigma_- - \sigma_-\rho\sigma_+ - \sigma_-\sigma_+\rho\sigma_-\sigma_+\right] \\ & -\left(\frac{\Gamma_\mathrm{r}}{2}\frac{\delta_\mathrm{qh}^2}{\Omega_\mathrm{R}^2} + \frac{\Gamma_\varphi}{2}\frac{\Omega_\mathrm{R0}^2}{\Omega_\mathrm{R}^2}\right)\left[\sigma_+\sigma_-\rho\sigma_+\sigma_- - \sigma_+\rho\sigma_- - \sigma_-\rho\sigma_+ + \sigma_-\sigma_+\rho\sigma_-\sigma_+\right] \\ & +\left(\frac{\Gamma_\varphi}{2} - \left(\Gamma_\varphi - \Gamma_\mathrm{r}\right)\frac{\Omega_\mathrm{R0}^2}{4\Omega_\mathrm{R}}\right)\left[\sigma_z\rho\sigma_z - \rho\right]. \end{aligned} \tag{C.49}$$

The above equation can be brought to a more transparent form if the identities

$$2\sigma_+\sigma_-\rho\sigma_+\sigma_- - 2\sigma_-\sigma_+\rho\sigma_-\sigma_+ = \sigma_+\sigma_-\rho + \rho\sigma_+\sigma_- - \sigma_-\sigma_+\rho - \rho\sigma_-\sigma_+ \tag{C.50}$$

and

$$\begin{aligned} \sigma_+\sigma_-\rho\sigma_+\sigma_- - \sigma_-\sigma_+\rho\sigma_-\sigma_+ =& \frac{1}{2}\left(\sigma_z\rho\sigma_z + \rho\right) \\ =& \frac{1}{2}\left(\sigma_z\rho\sigma_z - \rho + \sigma_+\sigma_-\rho + \sigma_-\sigma_+\rho + \rho\sigma_-\sigma_+ + \rho\sigma_+\sigma_-\right) \end{aligned} \tag{C.51}$$

are used in the first and second line of (C.49), respectively. In addition, with $\frac{\delta_\mathrm{qh}^2}{\Omega_\mathrm{R}^2} = 1 - \frac{\Omega_\mathrm{R0}^2}{\Omega_\mathrm{R}^2}$ the Lindblad term can be written as

$$\begin{aligned} L_{\mathrm{q,dr}} =& \frac{\Gamma_\mathrm{r}}{4}\frac{\delta_\mathrm{qh}}{\Omega_\mathrm{R}}\left[-\sigma_+\sigma_-\rho - \rho\sigma_+\sigma_- + \sigma_-\sigma_+\rho + \rho\sigma_-\sigma_+ - 2\sigma_+\rho\sigma_- + 2\sigma_-\rho\sigma_+\right] \\ & +\left(\frac{\Gamma_\mathrm{r}}{4}\left(\frac{\Omega_\mathrm{R0}^2}{\Omega_\mathrm{R}^2} - 1\right) - \frac{\Gamma_\varphi}{4}\frac{\Omega_\mathrm{R0}^2}{\Omega_\mathrm{R}^2}\right) \\ & \times\left[\sigma_+\sigma_-\rho + \rho\sigma_+\sigma_- + \sigma_-\sigma_+\rho + \rho\sigma_-\sigma_+ - 2\sigma_-\rho\sigma_+ - 2\sigma_+\rho\sigma_-\right] \\ & +\left(\frac{\Gamma_\mathrm{r}}{4}\left(\frac{\Omega_\mathrm{R0}^2}{\Omega_\mathrm{R}^2} - 1\right) - \frac{\Gamma_\varphi}{4}\frac{\Omega_\mathrm{R0}^2}{\Omega_\mathrm{R}^2} + \frac{\Gamma_\varphi}{2} - \left(\Gamma_\varphi - \Gamma_\mathrm{r}\right)\frac{\Omega_\mathrm{R0}^2}{4\Omega_\mathrm{R}}\right)\left[\sigma_z\rho\sigma_z - \rho\right]. \end{aligned} \tag{C.52}$$

When rearranged as

$$\begin{aligned} L_{\mathrm{q,dr}} =& \frac{1}{2}\left(\frac{\Gamma_\mathrm{r}}{2}\left(1 - \frac{\delta_\mathrm{qh}}{\Omega_\mathrm{R}}\right) + \left(\Gamma_\varphi - \Gamma_\mathrm{r}\right)\frac{\Omega_\mathrm{R0}^2}{2\Omega_\mathrm{R}^2}\right)\left[2\sigma_+\rho\sigma_- - \sigma_-\sigma_+\rho - \rho\sigma_-\sigma_+\right] \\ & +\frac{1}{2}\left(\frac{\Gamma_\mathrm{r}}{2}\left(1 + \frac{\delta_\mathrm{qh}}{\Omega_\mathrm{R}}\right) + \left(\Gamma_\varphi - \Gamma_\mathrm{r}\right)\frac{\Omega_\mathrm{R0}^2}{2\Omega_\mathrm{R}^2}\right)\left[2\sigma_-\rho\sigma_+ - \sigma_+\sigma_-\rho - \rho\sigma_+\sigma_-\right] \\ & +\frac{1}{2}\left(\Gamma_\varphi - \frac{\Gamma_\mathrm{r}}{2} - \left(\Gamma_\varphi - \Gamma_\mathrm{r}\right)\frac{\Omega_\mathrm{R0}^2}{\Omega_\mathrm{R}^2}\right)\left[\sigma_z\rho\sigma_z - \rho\right]. \end{aligned} \tag{C.53}$$

[21] These terms are neglected because in a frame rotating with the additional probing signal they are fast oscillating. Nevertheless, if a spectral analysis without the probe is to be achieved they should be taken into account.

it is possible to identify a rate for excitation, relaxation, and dephasing as given by the first, second, and third line of the above equation, respectively (compare to (B.18)).

To analyze the coupling of the fundamental mode to the dressed system, the influence of the operators σ_x and σ_z of the original qubit basis on the dressed states needs to be calculated. To start with σ_x applied on the dressed states, it reads

$$\begin{aligned}\sigma_x|1N\rangle =&\sigma_x(\sin\theta|gN\rangle+\cos\theta|en-1\rangle)=\sin\theta|eN\rangle+\cos\theta|gn-1\rangle\\ =&\sin\theta\cos\theta|1N+1\rangle+\sin^2\theta|2N+1\rangle\\ &+\sin\theta\cos\theta|1N-1\rangle-\cos^2\theta|2N-1\rangle,\end{aligned} \tag{C.54}$$

$$\begin{aligned}\sigma_x|2N\rangle =&\sigma_x(-\cos\theta|gN\rangle+\sin\theta|en-1\rangle)=-\cos\theta|eN\rangle+\sin\theta|gn-1\rangle\\ =&-\cos^2\theta|1N+1\rangle-\sin\theta\cos\theta|2N+1\rangle\\ &+\sin^2\theta|1N-1\rangle-\sin\theta\cos\theta|2N-1\rangle.\end{aligned} \tag{C.55}$$

Here, no interactions between levels of the same manifold are found. The σ_x term instead couples each level of one manifold to the two levels of the manifold above (N+1) and below (N-1). This interaction corresponds to the Rabi frequency shifted transition frequencies. They also may be probed (see chapter 5.6) and play an important role in quantum optics [110], since amplification and damping may also be found there. A transition between the Rabi levels of one manifold is given by the σ_z interaction, as

$$\begin{aligned}\sigma_z|1N\rangle =&\sigma_z(\sin\theta|gN\rangle+\cos\theta|en-1\rangle)=-\sin\theta|gN\rangle+\cos\theta|en-1\rangle\\ =&-\sin^2\theta|1N\rangle+\sin\theta\cos\theta|2N\rangle\\ &+\cos^2\theta|1N\rangle+\sin\theta\cos\theta|2N\rangle,\end{aligned} \tag{C.56}$$

$$\begin{aligned}\sigma_z|2N\rangle =&\sigma_z(-\cos\theta|gN\rangle+\sin\theta|en-1\rangle)=\cos\theta|gN\rangle+\sin\theta|en-1\rangle\\ =&\sin\theta\cos\theta|1N\rangle-\cos^2\theta|2N\rangle\\ &+\sin\theta\cos\theta|1N\rangle+\sin\theta\cos\theta|2N\rangle.\end{aligned} \tag{C.57}$$

The transition matrix elements can be summarized in the form[22]

$$\sigma_z\rightarrow\sin 2\theta\,\sigma_x+\cos 2\theta\,\sigma_z \tag{C.58}$$

[22]Note, in this work a discrimination between the Pauli operators in flux, original qubit, or dressed basis is not used. They are usually multiplied with energies or frequencies that have indices defining the basis. Nevertheless, one should always be aware, which basis is used.

C.4 Eigenbasis of the multiphoton driven qubit

As mentioned in 5.6, the relaxation rates of the qubit are modified when the basis is changed by a rotation around the y-axis. This change of basis is expressed by a unitary transformation $\hat{U}_8 = \mathrm{e}^{\mathrm{i}\theta\sigma_y}$ and $\tan 2\theta = \Omega_{k0}/\delta_{\mathrm{q}k}$ which is equivalent to a rotation given by $\cos\theta + \mathrm{i}\sigma_y \sin\theta$. For analyzing its influence, in a first step the transformation of the basic operators is given by

$$\begin{aligned}
\hat{U}_8^\dagger \sigma_+ \hat{U}_8 &= -\sin\theta\cos\theta\sigma_z + \cos^2\theta\sigma_+ - \sin^2\theta\sigma_-, \\
\hat{U}_8^\dagger \sigma_- \hat{U}_8 &= -\sin\theta\cos\theta\sigma_z - \sin^2\theta\sigma_+ + \cos^2\theta\sigma_-, \\
\hat{U}_8^\dagger \sigma_+\sigma_- \hat{U}_8 &= \cos^2\theta\sigma_+\sigma_- + \sin\theta\cos\theta(\sigma_+ + \sigma_-) + \sin^2\theta\sigma_-\sigma_+, \\
\hat{U}_8^\dagger \sigma_z \hat{U}_8 &= \cos 2\theta\sigma_z + \sin 2\theta(\sigma_+ + \sigma_-).
\end{aligned} \tag{C.59}$$

Then the transformation of the Lindblad term is done by

$$\begin{aligned}
L_k =& \hat{U}_8^\dagger L_{\mathrm{q}} \hat{U}_8 \\
=& \frac{\Gamma_{\mathrm{r}}}{2}\left(2\hat{U}_8^\dagger\sigma_-\hat{U}_8\rho\hat{U}_8^\dagger\sigma_+\hat{U}_8 - \hat{U}_8^\dagger\sigma_+\sigma_-\hat{U}_8\rho - \rho\hat{U}_8^\dagger\sigma_+\sigma_-\hat{U}_8\right) \\
&+ \frac{\gamma_\phi}{2}\left(\hat{U}_8^\dagger\sigma_z\hat{U}_8\rho\hat{U}_8^\dagger\sigma_z\hat{U}_8 - \rho\right).
\end{aligned} \tag{C.60}$$

Using the relations in (C.59) the transformation can be carried out

$$\begin{aligned}
L_k =& \frac{\Gamma_{\mathrm{r}}}{2}\Bigg(\frac{\sin^2 2\theta}{2}\left[\sigma_z\rho\sigma_z - \sigma_+\rho\sigma_+ - \sigma_-\rho\sigma_-\right] + \sin 2\theta\sin^2\theta\left[\sigma_+\rho\sigma_z + \sigma_z\rho\sigma_-\right] \\
&- \sin 2\theta\cos^2\theta\left[\sigma_-\rho\sigma_z + \sigma_z\rho\sigma_+\right] + 2\cos^4\theta\sigma_-\rho\sigma_+ + 2\sin^4\theta\sigma_+\rho\sigma_- \\
&- \cos^2\theta\left[\sigma_+\sigma_-\rho + \rho\sigma_+\sigma_-\right] - \sin^2\theta\left[\sigma_-\sigma_+\rho + \rho\sigma_-\sigma_+\right] \\
&\frac{\sin 2\theta}{2}\left[\sigma_+\rho + \sigma_-\rho + \rho\sigma_+ + \rho\sigma_-\right]\Bigg) \\
&+ \frac{\gamma_\varphi}{2}\left(\cos^2 2\theta\sigma_z\rho\sigma_z + \sin^2 2\theta\left[\sigma_+\rho\sigma_+ + \sigma_-\rho\sigma_- + \sigma_+\rho\sigma_- + \sigma_-\rho\sigma_+\right]\right. \\
&\left.+ \sin 2\theta\cos 2\theta\left[\sigma_z\rho\sigma_+ + \sigma_z\rho\sigma_- + \sigma_+\rho\sigma_z + \sigma_-\rho\sigma_z\right] - \rho\right).
\end{aligned} \tag{C.61}$$

As in the last chapter only terms that remain after a RWA are kept

$$\begin{aligned}
L_k =& \frac{\Gamma_\mathrm{r}}{2}\frac{\sin^2 2\theta}{2}\left(\sigma_z\rho\sigma_z - \sigma_-\rho\sigma_+ - \sigma_+\rho\sigma_-\right) \\
&+ \frac{\Gamma_\mathrm{r}}{2}\left(\cos^2\theta\left[2\sigma_-\rho\sigma_+ - \sigma_+\sigma_-\rho - \rho\sigma_+\sigma_-\right] + \sin^2\theta\left[2\sigma_+\rho\sigma_- - \sigma_-\sigma_+\rho - \rho\sigma_-\sigma_+\right]\right) \\
&+ \frac{\gamma_\varphi}{2}\sin^2 2\theta\left(-\sigma_z\rho\sigma_z + \sigma_+\rho\sigma_- + \sigma_-\rho\sigma_+\right) + \frac{\gamma_\varphi}{2}\left(\sigma_z\rho\sigma_z - \rho\right). \\
=& \left(\frac{\Gamma_\mathrm{r}}{2} - \gamma_\varphi\right)\frac{\sin^2 2\theta}{2}\left(\sigma_z\rho\sigma_z - \sigma_-\rho\sigma_+ - \sigma_+\rho\sigma_-\right) + \frac{\gamma_\varphi}{2}\left(\sigma_z\rho\sigma_z - \rho\right) \\
&+ \frac{\Gamma_\mathrm{r}}{2}\left(\cos^2\theta\left[2\sigma_-\rho\sigma_+ - \sigma_+\sigma_-\rho - \rho\sigma_+\sigma_-\right] + \sin^2\theta\left[2\sigma_+\rho\sigma_- - \sigma_-\sigma_+\rho - \rho\sigma_-\sigma_+\right]\right).
\end{aligned} \tag{C.62}$$

With $0 = \rho - \rho$ added to the first term, and replacing the positive ρ by $(\sigma_+\sigma_-\rho + \rho\sigma_+\sigma_- + \sigma_-\sigma_+\rho + \rho\sigma_-\sigma_+)/2$ a more transparent form is achieved:

$$\begin{aligned}
L_k =& \left(\frac{\Gamma_\mathrm{r}}{2}\cos^2\theta - \left(\frac{\Gamma_\mathrm{r}}{2} - \gamma_\varphi\right)\frac{\sin 2\theta}{4}\right)\left[2\sigma_-\rho\sigma_+ - \sigma_+\sigma_-\rho - \rho\sigma_+\sigma_-\right] \\
&+ \left(\frac{\Gamma_\mathrm{r}}{2}\sin^2\theta - \left(\frac{\Gamma_\mathrm{r}}{2} - \gamma_\varphi\right)\frac{\sin 2\theta}{4}\right)\left[2\sigma_+\rho\sigma_- - \sigma_-\sigma_+\rho - \rho\sigma_-\sigma_+\right] \\
&+ \left(\frac{\gamma_\varphi}{2} + \left(\frac{\Gamma_\mathrm{r}}{2} - \gamma_\varphi\right)\frac{\sin^2 2\theta}{2}\right)\left[\sigma_z\rho\sigma_z - \rho\right]
\end{aligned} \tag{C.63}$$

Substituting the trigonometric functions as well as the pure dephasing with $\gamma_\varphi = \Gamma_\varphi - \Gamma_\mathrm{r}/2$ the Lindblad term in the new basis takes the exact same form as C.53.

$$\begin{aligned}
L_k =& \frac{1}{2}\left(\frac{\Gamma_\mathrm{r}}{2}\left(1 + \frac{\delta_\mathrm{qk}}{\Omega_\mathrm{k}}\right) + \left(\Gamma_\varphi - \Gamma_\mathrm{r}\right)\frac{\Omega_{\mathrm{k}0}^2}{2\Omega_\mathrm{k}^2}\right)\left[2\sigma_-\rho\sigma_+ - \sigma_+\sigma_-\rho - \rho\sigma_+\sigma_-\right] \\
&+ \frac{1}{2}\left(\frac{\Gamma_\mathrm{r}}{2}\left(1 - \frac{\delta_\mathrm{qk}}{\Omega_\mathrm{k}}\right) + \left(\Gamma_\varphi - \Gamma_\mathrm{r}\right)\frac{\Omega_{\mathrm{k}0}^2}{2\Omega_\mathrm{k}^2}\right)\left[2\sigma_+\rho\sigma_- - \sigma_-\sigma_+\rho - \rho\sigma_-\sigma_+\right] \\
&+ \frac{1}{2}\left(\Gamma_\varphi - \frac{\Gamma_\mathrm{r}}{2} - \left(\Gamma_\phi - \Gamma_\mathrm{r}\right)\frac{\Omega_{\mathrm{k}0}^2}{\Omega_\mathrm{k}^2}\right)\left[\sigma_z\rho\sigma_z - \rho\right].
\end{aligned} \tag{C.64}$$

This equation allows identifying the relaxation, excitation, and dephasing rates. Please note, in the last two chapters two different ways for calculation of the relaxation rates by a basis change are sketched.

C.5 Two-photon interaction with the fundamental mode

In the Hamiltonian (5.34) an effective two-level system is coupled by an off-diagonal and a diagonal coupling term to the fundamental mode of the resonator. The latter, proportional to

σ_z may be transformed into a two-photon off-diagonal term. The Hamiltonian considered is

$$H_\mathrm{t} = \frac{\hbar\Omega_\mathrm{k}}{2}\sigma_z + \hbar\left[a^\dagger + a\right](g_{\mathrm{x}k}\sigma_x + g_{\mathrm{z}k}\sigma_z) + \hbar\omega_0 a^\dagger a + \Omega_\mathrm{p}\left(a^\dagger \mathrm{e}^{-\mathrm{i}\omega_\mathrm{p}t} + a\mathrm{e}^{\mathrm{i}\omega_\mathrm{p}t}\right), \quad \text{(C.65)}$$

where the short abbreviations $g_{\mathrm{z}k}$ and $g_{\mathrm{x}k}$ are introduced for the diagonal and off-diagonal coupling constants. To identify the two photon resonances a unitary transformation $\hat{U}_9 = \mathrm{e}^{\frac{g_{\mathrm{z}k}}{\omega_0}(a^\dagger - a)\sigma_z}$ will be applied. Note, the generator $G = \frac{g_{\mathrm{z}k}}{\omega_0}(a^\dagger - a)\sigma_z$ is small for $g_{\mathrm{z}k}\sqrt{N} \ll \omega_0$. This requirement is fulfilled for the experimental parameters. Thus the transformation can be expanded to first order in G only. Then it results in [23]

$$\tilde{H}_\mathrm{t} = \hat{U}_9 H_\mathrm{t} \hat{U}_9^\dagger \approx \tilde{H}_\mathrm{t} + [G, H_\mathrm{t}] \quad \text{(C.66)}$$

for the transformed Hamiltonian, since $G^\dagger = -G$. The transformation of the different components of (C.65) is

$$\begin{aligned}
&\left[\left(a^\dagger - a\right)\sigma_z, \sigma_z\right] = 0 \\
&\left[\left(a^\dagger - a\right)\sigma_z, \left(a^\dagger + a\right)\sigma_x\right] = 2\mathrm{i}\sigma_y\left(a^\dagger a^\dagger - aa\right) \\
&\left[\left(a^\dagger - a\right)\sigma_z, \left(a^\dagger + a\right)\sigma_z\right] = -2 \\
&\left[\left(a^\dagger - a\right)\sigma_z, a^\dagger a\right] = -\sigma_z\left(a^\dagger + a\right) \\
&\left[\left(a^\dagger - a\right)\sigma_z, a^\dagger \mathrm{e}^{-\mathrm{i}\omega_\mathrm{p}t} + a\mathrm{e}^{\mathrm{i}\omega_\mathrm{p}t}\right] = 2\cos\omega_\mathrm{p}t\,\sigma_z,
\end{aligned} \quad \text{(C.67)}$$

where the second line gives the two-photon off-diagonal coupling, the fourth line cancels the σ_z coupling term in $\tilde{H}_\mathrm{t}$ and the time dependence of the last line may be canceled by a RWA. The final Hamiltonian then reads

$$\begin{aligned}
\tilde{H}_\mathrm{t} = &\frac{\hbar\Omega_k}{2}\sigma_z + \hbar g_{\mathrm{x}k}\left[a^\dagger + a\right]\sigma_x + \hbar\omega_0 a^\dagger a + \Omega_\mathrm{p}\left(a^\dagger e^{-i\omega_p t} + a\mathrm{e}^{\mathrm{i}\omega_\mathrm{p}t}\right) \\
&+ 2\mathrm{i}\hbar\frac{g_{\mathrm{x}k}g_{\mathrm{z}k}}{\omega_0}\sigma_y\left(a^\dagger a^\dagger - aa\right)
\end{aligned} \quad \text{(C.68)}$$

Note, also the dissipative Lindblad term of the resonator's fundamental mode would be influenced from the transformations above. Nevertheless, the additional terms can be dropped in RWA, since all would oscillate with multiples of the probing frequency in a rotating frame.

[23] Compare to the Schrieffer-Wolff transformation [88, 119].

List of Symbols

Constants

e	elementary charge
$\hbar$	reduced Planck constant
h	Planck constant
i	imaginary unit
k_B	Boltzmann constant
μ_0	vacuum permeability
Φ_0	magnetic flux quantum
π	ratio of a circle's circumference to its diameter

Variables

α	scaling factor of the small junction in a flux qubit loop
α_h	expectation value of the coherent state of a resonator's harmonic
α_n, α_n^*	unitless field amplitude in the resonator and its complex conjugate, respectively
$\alpha_n^{(\mathrm{l})}, \alpha_n^{(\mathrm{r})}$	unitless field amplitudes for left and right traveling waves of mode n, respectively
$\chi(\vec{r})$	phase of the wave function
Δ	minimal energy level splitting of qubit - qubit gap
Δx	discrete cell sizes
$\delta(x)$	Dirac delta function
δ_hd	harmonic-driving frequency detuning
Δ_L	qubit gap of the lasing sample
δ_qd	qubit-drive detuning
δ_qh	qubit-resonator harmonic detuning
$\delta_\mathrm{qp}, \delta_\mathrm{rp}$	qubit-probe and resonator-probe detuning, respectively

δ_{qr}	qubit-resonator detuning
δ_{Rp}	detuning between probe and Rabi frequency
Δ'_k	redefined qubit gap induced by the k-th. resonance with the driving signal
$\delta_{\mathrm{q}k}$	detuning of the qubit frequency from its k-th. resonance with the driving signal
$\delta_{k\mathrm{p}1}, \delta_{k\mathrm{p}2}$	detuning between multiphoton split two level system probing signal
δ_{nm}	Kronecker delta
$\widetilde{\delta}_{\mathrm{qp}}, \widetilde{\delta}_{\mathrm{rp}}, \widetilde{\delta}_{\mathrm{Rp}}$	redefined qubit-probe, resonator-probe, and Rabi-probe detuning including photon decay and decoherence, respectively
$\widetilde{\delta}_{\mathrm{Rp}}$	redefined detuning between probe and Rabi frequency including decoherence
$\widetilde{\delta}_{k\mathrm{p}2}$	redefined detuning between multiphoton split state and probing signal including decoherence
ε	energy bias of qubit
ε_{L}	energy bias of the lasing sample
η	abbreviation for qubit drive as part of the generator of a unitary transformation
$\gamma_{\varphi\mathrm{L}}$	pure dephasing of the lasing sample
Γ_{rL}	relaxation rate of the lasing sample
$\Gamma_{\mathrm{r}}, \Gamma_{\mathrm{e}}, \Gamma_{\varphi}\gamma_{\varphi}$	qubit relaxation, excitation, decoherence, and pure dephasing rate
$\Gamma_{\mathrm{r}}^{(\mathrm{dr})}, \Gamma_{\mathrm{e}}^{(\mathrm{dr})}, \gamma_{\varphi}^{(\mathrm{dr})}$	respective relaxation, excitation, and dephasing rate of the effective dressed two level system
Γ'_{φ}	modified decoherence rate of the qubit
$\Gamma_{\mathrm{r}k}, \Gamma_{\mathrm{e}k}, \gamma_{\varphi k}, \Gamma_{\varphi k}$	respective relaxation, excitation, dephasing, and decoherence rate of the multi-photon dressed qubit
$\Gamma'_{\mathrm{dr}\varphi}$	modified decoherence rate of the effective dressed two level system
Γ_{k1}, Γ_{k2}	abbreviations for including the relaxation to the Maxwell-Bloch equations
λ_{L}	London penetration depth
λ	wavelength
μ_{q}	magneton of a qubit
ν	frequency
$\hat{\Omega}_{\mathrm{R}}$	Rabi operator
Ω'_{cl}	qubit bias dependent driving amplitude of the qubit
ω_0	circular eigenfrequency of the resonator's fundamental mode
Ω_{d}	driving amplitude of the resonator

Ω_h	driving amplitude of the qubit by the signal in the harmonic
ω_h	circular frequency of the qubit harmonic
Ω'_h	argument of the Bessel function
Ω_p	amplitude of the probing field
ω_q	eigenfrequency of the qubit - frequency splitting of the qubit
Ω_R	circular Rabi frequency
ω_d	circular driving frequency
Ω_cl	driving amplitude of the qubit
Ω_R0	on-resonance Rabi frequency
ω_k	circular frequency of mode k in the external transmission line
ω_n	circular frequency of the n-th. resonator mode
ω_p	circular frequency of the probing field
Ω_{k0}	additional on resonance splitting by the driving signal at the k-th. resonance
Ω_k	generalized splitting around the k-th. resonance
χ_1, χ_2	phases of the wave functions on the two sides of Josephson junction
$\hat{\phi}_n$	flux field operator for mode n
$\hat{\varphi}$	generalized coordinate (phase) operator
Φ	magnetic flux
ϕ	flux field variable of the resonator
$\phi^{(\mathrm{l})}, \phi^{(\mathrm{r})}$	time dependent flux field amplitudes for left and right traveling waves, respectively
Φ_e	externally applied magnetic flux
Φ_n	flux in cell n
ϕ_n	time dependent flux field amplitude, canonical variable
$\Psi(\vec{r})$	wave funtion
Ψ_1, Ψ_2	wave functions on the two sides of Josephson junction
φ_1, φ_2	phase difference at the two large junctions of a qubit loop
φ	phase difference at a Josephson junction
$\rho, \rho_\mathrm{S}, \rho_\mathrm{R}, \rho_\mathrm{q}, \rho_\mathrm{r}$	density matrices in general, for a system, a reservoir, the qubit, and the resonator, respectively
ρ_+, ρ_-	sum and difference of the qubit's coherences
ρ_0	population difference between upper and lower qubit level
ρ_{ij}	elements of the density matrix of the effective dressed-two-level system
σ	normal conductance
σ_+, σ_-	rasing and lowering qubit operators, respectively
$\sigma_x, \sigma_y, \sigma_z$	Pauli matrices

τ	mean time of electron lattice interaction
θ	state mixing angle
Ξ	inverse of a transformation matrix
ξ	small expansion parameter
$\vec{A}$	vector potential
$a^\dagger, a$	creation and annihilation operator for the fundamental resonator mode
A_q	area of a flux qubit
A_n, B_n	multiplication constants
$a_n^\dagger, a_n$	creation and annihilation operator for the n-th. mode of the resonator
$b_{k,\mathrm{L}}^\dagger b_{k,\mathrm{L}}, b_{k,\mathrm{R}}^\dagger b_{k,\mathrm{R}}$	creation and annihilation operators in the left and right external transmission lines, respectively
C	capacitance of lumped element representation of the resonator
c	capacitance per unit length
C_c	coupling capacitance of the resonator
C_J	capacitance of Josephson junction
$C_{\mathrm{J}i}$	capacitance of the i-th. Josephson junction of a qubit loop
D	integration sphere
d_q	distance of the qubit from the central conduction line of the resonator
$\langle Y \rangle, \langle Y \rangle_0$	respective expectation value with and without coupling for operator Y
$\vec{E}$	electric field
E_1, E_2	eigenenergies on the two sides of Josephson junction
E_C	charging energy
E_J	Josephson coupling energy
E_k	kinetic energy
$E_{\pm,N}$	eigenenergies of the pair of states on step N of the dressed ladder
f	friction of a qubit due external magnetic field
G	energy gap of a superconductor
g	coupling constant between resonator and qubit
g_Δ, g_ε	respective off-diagonal and diagonal coupling constant
g_h	Hamiltonian of a qubit coupled to the resonator's harmonic
g_L	coupling constant of the lasing sample
$g_\mathrm{dr}, \Gamma_{\mathrm{dr}\varphi}, \Gamma_{\mathrm{dr}1}, \Gamma_{\mathrm{dr}2}$	abbreviations including the coupling and the relaxation processes to the Maxwell-Bloch equations
g_k	coupling constant of the resonator field to the k-th. mode of the external transmission lines
$g_{\mathrm{x}k}, g_{\mathrm{z}k}$	off-diagonal and diagonal effective coupling between fundamental mode and the effective two level system induced by the k-th. resonance
$\mathscr{H}$	Hamilton function

$\tilde{H}_{\mathrm{dr}}$	Hamiltonian of the effective two level system coupled to the fundamental mode
$\tilde{H}_{\mathrm{R}}$	Hamiltonian of the effective two level dressed system
$\tilde{H}_r$	Hamiltonian of the resonator and the external transmission lines
$\vec{\delta H}_{\mathrm{e}}$	magnetic field fluctuations
$\vec{H}$	magnetic field
$\vec{H}_{\mathrm{e}}$	external magnetic field
H	Hamilton operator
H_{a}	driven fundamental mode Hamiltonian
H_{c}	coupling Hamiltonian of qubit and resonator
$H_{\mathrm{h,q}}$	Hamiltonian of a qubit coupled to the resonator's harmonic
H_{p}	Hamiltonian for the probing field
H_{q}	qubit Hamiltonian
h_{q}	vertical dimension of the qubit
H_{t}	total system Hamiltonian
H_d	driving Hamiltonian
$\tilde{I}$	current amplitude
I	current
I_0	zero point current of the resonator
I_{c}	critical current of a Josephson junction
I_{pL}	persistent current of the lasing sample
I_{p}	persistent current of a flux qubit
I_{q}	current operator of the qubit
I_{r}	current in the resonator (operator)
I_n	current in cell n
$I_{C_{\mathrm{c}}}$	current at the coupling capacitance
$\vec{j}_{\mathrm{N}}$	normal current density
$\vec{j}_{\mathrm{S}}$	superconducting current density
j_{c}	critical current density at a Josephson junction
J_l	Bessel function of the first kind
$\lvert 1N\rangle, \lvert 2N\rangle$	dressed-state vectors in the Dirac notation
$\lvert \alpha_{\mathrm{h}}\rangle$	state vector of the coherent state in the harmonic in Dirac notation
$\lvert g,N\rangle, \lvert e,N\rangle$	respective state vectors for ground and excited state qubit and N photons in the resonator in Dirac notation
$\lvert g\rangle, \lvert e\rangle$	state vectors for ground and excited state of the qubit in Dirac notation
$\lvert R\rangle, \lvert L\rangle$	state vectors for qubit states with right and left circulating current in Dirac notation, respectively
$\vec{k}$	wave vector of an electron

K	coupling energy between the wave functions on a Josephson junction
k_n	wave number of the n-th. resonator mode
$\hat{L}$	Lindblad operator of the effective dressed-two-level system
$\hat{L}_q$	Lindblad term of the qubit
$\hat{L}_r$	Lindblad term of the resonator
$\hat{L}_{ij}$	elements of the Lindblad operator of the effective dressed-two-level system
$\mathscr{L}$	Lagrangian
$\mathscr{L}_\mathrm{d}$	Lagrangian density of a transmission line
$\mathscr{L}_\mathrm{r}$	Lagrangian of the resonator
L	inductance of lumped element representation of the resonator
l	inductance per unit length
L_q	inductance of a qubit
l_q	horizontal dimension of the qubit
L_n	lumped element equivalent inductance of the resonator for mode n
M	mutual inductance
m	mass
$\hat{n}$	modified number operator for the dressed-states
N	photon number in the resonator
N_1, N_2	number of cooper pairs (charges) on the independent islands of a Josephson junction
n_1, n_2	densities of cooper pairs on the two sides of Josephson junction
n_N	density of normal charge carriers
n_S	density of superconducting charge carriers
$\hat{p}$	generalized momentum operator
$\hat{p}_n$	canonical momentum (charge field) operator for mode n
p	canonical momentum
$p_\mathrm{g}, p_\mathrm{e}$	probability for qubit ground and excited state, respectively
p_i	generalized momenta in a qubit loop, i is the index of the junction
p_n	canonical momentum of mode n
$\hat{Q}$	charge operator
$\vec{q}$	total wave vector of a cooper pair
Q	electric charge
q_S	cooper pair charge
Q_n	charge in cell n
r	resistance per unit length
R_L	load resistance of the transmission lines
R_N	normal resistance on a Josephson junction

$\vec{S}$	spin vector
S	length of the CPW resonator
s	phase velocity in the coplanar line
$S(\omega)$	noise spectrum
S_{out}	length of the external transmission lines
S_q	influence of the qubit to the transmission of the qubit
$S_q^{(\text{dr})}$	influence of the population of the effective dressed two level system to the transmission of the fundamental mode
$S_X(\omega)$	quantum noise spectral density
S_{S_X}	symmetrized noise spectral density
T	temperature
t	time
T_1, T_2	relaxation and decoherence time, respectively
T_{c}	critical temperature for superconducting phase transition
t_{r}	transmission through the resonator
t_i	initial time
$\hat{U}_i$	unitary transformation operators numbered with i as they appear in the text
U	potential energy
$\mathscr{V}$	interaction energy
$\mathscr{V}_{\text{r}}$	interaction Hamiltonian of the resonator and the external transmission lines
$\tilde{V}$	voltage amplitude
V	voltage
v	particle velocity
V_0	zero point voltage of the resonator
v_{D}	drift velocity
V_{out}	zero point voltage in the external transmission lines
V_{p}	input voltage of the probing field
V_{r}	voltage in the resonator (operator)
V_{in}	input voltage of input field applied to the resonator
V_n	voltage in cell n
$V_{\text{J}i}$	voltage at the i-th. Josephson junction of a qubit loop
$\tilde{x}$	translated coordinate
x, y, z	coordinates
$X_x, X_y, X_\pm$	x-, y-, and secondary components of the noise bath observable, respectively
$X_z, X_\perp$	z- and perpendicular components of a noise bath observable, respec-

	tively
Z	impedance of the transmission line
Z	load resistance and wave impedance of the external lines
Z_c	impedance of the coupling capacitance

References

[1] Gilbert Grynberg, Alain Aspect, and Claude Fabre. *Introduction to Quantum Optics: From the Semi-classical Approach to Quantized Light*. Cambridge University Press, 2010.

[2] J. P. Gordon, H. J. Zeiger, and C. H. Townes. Molecular microwave oscillator and new hyperfine structure in the microwave spectrum of nh3. *Physical Review*, 95(1):282–284, Jul 1954.

[3] T. H. Maiman. Stimulated optical radiation in ruby. *Nature*, 187(4736):493–494, Aug 1960.

[4] J. McKeever, A. Boca, A. D. Boozer, J. R. Buck, and H. J. Kimble. Experimental realization of a one-atom laser in the regime of strong coupling. *Nature*, 425(6955):268–271, Sep 2003.

[5] F. M. Penning. Die Glimmentladung bei niedrigem Druck zwischen koaxialen Zylindern in einem axialen Magnetfeld. *Physica*, 3(9):873–894, Nov 1936.

[6] Wolfgang Paul and Helmut Steinwedel. Notizen: Ein neues Massenspektrometer ohne Magnetfeld. *Zeitschrift für Naturforschung A*, 8(7):448–450, Jan 1953.

[7] Wolfgang Paul. Electromagnetic traps for charged and neutral particles. *Reviews of Modern Physics*, 62(3):531–540, Jul 1990.

[8] D. Wineland and H. Dehmelt. Proposed $10^{14}\delta\nu/\nu$ laser fluorescence spectroscopy on tl+ mono-ion oscillator iii (sideband cooling). *Bull. Am. Phys. Soc.*, 20:637, 1975.

[9] T. W. Hänsch and A. L. Schawlow. Cooling of gases by laser radiation. *Optics Communications*, 13(1):68–69, Jan 1975.

[10] D. J. Wineland, R. E. Drullinger, and F. L. Walls. Radiation-pressure cooling of bound resonant absorbers. *Physical Review Letters*, 40(25):1639–1642, Jun 1978.

[11] Herbert Walther, Benjamin T H Varcoe, Berthold-Georg Englert, and Thomas Becker. Cavity quantum electrodynamics. *Reports on Progress in Physics*, 69(5):1325–1382, Apr 2006.

[12] B. D. Josephson. Possible new effects in superconductive tunnelling. *Physics Letters*, 1(7):251–253, Jul 1962.

[13] A. O. Caldeira and A. J. Leggett. Influence of dissipation on quantum tunneling in macroscopic systems. *Physical Review Letters*, 46(4):211–214, Jan 1981.

[14] A. O. Caldeira and A. J. Leggett. Quantum tunnelling in a dissipative system. *Annals of Physics*, 149(2):374–456, Sep 1983.

[15] S. Washburn, R. Webb, R. Voss, and S. Faris. Effects of dissipation and temperature on macroscopic quantum tunneling. *Physical Review Letters*, 54(25):2712–2715, Jun 1985.

[16] Michel H. Devoret, John M. Martinis, and John Clarke. Measurements of macroscopic quantum tunneling out of the zero-voltage state of a current-biased Josephson junction. *Physical Review Letters*, 55(18):1908–1911, Oct 1985.

[17] J. Clarke, A. N. Cleland, M. H. Devoret, D. Esteve, and J. M. Martinis. Quantum mechanics of a macroscopic variable: The phase difference of a josephson junction. *Science*, 239(4843):992–997, Feb 1988.

[18] F. Balestro, J. Claudon, J. P. Pekola, and O. Buisson. Evidence of two-dimensional macroscopic quantum tunneling of a current-biased dc squid. *Physical Review Letters*, 91(15), Oct 2003.

[19] J. Niemeyer. Eine einfache Methode zur Herstellung kleinster Josephson-Elemente. *PTB-Mitt*, 84:251, 1974.

[20] G. J. Dolan. Offset masks for lift-off photoprocessing. *Applied Physics Letters*, 31(5):337–339, Sep 1977.

[21] Florent Lecocq, Ioan M Pop, Zhihui Peng, Iulian Matei, Thierry Crozes, Thierry Fournier, C'ecile Naud, Wiebke Guichard, and Olivier Buisson. Junction fabrication by shadow evaporation without a suspended bridge. *Nanotechnology*, 22(31):315302, Jul 2011.

[22] Y. Nakamura, Yu. A. Pashkin, and J. S. Tsai. Coherent control of macroscopic quantum states in a single-cooper-pair box. *Nature*, 398(6730):786–788, Apr 1999.

[23] J. E. Mooij, T. P. Orlando, L. Levitov, Lin Tian, Caspar H. van der Wal, and Seth Lloyd. Josephson persistent-current qubit. *Science*, 285(5430):1036–1039, Aug 1999.

[24] T. Orlando, J. Mooij, Lin Tian, Caspar van der Wal, L. Levitov, Seth Lloyd, and J. Mazo. Superconducting persistent-current qubit. *Physical Review B*, 60(22):15398–15413, Dec 1999.

[25] V. Bouchiat, D. Vion, P. Joyez, D. Esteve, and M. H. Devoret. Quantum coherence with a single cooper pair. *Physica Scripta*, T76(1):165, 1998.

[26] K. W. Lehnert, K. Bladh, L. F. Spietz, D. Gunnarsson, D. I. Schuster, P. Delsing, and R. J. Schoelkopf. Measurement of the excited-state lifetime of a microelectronic circuit. *Physical Review Letters*, 90(2):027002, Jan 2003.

[27] D. Born, V. I. Shnyrkov, W. Krech, Th. Wagner, E. Il'ichev, M. Grajcar, U. Hübner, and H.-G. Meyer. Reading out the state inductively and microwave spectroscopy of an interferometer-type charge qubit. *Physical Review B*, 70(18):180501(R), Nov 2004.

[28] A. Fay, E. Hoskinson, F. Lecocq, L. P. Lévy, F. W. J. Hekking, W. Guichard, and O. Buisson. Strong tunable coupling between a superconducting charge and phase qubit. *Physical Review Letters*, 100(18), May 2008.

[29] Jens Koch, Terri Yu, Jay Gambetta, A. Houck, D. Schuster, J. Majer, Alexandre Blais, M. Devoret, S. Girvin, and R. Schoelkopf. Charge-insensitive qubit design derived from the cooper pair box. *Physical Review A*, 76(4):042319, Oct 2007.

[30] J. A. Schreier, A. A. Houck, Jens Koch, D. I. Schuster, B. R. Johnson, J. M. Chow, J. M. Gambetta, J. Majer, L. Frunzio, M. H. Devoret, and et al. Suppressing charge noise decoherence in superconducting charge qubits. *Physical Review B*, 77(18):180502(R), May 2008.

[31] Edward Farhi, Jeffrey Goldstone, Sam Gutmann, and Michael Sipser. Quantum computation by adiabatic evolution. quant-ph/0001106, 2000.

[32] M. Grajcar, A. Izmalkov, and E. Il'ichev. Possible implementation of adiabatic quantum algorithm with superconducting flux qubits. *Physical Review B*, 71:144501, 2005.

[33] S. Ashhab, J. R. Johansson, and Franco Nori. Decoherence in a scalable adiabatic quantum computer. *Physical Review A*, 74(5):052330, 2006.

[34] Ya. Greenberg, A. Izmalkov, M. Grajcar, E. Il'ichev, W. Krech, H.-G. Meyer, M. Amin, and Alec van den Brink. Low-frequency characterization of quantum tun-

neling in flux qubits. *Physical Review B*, 66(21):214525, Dec 2002.

[35] E. Il'ichev, Th. Wagner, L. Fritzsch, J. Kunert, V. Schultze, T. May, H. E. Hoenig, H. G. Meyer, M. Grajcar, D. Born, and et al. Characterization of superconducting structures designed for qubit realizations. *Applied Physics Letters*, 80(22):4184, 2002.

[36] E. Il'ichev, N. Oukhanski, A. Izmalkov, Th. Wagner, M. Grajcar, H.-G. Meyer, A. Yu. Smirnov, Alec Maassen van den Brink, M. H. S. Amin, and A. M. Zagoskin. Continuous monitoring of rabi oscillations in a Josephson flux qubit. *Physical Review Letters*, 91(9):097906, Aug 2003.

[37] M. Grajcar, A. Izmalkov, S. H. W. van der Ploeg, S. Linzen, E. Il'ichev, Th. Wagner, U. Hübner, H. G. Meyer, Alec Maassen van den Brink, S. Uchaikin, and A. M. Zagoskin. Direct josephson coupling between superconducting flux qubits. *Physical Review B*, 72,:020503 (R), 2005.

[38] A. Izmalkov, M. Grajcar, E. Il'ichev, Th. Wagner, H.-G. Meyer, A. Smirnov, M. Amin, Alec van den Brink, and A. Zagoskin. Evidence for entangled states of two coupled flux qubits. *Physical Review Letters*, 93(4):037003, Jul 2004.

[39] A. Izmalkov, M. Grajcar, S. H. W. van der Ploeg, U. Hübner, E. Il'ichev, H.-G. Meyer, and A. M. Zagoskin. Measurement of the ground-state flux diagram of three coupled qubits as a first step towards the demonstration of adiabatic quantum computation. *Europhysics Letters*, 76(3):533–539, Nov 2006.

[40] M. Grajcar, A. Izmalkov, S. H. W. van der Ploeg, S. Linzen, T. Plecenik, Th. Wagner, U. Hübner, E. Il'ichev, H.-G. Meyer, A. Yu. Smirnov, Peter J. Love, Alec Maassen van den Brink, M. H. S. Amin, S. Uchaikin, and A. M Zagoskin. Four-qubit device with mixed couplings. *Physical Review Letters*, 96(4):047006, Feb 2006.

[41] Alexandre Blais, Alexander Maassen van den Brink, and Alexandre M. Zagoskin. Tunable coupling of superconducting qubits. *Physical Review Letters*, 90(12):127901, Mar 2003.

[42] Alec Maassen van den Brink, A. J. Berkley, and M. Yalowsky. Mediated tunable coupling of flux qubits. *New Journal of Physics*, 7:230–230, Jan 2005.

[43] S. H. W. van der Ploeg, A. Izmalkov, Alec van den Brink, U. Hübner, M. Grajcar, E. Il'ichev, H.-G. Meyer, and A. Zagoskin. Controllable coupling of superconducting flux qubits. *Physical Review Letters*, 98(5):057004, Feb 2007.

[44] Peter Groszkowski, Austin G. Fowler, Felix Motzoi, and Frank K. Wilhelm. Tunable coupling between three qubits as a building block for a superconducting quantum computer. *Physical Review B*, 84(14), Oct 2011.

[45] Erik Lucero, M. Hofheinz, M. Ansmann, Radoslaw C. Bialczak, N. Katz, Matthew Neeley, A. D. O'Connell, H. Wang, A. N. Cleland, and John M. Martinis. High-fidelity gates in a single Josephson qubit. *Physical Review Letters*, 100(24):247001, Jun 2008.

[46] J. M. Chow, J. M. Gambetta, L. Tornberg, Jens Koch, Lev S. Bishop, A. A. Houck, B. R. Johnson, L. Frunzio, S. M. Girvin, and R. J. Schoelkopf. Randomized benchmarking and process tomography for gate errors in a solid-state qubit. *Physical Review Letters*, 102(9):090502, Mar 2009.

[47] T. Yamamoto, Yu. A. Pashkin, O. Astafiev, Y. Nakamura, and J. S. Tsai. Demonstration of conditional gate operation using superconducting charge qubits. *Nature*, 425(6961):941–944, Oct 2003.

[48] J. H. Plantenberg, P. C. de Groot, C. J. P. M. Harmans, and J. E. Mooij. Demonstration of controlled-not quantum gates on a pair of superconducting quantum bits. *Nature*, 447(7146):836–839, Jun 2007.

[49] A. O. Niskanen, K. Harrabi, F. Yoshihara, Y. Nakamura, S. Lloyd, and J. S. Tsai. Quantum coherent tunable coupling of superconducting qubits. *Science*, 316(5825):723–726, May 2007.

[50] I. Siddiqi, R. Vijay, F. Pierre, C. M. Wilson, M. Metcalfe, C. Rigetti, L. Frunzio, and M. H. Devoret. RF-driven Josephson bifurcation amplifier for quantum measurement. *Physical Review Letters*, 93(20):207002, Nov 2004.

[51] R. McDermott, R.W. Simmonds, M. Steffen, K.B. Cooper, K. Cicak, K.D. Osborn, Seongshik Oh, D.P. Pappas, and John M. Martinis. Simultaneous state measurement of coupled Josephson phase qubits. *Science*, 307(5713):1299–1302, Feb 2005.

[52] M. Steffen, M. Ansmann, R. C. Bialczak, N. Katz, E. Lucero, R. McDermott, M. Neeley, E. M. Weig, A. N. Cleland, and J. M. Martinis. Measurement of the entanglement of two superconducting qubits via state tomography. *Science*, 313(5792):1423–1425, Sep 2006.

[53] L. DiCarlo, J. M. Chow, J. M. Gambetta, Lev S. Bishop, B. R. Johnson, D. I. Schuster,

J. Majer, A. Blais, L. Frunzio, S. M. Girvin, and et al. Demonstration of two-qubit algorithms with a superconducting quantum processor. *Nature*, 460(7252):240–244, Jun 2009.

[54] A. Fedorov, L. Steffen, M. Baur, M. P. da Silva, and A. Wallraff. Implementation of a toffoli gate with superconducting circuits. *Nature*, 481(7380):170–172, Dec 2011.

[55] John Clarke and Frank K. Wilhelm. Superconducting quantum bits. *Nature*, 453(7198):1031–1042, Jun 2008.

[56] R. McDermott. Materials origins of decoherence in superconducting qubits. *IEEE Transactions on Applied Superconductivity*, 19(1):2–13, Feb 2009.

[57] F. G. Paauw, A. Fedorov, C. J. P. M Harmans, and J. E. Mooij. Tuning the gap of a superconducting flux qubit. *Physical Review Letters*, 102(9):090501, Mar 2009.

[58] Alexandre Blais, Ren-Shou Huang, Andreas Wallraff, S. Girvin, and R. Schoelkopf. Cavity quantum electrodynamics for superconducting electrical circuits: An architecture for quantum computation. *Physical Review A*, 69(6):062320, Jun 2004.

[59] A. Wallraff, D. I. Schuster, A. Blais, L. Frunzio, R.-S. Huang, J. Majer, S. Kumar, S. M. Girvin, and R. J. Schoelkopf. Strong coupling of a single photon to a superconducting qubit using circuit quantum electrodynamics. *Nature*, 431(7005):162–167, Sep 2004.

[60] Abdufarrukh Abdumalikov, Oleg Astafiev, Yasunobu Nakamura, Yuri Pashkin, and JawShen Tsai. Vacuum rabi splitting due to strong coupling of a flux qubit and a coplanar-waveguide resonator. *Physical Review B*, 78(18):180502(R), Nov 2008.

[61] G. Oelsner, S. H. W. van der Ploeg, P. Macha, U. Hübner, D. Born, S. Anders, E. Il'ichev, H.-G. Meyer, M. Grajcar, S. Wünsch, M. Siegel, A. N. Omelyanchouk, and O. Astafiev. Weak continuous monitoring of a flux qubit using coplanar waveguide resonator. *Physical Review B*, 81(17):172505 (R), May 2010.

[62] Hanhee Paik, D. I. Schuster, Lev S. Bishop, G. Kirchmair, G. Catelani, A. P. Sears, B. R. Johnson, M. J. Reagor, L. Frunzio, L. I. Glazman, and et al. Observation of high coherence in Josephson junction qubits measured in a three-dimensional circuit qed architecture. *Physical Review Letters*, 107(24):240501, Dec 2011.

[63] Chad Rigetti, Jay M. Gambetta, Stefano Poletto, B. L. T. Plourde, Jerry M. Chow, A. D. Córcoles, John A. Smolin, Seth T. Merkel, J. R. Rozen, George A. Keefe, and

et al. Superconducting qubit in a waveguide cavity with a coherence time approaching 0.1 ms. *Physical Review B*, 86(10):100506(R), Sep 2012.

[64] J. Q. You and Franco Nori. Atomic physics and quantum optics using superconducting circuits. *Nature*, 474(7353):589–597, Jun 2011.

[65] O. Astafiev, A. M. Zagoskin, A. A. Abdumalikov, Yu. A. Pashkin, T. Yamamoto, K. Inomata, Y. Nakamura, and J. S. Tsai. Resonance fluorescence of a single artificial atom. *Science*, 327(5967):840–843, Feb 2010.

[66] Mika A. Sillanpää, Jian Li, Katarina Cicak, Fabio Altomare, Jae I. Park, Raymond W. Simmonds, G. S. Paraoanu, and Pertti J. Hakonen. Autler-townes effect in a superconducting three-level system. *Physical Review Letters*, 103(19):193601, Nov 2009.

[67] A. A. Abdumalikov, O. Astafiev, A. M. Zagoskin, Yu. A. Pashkin, Y. Nakamura, and J. S. Tsai. Electromagnetically induced transparency on a single artificial atom. *Physical Review Letters*, 104(19):193601, May 2010.

[68] O. Astafiev, K. Inomata, A. O. Niskanen, T. Yamamoto, Yu. A. Pashkin, Y. Nakamura, and J. S. Tsai. Single artificial-atom lasing. *Nature*, 449(7162):588–590, Oct 2007.

[69] H. Kamerlingh Onnes. Further experiments with liquid helium. d. on the change of electrical resistance of pure metals at very low temperatures, etc. v. the disappearance of the resistance of mercury. *KNAW, Proceedings*, 14:113–115, May 1911.

[70] W. Buckel and Reinhold Kleiner. *Superconductivity: Fundamentals and Applications (Physics)*. Wiley-VCH, 2004.

[71] J. Bardeen, L. N. Cooper, and J. R. Schrieffer. Theory of superconductivity. *Physical Review*, 108(5):1175–1204, Dec 1957.

[72] W. Meissner and R. Ochsenfeld. Ein neuer effekt bei eintritt der supraleitfähigkeit. *Die Naturwissenschaften*, 21(44):787–788, Nov 1933.

[73] F. London and H. London. The electromagnetic equations of the supraconductor. *Proceedings of the Royal Society of London. Series A, Mathematical and PhysicalSciences*, 149(866):71–88, Mar 1935.

[74] Siegfried Hunklinger. *Festkörperphysik*. Oldenbourg Wissensch.Vlg, 2007.

[75] V.L. Ginzburg and L.D. Landau. On the theory of superconductivity. In Dirk Ter-Haar, editor, *L. D. Landau, Collected papers*, chapter 73, page 546. Oxford, Pergamon Press, 1965.

[76] R. Doll and M. Näbauer. Experimental proof of magnetic flux quantization in a superconducting ring. *Physical Review Letters*, 7(2):51–52, Jul 1961.

[77] Bascom Deaver and William Fairbank. Experimental evidence for quantized flux in superconducting cylinders. *Physical Review Letters*, 7(2):43–46, Jul 1961.

[78] Robert B. Leighton, Matthew Sands, and Richard P. Feynman. *Feynman Vorlesungen über Physik 3, Quantenmechanik*. Oldenbourg Wissensch.Vlg, 1988.

[79] W. C. Stewart. Current-voltage characteristics of josephson junctions. *Applied Physics Letters*, 12(8):277, 1968.

[80] D. E. McCumber. Tunneling and weak-link superconductor phenomena having potential device applications. *Journal of Applied Physics*, 39(6):2503, 1968.

[81] K. K. Likharev. *Dynamics of Josephson Junctions and Circuits*. CRC Press, 1986.

[82] Yuriy Makhlin, Gerd Schön, and Alexander Shnirman. Quantum-state engineering with josephson-junction devices. *Reviews of Modern Physics*, 73(2):357–400, May 2001.

[83] Yuriy Makhlin and Alexander Shnirman. Dephasing of solid-state qubits at optimal points. *Physical Review Letters*, 92(17):178301, Apr 2004.

[84] D. Vion, A. Aassime, A. Cottet, P. Joyez, C. Pothier, C. Urbina, D. Esteve, and M. H.. Devoret. Manipulating the quantum state of an electrical circuit. *Science*, 296(5569):886–889, May 2002.

[85] F. Yoshihara, K. Harrabi, A. Niskanen, Y. Nakamura, and J. Tsai. Decoherence of flux qubits due to 1/f flux noise. *Physical Review Letters*, 97(16):167001, Oct 2006.

[86] P. Macha, S. H. W. van der Ploeg, G. Oelsner, E. Il'ichev, H.-G. Meyer, S. Wünsch, and M. Siegel. Losses in coplanar waveguide resonators at millikelvin temperatures. *Applied Physics Letters*, 96(6):062503, 2010.

[87] G. Ithier, E. Collin, P. Joyez, P. Meeson, D. Vion, D. Esteve, F. Chiarello, A. Shnirman, Y. Makhlin, J. Schriefl, and G. Schön. Decoherence in a superconducting quantum bit circuit. *Physical Review B*, 72(13):134519, Oct 2005.

[88] Julian Hauss, Arkady Fedorov, Stephan André, Valentina Brosco, Carsten Hutter, Robin Kothari, Sunil Yeshwanth, Alexander Shnirman, and Gerd Schön. Dissipation in circuit quantum electrodynamics: lasing and cooling of a low-frequency oscillator. *New Journal of Physics*, 10(9):095018, Sep 2008.

[89] F. Bloch. Generalized theory of relaxation. *Physical Review*, 105(4):1206–1222, Feb 1957.

[90] A. G. Redfield. On the theory of relaxation processes. *IBM Journal of Research and Development*, 1(1):19–31, Jan 1957.

[91] Marlan O. Scully and M. Suhail Zubairy. *Quantum Optics*. Cambridge University Press, 1997.

[92] M. Göppl, A. Fragner, M. Baur, R. Bianchetti, S. Filipp, J. M. Fink, P. J. Leek, G. Puebla, L. Steffen, and A. Wallraff. Coplanar waveguide resonators for circuit quantum electrodynamics. *Journal of Applied Physics*, 104(11):113904, 2008.

[93] A. N. Omelyanchouk, S. N. Shevchenko, Ya. S. Greenberg, O. Astafiev, and E. Il'ichev. Quantum behavior of a flux qubit coupled to a resonator. *Low Temperature Physics*, 36(10):893, 2010.

[94] Christian Kraglund Andersen, Gregor Oelsner, Evgeni Il'ichev, and Klaus Mølmer. Quantized resonator field coupled to a current-biased Josephson junction in circuit qed. *Physical Review A*, 89(3):033853, Mar 2014.

[95] Bernard Yurke and John Denker. Quantum network theory. *Physical Review A*, 29(3):1419–1437, Mar 1984.

[96] Wolfgang P. Schleich. *Quantum Optics in Phase Space*. Wiley-VCH, 2001.

[97] R.-S. Huang. *Qubit-resonaor system as an application to quantum computation*. PhD thesis, Department of Physics, Indiana Universty, 2004.

[98] H. Bateman. On dissipative systems and related variational principles. *Physical Review*, 38(4):815–819, Aug 1931.

[99] H. Dekker. Classical and quantum mechanics of the damped harmonic oscillator. *Physics Reports*, 80(1):1–110, Dec 1981.

[100] M. Grajcar, S. H. W. van der Ploeg, A. Izmalkov, E. Il'ichev, H.-G. Meyer, A. Fedorov, A. Shnirman, and Gerd Schön. Sisyphus cooling and amplification by a superconducting qubit. *Nature Physics*, 4(8):612–616, Jul 2008.

[101] Christian Enss and Siegfried Hunklinger. *Tieftemperaturphysik*. Springer Berlin Heidelberg, 2000.

[102] M. Kamon, M.J. Ttsuk, and J.K. White. Fasthenry: a multipole-accelerated 3-D induc-

tance extraction program. *IEEE Trans. Microwave Theory Techn.*, 42(9):1750–1758, 1994.

[103] Yu-xi Liu, J. Q. You, L. F. Wei, C. P. Sun, and Franco Nori. Optical selection rules and phase-dependent adiabatic state control in a superconducting quantum circuit. *Physical Review Letters*, 95(8):087001, Aug 2005.

[104] Yu-xi Liu, Cheng-Xi Yang, Hui-Chen Sun, and Xiang-Bin Wang. Coexistence of single- and multi-photon processes due to longitudinal couplings between superconducting flux qubits and external fields. *New Journal of Physics*, 16(1):015031, Jan 2014.

[105] S. N. Shevchenko, S. Ashhab, and Franco Nori. Inverse landau-zener-stückelberg problem for qubit-resonator systems. *Physical Review B*, 85(9):094502, Mar 2012.

[106] Ya. Greenberg and E. Il'ichev. Quantum theory of the low-frequency linear susceptibility of interferometer-type superconducting qubits. *Physical Review B*, 77(9):094513, Mar 2008.

[107] F. Bloch. Nuclear induction. *Physical Review*, 70(7-8):460–474, Oct 1946.

[108] Yvan Castin and Klaus Mølmer. Maxwell-bloch equations: A unified view of nonlinear optics and nonlinear atom optics. *Physical Review A*, 51(5):R3426–R3428, May 1995.

[109] S. N. Shevchenko, G. Oelsner, Ya. S. Greenberg, P. Macha, D. S. Karpov, M. Grajcar, U. Hübner, A. N. Omelyanchouk, and E. Il'ichev. Amplification and attenuation of a probe signal by doubly dressed states. *Physical Review B*, 89(18):184504, May 2014.

[110] C Cohen-Tannoudji, J. Dupont-Rock, and G. Grynberg. *Atom-Photon Interactions, Basic Principles and Applications*. John Wiley, 1998.

[111] Ya. Greenberg and E. Il'ichev. Low-frequency rabi spectroscopy of dissipative two-level systems: Dressed-state approach. *Physical Review B*, 76(10):104520, Sep 2007.

[112] G. Oelsner, P. Macha, O. V. Astafiev, E. Il'ichev, M. Grajcar, U. Hübner, B. I. Ivanov, P. Neilinger, and H.-G. Meyer. Dressed-state amplification by a single superconducting qubit. *Physical Review Letters*, 110(5):053602, Jan 2013.

[113] U. Fano. Effects of configuration interaction on intensities and phase shifts. *Physical Review*, 124(6):1866–1878, Dec 1961.

[114] E. del Valle and F. P. Laussy. Regimes of strong light-matter coupling under incoherent

excitation. *Physical Review A*, 84(4):043816, Oct 2011.

[115] Ya. S. Greenberg, E. Il'ichev, G. Oelsner, and S. N. Shevchenko. Resonance at the rabi frequency in a superconducting flux qubit. *AIP Conference Proceedings*, 1619:89, 2014.

[116] P. Neilinger, M. Rehák, M. Grajcar, G. Oelsner, U. Hübner, and E. Il'ichev. Two-photon lasing by a superconducting qubit. *Physical Review B*, 91(10):104516, Mar 2015.

[117] D. S. Karpov, G. Oelsner, S. N. Shevchenko, Ya. S. Greenberg, and E. Il'ichev. Signal amplification in a qubit-resonator system. *Low Temperature Physics*, 42(3):189–195, Mar 2016.

[118] D.-G. Welsch. Lecture notes: Statistische Physik. University Lecture, 2006.

[119] J. R. Schrieffer and P. A. Wolff. Relation between the anderson and kondo hamiltonians. *Physical Review*, 149(2):491–492, Sep 1966.

[120] P. Neilinger, S. N. Shevchenko, J. Bogar, M. Rehak, G. Oelsner, D. S. Karpov, U. Hübner, O. Astafiev, M. Grajcar, and E. Il'ichev. Landau-zener-stückelberg-majorana lasing in circuit quantum electrodynamics. *Physical Review B*, 94(9):094519, Sep 2016.

Publications in Peer-reviewed Journals

[P 1] P. Macha, S. H. W. van der Ploeg, G. Oelsner, E. Il'ichev, H.-G. Meyer, S. Wünsch, and M. Siegel, Losses in coplanar waveguide resonators at millikelvin temperatures. *Applied Physics Letters* 96, 062503 (2010)

[P 2] G. Oelsner, S. H. W. van der Ploeg, P. Macha, U. Hübner, D. Born, S. Anders, E. Il'ichev, H.-G. Meyer, M. Grajcar, S. Wünsch, M. Siegel, A. N. Omelyanchouk, and O. Astafiev, Weak continuous monitoring of a flux qubit using coplanar waveguide resonator. *Physical Review B* 81, 172505(R) (2010)

[P 3] G. Oelsner, P. Macha, O. V. Astafiev, E. Il'ichev, M. Grajcar, U. Hübner, B. I. Ivanov, P. Neilinger, and H.-G. Meyer, Dressed-State Amplification by a Single Superconducting Qubit. *Physical Review Letters* 110, 053602 (2013)

[P 4] G. Oelsner, L. S. Revin, E. Il'ichev, A. L. Pankratov, H.-G. Meyer, L. Grönberg, J. Hassel, L. S. Kuzmin, Underdamped Josephson junction as a switching current detector. *Applied Physics Letters* 103, 142605 (2013)

[P 5] C. K. Andersen, G. Oelsner, E. Il'ichev, and K. Mølmer, Quantized resonator field coupled to a current-biased Josephson junction in circuit QED. *Physical Review A* 89, 033853 (2014)

[P 6] M. Rehák, P. Neilinger, M. Grajcar, G. Oelsner, U. Hübner, E. Il'ichev, and H.-G. Meyer, Parametric amplification by coupled flux qubits. *Applied Physics Letters* 104, 162604 (2014)

[P 7] S. N. Shevchenko, G. Oelsner, Ya. S. Greenberg, P. Macha, D. S. Karpov, M. Grajcar, U. Hübner, A. N. Omelyanchouk, and E. Il'ichev, Amplification and attenuation of a probe signal by doubly dressed states. *Physical Review B* 89, 184504 (2014)

[P 8] P. Macha, G. Oelsner, J.-M. Reiner, M. Marthaler, S. André, G. Schön, U. Hübner, H.-

G. Meyer, E. Il'ichev, and A. V. Ustinov, Implementation of a quantum metamaterial using superconducting qubits. *Nature Communications* 5, 5146 (2014)

[P 9] Ya. S. Greenberg, E. Il'ichev, G. Oelsner, and S. N. Shevchenko, Resonance at the Rabi frequency in a superconducting flux qubit. *AIP Conference Proceedings* 1619, 89 (2014)

[P 10] P. Neilinger, M. Rehák, M. Grajcar, G. Oelsner, U. Hübner, and E. Il'ichev, Two-photon lasing by a superconducting qubit. *Physical Review B* 91, 104516 (2015)

[P 11] P. Neilinger, G. Oelsner, M. Grajcar, B. I. Ivanov, I. L. Novikov, and E. V. Il'ichev, A microwave splitter for superconducting quantum circuits. *Technical Physics Letters*, 41, 314 (2015)

[P 12] D. S. Karpov, G. Oelsner, S. N. Shevchenko, Ya. S. Greenberg, and E. Il'ichev, Signal amplification in a qubit-resonator system. *Low Temperature Physics* 42, 246 (2016)

Conference Contributions

[C 1] G. Oelsner, S. H. W. van der Ploeg, E. Il'ichev, and H.-G. Meyer, Towards a readout of flux qubits using ballistic fluxons. *Euroflux*, Avignon, France, (2009)

[C 2] G. Oelsner, S. H. W. van der Ploeg, and E. Il'ichev, Towards a ballistic readout system for flux qubits at 10 mK. *S-PULSE Savoie workshop on Superconducting Electronics*, Chambery, France (2009)

[C 3] G. Oelsner, S. H. W. van der Ploeg, M. Grajcar, P. Macha, U. Hübner, D. Born, E. Il'ichev, H.-G. Meyer, S. Wünsch, and M. Siegel, High frequency readout of supeconducting flux qubit *Kryoelektronische Bauelemente* Oberhof, Germany (2009)

[C 4] G. Oelnser, M. Grajcar, P. Macha, O. Astafiev, E. Il'ichev, H.-G. Meyer, Nonlinear effects in a driven flux qubit - oscillator system. *Superconductivity Centennial Conference 2011 EUCAS-ISEC-ICMC 2011* The Hague, The Netherlands (2011)

[C 5] G. Oelsner, P. Macha, E. Il'ichev, M. Grajcar, O. Astafiev, U. Hübner, S. Anders, and H.-G. Meyer, Single atom lasing of a dressed flux qubit. *SOLID workshop*, Grenoble, France (2012)

[C 6] P. Macha, G. Oelsner, M. Jerger, U. Hübner, S. Butz, E. Il'ichev, A. V. Ustinov, and H.-G. Meyer, Quantum metamaterials with superconducting flux qubits. *76. Jahrestagung der DPG und DPG-Frühjahrstagung*, Berlin, Germany (2012)

[C 7] G. Oelsner, P. Macha, M. Grajcar, O. Astafiev, E. Il'ichev, B. Ivanov, U. Hübner, S. Anders, and H.-G. Meyer, Single atom lasing of a dressed flux qubit *76. Jahrestagung der DPG und DPG-Frühjahrstagung*, Berlin, Germany (2012)

[C 8] G. Oelsner, Ya. S. Greenberg, P. Macha, O. Astafiev, E. Il'ichev, M. Grajcar, B. Ivanov, U. Hübner, P. Neilinger, and H.-G. Meyer, Interactions of a microwave-dressed-qubit with a quantum harmonic oscillator. *Mesoscopic Structures: Fundamentals and Ap-*

plications (MSFA) Novosibirsk, Russia (2013)

[C 9] P. Neilinger, M. Grajcar, G. Oelsner, P. Macha, B. Ivanov, and E. Il'ichev, Parametric amplification using nonlinearity of superconducting flux qubit. *Mesoscopic Structures: Fundamentals and Applications (MSFA)* Novosibirsk, Russia (2013)

[C 10] P. Macha, G. Oelsner, J.-M. Reiner, M. Marthaler, S. André, G. Schön, U. Hübner, H.-G. Meyer, E. Il'ichev, and A.V. Ustinov, Superconducting qubits coupled to a resonator: a path towards quantum metamaterials. *Mesoscopic Structures: Fundamentals and Applications (MSFA)* Novosibirsk, Russia (2013)

[C 11] P. Neilinger, M. Trgala, M. Ženlička, M. Grajcar, P. Szabo, P. Samuely, G. Oelsner, U. Hübner, and E. Il'ichev, Comparison of finite quasiparticle lifetime in disordered superconductors measured by microwaves and tunneling spectroscopy. *Mesoscopic Structures: Fundamentals and Applications (MSFA)* Novosibirsk, Russia (2013)

[C 12] G. Oelsner, L. S. Revin, E. Il'ichev, A. L. Pankratov, B. Ivanov, H.-G. Meyer, L. Grönberg, J. Hassel, L.S. Kuzmin, Underdamped Josephson junction as a switching current detector. *Corfu Summer Institute - iQIT integrated Quantum Information Technology*, Corfu, Greece (2013)

[C 13] G. Oelsner and E. Il'ichev, Underdamped Josephson Junction as quantum detector. *Superconducting Nanocircuits (SNC)*, Maratea, Italy (2014)

Ehrenwörtliche Erklärung

Ich erkläre hiermit ehrenwörtlich, dass ich die vorliegende Arbeit selbstständig, ohne unzulässige Hilfe Dritter und ohne Benutzung anderer als der angegebenen Hilfsmittel und Literatur angefertigt habe. Die aus anderen Quellen direkt oder indirekt übernommenen Daten und Konzepte sind unter Angabe der Quellen gekennzeichnet.

Bei der Auswahl und Auswertung folgenden Materials haben mir die nachstehend aufgeführten Personen in der jeweils beschriebenen Weise unentgeltlich geholfen:

1. Mit Prof. Evgeni Il'ichev diskutierte ich die experimentellen Ergebnisse.
2. Die in der Arbeit präsentierten Proben wurden im Reinraum von Uwe Hübner und Solveig Anders nach von mir erstellten Designs hergestellt.

Weitere Personen waren an der inhaltlich-materiellen Erstellung der vorliegenden Arbeit nicht beteiligt. Insbesondere habe ich hierfür nicht die entgeltliche Hilfe von Vermittlungs- bzw. Beratungsdiensten (Promotionsberater oder andere Personen) in Anspruch genommen. Niemand hat von mir unmittelbar oder mittelbar geldwerte Leistungen für Arbeiten erhalten, die im Zusammenhang mit dem Inhalt der vorgelegten Dissertation stehen.

Die Arbeit wurde bisher weder im In- noch im Ausland in gleicher oder ähnlicher Form einer anderen Prüfungsbehörde vorgelegt.

Die geltende Promotionsordnung der Physikalisch-Astronomischen Fakultät ist mir bekannt.

Ich versichere ehrenwörtlich, dass ich nach dem besten Wissen die reine Wahrheit gesagt und nichts verschwiegen habe.

Jena, 25. April 2016 Unterschrift des Verfassers

Zusammenfassung

In dieser Arbeit werden die Wechselwirkungen eines künstlichen Atoms mit einem Resonator hoher Güte untersucht und daraus ein neues Konzept zur Erzeugung schmalbandiger, kohärenter Mikrowellenstrahlung (Lasing) entwickelt. Das System entspricht dabei der klassischen Architektur der Quantenelektrodynamik in einer Kavität. Dabei wird ein supraleitendes Qubit als Atom genutzt. Dies ist ein supraleitender Ring, der mindestens einen Josephson Kontakt als nicht lineares Element enthält. Das Qubit kann daher als ein Harmonischer Oszillator mit nicht-linearem Potential verstanden werden. Damit entsteht ein Objekt mit nicht äquidistanten Energieniveaus, sodass einzelne Übergänge mit verschiedenen Frequenzen angeregt werden können.

Seit dem Nachweis und der Manipulation kohärenter Oszillationen eines supraleitenden Schaltkreises [22] entwickelt sich das Feld solcher Festkörperquantensysteme hauptsächlich in zwei Richtungen. Auf der einen Seite stehen Experimente mit dem Ziel eines funktionierenden Quantencomputers. Der Fokus liegt dabei auf der Realisierung von Quantengates [45–54] und der Verbesserung der Kohärenz [30, 57, 62, 63]. Wie auch der vorliegenden Arbeit zu entnehmen, zeigen sich andererseits in vielen Experimenten Parallelen zwischen natürlichen Atomen und Festkörperquantensysteme. Dies konnte eindrucksvoll anhand von originär quantenoptischen Experimenten an supraleitenden Quantenschaltkreisen gezeigt werden. Dazu zählen die Beobachtung der Vakuum-Rabi Aufspaltung [59], die Resonanzfluoreszenz eines einzelnen Qubits [65], die Beobachtung des Autler-Townes Effektes [66] und die elektromagnetisch induzierte Transparenz [67].

Bei experimentellen Untersuchungen macht man sich die hohe Kontrollierbarkeit dieser makroskopischen Quantensysteme zunutze. Da diese als Schaltkreise entworfen und hergestellt werden, kann z.B. das Regime starker Kopplung relativ einfach erreicht und kontrolliert werden [59,60]. Dies bedeutet, dass die Kopplung zwischen dem Strahlungsfeld und dem künstlichen Atom jegliche Verlustprozesse der beteiligten Systeme übersteigt. Letztere sind aller-

dings bei supraleitenden Quantensystemen signifikant höher als die entsprechenden Raten bei natürlichen Atomen, was ebenfalls eine Auswirkung der Größe der Schaltkreise und der damit einhergehenden starken Kopplung an Störfeldern ist. Damit konnte die starke Kopplung eines einzelnen Festkörperquantensystems an das Strahlungsfeld in einer supraleitenden Kavität zur Realisierung eines Einzel-Atom-Lasers im Mikrowellenbereich genutzt werden [68]. Hier wurden drei Energielevel des künstlichen Quantenobjektes verwendet. Mit voller Kontrolle über den Übergang vom niedrigsten zum höchsten Level und einer schnellen Relaxation in das mittlere Niveau konnte eine Besetzungsinversion erzeugt werden. Das klassische Laser Regime ist damit reproduziert [1].

Im Gegensatz dazu zeigt und analysiert diese Arbeit erstmals ein Konzept, in dem ausschließlich zwei Energieniveaus benötigt werden, um eine inverse Besetzung zu erzeugen und Lasing eines einzelnen künstlichen Atoms nachzuweisen.

Dazu werden zunächst die beiden hier verwendeten Komponenten eines solchen Einzel-Atom-Lasers, das Flussqubit als künstliches Zwei-Niveau-System und der supraleitende Resonator als Strahlungskavität, beschrieben und theoretisch analysiert. Physikalische Grundprinzipien, supraleitende Effekte und die Geometrie der Systeme ermöglichen eine quantenoptische Beschreibung. Diese beinhaltet ebenfalls die Kopplung an die Umgebung. Mit einer allgemeinen Reservoir-Theorie können die dissipativen Prozesse, wie Relaxation und Dekohärenz im Qubit sowie das Abklingen der Photonenzahl und die Linienbreite des Resonators, begründet und mathematisch erfasst werden. Dies dient als Grundlage zur Beschreibung und Analyse von experimentellen Ergebnissen.

Experimentelle Untersuchen wurden in einem Mischungskühler bei Temperaturen nahe dem absoluten Nullpunkt durchgeführt, da einerseits die Sprungtemperatur zur Supraleitung unterschritten sein muss und es zweitens von entscheidender Bedeutung ist, dass sowohl für Qubit als auch Resonator keine thermischen Anregungen aus dem Grundzustand auftreten. Letzteres setzt Anforderungen sowohl an geringe Temperaturen als auch an ein geringes Rauschlevel der Eingangssignale, da die Energieaufspaltungen der beteiligten Systeme im Mikrowellenbereich liegen. Der Messplatz wurde dahingehend entwickelt und angepasst. Das beinhaltet eine Verankerung der Proben für guten thermischen Kontakt und eine Minimierung des eingetragenen Rauschens bei der Verkabelung und durch Abschirmung.

Das Probendesign wurde so ausgelegt, dass der Resonator zur Charakterisierung des angekoppelten Qubits dient, also als Detektor für den Qubitzustand. Orientierend an vorhergehenden Arbeiten [36, 39, 43] bedeutet dies, dass die Linienbreite des Resonators kleiner ist

als die durch das Qubit verursachte Verschiebung der Resonanzfrequenz im Grundzustand, oft auch als dispersive Verschiebung oder Krümmung des Grundzustandes beschrieben. Im Vergleich zu den zuvor verwendeten Resonatoren aus diskreten Elementen müssen Wellenleiterresonatoren daher eine sehr viel höhere Güte aufweisen, da auch die Eigenfrequenzen entsprechend höher liegen.

Anhand einer ersten Serie experimenteller Untersuchen wird gezeigt, dass alle wesentlichen Parameter der Einzelsysteme durch kontinuierliche Messung der Transmission eines Probensignals durch den Resonator bestimmt werden können. Die Kopplung zwischen Fluss-Qubit und Resonator wird durch eine Kopplungsinduktivität erzeugt. Diese wirkt sich auf die Transmissionseigenschaften des Resonators aus. Mit Hilfe der sogenannten Zwei-Ton-Spektroskopie wurde die Energieaufspaltung des Qubits in Abhängigkeit vom externen Kontrollfeld bestimmt. Dabei wird ein zusätzliches Mikrowellensignal mit variierender Frequenz eingestrahlt. Dieses hebt bei Resonanz mit dem Übergang des Qubits die dispersive Verschiebung auf. Vergleichend wird dabei auf zwei Proben eingegangen und Unterschiede in den Messergebnissen erklärt, die durch eine unterschiedliche minimale Energieaufspaltung zustande kommen. Detailliert wird auf die Entstehung der Spektroskopielinie eingegangen und der Einfluss der Zerfallsraten des Qubits diskutiert. Diese können ebenso wie die Kopplungskonstante zwischen Qubit und Resonator bestimmt werden. Mit Hilfe des Dichtematrix-Formalismus werden Erwartungswerte des Feldes und der Besetzung der Qubitzustände berechnet und mit experimentellen Ergebnissen verglichen. Dabei wird eine sehr gute Übereinstimmung zwischen Theorie und Experiment gefunden. Gleichzeitig dient die mathematische Beschreibung als Prototyp für weitere Untersuchungen.

In weiteren experimentellen und theoretischen Untersuchungen wird die Wirkung eines starken Mikrowellensignals, das mit einer Frequenz nahe einer Harmonischen des Resonators angelegt wird, untersucht. Experimentelle Ergebnisse, wie der Übergang vom dispersiven zum resonanten Regime, können mit einer AC-Zeeman Verschiebung erklärt werden. Dabei verändert die hohe Photonenanzahl im Resonator effektiv die Energieaufspaltung des Qubits. Mit Hilfe einer Drei-Ton Spektroskopie wird dies überzeugend experimentell bestätigt. Daraus entsteht die Möglichkeit, mit dem zusätzlichen Mikrowellensignal einen weiteren Kontrollparameter einzuführen.

Im Rahmen der Beschreibung mit geordneten Zuständen (dressed states) kann der Einfluss auf effektive Energieaufspaltung und Relaxationsraten nachvollzogen werden. Von entscheidender Bedeutung ist dabei, dass sowohl Zerfall aber auch Anregung des Systems, abhän-

gig vom Vorzeichen der Verstimmung des Mikrowellensignals zum Qubit, erreicht werden können. Im Resonanzfall ist dagegen lediglich eine ausgeglichene Besetzung zu erreichen. Anhand von Leveldiagrammen und Berechnung wird dies begründet. Dabei wird das System aus Qubit und hochangeregtem Strahlungsfeld zu einem effektiven Zwei-Niveau-System reduziert. Darin ist die Anregungsrate proportional zur Zerfallsrate des originalen Qubits. Gekoppelt an die fundamentale Mode des Resonators werden damit analytische Berechnungen durchgeführt. In einer Reihe von Experimenten werden sowohl Verstärkung als auch Abschwächung eines Testsignals nachgewiesen.

Zum Nachweis des Lasing-Effekts wurde eine spezielle Probe hergestellt. Dabei dient ein in der Nähe des Qubits eingebrachter Goldwiderstand der Erhöhung der Relaxationsraten und damit der schnelleren Anregung im effektiven System. In einer Reihe von Experimenten werden optimale Bedingungen für den Verstärkungseffekt ermittelt. Außerdem zeigt eine Leistungsabhängigkeit den additiven Charakter der Verstärkung des Testsignals. Unabhängig von der Eingangsleistung ist die Anzahl der zusätzlichen Mikrowellenphotonen pro Zyklus nur durch das Verhältnis der Anregungsrate, der System-Resonator Kopplung und der Zerfallsrate des Resonators bestimmt.

Eine spektrale Analyse ohne Testsignal zeigt selbsterhaltende Oszillationen und damit den Lasing-Effekt. Diese werden durch eine Erhöhung der abgestrahlten Leistung und einer Verringerung der Linienbreite um 20 % im Vergleich zur thermischen Resonatoranregung nachgewiesen. Kontrollmessungen an verschiedenen Arbeitspunkten schließen außerdem andere mögliche Ursachen einer Signalerhöhung aus. In weiteren Optimierungen mit unseren Kollegen aus Bratislava, die über diese Arbeit hinausgehen, konnte die Verstärkung auf den Faktor neun erhöht werden [116].

Weitere Messungen der Transmission eines schwachen Testsignals bei Frequenzen nahe der Fundamentalmode und unter starker auf das Qubit wirkender Mikrowellenleistungen zeigen außerdem ein reiches Spektrum an Verstärkungs- und Abschwächungsregionen. Daher wird abschließend das Gesamtsystem in einem generalisierten Ansatz beschrieben. Dadurch können Multiphotoneninteraktionen sowohl zur Anregung des Qubits als auch in der Kopplung an den Resonator in die Berechnung einbezogen werden und diese in den Messresultaten erklärt und zugeordnet werden. Allerdings finden sich auch einige Facetten, wie z.B. eine Verstärkung nahe dem Entartungspunkt des künstlichen Atoms, die von dem Modell noch nicht erfasst sind. Dies kann in den verwendeten Näherungen, wie der Restriktion auf zwei Energieniveaus des Qubits, begründet liegen. Dennoch kann das entwickelte theoretische

Modell zur Beschreibung einer Vielzahl von Experimenten der Pump-Probe-Technik genutzt werden. Aktuelle Untersuchungen befassen sich mit einer weiteren Verallgemeinerung im Rahmen von sogenannten Rabi-ähnlichen Oszillationen, welche durch Landau-Zener-Stückelberg-Majorana Übergängen zustande kommen [120].

Die Nutzung eines starken Mikrowellensignals zur Manipulation der Zustände und Besetzungen eines künstlichen Atoms hat neben einem fundamentalen Interesse verschiedene mögliche Anwendungsbereiche. Diese reichen von einer von der Verstärkung eines Testsignals über die Signalerzeugung auf einem Chip bis zu einer zusätzlichen Kontrolle über die Energieaufspaltung des Qubits. Damit wird die Palette der Werkzeuge für quantenoptische Experimente auf einem Chip erweitert und ein Beitrag zum besseren Verständnis für die Wechselwirkung zwischen (künstlichen) Atomen und elektromagnetischer Strahlung geleistet.